ISSN 1880-8468

# Technical Report of International Development Engineering
国際開発工学報告

TRIDE-2011-01 February 15, 2011

# Abstracts of Master Theses Presented in February 2011

Department of International Development Engineering,
Graduate School of Science and Engineering,
Tokyo Institute of Technology
**http://www.ide.titech.ac.jp/TR**

# Preface

Master theses of Department of International Development Engineering, Tokyo Institute of Technology were presented successfully on August 3, 2010 and February 15, 2011. This technical report consists of the abstracts of those theses.

**Technical Report of International Development Engineering**
**TRIDE-2011-03**

## Table of Contents

# Energetical consideration of the effect of a sinusoidal surface roughness on the pin-on-disk contact processes

Student Number: 08M18039 Name: Takashi OTAKE Supervisor: Kunio TAKAHASHI

# 表面粗さのある物体の接触過程に対する系のエネルギーに基づく検討

大竹貴士

表面粗さの凝着現象に対する影響を理解することは重要である. 本研究では正弦波状表面粗さを持つ剛体球と平面弾性体の軸対称接触モデルを考え, 系のトータルエネルギーを計算した. 外力の載荷過程と除荷過程に於いて接触半径が異なることをエネルギーカーブを用いて説明し, ファミが行った実験との比較を行った.

## 1 Introduction

A surface roughness plays a significant role in the control of the adhesion force. Theoretically, Johnson has clarified the adhesion process between elastic spheres and obtained the force curve , which is the relation between the penetration distance and the external force[1]. In experiments, Fami observed hysteresis between the penetration distance and the contact radius [2]. Lei discuss about the effect of the surface roughness on hysteresis loops experimentally[3]. Guduru has proposed a theory that a contact between a flat elastic half-space and a rigid sphere with a sinusoidal surface roughness[4]. Guduru has obtained the force curve of the model, and the force curve suggested there is more than one solution of the penetration distance when the force is applied, but the contact process isn't clarified.

In this study, total energy of an axisymmetric contact model between a rigid sphere with a sinusoidal surface roughness and a flat elastic half space is calculated , and a discussion about contact processes from the view point of local minimums of energy curves is carried out in order to clarify the effect of the surface roughness on the hysteresis.

## 2 Model of an axisymmetric contact with a sinusoidal surface roughness

Figure. 1 shows an axisymmetric contact model between a rigid sphere with sinusoidal surface roughness and a flat elastic half space. The rigid surface profile is expressed as eq.(1)[4].

$$y = \frac{r^2}{2R} + A\left(1 - \cos\left(\frac{2\pi r}{\lambda}\right)\right) \tag{1}$$

It is assumed that surface roughness is the sinusoidal which amplitude is $A$, and wavelength is $\lambda$. The sphere curvature is $R$, Young's modulus of the elastic half-space is $E$, Poisson ratio is $\nu$, an external force is $P$ , a contact radius is $a$, a penetration distance is $h$, energy is $U$, work of the adhesion per

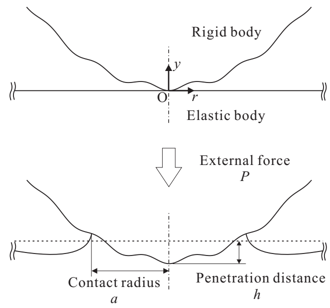


Fig. 1: axisymmetric contact model with a sinusoidal surface roughness

unit area is $\gamma$. In this study, we have nomalized each factors as follows.

$$\bar{U} = \frac{U}{2E^*\lambda^3}, \bar{P} = \frac{P}{2E^*\lambda^2}, \bar{h} = \frac{h}{\lambda}, \bar{a} = \frac{a}{\lambda}, \bar{A} = \frac{A}{\lambda},$$
$$\bar{\lambda} = \frac{\lambda}{R}, \gamma' = \frac{2\pi\gamma}{E^*R}, E^* = \frac{E}{1-\nu^2}$$

## 3 Total energy of the model

The total energy of the model is defined as eq.(2).$\bar{U}_e$ is the elastic energy,$\bar{U}_a$ is the work of the adhesion, $\bar{U}_m$ is the mechanical potential energy.

$$\bar{U}_{total} = \bar{U}_e + \bar{U}_a + \bar{U}_m \tag{2}$$

where,

$$\bar{U}_e = \int_0^{\bar{a}} \bar{P}_1 \frac{d\bar{h}}{d\bar{a}} d\bar{a} - \frac{\bar{P}_1^2 - \bar{P}^2}{2\bar{a}} \tag{3}$$

$$\bar{U}_a = -\frac{\gamma' \bar{a}^2}{4\bar{\lambda}} \tag{4}$$

$$\bar{U}_m = -\bar{P}\left(\bar{h} - \frac{\bar{P}_1 - \bar{P}}{\bar{a}}\right) \tag{5}$$

where,

$$\bar{P}_1 = (2\bar{\lambda} + 4\pi^2\bar{A})\frac{\bar{a}^3}{3} + \frac{\pi\bar{A}\bar{a}}{2}H_1(2\pi\bar{a}) - \pi^2\bar{A}\bar{a}^2H_2(2\pi\bar{a}) \tag{6}$$

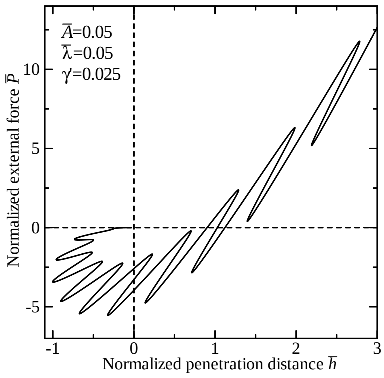


Fig. 2: force curve of the axisymmetric contact model with a sinusoidal surface roughness

$$\bar{h} = \bar{\lambda}\bar{a}^2 + \pi^2 \bar{A}\bar{a}H_0(2\pi\bar{a}) \tag{7}$$

$$H_n(z) = \frac{2\left(\frac{z}{2}\right)^n}{\sqrt{\pi}\Gamma\left(n+\frac{1}{2}\right)} \int_0^1 (1-t^2)^{n-\frac{1}{2}} \sin(zt)dt \tag{8}$$

# 4 Energetical consideration

Guduru has obtained the relation between the external force and the penetration distance(Fig.2), but contact processes hasn't been clarified[4]. In this section, we discuss about contact processes on the force curve considering the local minimum of the energy curve.(energetical consideration)

## 4.1 Loading process

Fig.3-Fig.6 shows the loading process. The intitial contact is $S_0$(Fig.3). Based on energetical consideration, it is clarified that the contact radius changes to $S_1$. Next, the external force changes to 2.0 from 0.0, the contact radius shift is $S_1 \to S_2$. Fig.4 shows corresponding points($S_0 \to S_1 \to S_2$) of this loading process on the force curve.

Next, the external force changes to 2.6 from 2.0, the contact radius shift is $S_2 \to S_3 \to S_4 \to S_5$ In Fig.5, Fig.6. It is shown that the energy curve at $S_3$ is not the local minimum when the external force is 2.38... . Consequently, the contact radius shift is $S_4$ from $S_3$ when the external force isn't varied.

## 4.2 Unloading process

Fig.7-Fig.10 shows the unloading process. The external force changes to 1.0 from 10.0, the contact state shift is $S_6 \to S_8$. Fig.8 shows corresponding points($S_6 \to S_7 \to S_8$) of this unloading process on the force curve.

Next, the external force changes to 0.0 from 1.0, the contact state shift is $S_8 \to S_9 \to S_{10} \to S_{11}$ In Fig.9, Fig.10. It is shown that the energy curve at $S_9$ is not the local minimum when the external force

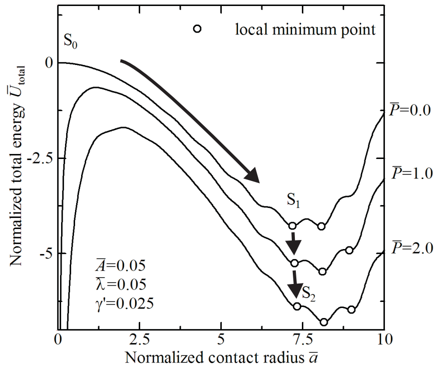


Fig. 3: energy curves in loading process

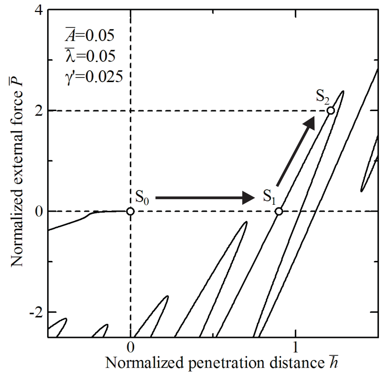


Fig. 4: force curve in loading process

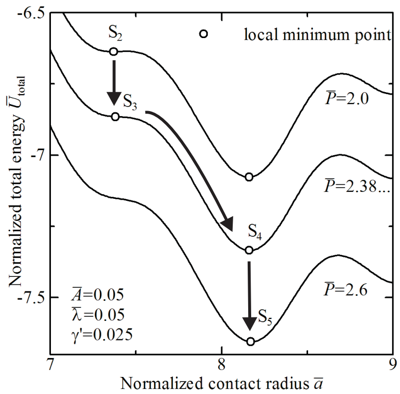


Fig. 5: dissipation of the local minimum in loading process

is 0.39... . Consequently, the contact radius shift is $S_{10}$ from $S_9$ when the external force isn't varied.

## 4.3 Detaching process

Fig.11,Fig.12 shows the detaching process. When the external pressure changes to -5.54... , the local minimum dissipate in Fig.11.($S_{13}$) Consequently, the contact radius changes to 0.0, and the detachment occurs. Fig.12 shows the detaching process on the force curve.

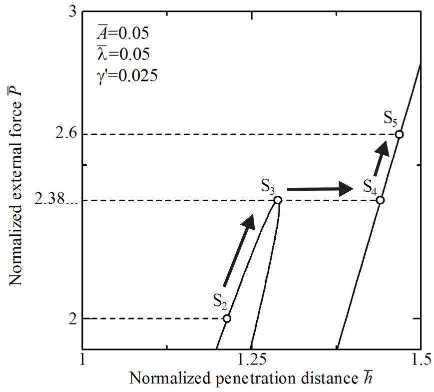


Fig. 6: jump of penetration distance in loading process

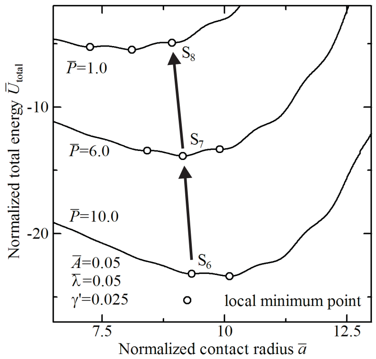


Fig. 7: energy curves in unloading process

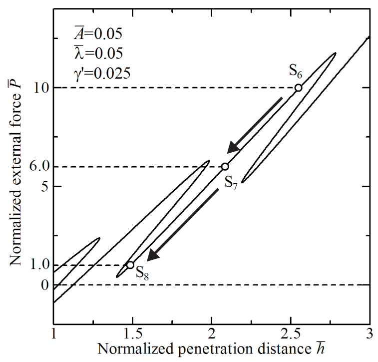


Fig. 8: force curve in unloading process

## 4.4 Hysteresis based on the energetical consideration

Based on the energetical consideration, the hysteresis of contact process between loading process and unloading process is obtained(Fig.13). In JKR-theory(no surface roughness model), the hysteresis of contact processes doesn't exist. So, these results suggest a possibility that the surface roughness effects on contact processes.

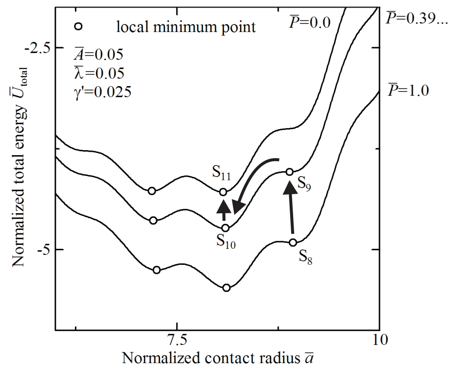


Fig. 9: dissipation of the local minimum in unloading process

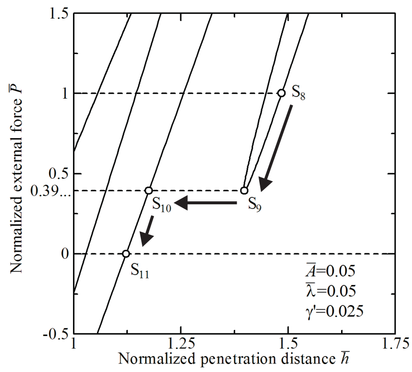


Fig. 10: jump of the penetration distance in unloading process

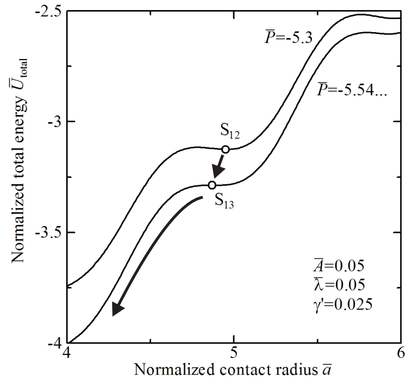


Fig. 11: energy curves in detaching process

# 5 Comparison to the experimental results

Fig.14 is Fami's experimental results about JKR contact model , and it shows a tendency that the adhesion hysteresis diminish as the contact radius increased[2]. Fig.15 is the relation between the penetration distance and the contact radius based on the energetical consideration. The curve drawn as a short dash line is expressed as eq.(9.)

$$h_G(a) = \bar{\lambda}\bar{a}^2 + \pi^2\bar{A}\bar{a}H_0(2\pi\bar{a}) - \sqrt{\frac{\gamma'\bar{a}}{\bar{\lambda}}} \qquad (9)$$

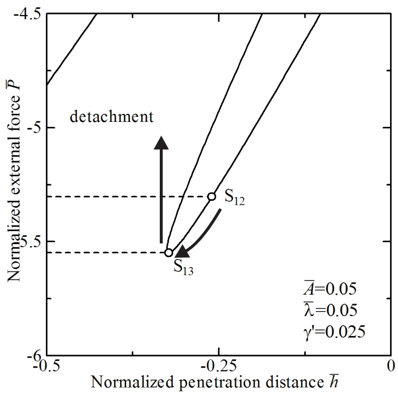


Fig. 12: force curve in detaching process

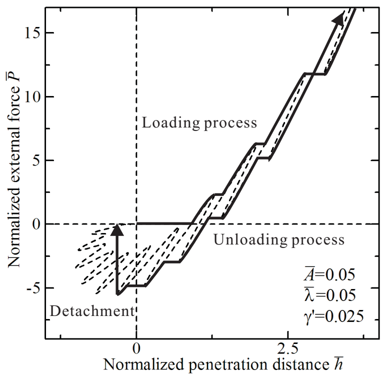


Fig. 13: hysteresis based on energetical consideration

To clarify the effect of the surface roughness on the hysteresis, we define eq.(10) as the measurement of the hysteresis. $h_J$ is the penetration distance of JKR contact model.

$$\frac{h_G - h_J}{h_J} = \frac{\pi^2 \bar{A}\bar{a}H_0(2\pi\bar{a})}{\bar{\lambda}\bar{a}^2 - \sqrt{\frac{\gamma'\bar{a}}{\bar{\lambda}}}} \tag{10}$$

,where

$$h_J(a) = \bar{\lambda}\bar{a}^2 - \sqrt{\frac{\gamma'\bar{a}}{\bar{\lambda}}} \tag{11}$$

In eq.(10), $H_0$ is the struve function, and the value is decreased as the contact radius increased. Consequently,

$$\frac{h_G - h_J}{h_J} \propto \frac{1}{\bar{a}} \tag{12}$$

eq.(12) means that there is a similar tendency between experimental results and the energetic consideration.

In the experiment, There is the surface roughness distribution exists in the direcion of rotation, but the sinusoidal surface roughness of the axisymmetric model don't achieve. So, the results doesn't assent, but there is a possibility that the energetic consideration of the axisymmetric model expresses the tendency of the effect of the surface roughness on the adhesion contact.

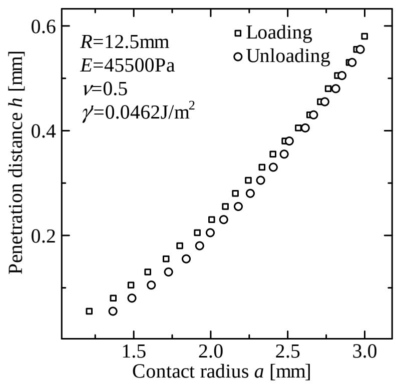


Fig. 14: Fami's experimental results

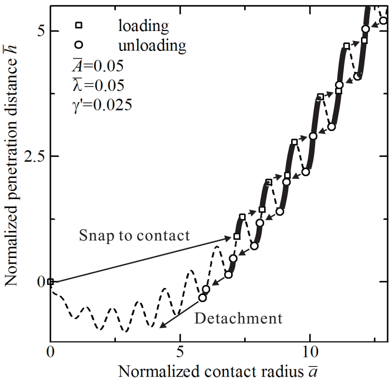


Fig. 15: hysteresis of the penetration distance between loading and unloading process

# 6 Conclusion

We calculate total energy of the model an axisymmetric contact with a sinusoidal surface roughness, and obtain local minimums of energy curves. Based on the energetical consideration, we clarify the contact process in the loading, unloading, and detachment process. We get the hysteresis based on the energetical consideration, and compared with the experimental results of JKR contact model.

# References


[1] Johnson,K.L.,Kendall,K. and Roberts,A.D.R., "Surface energy and the contact of elastic solids", *Proc.Roy.Soc.London* 1971, A, 324, 301-313.

[2] Fami,M., "Time dependence of the adhesion contact between elastic plane and rigid sphere", *Bachelor Thesis(Tokyo Institute of Technology)*, 2008.

[3] Lei,L., "Experimental study on adhesion behavior between rough surfaces of solid bodies", *Master Thesis(Tokyo Institute of Technology)*, 2008.

[4] Guduru,P.R., "Detachment of a rigid sorid from an elastic wavy surface:Theory", *J.Mecs.Phys.Solids*, 2007, Vol.55, 445-472

# Numerical Analysis of Non-axisymmetric Flow between Concentric Spheres Using a Spectral Finite Difference Scheme

Student Number: 08M18080 Name: Toru SANO Supervisor: Yoshihiro MOCHIMARU

# スペクトル差分法による同心二球間非軸対称自然対流の数値解析

佐野 徹

スペクトル差分法の三次元非軸対称流れへの適用性について検討を行う．三次元流れとして同心二球間自然対流を想定した．球間の流体は実質的に非圧縮性ニュートン流体で満たされ，球の中心を通る軸に対し下向きに重力が作用しているものとし，三次元定常流れを求積する．低グラスホフ数に対するある温度分布に対応する境界値問題を解く範囲では，適用は可能であることが判明した．

## 1. Introduction

A spectral finite difference scheme was developed by MOCHIMARU [1]. This is a method for improving numerical computation, where one or two independent variables in space are separated even for the nonlinear convective terms. Thus the number of independent variables is reduced by one or two respectively, and the numerical computation time is greatly reduced.

The scheme has been used mainly for two-dimensional numerical analyses [2]. For this reason, in this study, to investigate its adaptability to three-dimensional numerical analysis, analyzed is a non-axisymmetric flow between concentric spheres using the spectral finite difference scheme.

## 2. Numerical analysis

### 2.1 Physical models and assumptions

Physical models are as follows: Natural convection is generated between the concentric spheres. An analysis domain is three-dimensional space. A spherical polar coordinates, ($r$, $\theta$, $\phi$), is used. Assumptions are as follows: Fluid between the concentric spheres is assumed to be incompressible and Newtonian. Flow is steady.

### 2.2 Mathematical models

Under these physical models and assumptions, the basic equations derived from the equation of continuity, the equation of motion with buoyancy under Boussinesq approximation, and the equation of energy are expressed as

$$\nabla \cdot \boldsymbol{\upsilon} = 0, \tag{1}$$

$$\rho_0 \frac{D\boldsymbol{\upsilon}}{Dt} = -\nabla p + \rho_0\left[1-\beta(T-T_0)\right]\boldsymbol{g} + \mu_0 \nabla^2 \boldsymbol{\upsilon}, \tag{2}$$

$$\rho_0 c_p \frac{DT}{Dt} = \kappa \nabla^2 T, \tag{3}$$

respectively, where $\boldsymbol{\upsilon}$, $\rho_0$, $t$, $p$, $\beta$, $T$, $T_0$, $\boldsymbol{g}$, $\mu_0$, $c_p$ and $\kappa$ are velocity vector, density of fluid, time, pressure, coefficient of thermal expansion, temperature, reference temperature, gravitational acceleration vector, viscosity of fluid, specific heat at constant pressure and thermal conductivity, respectively.

In solving the basic equations, three-dimensional vorticity, $\boldsymbol{\omega}$, and three-dimensional stream function, $\boldsymbol{\psi}$, are introduced so that

$$\boldsymbol{\omega} = \nabla \times \boldsymbol{\upsilon}, \tag{4}$$

$$\boldsymbol{\upsilon} = \nabla \times \boldsymbol{\psi}. \tag{5}$$

The vorticity transport equation, Eq. (6), is derived from Eq. (2), and relationship between three-dimensional vorticity and three-dimensional stream function, Eq. (7), is given by Eqs. (4) and (5).

$$\frac{D\boldsymbol{\omega}}{Dt} = -\beta \nabla T \times \boldsymbol{g} + (\boldsymbol{\omega}\cdot\nabla)\boldsymbol{\upsilon} + \frac{\mu_0}{\rho_0}\nabla^2 \boldsymbol{\omega}, \tag{6}$$

$$\begin{aligned} \boldsymbol{\omega} &= \nabla \times (\nabla \times \boldsymbol{\psi}) \\ &= \nabla(\nabla\cdot\boldsymbol{\psi}) - \nabla^2 \boldsymbol{\psi}. \end{aligned} \tag{7}$$

Let $Gr$ denote a Grashof number, which is defined as

$$Gr = \frac{{\rho_0}^2\, g\, \beta\, a^3 (T_h - T_c)}{{\mu_0}^2}, \tag{8}$$

where $a$ is an outer sphere radius, $(T_h - T_c)$ is the maximum temperature difference in the fluid. Then Eqs. (6) and (7) are non-dimensionalized using the following reference values:

- reference length: $a$.
- reference velocity: $\upsilon_0 = \mu_0 \sqrt{Gr} / (\rho_0\, a)$.
- reference temperature: $T_0 = T_h - T_c$.

Thus, the following non-dimensionalized vorticity transport equation and the relationship between three-dimensional vorticity and three-dimensional stream function are obtained:

$$\begin{aligned} &\frac{\partial \omega_r}{\partial t} + \upsilon_r \frac{\partial \omega_r}{\partial r} + \frac{\upsilon_\theta}{r}\frac{\partial \omega_r}{\partial \theta} + \frac{\upsilon_\phi}{r\sin\theta}\frac{\partial \omega_r}{\partial \phi} \\ &- \frac{\upsilon_\theta \omega_\theta + \upsilon_\phi \omega_\phi}{r} - \omega_r \frac{\partial \upsilon_r}{\partial r} - \frac{\omega_\theta}{r}\frac{\partial \upsilon_r}{\partial \theta} \\ &- \frac{\omega_\phi}{r\sin\theta}\frac{\partial \upsilon_r}{\partial \phi} \\ &= \frac{1}{r}\frac{\partial T}{\partial \phi} + \frac{1}{\sqrt{Gr}}\left(\nabla^2 \omega_r - \frac{2\omega_r}{r^2} - \frac{2}{r^2}\frac{\partial \omega_\theta}{\partial \theta}\right. \\ &\left. - \frac{2\omega_\theta \cot\theta}{r^2} - \frac{2}{r^2 \sin\theta}\frac{\partial \omega_\phi}{\partial \phi}\right), \end{aligned} \tag{9}$$

$$\frac{\partial \omega_\theta}{\partial t} + \upsilon_r \frac{\partial \omega_\theta}{\partial r} + \frac{\upsilon_\theta}{r}\frac{\partial \omega_\theta}{\partial \theta} + \frac{\upsilon_\phi}{r\sin\theta}\frac{\partial \omega_\theta}{\partial \phi} + \frac{\upsilon_\theta \omega_r - \upsilon_\phi \omega_\phi \cot\theta}{r} - \omega_r \frac{\partial \upsilon_\theta}{\partial r} - \frac{\omega_\theta}{r}\frac{\partial \upsilon_\theta}{\partial \theta} - \frac{\omega_\phi}{r\sin\theta}\frac{\partial \upsilon_\theta}{\partial \phi}$$
$$= \frac{\cot\theta}{r}\frac{\partial T}{\partial \phi} + \frac{1}{\sqrt{Gr}}\left(\nabla^2 \omega_\theta + \frac{2}{r^2}\frac{\partial \omega_r}{\partial \theta} - \frac{\omega_\theta}{r^2 \sin^2\theta} - \frac{2\cos\theta}{r^2\sin^2\theta}\frac{\partial \omega_\phi}{\partial \phi}\right), \tag{10}$$

$$\frac{\partial \omega_\phi}{\partial t} + \upsilon_r \frac{\partial \omega_\phi}{\partial r} + \frac{\upsilon_\theta}{r}\frac{\partial \omega_\phi}{\partial \theta} + \frac{\upsilon_\phi}{r\sin\theta}\frac{\partial \omega_\phi}{\partial \phi} + \frac{\upsilon_\phi \omega_r + \upsilon_\phi \omega_\theta \cot\theta}{r} - \omega_r \frac{\partial \upsilon_\phi}{\partial r} - \frac{\omega_\theta}{r}\frac{\partial \upsilon_\phi}{\partial \theta} - \frac{\omega_\phi}{r\sin\theta}\frac{\partial \upsilon_\phi}{\partial \phi}$$
$$= -\frac{\cos\theta}{r}\frac{\partial T}{\partial \theta} - \sin\theta\frac{\partial T}{\partial r} + \frac{1}{\sqrt{Gr}}\left(\nabla^2 \omega_\phi - - \frac{\omega_\phi}{r^2 \sin^2\theta} + \frac{2}{r^2\sin\theta}\frac{\partial \omega_r}{\partial \phi} + \frac{2\cos\theta}{r^2\sin^2\theta}\frac{\partial \omega_\theta}{\partial \phi}\right), \tag{11}$$

$$\omega_r = \frac{1}{r^2}\frac{\partial \psi_\theta}{\partial \theta} + \frac{\psi_\theta \cos\theta}{r^2\sin\theta} + \frac{\cos\theta}{r\sin\theta}\frac{\partial \psi_\theta}{\partial r} + \frac{1}{r}\frac{\partial \psi_\theta}{\partial r\partial \theta} - \frac{\cos\theta}{r^2\sin\theta}\frac{\partial \psi_r}{\partial \theta} - \frac{1}{r^2}\frac{\partial^2 \psi_r}{\partial \theta^2} - \frac{1}{r^2\sin^2\theta}\frac{\partial^2 \psi_r}{\partial \phi^2} + \frac{1}{r^2\sin\theta}\frac{\partial \psi_\phi}{\partial \phi} + \frac{1}{r\sin\theta}\frac{\partial^2 \psi_\phi}{\partial \phi \partial r}, \tag{12}$$

$$\omega_\theta = \frac{1}{r^2\sin\theta}\frac{\partial^2 \psi_\phi}{\partial \theta\partial \phi} + \frac{\cos\theta}{r^2\sin^2\theta}\frac{\partial \psi_\phi}{\partial \phi} - \frac{1}{r^2\sin^2\theta}\frac{\partial^2 \psi_\theta}{\partial \phi^2} - \frac{2}{r}\frac{\partial \psi_\theta}{\partial r} - \frac{\partial^2 \psi_\theta}{\partial r^2} + \frac{1}{r}\frac{\partial \psi_r}{\partial r\partial \theta}, \tag{13}$$

$$\omega_\phi = \frac{1}{r\sin\theta}\frac{\partial^2 \psi_r}{\partial \phi\partial r} - \frac{2}{r}\frac{\partial \psi_\phi}{\partial r} - \frac{\partial^2 \psi_\phi}{\partial r^2} - \frac{1}{r^2}\frac{\partial^2 \psi_\phi}{\partial \theta^2} - \frac{\cos\theta}{r^2\sin\theta}\frac{\partial \psi_\phi}{\partial \theta} + \frac{\psi_\phi}{r^2\sin^2\theta} - \frac{\cos\theta}{r^2\sin^2\theta}\frac{\partial \psi_\theta}{\partial \phi} + \frac{1}{r^2\sin\theta}\frac{\partial^2 \psi_\theta}{\partial \theta\partial \phi}. \tag{14}$$

### 2.3 Analytical solution of the energy equation

For low $Gr$, Eq. (3) can be approximated by a heat conduction equation. That is, a boundary value problem corresponding to Eq. (15) is solved.

$$T = r\sin\theta\sin\phi. \tag{15}$$

### 2.4 Fourier series expansion

In order to express the physical quantities and to decompose the basic equations into each spectral component, the following Fourier series expansion is used:

$$\begin{bmatrix} \omega_r \\ \omega_\theta \\ \omega_\phi \\ \psi_r \\ \psi_\theta \\ \psi_\phi \end{bmatrix} = \sum_{n=0}^{\infty} \begin{bmatrix} \omega_{rcn} \\ \omega_{\theta cn} \\ \omega_{\phi cn} \\ \psi_{rcn} \\ \psi_{\theta cn} \\ \psi_{\phi cn} \end{bmatrix} \cos n\phi + \sum_{n=1}^{\infty} \begin{bmatrix} \omega_{rsn} \\ \omega_{\theta sn} \\ \omega_{\phi sn} \\ \psi_{rsn} \\ \psi_{\theta sn} \\ \psi_{\phi sn} \end{bmatrix} \sin n\phi. \tag{16}$$

$\omega_{rcn}, \cdots, \psi_{\phi sn}$ are the Fourier coefficients, which are the function of $\theta$, $r$, and $t$.

Substituting Eq. (16) into the basic equations (9)-(14) gives the following form:

$$\sum_{k=0}^{\infty} F_{ck} \cos k\phi + \sum_{k=1}^{\infty} F_{sk} \sin k\phi = 0, \tag{17}$$

where $F_{ck}, F_{sk}$ are Fourier coefficients. Equation (17) gives

$$F_{ck} = 0,\ F_{sk} = 0. \tag{18}$$

Thus the spatial variable, $\phi$, is separated.

### 2.5 Introduction of new variables

In order to avoid $1/\sin\theta$ in the basic equations, the following new variables except for $\omega_{rc1}$, $\omega_{rs1}$, $\psi_{rc1}$ and $\psi_{rs1}$ are introduced:

$$\begin{bmatrix} \omega_{frcn} \\ \omega_{frsn} \\ \omega_{f\theta cn} \\ \omega_{f\theta sn} \\ \omega_{f\phi cn} \\ \omega_{f\phi sn} \\ \psi_{frcn} \\ \psi_{frsn} \\ \psi_{f\theta cn} \\ \psi_{f\theta sn} \\ \psi_{f\phi cn} \\ \psi_{f\phi sn} \end{bmatrix} = \frac{1}{\sin^2\theta} \begin{bmatrix} \omega_{rcn} \\ \omega_{rsn} \\ \omega_{\theta cn} \\ \omega_{\theta sn} \\ \omega_{\phi cn} \\ \omega_{\phi sn} \\ \psi_{rcn} \\ \psi_{rsn} \\ \psi_{\theta cn} \\ \psi_{\theta sn} \\ \psi_{\phi cn} \\ \psi_{\phi sn} \end{bmatrix}. \tag{19}$$

For $\omega_{rc1}$, $\omega_{rs1}$, $\psi_{rc1}$ and $\psi_{rs1}$, the following new variables are used:

$$\begin{bmatrix} \omega_{frc1} \\ \omega_{frs1} \\ \psi_{frc1} \\ \psi_{frs1} \end{bmatrix} = \frac{1}{\sin\theta} \begin{bmatrix} \omega_{frc1} \\ \omega_{frs1} \\ \psi_{frc1} \\ \psi_{frs1} \end{bmatrix}. \quad (20)$$

### 2.6 Fourier series expansion

Furthermore, in order to express the physical quantities and to decompose the basic equations into each spectral component, the following Fourier series expansion is used:

$$\begin{bmatrix} \omega_{frcn} \\ \omega_{frsn} \\ \omega_{f\theta cn} \\ \omega_{f\theta sn} \\ \omega_{f\phi cn} \\ \omega_{f\phi sn} \\ \psi_{frcn} \\ \psi_{frsn} \\ \psi_{f\theta cn} \\ \psi_{f\theta sn} \\ \psi_{f\phi cn} \\ \psi_{f\phi sn} \end{bmatrix} = \sum_{m=0}^{\infty} \begin{bmatrix} \omega_{frcncm} \\ \omega_{frsncm} \\ \omega_{f\theta cncm} \\ \omega_{f\theta sncm} \\ \omega_{f\phi cncm} \\ \omega_{f\phi sncm} \\ \psi_{frcncm} \\ \psi_{frsncm} \\ \psi_{f\theta cncm} \\ \psi_{f\theta sncm} \\ \psi_{f\phi cncm} \\ \psi_{f\phi sncm} \end{bmatrix} \cos m\theta + \sum_{m=1}^{\infty} \begin{bmatrix} \omega_{frcnsm} \\ \omega_{frsnsm} \\ \omega_{f\theta cnsm} \\ \omega_{f\theta snsm} \\ \omega_{f\phi cnsm} \\ \omega_{f\phi snsm} \\ \psi_{frcnsm} \\ \psi_{frsnsm} \\ \psi_{f\theta cnsm} \\ \psi_{f\theta snsm} \\ \psi_{f\phi cnsm} \\ \psi_{f\phi snsm} \end{bmatrix} \sin m\theta. \quad (21)$$

$\omega_{frcncm}, \cdots, \psi_{f\phi snsm}$ are the Fourier coefficients, which are the function of $r$ and $t$.

Similarly, the spatial variable, $\theta$, is separated.

### 2.7 Governing equations

In a numerical analysis, only linear terms are used in Eqs. (9)-(14). In addition, Fourier coefficients only of $\cos 0\phi$, $\cos\phi$, $\sin\phi$, $\cos 0\theta$, $\cos\theta$ and $\sin\theta$ are used at the Fourier series expansions. The following governing equations (22)-(27) are used for a numerical analysis.

$$\frac{\partial^2 \omega_{frc1c0}}{\partial r^2} + \frac{2}{r}\frac{\partial \omega_{frc1c0}}{\partial r} - \frac{4\omega_{frc1c0}}{r^2} - \frac{2\omega_{f\phi s1c0}}{r^2} + \sqrt{Gr} = 0, \quad (22)$$

$$\frac{2\psi_{frc1c0}}{r^2} + \frac{\psi_{f\phi s1c0}}{r^2} + \frac{1}{r}\frac{\partial \psi_{f\phi s1c0}}{\partial r} - \omega_{frc1c0} = 0, \quad (23)$$

$$\frac{1}{4}\frac{\partial^2 \omega_{f\theta c1c1}}{\partial r^2} + \frac{1}{2r}\frac{\partial \omega_{f\theta c1c1}}{\partial r} - \frac{\omega_{f\theta c1c1}}{r^2} + \frac{2\omega_{frc1c0}}{r^2} - \frac{2\omega_{f\phi s1c0}}{r^2} + \sqrt{Gr} = 0, \quad (24)$$

$$\frac{1}{4}\frac{\partial^2 \psi_{f\theta c1c1}}{\partial r^2} + \frac{1}{2r}\frac{\partial \psi_{f\theta c1c1}}{\partial r} - \frac{\psi_{f\theta c1c1}}{r^2} - \frac{3\psi_{f\phi s1c0}}{r^2} - \frac{1}{r}\frac{\partial \psi_{frc1c0}}{\partial r} + \frac{\omega_{f\theta c1c1}}{4} = 0, \quad (25)$$

$$\frac{1}{2}\frac{\partial^2 \omega_{f\phi s1c0}}{\partial r^2} + \frac{1}{r}\frac{\partial \omega_{f\phi s1c0}}{\partial r} - \frac{\omega_{f\phi s1c0}}{r^2} - \frac{2\omega_{frc1c0}}{r^2} - \frac{\omega_{f\theta c1c1}}{r^2} - \sqrt{Gr} = 0, \quad (26)$$

$$\frac{1}{2}\frac{\partial^2 \psi_{f\phi s1c0}}{\partial r^2} + \frac{1}{r}\frac{\partial \psi_{f\phi s1c0}}{\partial r} + \frac{1}{r}\frac{\partial \psi_{frc1c0}}{\partial r} + \frac{\omega_{f\phi s1c0}}{2} = 0. \quad (27)$$

### 2.8 Boundary conditions

No-slip conditions at the boundaries apply. That is, along the boundaries

$$\boldsymbol{\upsilon} = (\upsilon_r, \upsilon_\theta, \upsilon_\phi) = (0, 0, 0). \quad (28)$$

Equation (28) can be decomposed into the Fourier series expansion in $\phi$ and $\theta$ along the boundaries. That is, No-slip conditions at an inner wall and outer wall are given by

$$\psi_{f\theta c1c1} + \psi_{f\phi s1c0} = 0, \quad (29)$$

$$\frac{\psi_{frc1c0}}{r} + \frac{\psi_{f\phi s1c0}}{2r} + \frac{1}{2}\frac{\partial \psi_{f\phi s1c0}}{\partial r} = 0, \quad (30)$$

$$\frac{\psi_{frc1c0}}{r} - \frac{\psi_{f\theta c1c1}}{4r} - \frac{1}{4}\frac{\partial \psi_{f\theta c1c1}}{\partial r} = 0. \quad (31)$$

Especially, without loss of generality, at the inner wall,

$$\psi_{frc1c0} = 0. \quad (32)$$

### 2.9 Numerical integration

Runge-Kutta method of 4th order can be used for a numerical integration. The numerical integration is computed from the inner boundary toward the outer boundary. Accordingly, a steady solution is obtained by a linear combination of a special solution and an auxiliary solution.

## 3. Results and discussions

### 3.1 Numerical results

Figure 1 shows velocity vectors and temperature at *y-z* plane, $Gr = 1.0$ . And Fig. 2 shows velocity vectors at *z-x* plane, $Gr = 1.0$ . Likewise, Fig. 3 shows velocity vectors and temperature at *y-z* plane, $Gr = 0.01$ . And Fig. 4 shows velocity vectors at *z-x* plane, $Gr = 0.01$ .

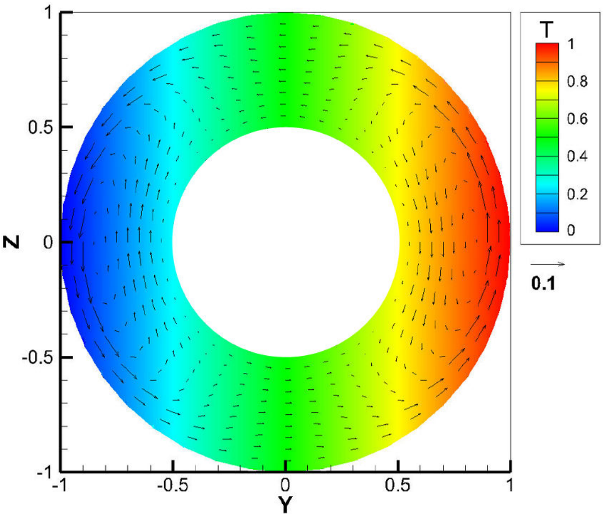


Fig. 1 Velocity vectors and temperature at $y$-$z$ plane, $Gr$ = 1.0 .

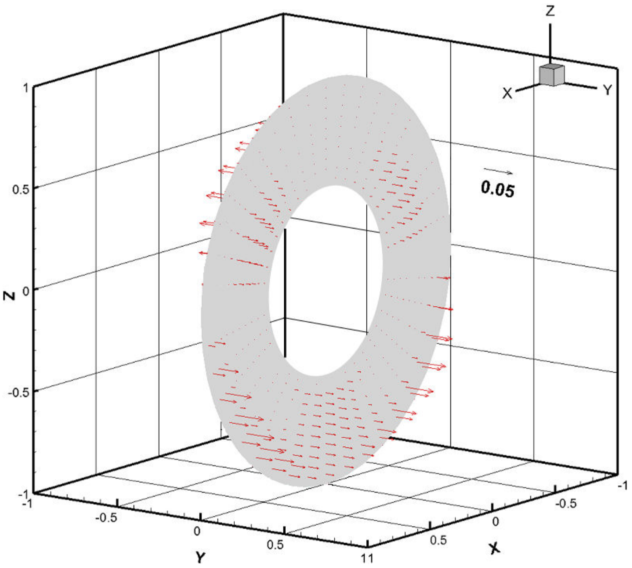


Fig. 2 Velocity vectors at $z$-$x$ plane, $Gr$ = 1.0 .

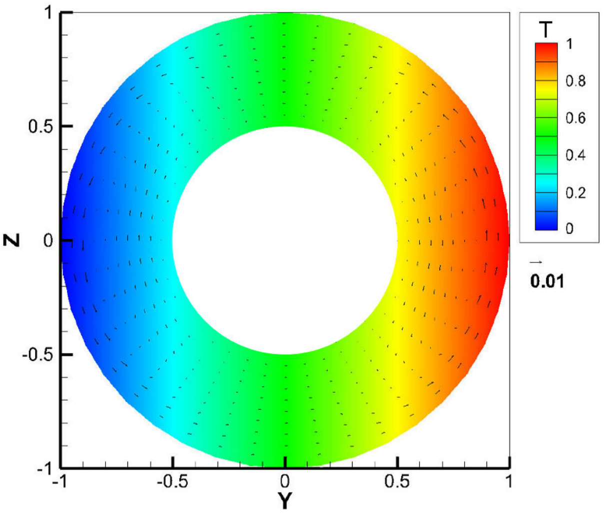


Fig. 3 Velocity vectors and temperature at $y$-$z$ plane, $Gr$ = 0.01 .

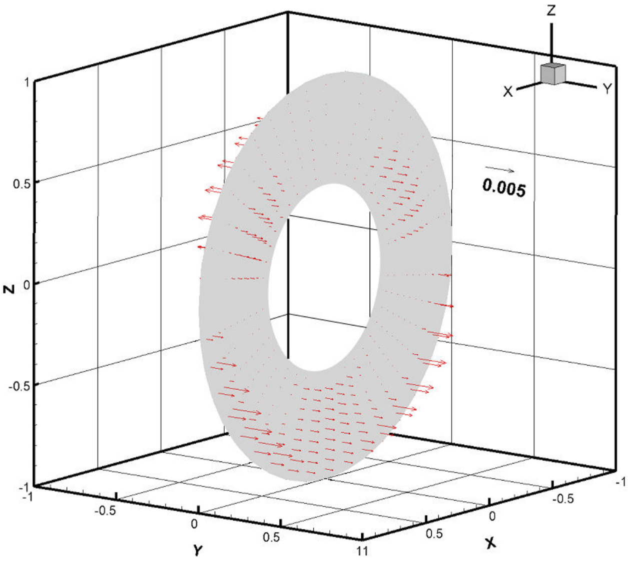


Fig. 4 Velocity vectors at $z$-$x$ plane, $Gr$ = 0.01 .

### 3.2 Discussions

In Figs. 1 and 3, two circulations are shown at both sides of $y$-axis. In addition, a flow is generated along the outer boundary. In Figs. 2 and 4, some larger velocity vectors can be confirmed at both sides of $x$-axis.

## 4. Conclusion

In order to investigate its adaptability of a spectral finite difference scheme to a three-dimensional numerical analysis, analyzed is a three-dimensional flow between concentric spheres using the scheme. As a result of the analyses, it has been found that one three-dimensional model can be analyzed using the scheme. The accuracy of the simulation would be improved by taking into account the non-liner terms and high-order Fourier coefficients.

## References

[1] Mochimaru, Y., New way for simulation of transient natural convection heat transfer, *International Journal of Heat and Fluid Flow*, Vol.8, No.3(1987), pp.235-239.

[2] Mochimaru, Y., A Spectral Finite Difference Scheme and its Effectiveness, *Proc. 26th Ann. Iranian Mathematics Conference*, Vol.2(1995), pp.245-254.

# Microwave-assisted synthesis of protoberberine and its characteristic

Student Number: 08M51479 Name: Makoto Suzuki Supervisor: Sachio Hirose, Kiyohiko Nakasaki

# マイクロ波によるベルベリン誘導体の合成とその特性に関する研究

鈴木 真

本研究では、ベルベリンの代謝物であるベルベリン誘導体を合成するため、マイクロ波を用いてベルベリンからベルベリン誘導体の合成方法を検討し、反応温度、初期 pH、反応時間の反応への影響を明らかにする。オートクレーブによる加熱方法とマイクロ波による加熱方法とを比較する。次に、様々な添加剤を添加し、添加剤による反応への影響を明らかにした。また、溶媒についても検討を行った。添加剤と溶媒を変えることにより異なるベルベリン誘導体を選択的に合成できることを明らかにした。

## 1. Introduction

Protoberberine alkaloids have various activities such as antimicrobial [1], anti-inflammatory [2], antimalarial [3], and anti-diabetic activities [4]. Among them, berberine (BER) has a long history of medicinal use in traditional medicine and it has been widely investigated. However, only few researches have been studied the activities of other protoberberines. Recently, it was reported that BER was metabolized to be protoberberines such as berberrubine (BBR), columbamine, dehydro-discretamine, demethylene-berberine (DMB), jatrorrhizine (JAT), and thalifendine (TLF), which were observed in human urine (Fig. 1) [5]. This evidence suggested that the pharmacological effect of BER could be derived from its metabolites. However, they are too complex for cost-effective chemical synthesis and the plants contain very small amount of protoberberines. Therefore, it is difficult to study the pharmacological effects of protoberberines.

Microwave energy has been widely used for heating food materials, and recently, there has been an increasing interest in using microwave as heat source for chemical synthesis. Microwave-assisted synthesis has been used for the synthesis of some chemical compounds, for example, for deacetylation [6], and for cross-coupling reaction [7]. In many cases, shorter reaction time and higher selectivity were observed comparing with conventional heating method. However, only an experiment for producing of BBR from BER was conducted using microwave at atmospheric pressure [8] and the characteristics of microwave-assisted synthesis are not fully understood. In addition, no method has been reported for the synthesis of TLF.

The purpose of this research is to develop a method for microwave-assisted synthesis of protoberberines from BER and compare to the synthesis using autoclave. In addition, the effects of additives and solvent are investigated.

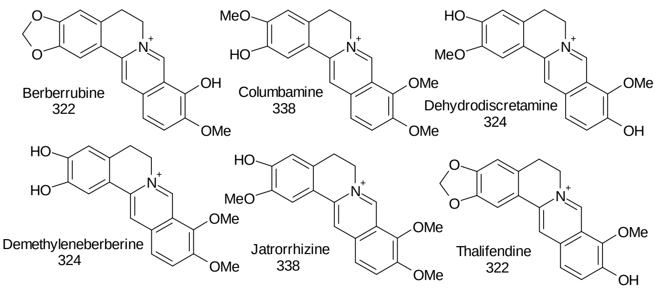


Fig.1 Metabolites of BER

## 2. Materials and Methods

### 2.1 Materials

All chemicals were purchased from Wako Pure Chemicals Co., Japan. Ultra pure water produced by the Milli-Q Advantage vessel (Millipore, USA) was used in this study.

### 2.2 Microwave-assisted synthesis

The microwave apparatus Mars-X (CEM, USA), as shown in Fig. 2, was used for microwave-assisted synthesis. It can be operated with an output power of up to 1600 W (2450 MHz). The temperature was measured using the fiber optic temperature probe RTP-300 Plus, and pressure was measured using the ESP-1500 Plus.

The microwave apparatus automatically adjusted the radiated power when the actual temperature reached the set temperature. The experiments were performed in a Teflon-made Green Chem vessel with a capacity of 100 mL, which could operate under a temperature of up to 180℃ and a pressure of up to 1.38 MPa (200 PSI). The initial output power was set at 300 W. A volume of 20 mL of BER solution (2 mmol / L) was put in the vessel and radiated by microwave. The reaction vessel was cooled down for 30 min before filtration.

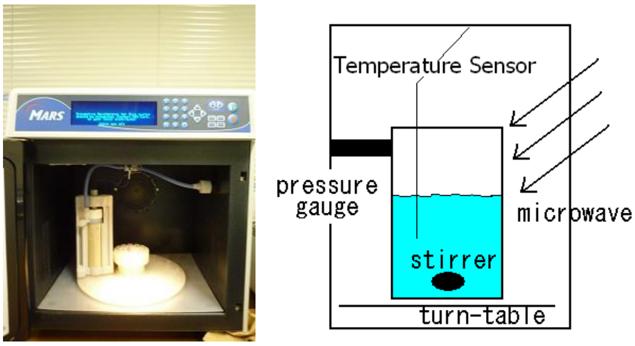


Fig. 2 Microwave apparatus

## 2.3 Autoclave synthesis

The autoclave used for autoclave synthesis was shown in Fig. 3. The temperature was measured using thermocouple and pressure was measured by pressure gage. The autoclave automatically adjusted the output power when the actual temperature reached the set temperature. The output power was set at 100 V. A solution (20 mL) of 2 mmol/L berberine was used for the reaction. The reaction vessel was cooled down for 1 h before filtration.

## 2.4 Effect of initial pH

The initial pH of the solution was adjusted to 3-11 using sodium hydroxide and hydrochloric acid. The pH was measured by pH meter model F-55 (Horiba, Japan).

## 2.5 Effect of additives

Each additive (0.5g) was added into 20 mL of BER solution. After the reaction, the solution was filtered by No. 40 (Whatman, UK). The filtered additive was desorbed in methanol (20mL) for 24 h.

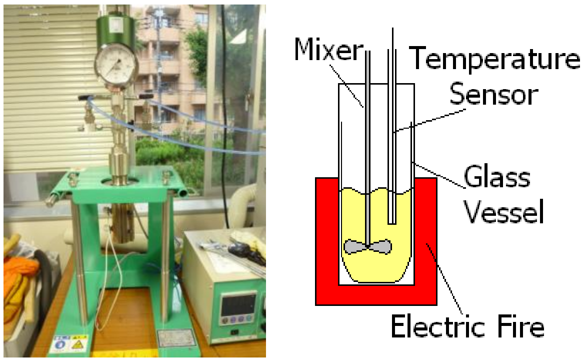


Fig. 3 Autoclave

## 2.6 Effect of solvents

A BER solution (2 mmol/L) was prepared in each solvent. All the sample was filtered through filter paper No.40. The filtrate was diluted 5 times in ultra pure water, and then filtered using a 0.45-μm membrane filter (Toyo Roshi Kaisha, Japan) for liquid chromatography mass spectrometry (LC/MS) analysis.

## 2.7 LC/MS analysis

The quantification of BBR, BER, DMB, and TLF was performed using LC/MS-2010EV apparatus (Shimadzu, Japan). The separation was carried out in a ZORBAX Eclipse XDB column (3.5 μm, 2.1 × 150mm) (Agilent Technology, USA). The mobile phase, which consisted of a 0.1% formic acid aqueous solution (A) and methanol (B), was delivered at a flow rate of 0.2 mL/min using the following gradient program: 25% (B) for 0–15 min, 25–30% (B) for 15–32 min, 30-70% (B) for 32–47 min 70% (B) for 47–52 min, and 25% (B) for 52–60 min. The sample injection volume was 1 μL, and the column temperature was maintained at 40°C. The UV spectra were obtained by scanning the samples in the range of 200–470 nm. The amounts of BBR, BER, DMB, and TLF were calculated from the peak area at 345 nm.

# 3. Results and discussion

## 3.1 LC/MS analysis

Fig. 4 shows UV chromatogram at 345 nm of the BER solution after radiated by microwave for 30 min. DMB , TLF , BBR , and BER were observed at retention time of 14.5 min, 21.4 min, 29.3 min, and 29.9 min, respectively. The compounds were determined by its retention time, mass to charge radio (*m/z*) and comparing with literature.

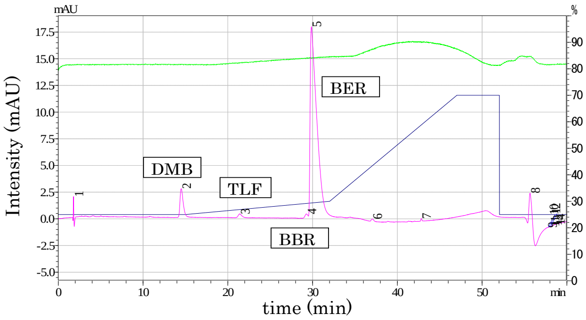


Fig. 4 UV chromatogram at 345 nm

### 3.2 Effect of temperature

Fig. 5 shows the peak area of protoberberines by microwave-assisted synthesis. DMB was not observed at the temperature up to 120℃. The DMB yield increased with an increase in the temperature above 140℃. The peak area of DMB was highest at 180℃. The reaction was performed at the temperature up to 180℃ because of the limit thermal-resistance of microwave vessel (200℃).

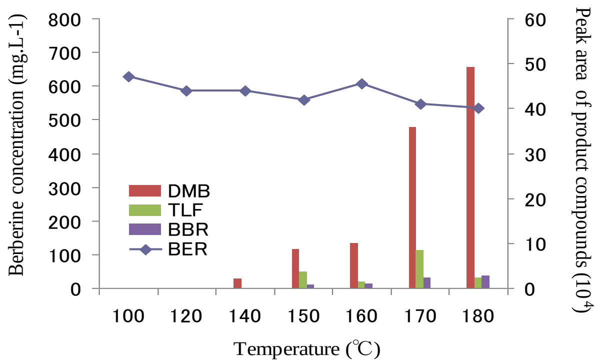


Fig. 5 Effect of temperature

### 3.3 Effect of initial pH

Fig. 6 shows the effect of initial pH. DMB was produced when the experiment conducted in the initial pH from 2.7 to 8, but DMB peak area was highest around the initial pH 6-7. However, DMB peak area was decreased at pH 9 and was not observed at pH 11. On the other hand, BBR was generated at pH 11 as a major production compound.

### 3.4 Effect of reaction time

Microwave heated BER solution to 180℃ in 5 min. On the other hand, it took 30 min for the experiment by autoclave. Fig. 7 and Fig. 8 show the effect of reaction time by microwave and autoclave. The peak area of protoberberines increased with an increase in the reaction time. Microwave-assisted synthesis gave faster reaction than that of autoclave. Within 90 min of microwave radiation, BER was decreased by 75% of initial concentration.

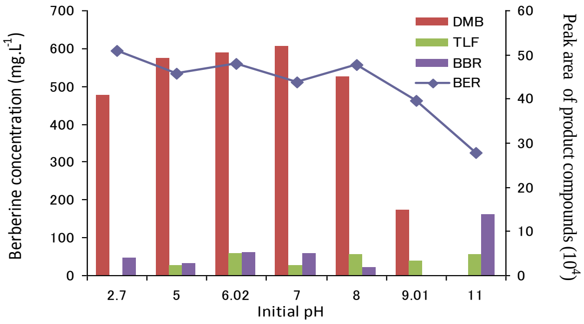


Fig. 6 Effect of initial pH

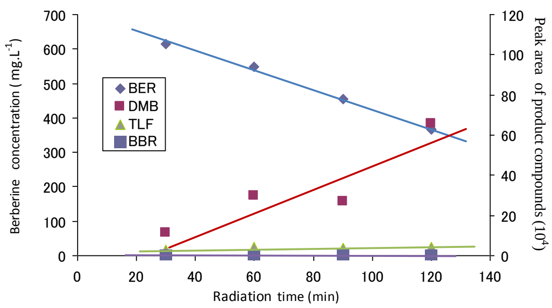


Fig. 7 Effect of reaction time (MW)

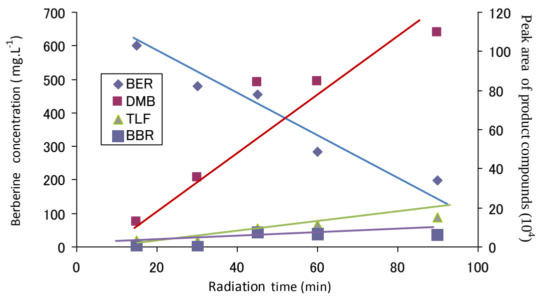


Fig. 8 Effect of reaction time (Autoclave)

### 3.5 Effect of additives

The additive material such as cellulose and Iron oxide could absorbed microwave and increased the surface temperature. Thus, they may enhance the degradation of BER and increase the amount of other protoberberines. Fig. 10 and Fig. 11 show the effect of additives by microwave and autoclave. In microwave radiation, Carboflon and cellulose gave higher yield of DMB compared to experiment without the additive. Fe and $Co_3O_4$ produced BBR as main product. SiC, Al, and $Fe_3O_4$ gave low yield of DMB. On the other hand, DMB was not observed when using CuO, CuI, $Fe_3O_4$, and Co. TLF was produced when using $Cu_2O$ and CoO as the additives. From this result, only some materials can increase protoberberines. The other characteristic of the additives rather than microwave absorbing ability could cause the difference in the amount and molecular structure of protoberberines.

In most experiment using the additives, microwave-assisted synthesis gave higher yields of protoberberines compared to those of autoclave synthesis. However, SiC, Al, and CuI gave lower yields of DMB.

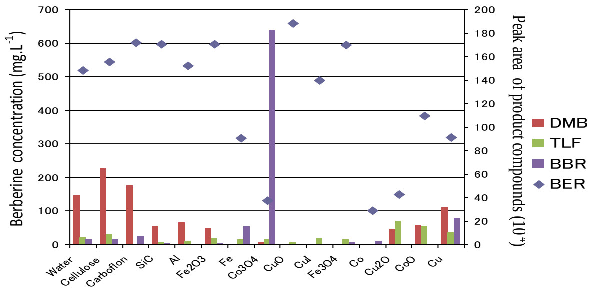


Fig. 9 Effect of additive (MW)

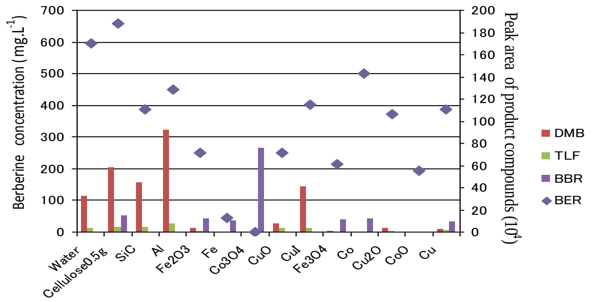


Fig. 10 Effect of additive (Autoclave)

Fig. 11 shows the effect of amount of cellulose on the degradation of BER and peak area of protoberberines. As the amount of cellulose increased, peak area of DMB was increased, while there was no big different for the peak area of TLF and BBR. In addition, the peak area of DMB by using 5 g cellulose was decreased compared to 2 g.

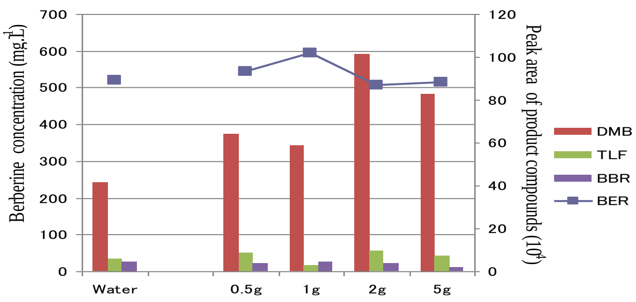


Fig. 11 Effect of cellulose weight (MW)

### 3.6 Effect of solvents

Fig. 12 and Fig. 13 shows the effect of solvent and 1-propanol solution on the yield of protoberberines. the solution of 20-60% ethanol and 20-100% ethylene glycol gave lower yield of protoberberines than water. When using pure 1-propanol as a solvent, the main compound was BBR. However, for the 1-propanol aqueous solution the peak area of BBR decreased. The more water contents, the more DMB was generated. Mixed solvent inhibited the reaction.

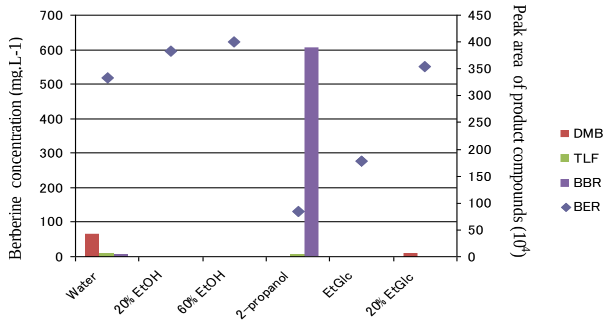


Fig. 12 Effect of solvent (MW)

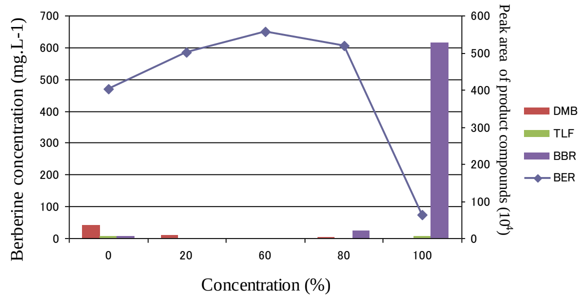


Fig. 13 Effect of 1-propanol (MW)

### 4. Conclusion

This study shows that it is possible to use microwave as a heat source for synthesis of protoberberines. Using additives such as $Cu_2O$ and CoO, TLF was synthesized from BER with microwave radiation. BBR was produced selectively when using $Co_3O_4$ as the additive or 1-propanol as solvent. Microwave-assisted synthesis gave faster reaction for production of protoberberines than that of autoclave.

### Reference

[1] Iwasa, et al..,J. Nat. Prod., 61, 1150-1153 (1998)
[2] Kuo, et al.,Cancer Lett., 203, 127-137 (2004)
[3] Iwasa, et al., Eur. J. Med. Chem., 34, 1077-1083 (1999)
[4] Ko, et al., Biol.Pharm. Bull., 28, 1431-1437 (2005)
[5] Feng, et al.: DMD., 36, 2159-2165 (2008)
[6] Varma, R. S. et al., J. Chem. Soc. Perkin. Trans. 1, 999 (1993)
[7] Kabalka. G. W, et al., Tetrahedron Lett., 41, 5151 (2000)
[8] Das, B. et al., Synth. Commun., 32, 19, 3027-3029 (2002)

# MODELING THE DOMESTIC FRESH PRODUCT SUPPLY CHAIN IN BANGLADESH

**Student number: 08M51485** **Name: Rubel DAS** **Supervisor: Shinya HANAOKA**

This study focuses on the fresh product (such as vegetable, flower etc.) distribution system in developing country, focusing on Bangladesh, a South Asian country. Domestic fresh-product distribution in developing country faces difficulties from endogenous distribution system. Reasons for it can be enumerated as immature infrastructure, socio-economic aspect, shortcoming of farming system, low information flow etc. Involvement of intermediary, who acts as link between farmer and consumer, makes the deficiency severe. This total system creates postharvest wastage, low bargain power of farmer, higher distribution cost, and also exposure to health risk. To overcome the endogenous problems, supply chain redesign strategy has been adopted. Bargain power can be increased by making cooperative. Horizontal cooperation accumulates their product and gets higher scale of transport efficiency. Poor distribution system of vegetable in city level is one of the reasons for high price. Mathematical formulation was proposed to solve this problem. Service level and fixed charge facility location model were combined to make a integrated model. This model dictates the location of distribution center and allocation of demand point. Distribution in city level was assumed to be conducted as Cooperative Distribution System (CDS), which is cheaper than the uncoordinated distribution. Sensitivity analysis was done to show the trade-off between service level and transportation cost.

## 1. Introduction

Unlike developed country, developing country economy is dependent on agriculture. Bangladesh (study area), a South Asian country, is an example of agriculture dependent country, where agriculture is contributing 23% of the Gross Domestic Product (GDP) in 2006 and absorbs more than 62% work force. Total land area under vegetable cultivation has increasing trend. Instead of good production, farmer still cannot get benefit it. It is said that if transport services are infrequent or poor quality or expensive, then farmer will be at a disadvantage when they attempt to sell their product. Addition to transport service, vegetable grower are facing problem from perishability and seasonality attribute of product, requirement of conditioned storage, product variation (due to weather and biological factors) etc.

Besides farmer's deficiency, developing country is facing problem from high distribution cost and consequence is higher food price. To minimize the burden of poor consumer, developing country focus on subsidy, price fixing, food aid program etc. But little attention is paid in lowering the cost for food distribution. By considering this situation, it is found that there is a gap where supply chain management, which deals with the efficient product distribution with minimum cost, can be applied to fill up the gap.

Therefore, this research focused on identification of limitation of current vegetable distribution and on formulation of new proposed supply chain. More specifically, this research covers the following issues:

- Identify current vegetable distribution system and limitation.
- Redesign the role of actor in fresh product flow.
- Formulate a mathematical model for facility location for fresh product distribution by using integer programming.

## 2. Existing distribution system

This research focuses on domestic distribution. Farmer has two options for selling vegetable, one is local (short distance from farm location) sell and another is distance market (usually Dhaka, Chittagong etc.).

Differences between two different option are the number of intermediary (is defined as the vegetable owner between farmer and retailer) and transport mode. Unlike local distribution, distance market distribution needs a number of intermediaries (as shown in Figure 1). Those intermediaries are known as different name depending on position oneself in vegetable distribution chain: Faria, Bepary, Arathdar, Paikar etc (equivalent English term can be found in the box beside Figure 1).

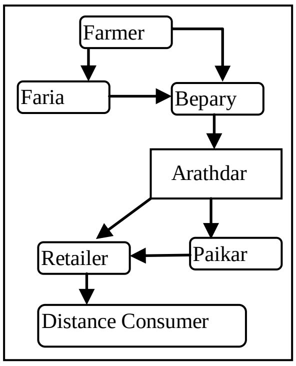


*Equivalent english term:*
*Faria*= Collector (in village).
*Bepary*= Trader and transporter.
*Arathdar*= Commission agent.
*Paikar*= Distributor (in city level)

**Figure 1: Relationship among intermediary**

Different types of modes are being used to complete a full chain. Farmer and Faria use van. Truck is used to carry vegetable to distance market by Bepary and CNG (a three wheel motorized vehicle), pickup, Rickshaw (a three wheel non-motorized vehicle) etc. are used for vegetable distribution in city level by Paikar and Retailer. Each transport mode has different capacity and speed; and so different cost structure.

## 3. Limitation of current product flow

Small scale farmer stay always in disadvantage position during selling vegetable. Situations compel them to produce staple crop which is regarded as less profitable. Besides this, there are a number of limitations in current product flow, described below.

- Bargain power: Farmer does not have bargain power in selling vegetable; that is required for Pareto efficient marketing system.
- Transaction based business: Intermediary does not have fixed investment in vegetable business; which makes them more flexible to leave the business. This situation makes the business environment with no purposeful intention to deliver the best products.
- Quality declination: Vegetable quality deteriorates for poor marketing system and transportation system. Other reason for deterioration can be identified as poor packaging and handling methods.
- Long marketing time: Marketing processing of vegetable takes long time in existing system.
- Price difference: Price difference of same product can be found in short distance outlet. Table 1 can describe this situation.

**Table 1. Price of bean within short distance**

| | Kawran bazar | Hatirpul bazar | Polashi bazar |
|---|---|---|---|
| Bean price | 55 tk/kg | 65 tk/kg | 70 tk/kg |
| Distance from kawran bazar | 0 | 1.14 km | 2.7 km |
| based on survey data, 2009 | | | |

## 4. Proposed new supply chain

Deficiency of existing supply chain (involvement of intermediary, inefficient transport system etc.) occurs due to scaling problem of farmer. This scaling problem also increases transaction cost (information cost, negotiation cost, monitoring cost (Hobbs, 1997)).

Horizontal cooperation has potential to reduce the transaction cost. The negotiation cost depends on market structure; cooperation can increase the bargain power. Monitoring cost can be decreased by aggregating product in same place which is possible in cooperation.

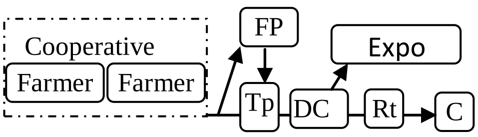


Legend:
FP= Food processor — Tp=Transporter
DC = Distribution center — Rt=Retailer
Expo= Exporter — C= Consumer

**Figure 2: Proposed new supply chain**

With the fulfillment of scale, cooperative get a potentiality to contract with transporter, a third party. Transporter, supposed to optimize transport cost, is assigned for long haul starting from village. Transporter delivers vegetable to DC. DC is designed as a store point, from where vegetable is distributed to Rt by cooperative delivery system (CDS). CDS is successful in the delivery environment where the sizes of deliveries are small (Qureshi et al, 2005). Inclusion of food processor and export agent, increase the scope of value addition in vegetable.

Table (2) and Table (3) illustrate expected change of supply chain after implementing proposed new supply chain. Proposed supply chain consists of lower number of actor compare to existing product flow chain.

**Table 2. Difference between current and proposed supply chain**

| Criteria | Existing product flow | New supply chain |
|---|---|---|
| Farmer power | Limited bargain power. | Has cooperative. |
| Transport service | On spot transport service. | Have contract with transport provider. |
| Flexibility (intermediary) | Anyone can leave business any moment. | Strong commitment. |
| Value addition | Little scope for value addition. | Increase the scope for value addition. |
| City transport | Non-integrated. | Integrated. |

New supply chain makes an environment of strong commitment for providing good service to customer. City level distribution of existing chain is done by non-integrated way, which loses scale of economies; Distribution in proposed model is done by cooperative distribution system.

**Table 3. Role change of actors**

| Role player | Current product flow | Proposed supply chain | Difficulties |
|---|---|---|---|
| Faria (Collector) | • Buy product from farmers and sell to Bepary. | • No transaction in village. • Farmer brings in cooperative. | • Intermediate means of transport is required. |
| Bepary (Trader) | • Buy product from farmers or Faria. • Transport product to distant market. | • No transaction in production zone. • Role change to distribution center owner. | • Contract with dedicated carriers for transporting product. |
| Paikar (Distributor) | • Buy product from Bepary. | • Transaction between retailer and distribution center. | • Needs city based transport operator. |

## 5. Mathematical formulation

The choice of location for DC is among the most critical strategic decisions. Both the cost of a distribution system and the level of service provided by the system are significantly affected by the number, size and location of DC, as well as by the decision on which customers to serve from each center.

Distribution system can be represented as directed nodes and arcs. Examples of infrastructure as nodes include retailer location, distribution center. Roads that connect nodes can be represented as arc.

This research solved the facility location model by integrating two models; one is fixed charge facility location model and another is minimized uncovered demand.

### 5.1. Fixed charge facility location model

Fixed charge facility location model is formulated by the minimization form. It makes trade-off between fixed cost and distribution cost.

$$\min z_1 = \sum_i a_i x_i + \sum_{ij} \alpha d_j c_{ij} f_{ij} \qquad (1)$$

Such that
$$\textstyle\sum_i f_{ij} = 1 \qquad (2)$$
$$f_{ij} \leq x_i \qquad (3)$$
$$x_i \in \{0,1\} \qquad (4)$$
$$f_{ij} \in \{0,1\} \qquad (5)$$

In this formula, fixed cost consists of rent, utilities and labor cost. Distribution cost represents transport cost. In general transport cost can be reduced by opening many facilities.

The objective function (equation 1) shows the trade-off between fixed cost and distribution cost. '$\alpha$' represents transport cost per distance per unit of demand and $a_i$ indicates fixed cost for opening DC at site 'i'. '$d_j$' and '$c_{ij}$' represent demand at 'j' and distance of 'j' from site 'i' respectively. Equation (2) represent all demand must be satisfied. Another interpretation of this equation is that one customer can accept vegetable from only one facility.

Equation (3) indicates one facility cannot serve customer if it is decided to shutdown. Only open facility can serve product to customer. Again if one facility serves at least one customer, this facility cannot be closed. Equation (4) and equation (5) are binary decision variables for site location ($x_i$) and demand point allocation ($f_{ij}$).

### 5.2. Minimize uncovered demand

The minimal uncovered demand problem identifies 'N' locations that minimize the amount of uncovered demand within a distance S (threshold distance for coverage) of at least.

$$\min z_2 = \sum_{ij} d_j q_{ij} f_{ij} \qquad (6)$$

Such that
$$\textstyle\sum_i f_{ij} = 1 \qquad (7)$$
$$\textstyle\sum_i x_i = N \qquad (8)$$
$$f_{ij} \leq x_i \qquad (9)$$
$$x_i \in \{0,1\} \qquad (10)$$
$$f_{ij} \in \{0,1\} \qquad (11)$$

The objective function (equation 6) illustrates the minimized of cost for uncovered demand. $q_{ij}$ is a binary variable, it takes the value equal 1 if a facility at candidate site 'i' cannot cover demand at 'j'; otherwise its value is zero (0). $d_j$ , $f_{ij}$ and $x_i$ explanation are similar to section 5.1. Equation (8) indicates that total number of open facility is a given constraint for minimize uncovered demand.

### 5.3. Integrated model for facility location

Whereas fixed charge facility location model focuses on cost and minimize uncovered demand focuses on service quality; those two models have been combined to select DC site for vegetable distribution in Dhaka. Integrated model is as follows.

$$\min z = \sum_i a_i x_i + \sum_{ij} \alpha d_j c_{ij} f_{ij} + \sum_{ij} w d_j q_{ij} f_{ij} \qquad (12)$$

such that
$$\textstyle\sum_i f_{ij} = 1 \qquad (13)$$
$$f_{ij} \leq x_i \qquad (14)$$
$$x_i \in \{0,1\} \qquad (15)$$
$$f_{ij} \in \{0,1\} \qquad (16)$$

In equation (12), 'w' is the weight given to the term of uncovered demand. All demand will be served but the uncovered demand will be served at a lower level of service. If 'w' is very large, the integrated model is equivalent to minimizing uncovered demand. On the other hand, for small value of 'w', the model turns to fixed cost facility location model.

## 6. Data and parameter

The author had made a survey in study area, required information were collected during this time.

Demand point location was decided after dividing Dhaka city in 27 zones according to thana boundary (lowest administrative unit). Each zone demand was computed following the function of zone population and daily consumption.

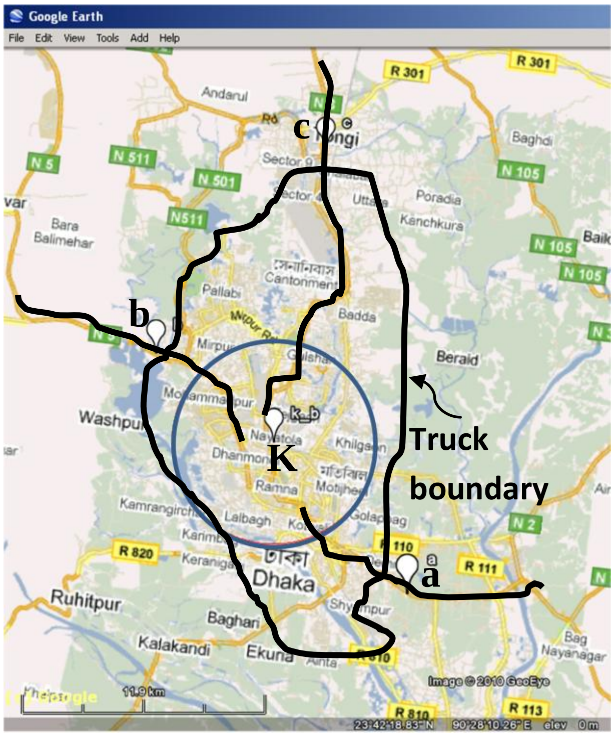


Source: Google earth, 2010.

**Figure 3: Location of four potential sites**

Potential facility location (shown in figure 3) were outside of truck restriction area (Big truck cannot enter in Dhaka city in day time). Transport cost data, based on survey, has been shown in table 4. Coverage factor ($q_{ij}$) was calculated by following equation 17(e. g. y=10 km).

$$\begin{aligned} &if\ c_{ij} > y\ then\ q_{ij} = 1 \\ &otherwise, q_{ij} = 0 \end{aligned} \qquad (17)$$

Road distance was collected from Google earth. To convert to actual distance 'circuity factor' has been used. It was done by following equation 18.

$$actual\_distance = 1.1 * Google\ earth\_distance \quad (18)$$

**Table 4. Transport cost**

| | Mini truck | Truck | Rickshaw / van | Taxi |
|---|---|---|---|---|
| Distance(km) | 60 | 200 | 5 | 15 |
| Capacity (kg) | 3,200 | 12,000 | 40 | 40 |
| Cost (taka) | 5,000 | 15,000 | 200 | 500 |
| Total cost (taka per kg-km) | 0.03 | 0.01 | 1.00 | 0.83 |

## 7. Results and analysis

Different scenarios were considered for DC site location and demand point allocation. In the first scenario, traffic congestion and Dhaka transport system was ignored (all potential location were considered). Second scenario was made considering transportation system, (potential site, k was omitted). It is because k is in center of Dhaka city, which create congestion in Dhaka.

**Table 5. Model comparison**

| | Model 1 | Model 2 |
|---|---|---|
| Objective value | 30.4 million [taka] 434,000 [USD] | 35.9 million [taka] 513,000 [USD] |
| Open facility | 1 | 2 |
| Demand point allocated at ‘a’ | 0 | 11 |
| Demand point allocated at ‘b’ | 0 | 16 |
| Demand point allocated at ‘c’ | 0 | 0 |
| Demand point allocated to Kawran bazar | 27 | 0 (closing K) |

In scenario one, it can found that for small $\alpha$ value, model suggest to open k. with the increase of $\alpha$ value model suggest to open new facility, it can be found in figure 4.

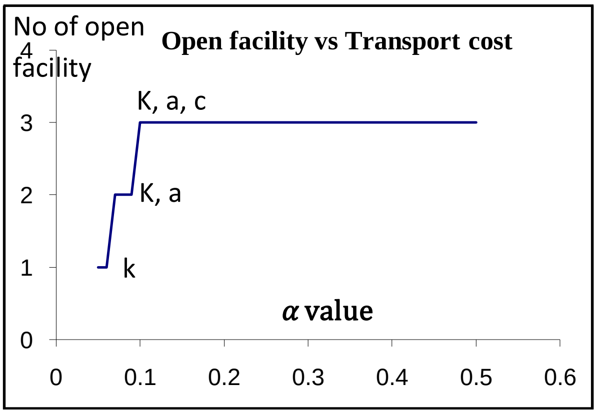


**Figure 4: Model 1 output**

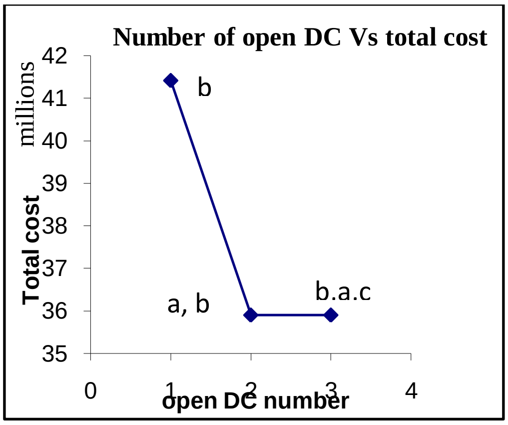


**Figure 5: Relationship of cost and open DC**

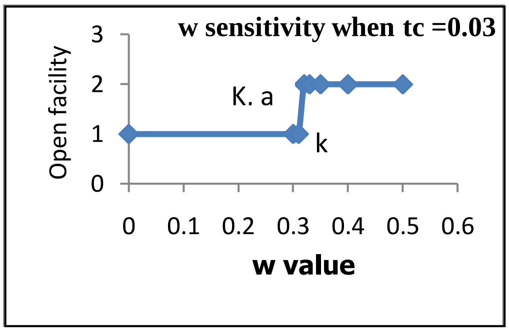


**Figure 6: Sensitivity of w value, in selecting facility location and allocation (single sensitivity is shown).**

To reduce the congestion and for improving the transportation system in Dhaka city, scenario two were made. Figure 5 (mode 2 output) illustrates the relationship between cost and number of open facility. It can be seen that in model 1 ‘b’ was not suggested to open. It can be said that model 2 output can be applied for improving the transport system in dhaka city, with minimizing vegetable distribution cost. Table 5 compare the model 1 and model 2 output. It also shows the allocation of demand point. Figure 6 shows sensitivity of ‘w’ values.

## 8. Conclusion

Intermediaries are looting the profit share of farmer. It is required to lower the number of intermediary for completing chain. Number of intermediaries can be minimized by proposed new supply chain model. Vegetable price in city level increase due to high distribution cost. Cost can be reduced by CDS. To do this DC is required. DC has been selected by following mathematical formulation.

### References


- Hobbs, J.E. (1996). A Transaction Cost Approach to Supply Chain Management, Supply Chain Management, 1(2: 15–27)
- Qureshi, A. G., Hanaoka, S. (2005). Analysis of the effects of a cooperative deliver system in Bankok. Proceeding of the 4th International Conference on city logistic, Langkawi, Malaysia, 2005.

# ANALYSIS OF SYNTHETIC CYLINDRICAL ARRAY BEAM-FORMING IN PRESENCE OF THE ELEMENTS POSITION-ERROR FOR SEMI-ANECHOIC CHAMBER EVALUATION

Student Number: 08M51491 Name: Karlisa Priandana Supervisor: Jun-ichi TAKADA

# 電波半無影響室評価用合成円筒アレーアンテナの素子位置誤差に対するビームフォーミング特性解析

カルリサ　プリアンダナ

本論文では、電波半無影響室の評価に供する円筒アレーアンテナの配列寸法と誤差を考慮し、低サイドローブビームフォーミング設計に対する実現可能なサイドローブ特性の評価を行った。ビーム形成には Dolph-Chebyshev アルゴリズムを用い、サイドローブレベルと素子位置誤差との関係を調べるためにモンテカルロシミュレーションを用いた。

## 1. Introduction

The rapid emergence of electromagnetic (EM) equipments has forced us to carefully conduct the electromagnetic compatibility (EMC) testing, to avoid the possibility of interference. Ideally, EMC testing is conducted in an open-area test site (OATS), an obstacle-free environment. However, it is inconvenient due to the high dependency on the changing factors of the environment. As a result, EMC test is conducted inside a semi-anechoic chamber (SAC): a room having walls and a ceiling equipped with EM absorbers, and a metallic ground. To simulate an OATS, SAC should be free from scattering waves other than the ground-reflected wave. However, in reality, the imperfect absorbers, corners, junctions, etc., may cause the SAC discrepancy from an ideal OATS. Therefore, evaluation of SAC is required.

This thesis proposes the utilization of beam-forming for SAC evaluation. The final goal of this research is to design the applicable beam-forming methodology for SAC evaluation. In this study, a synthetic cylindrical array antenna will be used. The low side-lobe requirement for SAC evaluation is realized by using Dolph-Chebyshev algorithm. Monte-Carlo simulations were conducted to find the optimal array parameters that can produce minimum side-lobe level at reasonable beam-width, under the antenna elements position-error.

## 2. Conventional Method of SAC Evaluation

Standardized validation methods to evaluate the SAC have been developed by CISPR/A [1]. The validation is established by finding the Site VSWR ($S_{\mathrm{VSWR}}$) of the SAC. Standing waves voltages are measured at discrete locations of receiving antenna (Fig. 1). By moving the antenna spatially, the phase between the direct and scattering (unwanted) waves will vary. When the waves add constructively, there is a peak response ($E_{\max}$) between the two antennas and when the waves add destructively, there is a minimum response ($E_{\min}$). $S_{\mathrm{VSWR}}$ is the ratio of the maximum peak to the minimum peak. For SAC of 1-18 GHz, the $S_{\mathrm{VSWR}}$ at each frequency of at least 50 MHz steps should be less than 2:1 (in linear scale) or 6 dB (in logarithmic scale). When there is no reflection (ideal case), the VSWR value will be 1:1 or 0 dB.

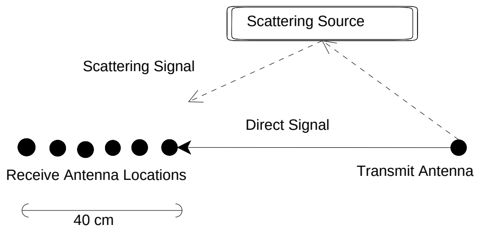


Figure 1. $S_{\mathrm{VSWR}}$ Measurement Points Along 40 cm Line

The disadvantage of this method is the inability to identify the reasons behind the SAC discrepancy from an ideal OATS. This is because the obtained output is only the $S_{\mathrm{VSWR}}$ with no other information about the source(s) of the scattering waves. Thus, the performance of SAC cannot be improved. Another limitation is that the frequency selective scattering may not be captured by this method.

## 3. Beam-Forming for SAC Evaluation

This thesis proposes a new method for SAC evaluation by beam-forming. The method offers an ability to identify the sources of scattering signals, including the frequency selective scattering. These advantages are superior to the standardized Site VSWR method. This method require a similar measurement system with that of Site VSWR method. However, different measurement positions will be used as a synthetic array antenna. In this method, some assumptions are taken:

1) The chamber discrepancy occurs due to some scattering waves that are caused by discrete points inside the SAC. Each of these points is modeled as an independent signal source, to be identified by beam-forming.
2) The distance between receiving array antenna center and the scattering point(s) are far enough, so that the plane wave approximation can be applied. The near-field analysis will be incorporated by using the spherical-wave radiation in the future.
3) The estimated Angle-of-Arrival (AoA) information of each detected signal path will be enough to determine the origins of each scattering wave.

A common non-parametric approach to find the AoA of the detected signal is beam-forming, which combines the

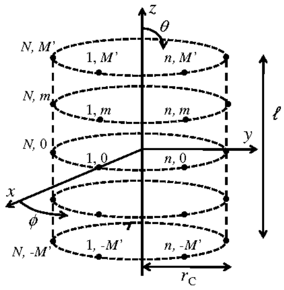


Figure 2. Geometry of Cylindrical Array Antenna

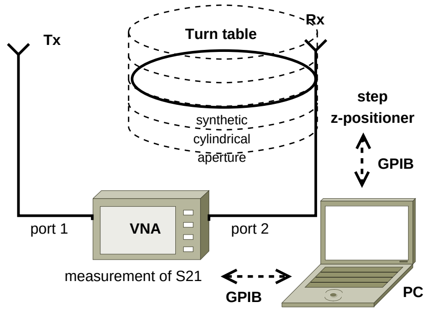


Figure 3. Measurement Set-Up for SAC Evaluation

received signal in such a way (by giving the appropriate weighting and delay), so that the beam can be directed to the desired direction. For SAC evaluation, the utilization of a synthetic cylindrical array antenna (Fig. 2) is proposed, considering its flexibility to get the desired beam-pattern in elevation and azimuth plane.

## 3.1. Measurement and Data Analysis

The SAC evaluation consists of a data measurement system and a data analysis (beam-forming). The measurement apparatus shown in Fig. 3 is the same with that used in the Site VSWR method. Only a single antenna element will be installed at each link of the vector network analyzer (VNA). A synthetic cylindrical aperture will be realized by moving the antenna at the receiver side, using a turn table and a step $z$-positioner. At each position, all the frequency transfer functions of interests (1 to 6 GHz with 10 MHz frequency steps) will be obtained from VNA. However, in the data analysis, each of the frequency transfer function will be separately analyzed. Note that the positioning error of the turn table and step $z$-positioner will cause some errors in the resultant synthetic cylindrical array due to the incorrect position of each antenna element.

The frequency transfer functions obtained from the VNA will be kept in a database, to be further analyzed by beam-forming. In the analysis, each frequency will be separately treated by using a frequency dependent interelement spacing (decimation) and weighting. The beam can be directed to the desired direction by choosing the desired steering angle, which will affect the weighting factor, as shown in Fig. 4. The received signals in the direction of side-lobes will be attenuated by the value of side-lobe level, |SLL|, of the beam. Our target is to be able to detect the signal(s) in the main-lobe direction only. Therefore, to avoid false alarm, the detection threshold should be set to a value higher than the SLL.

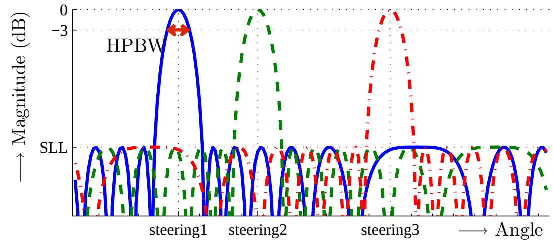


Figure 4. Example of 2D Antenna Beam-Pattern

To find the AoA of the detected signals, the steering angle should be continuously changed (beam-steering) to cover all the possible combinations of elevation and azimuth angle. The AoAs are the steering angles where the signal(s) is detected. However, since two signals separated by the half-power beam-width (HPBW) of the beam may not be distinguishable due to the high possibility of beam-pattern error/imperfection, the steering angle steps should be taken as the expected HPBW. In Fig. 4, HPBW is the angular width measured between the points on the main-lobe that are 3 dB below the magnitude peak. Therefore, the AoA resolution depends on the HPBW.

After the scattering signal detection is accomplished, other related information of the scattering signal such as the signal power, delay time, etc., can also be obtained. Therefore, the expected results of this evaluation are the AoA and delay time of each scattering signal (showing the sources of SAC discrepancy), and the scattering signal power. Note that the scattering signal relative power is highly related to the reflection coefficient of the chamber, so that this value can be used as one of the criteria for SAC compliance testing.

## 3.2. Requirement and Limitations

The target specification of beam-forming for this purpose is the maximum side-lobe level (MSLL) of -40 dB, to detect the weak scattering wave at the main-lobe direction apart from the strong waves at the side-lobes directions. To get the uniform low side-lobe beam-pattern, Dolph-Chebyshev weighting [2] is applied. Considering the smallest dimensions of SAC, the maximum antenna array physical dimensions in this study are considered as 2 m in height and 1 m in width.

# 4. Beam-Forming Simulations

Monte Carlo simulations, each of 10000 trials, were performed to find the mean MSLL under the influence of Gaussian antenna elements position-error. The obtained mean MSLL at different array parameters (under the limitation of maximum array dimensions) were used to design the optimal parameters of synthetic cylindrical array with minimum MSLL at reasonable half-power beam-width (HPBW).

Table 1 shows the variables utilized in the simulation. The investigated frequencies range from 1 to 6 GHz.

Table 1. Simulation Variables

| Variable | | Value |
|---|---|---|
| signal frequency | $f$ | [1, 6] GHz |
| std of linear error | $\delta d_{\mathrm{L}}$ | 1 mm |
| std of angular error | $\delta\phi$ | $0.1^o$ |
| array height | $l$ | $(M-1)d_{\mathrm{L}}$ |
| array radius | $r_{\mathrm{C}}$ | $(Nd_{\mathrm{C}})/(2\pi)$ |
| interelement spacing | $d_{\mathrm{L}}$, $d_{\mathrm{C}}$ | $\leq 0.5\lambda$ |
| defined side-lobe level | DSLL | -40 dB |

The antenna elements position-errors were assumed as Gaussian-distributed random errors with standard deviation of 1 mm in linear, and $0.1^o$ in angular. To get the sufficient samplings of continuous antenna aperture, the maximum interelement spacings $d_{\mathrm{L}}$ and $d_{\mathrm{C}}$, were limited to $0.5\lambda$. Since the target specification of MSLL is -40 dB, the defined side-lobe level (DSLL) in Chebyshev polynomials was set to be -40 dB.

Fig. 2 shows the geometry of a cylindrical array. In the figure, $\theta$ express the co-elevation angle, the angular deviation from the $z$-axis, whereas $\phi$ express the azimuth angle, the angular deviation from the $x$-axis at $xy$-plane. As can be seen from the figure, the array is composed of a uniform circular array (UCA) of $N$ elements and uniform linear array (ULA) of $M$ elements. Using the principle of pattern multiplication, the total pattern of the cylindrical array antenna is expressed as:

$$A(\theta,\phi) \quad = \quad A_{\mathrm{UCA}}(\theta,\phi)A_{\mathrm{ULA}}(\theta)F(\theta,\phi), \qquad (1)$$

where:

$$A_{\mathrm{UCA}}(\theta,\phi) = \sum_{n=1}^{N} w_n \exp(-jkr_{\mathrm{C}}\sin\theta\cos(\phi-\phi_n)), \quad (2)$$

$$A_{\mathrm{ULA}}(\theta) = \sum_{m=-M'}^{M'} w_m \exp(jkmd_{\mathrm{L}}\cos\theta), \qquad (3)$$

and $F(\phi,\theta)$ is the antenna element pattern. In the equations, $k$ is the wave-number of the incident wave, $r_{\mathrm{C}}$ is the UCA radius, $N$ is the number of UCA elements, $M = 2M'+1$ is the number of ULA elements, $d_{\mathrm{C}}$ is the circular interelement spacing, and $d_{\mathrm{L}}$ is the linear interelement spacing. The terms $w_n$ and $w_m$ express the weighting for the $n$th element of UCA and that for the $m$th element of ULA respectively. Dolph-Chebyshev algorithm was used for the weighting design, to obtain a uniform low side-lobes beam-pattern with optimal beamwidth [2]. Since this algorithm is only applicable to ULA, Davies transformation [3] was applied as the preprocessing technique to transform the UCA to a virtual ULA.

In the simulation, the investigation for elevation and azimuth beam patterns was separately conducted. The beam pattern in elevation mainly depends on the array factor of ULA, $A_{\mathrm{ULA}}(\theta)$ (3) and antenna element pattern (assumed as ideal vertical dipole, $F(\theta) = \sin\theta$), whereas that in azimuth plane, i.e. $\sin\theta = 1$, merely depends on the array factor of UCA, $A_{\mathrm{UCA}}(\phi)$ (2).

### 4.1. Uniform Linear Array

The first simulations were conducted to observe the elevation mean MSLL, $\mu_{\mathrm{MSLL}}$, in various linear interelement spacings, $d_{\mathrm{L}}$, and number of elements, $M$, within the maximum physical array height of $l = 2$ m. The relation between elevation MSLL and $d_{\mathrm{L}}$ under the influence of antenna elements position error and their corresponding HPBW for $f$ = 1 GHz and 6 GHz can be seen on Fig. 5 and Fig. 6. It is shown that the minimum achievable MSLL in $f$ = 1 GHz is -36.8 dB (at $d_{\mathrm{L}} = 0.5\lambda$ = 15 cm, $l = 1.8$ m, and $M = 13$). In $f$ = 6 GHz, -24.7 dB of minimum MSLL is obtained at $d_{\mathrm{L}} = 0.5\lambda$ = 2.5 cm, $l = 0.3$ m, and $M = 13$. The different trends of MSLL with respect to $d_{\mathrm{L}}$ in Fig. 6 occur due to the different aperture size of the array.

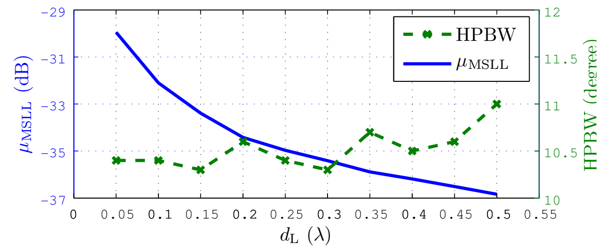


Figure 5. Elevation Performance vs. $d_{\mathrm{L}}$ ($f = 1$ GHz, $l \simeq 2$ m)

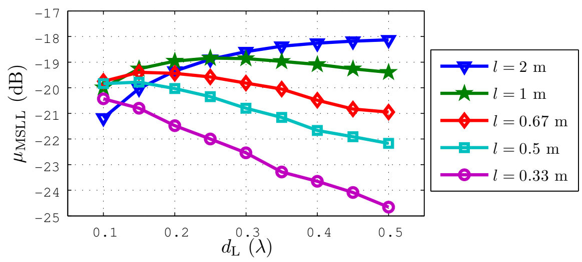


Figure 6. Elevation MSLL vs. $d_{\mathrm{L}}$ ($f = 6$ GHz, Various $l$)

Based on these results, the optimal measurement sampling for the linear array at each frequency is: 13 points, with $d_{\mathrm{L}} \simeq 0.5\lambda$. The sampling steps is determined by the highest frequency of 6 GHz, $d_{\mathrm{L}} = 2.5$ cm. The total array height is determined by the lowest frequency of 1 GHz, $l = (M-1)d_{\mathrm{L}} = 1.8$ m. Thus, the linear aperture should be measured by 73 points, each 2.5 cm apart.

For each frequency of $f = [1, 6]$ GHz with 10 MHz steps, 13 samples are taken for the data analysis (beamforming) with the corresponding linear spacings, $d_{\mathrm{L}}$, shown in Fig. 7. Note that by implementing this scheme, the linear aperture $l$ is electronically varied with respect to frequency. The expected performance in elevation for several frequencies of $f = [1, 6]$ GHz are shown in Fig. 8. It is shown that the range of elevation MSLL is $[-36.8, -24.7]$ dB, where higher MSLL is obtained at higher frequency, due to the linear error that are electronically larger. The elevation HPBW varied in the range of $11°, 20.4°]$ due to the different electronic aperture size, $l\,(\lambda)$. HPBW is inversely proportional to $l\,(\lambda)$.

### 4.2. Uniform Circular Array

These simulations were conducted to observe the azimuth mean MSLL, $\mu_{\mathrm{MSLL}}$, in various circular interelement spacings, $d_{\mathrm{C}}$, and number of elements, $N$, within the maximum physical array dimension of $r_{\mathrm{C}} = 0.5$ m. Related to the Davies transformation of UCA of $N$ elements,

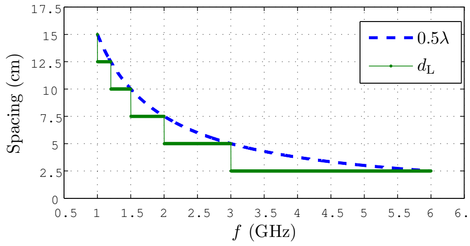


Figure 7. Frequency vs. Linear Interelement Spacings

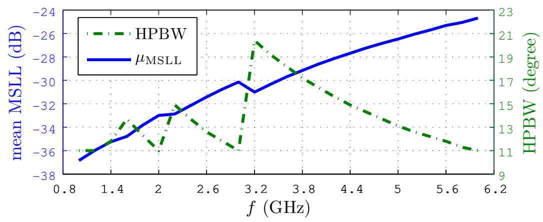


Figure 8. Elevation MSLL and HPBW at $f = [1, 6]$ GHz

care should be taken in choosing the number of virtual linear array, $N_\mathrm{V}$, to avoid the effect of *super-directivity*: inappropriate implementation of weighting resulting an error-sensitive beam-pattern.

It was obtained that the minimum azimuth MSLL in $f = 1$ and 6 GHz are obtained by using a UCA of $r_\mathrm{C} = 0.5$ m with $N = 314$ and $N = 215$ respectively. These two best measurement schemes are then compared in Fig. 9. The figure shows that the azimuth MSLL fluctuates in the range of $[-38.43, -0.9]$ dB for $N = 251$, and $[-38.62, -10.26]$ dB for $N = 314$. The occurrence of these fluctuations is related to the Davies transformation. The range of azimuth HPBW for both parameters is $[3.26°, 19.4°]$. Narrower HPBW is observed in the higher frequency due to larger electronic aperture.

From these results, the circular aperture of $r_\mathrm{C} = 0.5$ m should be measured in 314 points, each 1 cm apart. All these samples will be used for the data analysis (beam-forming) by choosing different values of virtual array $N_\mathrm{V}$ at each measurement frequency.

In the case of ULA, the physical height, $l$, can be decreased by taking fewer samples of the total measurements. However, different from ULA, the physical radius of UCA, $r_\mathrm{C}$, cannot be decreased. The reason is because one same measurement scheme is required for all measurement frequencies of $f = [1, 6]$ GHz, and at $f = 1$ GHz, maximum aperture is preferred to obtain a reasonable HPBW. Thus, the azimuth MSLL in 6 GHz can only be decreased by further decreasing $N_\mathrm{V}$, which is not preferable due to the significant widening of HPBW (proven by simulation).

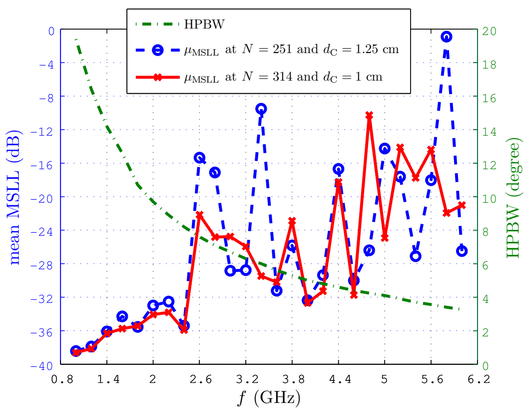


Figure 9. Azimuth MSLL and HPBW at $N = 251$ and $N = 314$

## 5. Conclusions and Future Works

The SAC evaluation by a synthetic cylindrical array beam-forming is proposed. This method offers an ability to identify the sources of SAC discrepancy by estimating the AoA of the detected signals. The frequency dependent scattering signals due to the frequency dependent reflections can also be detected. These advantages are superior to the current standardized (Site VSWR) method.

The influence of elements position-error on the performance of the array antenna was investigated by beam-forming simulations. It was found that the optimal geometry of synthetic cylindrical array antenna measurement for SAC evaluation is 1.8 m height and 1 m$\phi$ radius, with 2.5 cm (linear) and 1 cm (circular) interelement spacings.

In the data analysis, each frequency will be separately analyzed by using 13 linear samples with a corresponding $d_\mathrm{L}(f)$, and all circular samples with a corresponding $N_\mathrm{V}(f)$. Utilizing this scheme, the expected array performance under the influence of Gaussian elements position-error with standard deviation of 1 mm (linear) and $0.1^o$ (circular) are:

- Elevation MSLL = $[-36.8, -24.7]$ dB at HPBW = $[11°, 20.4°]$.
- Azimuth MSLL = $[-38.6, -10.3]$ dB at HPBW = $[3.3°, 19.4°]$.

The overall simulation results reveal the trade-off between MSLL (sensitivity) and HPBW (resolution).

In the future, the fluctuation in azimuth MSLL may be compensated by taking additional samplings at a smaller radius, to be used at the higher frequency. However, this will results in a longer measurement time and widening of HPBW. The far-field assumption taken in this study should also be justified by incorporating the spherical-wave propagation, since the relative size of the semi-anechoic chamber and that of the array may not satisfy this assumption.

## References

[1] CISPR 16-1-4, "Specification for Radio Disturbance and Immunity Measuring Apparatus and Methods – Part 1-4: Radio Disturbance and Immunity Measuring Apparatus – Antennas and Test Sites for Radiated Disturbance Measurements", Edition 3.0, April 2010.

[2] C. L. Dolph, "A Current Distribution for Broadside Arrays which Optimizes the Relationship between Beam Width and Sidelobe Level," *Proc. of the I.R.E. and Waves and Electrons*, pp. 335–348, June 1946.

[3] D. E. N. Davies, "A transformation between the phasing techniques required for linear and circular aerial arrays," *Proc. IEE*, vol. 112, no. 11, pp. 2041–2045, November 1965.

# PREPARATION OF ACTIVATED CARBONS WITH HIGH SURFACE AREA FROM BAGASSE FLY ASH

Student Number: 08M51500 Name: Chandra Wahyu PURNOMO Supervisor: Hirofumi HINODE

バガスフライアッシュを原料とした高比表面積活性炭の製造

プルノモ　チャンドラ　ワーユ

砂糖黍工業からの廃棄物であるバガスフライアッシュ(BFA)を原料とした高比表面積活性炭の製造およびフェノール吸着を行った。KOH または $ZnCl_2$ による化学的賦活、蒸気または $CO_2$ による物理的賦活および化学的賦活と物理的賦活の組み合わせによって様々な細孔径分布および表面特徴を有する活性炭が製造できた。キャラクタリゼーションが $N_2$ 吸着、塩基滴定、ゼロ電荷点分析および FT-IR により行った。活性炭のフェノール最大吸着容量は 303.03 mg/g であった。

## 1. Introduction

Activated carbons (AC) have always become a research interest due to their continuous usages in many areas. These materials have been synthesized from many types of carbonaceous precursors. One of the potential precursors is biomass waste due to low price and abundantly available. Many type of biomass such as woods [1], plant's shells and stones [2], have been studied for preparing activated carbons.

Meanwhile, a sugar industry emits approximately 5.5 kg of fly ash per metric ton of cane processed in the flue gases from the bagasse combustion [3]. In the case of Indonesia with around 30 million tons of annual production of cane, 16,500 tons of BFA per year can be produced nationwide. This large amount of biomass waste should be considered to be utilized properly. Furthermore, due to low efficiency of typical bagasse combustors, BFA contain a significant unburned carbon that promising to be used as AC precursors.

In this research, BFA was used for activated carbon precursor. Considering its initial porosity, it is expected that this material can be activated in a low temperature treatment and low chemical usages.

## 2. Experimental

### 2.1 Material

BFA was obtained from PT Madukismo, a sugar company in Yogyakarta province, Indonesia. Before any treatment, BFA was separated into three particle sizes by standard sieves. After sieving, the medium size BFA (0.7-1.4 mm) underwent washing and floating method for several time using distilled water. After this treatment, BFA was dried overnight and then stored in a dry sealed container.

### 2.2. Activation method

In this study, three activation methods have been employed. Each of detail procedure will be discussed in the next section. Meanwhile, sample ID classification is provided in Table 1.

#### 2.2.1. Physical activation

The dry pretreated BFA was weighed before activation. Then, it was placed inside a ceramic pipe. The internal diameter of the pipe was 3 cm with 30 cm in length. A horizontal automatic tubular furnace was used for heat treatment. After several minutes of nitrogen purge, the heating was started. In this procedure 15 $^{o}$C/min of heating rate was chosen and the flow of nitrogen was set at 150 ml/min.

For $CO_2$ activation, after reaching the final temperature, the nitrogen flow was replaced with $CO_2$ with the same flow rate. Meanwhile for steam activation, the nitrogen flow was reduced to 100 ml/min while the micro syringe was turned on to introduce water into the heater for steam generation. The flow of water was set at 0.3 ml/min.

Table 1: AC samples nomenclature

| Activation | Code | X | y | z |
|---|---|---|---|---|
| Physical | (X)T(y)t(z)Q | C for $CO_2$ or S for steam | Max. temp. in hundred $^oC$ | holding time duration in hours |
| Chemical | (X)(y)T(z)C | K for KOH or Z for $ZnCl_2$ | chemical agent/BFA weight ratio (R) | Max. temp. in hundred $^oC$ |
| Physiochemical | (X)(y)T(z)CQ | K for KOH or Z for $ZnCl_2$ | chemical agent/BFA weight ratio (R) | Max. temp. in hundred $^oC$ |

The treatment during final temperature was maintained for 1 to 2 hours of holding time. After that, the mixture was cooled down by natural cooling mechanism to room temperature under nitrogen flow of 150 ml/min. After reaching room temperature, the gas was closed and activated BFA was removed and weighted. The final weight was used for determining the yield of activated carbon product. The last step was labeling and storing the sample inside a desiccated storage box.

### 2.2.2. Chemical activation

The pre-dried medium size BFA before being subjected to heat treatment, it underwent chemical impregnation using zinc chloride or potassium hydroxide with certain weight ratios of chemical agent over BFA from 2 to 4. The impregnation was done by manual mixing BFA with the chemical concentrated solution at room temperature and then drying in an oven at 100 $^oC$ overnight. The impregnated BFA after weighing then placed inside a ceramic pipe and subjected to the same heat treatment as in physical activation.

After reaching the final temperature, the heating was hold for one hour before cooling to room temperature. After reaching room temperature, the activated BFA was removed from the pipe and washed using 0.5 N HCl solution several times followed by hot distilled water until constant pH of distillate was reached. After washing procedure the sample was dried overnight and weighed for calculating the product yield.

### 2.2.3. Physiochemical activation

This activation procedure was done for impregnated BFA simply by switching nitrogen flow with $CO_2$ in the heat treatment during holding time with the same flow rate. After activation, all samples were subjected to similar washing and drying procedure as in chemical activation method.

### 2.3. Carbon characterization

The samples textural properties have been characterized using nitrogen adsorption at 77 K by Autosorb 1 equipment from Quantachrome. The chemical property analyses were done by measuring the zero point charge ($pH_{ZPC}$), FT-IR (not shown in here) and also titration method.

### 2.4. Liquid adsorption

Liquid adsorption equilibrium of several selected samples has been carried out in a batch system. Each of adsorption point was repeated in duplicate and fitted by Langmuir equation:

$$Q = Qm \frac{K.C}{1+K.C} \qquad (1)$$

where Q is the amount of phenol adsorbed (mmol/g adsorbent), Qm is the monolayer adsorption capacity (mg adsorbate/g adsorbent), K is the affinity constant (L/mg adsorbate), and C is the equilibrium solution concentration of adsorbate (mg/L).

## 3. Results and discussion

This section is grouped based on the activation method. The sample's physical-chemical properties and phenol adsorption results are provided.

### 3.1. Physically activated carbons

### 3.1.1. Textural properties

Generally, $CO_2$ activation produced activated carbons with dominant microporosity. Meanwhile for steam activation, a significant development of mesopores can be observed by large values of mesopore volume (Table 2). Larger microporosity for steam activation in a similar activation condition with $CO_2$ activation can be observed as well. The larger pore development in steam activation has been compensated by lower yield.

Table 2: Porosity profile of physically activated carbons

| ID | Yield (%) | porosity | | |
|---|---|---|---|---|
| | | $V_{mic}$ (cc/g) | $V_{mes}$ (cc/g) | $S_{BET}$ ($m^2/g$) |
| CT7t1Q | 92 | 0.210 | 0.056 | 485 |
| CT8t1Q | 73 | 0.272 | 0.047 | 629 |
| CT8t2Q | 66 | 0.412 | 0.128 | 944 |
| ST7t1Q | 71 | 0.345 | 0.051 | 656 |
| ST8t1Q | 53 | 0.575 | 0.191 | 1,311 |
| ST8t2Q | 36 | 0.881 | 0.560 | 1,970 |

### 3.1.2. Surface Chemical Properties

The basic and acidic moieties have been investigated by Boehm titration method. Then, $pH_{ZPC}$ was also determined and provided in Table 3. In general, the physical activation produced basic activated carbon with only phenolic group can be quantified by the titration method. The steam activated samples exhibited higher basicity than $CO_2$ samples that were confirmed by lower acidity by titration method with the highest $pH_{ZPC}$ obtained by ST8t2Q sample at 10.76.

### 3.2. Chemical activated carbons

### 3.2.1. Textural properties

KOH activation produced activated carbon with significant development of microporosity with quite low mesoporosity as indicated by porosity data in Table 4. But for the highest R and temperature a significant mesopores was also developed. By this method, the highest porosity among all samples can be achieved by K4T7C sample with surface area of 2,571 $m^2/g$.

Meanwhile, $ZnCl_2$ samples exhibited significant development of mesopores. Microporosity was less developed by this method compared with KOH activation but higher yield can be obtained.

### 3.2.2. Surface Chemical Properties

The chemical activation produced acidic activated carbon with carboxylic, lactonic and phenolic group can be quantified by the titration method as presented in Table 3. KOH samples are more acidic than $ZnCl_2$ ones.

### 3.3. Physiochemical activated carbons

Combining the two activation methods will create activated carbon with unique porosity characteristic (Table 4). $ZnCl_2$ impregnation with R=2 coupled with $CO_2$ treatment will create similar pore distribution pattern with $ZnCl_2$ only activation but with further development of narrow microporosity. Meanwhile, in higher chemical ratio (R=3), the effect of $CO_2$ reduced significantly the development in mesopore range. Furthermore, KOH-$CO_2$ activation using R=3 also behaved in a similar way.

Table 4: Porosity profile of chemically and physiochemically activated samples

| ID | Yield (%) | porosity | | |
|---|---|---|---|---|
| | | $V_{mic}$ (cc/g) | $V_{mes}$ (cc/g) | $S_{BET}$ ($m^2/g$) |
| K2T6C | 87 | 0.569 | 0.055 | 1,306 |
| K3T6C | 56 | 0.644 | 0.102 | 1,441 |
| K3T7C | 51 | 0.960 | 0.093 | 2,180 |
| K4T6C | 57 | 0.942 | 0.057 | 2,158 |
| K4T7C | 48 | 1.135 | 0.189 | 2,571 |
| Z2T6C | 83 | 0.308 | 0.080 | 709 |
| Z3T6C | 81 | 0.417 | 0.157 | 946 |
| Z3T7C | 77 | 0.525 | 0.138 | 1,168 |
| Z4T6C | 82 | 0.378 | 0.125 | 853 |
| Z4T7C | 78 | 0.485 | 0.132 | 1,136 |
| Z2T6CQ | 77 | 0.528 | 0.140 | 1,200 |
| Z3T6CQ | 80 | 0.266 | 0.041 | 602 |
| K2T6CQ | 73 | 0.643 | 0.026 | 1,472 |
| K3T6CQ | 52 | 0.779 | 0.028 | 1,711 |

### 3.4. Phenol Adsorption

Selected activated carbon samples from above preparations have been tested to remove phenol from water. Then the performances have been compared with a commercial activated carbon (Norit SX Plus) and non-treated BFA.

### 3.4.1. Physically activated sample isotherms

The isotherm adsorptions data have been provided in Fig.1 along with the Langmuir plots. In general, the prepared activated carbon samples have better phenol adsorption capacity especially in low phenol concentration compare with the commercial one and non-activated BFA.

From the Figure, it shows that steam activated carbon have larger capacity in adsorbing phenol compare with $CO_2$ activated samples. The main factor for the capacity is the porosity profile of each sample. As described in previous section, steam activation provided higher porosity development than $CO_2$ activation. The highest monolayer phenol uptake (Qm) for this group was obtained by ST8t1Q sample at 270 mg/g.

Table 3: Chemical properties of AC samples

| Sample ID | Functional groups | | | Acidic (meq/g) | Basic (meq/g) | $pH_{zpc}$ |
|---|---|---|---|---|---|---|
| | Phenolic (meq/g) | Lactonic (meq/g) | Carboxylic (meq/g) | | | |
| CT8t1Q | 0.050 | 0.0 | 0.0 | 0.050 | 0.570 | 10.17 |
| CT8t2Q | 0.160 | 0.0 | 0.0 | 0.160 | 0.770 | 10.26 |
| ST8t1Q | 0.020 | 0.0 | 0.0 | 0.020 | 0.940 | 10.31 |
| ST8t2Q | 0.010 | 0.0 | 0.0 | 0.010 | 1.110 | 10.76 |
| K3T7C | 0.770 | 0.120 | 0.140 | 1.030 | 0.240 | 4.69 |
| K4T6C | 1.190 | 0.060 | 0.200 | 1.450 | 0.160 | 4.24 |
| Z3T7C | 0.230 | 0.040 | 0.140 | 0.410 | 0.150 | 5.71 |
| Z4T6C | 0.330 | 0.040 | 0.180 | 0.550 | 0.220 | 4.74 |

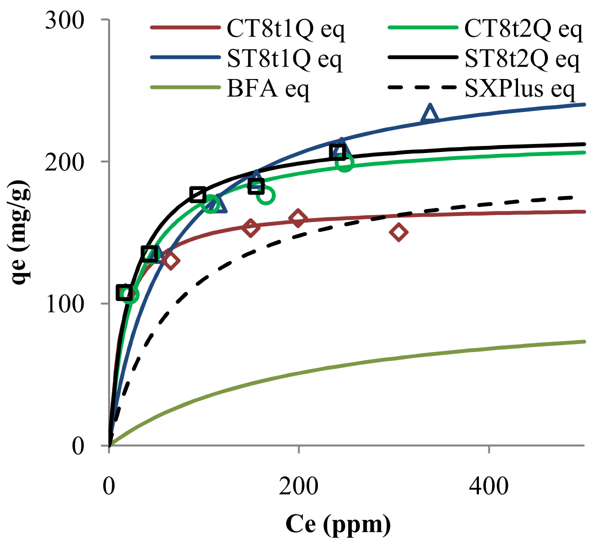


Figure 1: Phenol isotherms of selected physically activated carbons

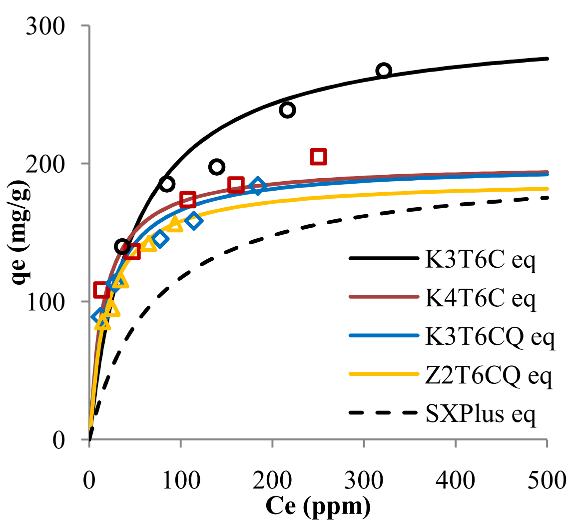


Figure 2: Phenol isotherms of selected chemically activated carbons

### 3.4.2. Chemically activated sample isotherms

The isotherms of several chemically and physiochemical activated carbon samples have been shown by Fig. 2. Similar to the previous adsorption results, the prepared samples exhibited higher phenol uptake than the commercial one. The highest capacity of 303 mg/g was obtained by K3T6C sample.

## 4. Conclusions

BFA has been confirmed as a promising precursor for preparing ACs with tailor-able physical and chemical properties. The prepared sample also has a superior performance for remediating phenol in aqueous solution.

## References

[1] F.C. Wu and R.L. Tseng, "Preparation of highly porous carbon from fir wood by KOH etching and $CO_2$ gasification for adsorption of dyes and phenols from water", Journal Colloid Interface Science, vol. 294, pp. 21–30, 2006.

[2] A. Aygun, S. Yenisoy-Karakas, and I. Duman, "Production of granular activated carbon from fruit stones and nutshells and evaluation of their physical, chemical and adsorption properties" Microporous and Mesoporous Materials, vol. 66, pp. 189–195, 2003.

[3] The World Bank Group, Pollution prevention and abatement handbook 1998: toward cleaner production, World Bank Inc., Washington D.C., 1999.

# Performance Evaluation of Cooperative Sensing in Disaster Affected Area

Student Number: 08M51516 Name: Santosh Khadka Supervisor: Jun-ichi TAKADA

# 被災地における協調センシングシステムの特性評価

サントス　カドカ

大規模災害発生時には、世界中からの援助隊が狭い地域に展開してそれぞれの通信システムを使用することが予想され、同じ周波数帯を使用することによる干渉問題が発生することが過去の事例から明らかになっている。本研究では、センサネットワークを用いて使用中の周波数帯を検出・データベース化することにより干渉問題を回避する方法を提案する。また、複数の周波数帯に対して災害発生前後におけるセンサネットワークの検出性能を比較することにより、提案手法の有効性を明らかにする。

## 1 Introduction

Spectrum sensing using energy detection have been studied extensively in past. Among them, the performance under fading channel has been studied by Kostylev [1] recently. He derived the expression of probability of detection $P_\mathrm{d}$ for Rayleigh fading, Nakagami and Rician channels. Similarly Digham in [2] presented the alternative analytical approach for the same fading channels. This work assumes the situation of a natural disaster that occurred in a major city and many emergency rescue teams come to the scene to carry out rescue operations. But due to lack of information about the uses of frequency band, they begin to interfere with one another after setting up their radio communications networks. So the task at hand is to design a wireless sensor network (WSN) that is capable of sensing the used frequency band in the area and keep record of them. This thesis evaluates and compare the performance of individual sensing and cooperative sensing using energy detection method in both pre- and post-disaster channels which is different form general fading channel.

## 2 Problem Statement and Objectives

After big disaster rescue teams from different states/ countries come to the scene to join rescue operation. Due to lack of information about the uses of frequency band, two or more teams might use same frequency band for their communication and might cause severe interference with each other which hinders the rescue operation. Considering this, the cluster based sensor network [3] in the area destroyed by earthquake as shown in Figure 1 that can sense all channels in the allocated emergency frequency band and update the information in the database was realized and its performance was analyzed in this study. In order to come up with more realistic solutions, following assumptions were made:

- The earthquake occurs in a residential area, Ookayama, Tokyo in Japan.
- Communication between the sensor nodes and the emergency radio are not possible.

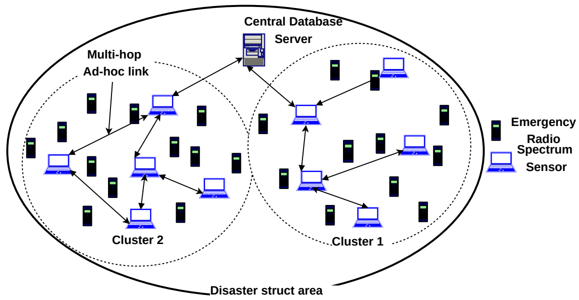


Figure 1: Cluster based sensor network

- The GNU Radio-USRP [4] software defined radio is the targeted implementation platform for spectrum sensing.
- Emergency rescue teams will use both analog and digital systems and transmit between 100 MHz and 1 GHz [5].
- The emergency radio signals are narrowband $\leq$ 25 KHz and prior information about their waveforms is not available.

Following these assumptions the objectives of this study are set as follows:

- To study the effect of antenna height on received signal strength and angle of arrival (AOA) to determine the suitable height of sensor for both sensing and geolocation.
- To evaluate and compare the performance of individual and cooperative sensing in pre and post-disaster scenario.
- To determine the number of sensors needed for spectrum sensing in the area considered.

## 3 Spectrum Sensing Technique

Detection of unknown deterministic signal using energy detector is a problem of binary hypothesis test. The probabilities of detection ($P_\mathrm{d}$) and false alarm ($P_\mathrm{fa}$) in case of non-fading environment where channel amplitude gain $h$ is assumed to be constant over measurement period, are given by Eq. (1) and (2) [1, 2, 6].

$$P_\mathrm{d} = P\left\{\mathcal{T} > \lambda | H_1\right\} = Q_\mathrm{m}(\sqrt{2\gamma}, \sqrt{\lambda}) \qquad (1)$$

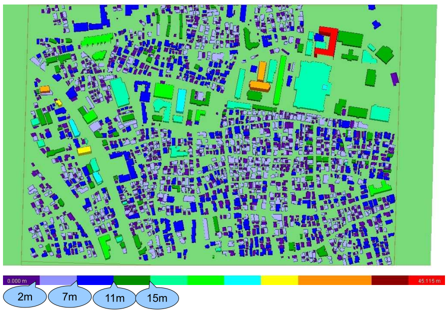


Figure 2: 3D model of destroyed area

$$P_{\rm fa} = P\left\{\mathcal{T} > \lambda | H_0\right\} = \frac{\Gamma(m, \lambda/2)}{\Gamma(m)} \qquad (2)$$

where $Q_{\rm m}(.,.)$is the generalized Marcum $Q$-function of $m^{th}$ order, $m$ is equal to $TW$, where $T$ is the sensing time and $W$ is the bandwidth of the signal, $\gamma$ is signal to noise ratio (SNR) and $\Gamma(.)$ and $\Gamma(.,.)$ are complete and incomplete gamma functions respectively.

When $h$ is varying due to shadowing / fading, the average $P_{\rm d}$ can be derived by averaging Eq. (1) over fading statistics [7],

$$P_{\rm d} = \int_x Q_{\rm m}(\sqrt{2\gamma}, \sqrt{\lambda}) f_\gamma(x) dx \qquad (3)$$

where $f_\gamma(x)$ is the PDF of SNR under fading. Performance of energy-detector for in different channel condition can be characterized through ROC (receiver operating characteristics) curve.

One issue in spectrum sensing is the hidden terminal problem, which occurs when sensors are shadowed or are in severe multipath fading. This problem can be solved by cooperative spectrum sensing where multiple sensors sense the radio environment and make the decision cooperatively. The cooperation between sensors can be achieved either by using soft cooperation scheme or by using hard cooperation scheme. In this study hard cooperation method using OR rule [7] as given below was used.

$$Q_{\rm d} = 1 - \prod_{i=1}^{n}(1 - P_{{\rm d},i}), \qquad (4)$$

$$Q_{\rm fa} = 1 - \prod_{i=1}^{n}(1 - P_{{\rm fa},i}), \qquad (5)$$

where $Q_{\rm d}$ and $Q_{\rm fa}$ are collaborative probabilities of detection and false alarm and $i = 1, .., n$ is the number of collaborating sensors.

# 4 Channel modeling of earthquake affected area

This study consider a scenario destroyed by earthquake whose model can be done by using site specific channel model like ray tracing propagation model. A commercial software, Wireless Insite, was used for ray tracing [8]. 3D model of earthquake affected area was imported in Wireless Insite. Assuming that

Table 1: Simulation Parameters

| | |
|---|---|
| Pulse Shape | Sinusoidal |
| Carrier Frequency | 200, 400, 800 MHz |
| Bandwidth | 25 kHz |
| Transmission power | 30 dBm |
| Antenna Type | Omnidirectional |
| Polarization | Vertical |
| Antenna gain( dBi) | 3 |
| VSWR | 1 |
| Transmiting antenna height( m) | 1.5 |
| Sensing time (T) | 1 ms |

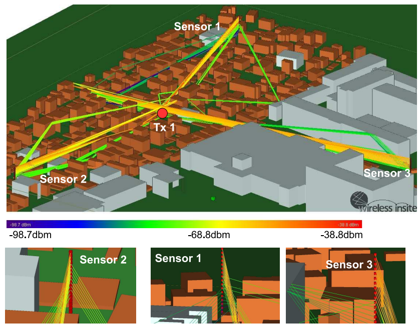


Figure 3: Propagation paths form Tx 1 to sensors

Ookayama area is affected by earthquake measuring upper shindo 7 and also assuming that most of the houses in this area were built after year 1982, following [9], earthquake affected Ookayama area was modeled by destroying almost 55% of wooden house and 20% of concrete houses using the edit tool of Wireless Insite as shown in Figure 2. Material properties of residential house were changed to wood. Building of Tokyo Institute of Technology and other tall buildings taller than 15m were assumed as concrete buildings and changed accordingly.

# 5 Simulation and results

## 5.1 Simulation Parameters

The simulation parameters for channel modeling were set in Wireless Insite following assumptions made in section 2 as shown in Table 1. The height of sensors was determined by observing path loss and angle of arrival at different antenna height and also considering the average height of houses. In Figure 3 it can be seen that at lower antenna height, the propagation path follows canyon propagation but as the height increase, they follows almost line of sight (LOS) path and this is very helpful for geolocation application. In Figure 4 it was found that at higher sensor height, path loss is less. Considering all these, height of the sensor was set to 15m.

520 emergency radio transmitters and 48 sensors were uniformly distributed in the disaster affected area. After setting all required parameter in Wireless Insite, simulation was run for 48 hours to get the required channel model parameters.

## 5.2 Spectrum sensing performance

The received signal power which is degraded by channel under consideration was obtained from Wireless

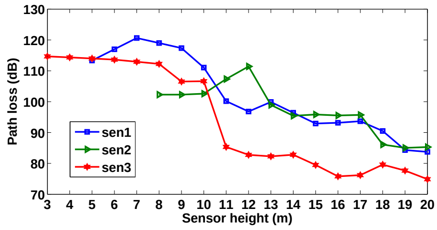


Figure 4: Path loss versus sensor height due to Tx 1

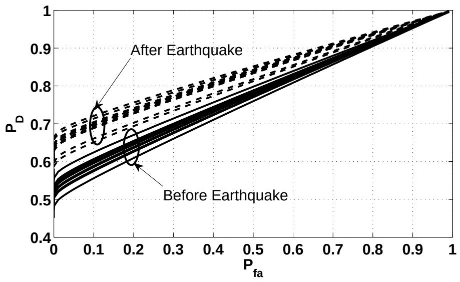


(a) At 200 MHz

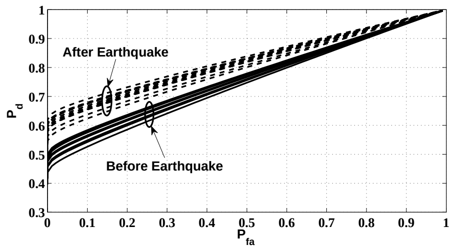


(b) At 400 MHz

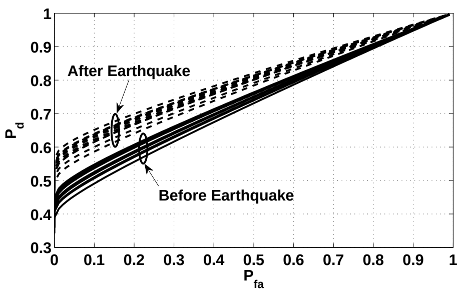


(c) At 800 MHz

Figure 5: Spectrum sensing performance

Insite and the total noise power of the receiver was practically determined to be −98 dBm for bandwidth of 25KHz in [3]. Using these datas performance of individual sensors under fading environment in terms of $P_{\mathrm{d}}$ and $P_{\mathrm{fa}}$ were evaluated.

12 out of 48 uniformly distributed sensors were selected randomly and $P_{\mathrm{d}}$ at different value of $P_{\mathrm{fa}}$ were calculated for 520 Tx location. Since all location suffers different fading, the average $P_{\mathrm{d}}$ at 12 sensors were calculated using Eq. 3. The whole procedure was repeated for 100 trials. ROC curve as shown in Figure 5(a), 5(b) and 5(c) for transmission frequency of 200, 400 and 800MHz respectively for scenarios before earthquake and after earthquake were plotted. These figures shows that as $P_{\mathrm{fa}}$ increases, $P_{\mathrm{d}}$ also increases.

Comparison of $P_{\mathrm{d}}$ at 10% $P_{\mathrm{fa}}$ before and after

Table 2: $P_{\mathrm{d}}$ at 10% $P_{\mathrm{fa}}$ before and after earthquake

| Frequency | Before Earthquake | After Earthquake |
|---|---|---|
| 200 (MHz) | 55% to 62% | 65.5% to 72% |
| 400 (MHz) | 52.6% to 58.4% | 62.2% to 69% |
| 800 (MHz) | 49% to 54.8% | 58.66% to 65% |

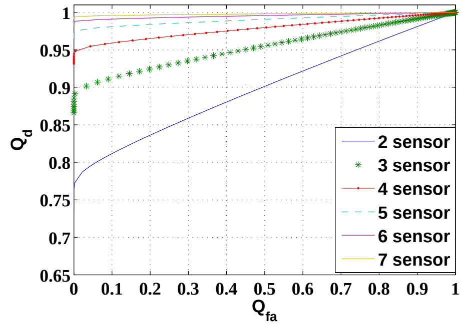


(a) Before Earthquake

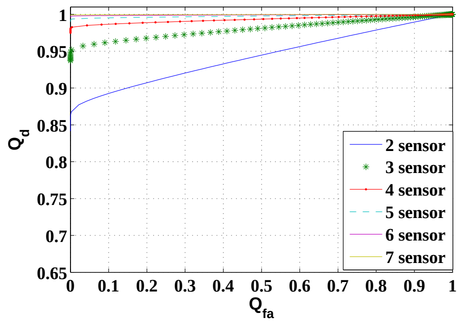


(b) After Earthquake

Figure 6: Cooperative sensing at 200 MHz

earthquake for different carrier frequency was shown in Table 2. Performance of sensors after disaster was found to be improved by 10% for all carrier frequency. It can be also seen from the table that at higher frequency the performance degrades. This is because path loss increases with increase in frequency.

## 5.3 Cooperative spectrum sensing performance

By using the performance of those individual sensors, cooperative sensing performance changing the number of cooperating sensors were evaluated. First of all the possible combination of 2 cooperating sensors to 7 cooperating sensors were calculated. Then cooperative performance in terms of $Q_{\mathrm{d}}$ and $Q_{\mathrm{fa}}$ of all those combination were calculated using Eq. 4 and 5 respectively and finally averaged over total number of combination of cooperating sensors. Performance of cooperative sensing at 3 different frequency were shown in Figure 6, 7 and 8 for scenarios before earthquake and after earthquake.

These figures shows that the cooperation between sensors drastically increases the performance of sensor network and also the performance after earthquake is better due to destruction of obstructing houses. It can be also observed that as the number of cooperating sensors increases the performance also increases but there is a limit beyond which significant

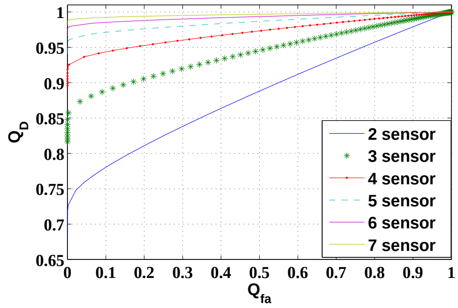


(a) Before Earthquake

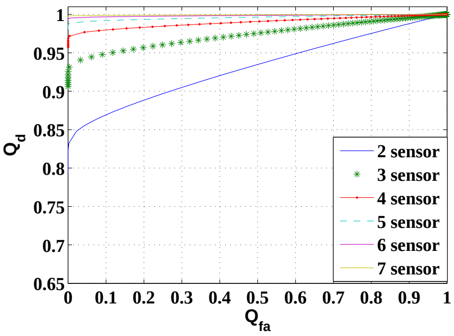


(b) After Earthquake

Figure 7: Cooperative sensing at 400 MHz

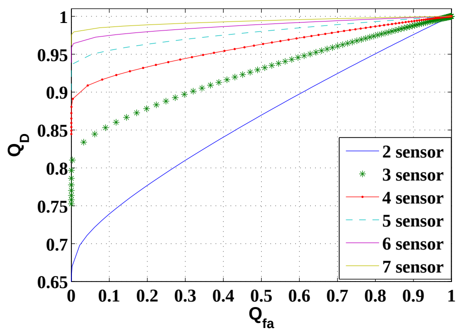


(a) Before Earthquake

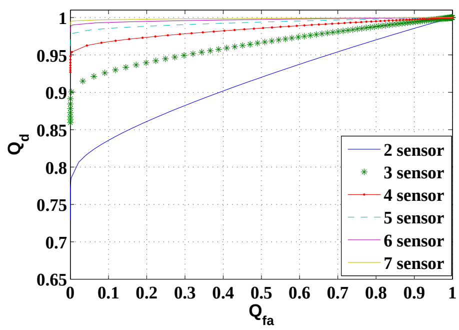


(b) After Earthquake

Figure 8: Cooperative sensing at 800 MHz

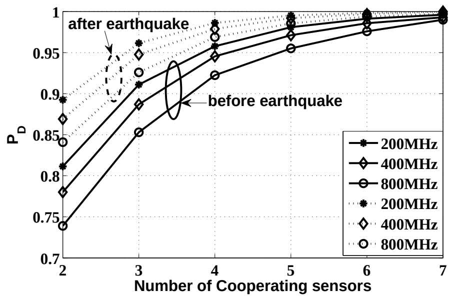


Figure 9: Comparison of cooperation

collaboration gain cannot be absorbed with increasing number of collaborating sensors.

Cooperation gain at different carrier frequency with increasing number of cooperating sensors were shown in Figure 9. Considering worse sensing case which is at 800 MHz, 92% $Q_{\mathrm{d}}$ can be obtained by 4 cooperating sensors in scenario before earthquake whereas 3 cooperating sensors can give same performance in after earthquake scenario.

# 6 Conclusion

Channel model of the specific area that was destroyed by earthquake was done by using site specific propagation modeling tool, Wireless Insite and the destroyed area was modeled using it's graphic edit tool. The height of sensors suitable for sensing and geolocation was determined. The performance of individual sensing and cooperative sensing in pre and post-disaster cases using energy detection method were analyzed at different emergency frequency band. It was found that sensors performs better in post-disaster case and at lower frequency. It was also found that cooperation between sensors increases the sensing performance but there exist a limitation beyond which significant cooperation gain cannot be achieved by increasing number of cooperating sensors.

# References


[1] V. I. Kostylev, "Energy detection of a signal with random amplitude," *Proc. of IEEE Internation Conference on Communications*, (ICC03), pp. 35753579, May 2003.

[2] F. F. Digham, M. S. Alouini, and M. K. Simon, "On the energy detection of unknown signals over fading channels," *Proc. of IEEE Internation Conference on Communications*, (ICC03), pp. 35753579, May 2003.

[3] M.A. Rahman, S. Khadka, Iswandi, M. Gahadza, A. Haniz, M. Kim, J. Takada, "Development of Spectrum Sensing System with GNU Radio and USRP to Detect Emergency Radios", *IEICE Technical Report*, SR2009-57, Oct. 2009.

[4] Ettus Research LLC, `http://www.ettus.com/`

[5] "Shuuhasuu-chou (Book of frequencies)," Sansai Books, vol. 176, 2007.

[6] H. Urkowitz, "Energy detection of unknown deterministic signals," *Proceedings of IEEE*, vol. 55, pp. 523231, April 1967.

[7] A. Ghasemi, E. S. Sousa, "Collaborative Spectrum Sensing for Opportunistic Access in Fading Environments," *First IEEE Proc. of DySPAN'05*, Nov. 2005.

[8] Remcom, "Wireless InSite Site-Specific Radio Propagation Prediction Software," User 痴 Manual, Ver. 2.0.5. 2004

[9] `http://www.bousai.go.jp/jishin/chubou/shutochokka/15/shiryou3.pdf`

# PROCESS OF METHANOL PRODUCTION FROM BY-PRODUCT OFF-GAS GENERATED IN COKING OF MONGOLIAN COAL

Student Number: 08M51522 Name: Jargalsaikhan Zoljargal Supervisor: Egashira Ryuichi

モンゴル産石炭のコークス化における副生ガスを原料としたメタノール製造プロセス

ジャルガルサイハン ゾルジャルガル

A Mongolian coal was carbonized in laboratory to characterize the generated off-gas. Furthermore the readily available technologies for methanol production from coking off-gas were explored. Based on these results, appropriate process flow diagram in case of Mongolia was synthesized and computational simulation and rough cost estimation were carried out for this process. Consequently, this process was proposed for efficient utilization of Mongolian coal resources.

## 1. Introduction

Establishment of the country's first cokemaking plant has currently being discussed in Mongolia. However there is lack of study on possible way of utilization of by-products of cokemaking, namely the coke-oven gas (COG) and coal tar [1].

Conventionally the off-gas generated in coking plants has been used as fuel for heating applications or passes out to atmosphere after combustion causing waste of energy and air pollution [2]. Alternatively, due to high concentration of hydrogen and methane, the COG has being considered as suitable source for production of methanol [3]. Methanol has appeared to be not only highly demanded feedstock for chemical industry but also a promising alternative fuel for transport vehicles and gas turbine power generation [4].

In the current study a Mongolian coal was carbonized at laboratory scale. The generated off-gas was analyzed by gas chromatography (GC) to demonstrate its suitability for methanol synthesis. Furthermore, the available technologies for conversion of COG to methanol were explored, and an appropriate process flow diagram (PDF) was synthesized. The computational simulation of the process was carried out using commercial process simulator. The resulting dimensions of streams, units, and energy balance were used for cost estimation of the process.

## 2. Study of Mongolian coal

The two main bituminous coal mines play an important role in economics of the country - Tavan-Tolgoi (TT) and Naryn-Sukhait (NS). However NS coal has not been studied to satisfactory extends, and therefore it was selected for the case study.

The examination of available data of previous studies allow classifying NS coal to high volatile weakly coking coal that cannot be used for cokemaking by its own (Table 1). In coking blend NS coal might be used as high volatile supplementary component if the base coal with strong caking property is available, such as Mongolian TT coal.

Furthermore, Mongolian NS coal was carbonized at temperatures up-to $900^0$C. The obtained off-gas was analyzed by GC. The carbonization apparatus consisted of electric furnace, fixed-bed reactor equipped with thermocouple and condensation system for removal of liquid and gaseous products (Fig.1). Table 2 shows the experimental conditions. The yield of coke was 67w% in average, the condensable liquid 18w% and off-gas 15w%. The off-gas was generally characterized by excess of hydrogen compared to carbon oxides, which was desirable for the methanol synthesis. It also contained considerable amount of methane which may become a source of syngas through reforming (Fig.2). Thus, the experiments have qualitatively proved that off-gas generated in carbonization of Mongolian NS coal could be suitable for synthesis of methanol.

## 3. Development of an appropriate process flow diagram for methanol production from coke-oven gas

It was assumed that the cokemaking plant will produce 1 million tons of coke per year. The amount of COG available for methanol synthesis would be approximately 259,875,000 cubic meters per year [5].

Various processes for each technological section of COG-to-MEOH plant were studied comparatively. The appropriate processes were selected according to following priorities: technological simplicity, low consumption of chemicals, less pollutants and low cost. Selection of deep desulfurization process within the methanol plant was closely affected by the selection of bulk desulfurization process in the by-product recovery cokemaking plant. Therefore relatively extended focus was paid on COG purification processes. For bulk desulfurization, the conventional absorption/stripping process was selected due to lower consumption of chemicals and less pollutant. Rectisol was selected for the deep desulfurization due to reliability and independence from consumable chemicals although it has higher investment and energy requirements. The tubular steam reformer was preferred to the autothermal reformer as it does not require expensive air separation unit (ASU) for pure oxygen. For methanol synthesis, low-pressure and low-temperature (LPLT) quench reactor was chosen due to easier operation and lower cost compared to LPLT tubular reactor, and the readiness for commercial application compared to the liquid phase reactor. For purification of raw methanol, the two-column distillation was preferred to single or multi-column distillation as those may either result in in-sufficient purity of methanol or higher cost and energy consumption. The literature indicates availability of gas turbines (GT) that can operate on low calorific purge gas from methanol synthesis after minor modification. Heat of GT exit gas as well as other excess process heat streams with temperatures higher than $300^{0}$C was assumed to be converted to electricity using steam turbine with 33% efficiency. The comparative technological study has revealed that methanol can be produced from COG using readily available and reliable processes.

The appropriate process flow diagram of the plant was developed based on these selected processes (Fig.3) and then simulated using a commercial process simulator ChemCAD III (Fig.4). The simulation has resulted in annual production of 104,500 tons methanol, 206,716 MWh electricity and 125,600 MWh heat for district heating. The methanol conversion efficiency of the plant was estimated at 43.4% and the total efficiency at 78.2%. The methanol conversion efficiency might be increased by improving water removal unit after SMR and increasing recycle ratio in the synthesis loop.

Several options were compared for further improvement of the process. A combination of coal firing coke ovens and coal gasification unit [2] with the hot raw COG cracking and hot gas cleaning [8] has appeared as the promising way to improve the production process, although it faces some technical difficulties to be overcome in the future. The dehydration of methanol into DME may also be considered as a possible improvement of the process since DME could be blended with LPG and thus increase the marketability of the products. Once the methanol production plant will be installed, the DME producing facility can be installed with small additional equipment cost of approximately 10% of that of the methanol producing facility [9].

## 4. Cost estimation for methanol production from coke-oven gas

The results of computational simulation were used for cost estimations. The capital cost of the plant was estimated at 166 MUSD2010 using scaling factor and installation factors available in literature. An installed cost method was used for estimation of production cost [6]. The sensitivity analysis has shown that methanol might be produced at cost of 62-213 USD/t or at 138 USD/t in the base case. Compared to the current price of methanol in Asian market at 310-350 USD/t [7], the obtained values allow concluding that production of methanol from COG with the selected process flow diagram could be economically feasible.

## 5. Conclusion

According to the results of this study, combination of cokemaking plant and synthetic methanol plant within the same production boundary has appeared feasible both technically and economically. Moreover it might contribute to reduction of country's total dependence on imported transport fuel and to the development of chemical process industry in Mongolia.

## References

[1] Ministry of Energy of Mongolia, "Current trend of coal sector", April 2010. Available at: www.mmre.energy.mn

[2] Sun et al, Study on a multifunctional energy system producing coking heat, Elsevier, Fuel 2009

[3] Lundgren et al, Methanol production at an integrated steel mill, 18th International Congress of Chemical and Process Engineering,2008, Prague, Czech Republic

[4] George A. Olah, Alain Goeppert, and G. K. Surya Prakash, "Beyond Oil and Gas: The Methanol Economy", 2009

[5] A.Kaufman et al, "Theory and practics of modern coking process", Ural State Technical University, 2005 (in Russian)

[6] N. Hamelinck, and C. Faaij, "Future prospects for production of methanol and hydrogen from biomass" Utrecht University, Copernicus Institute, Department of Science, Technology and Society, September 2001

[7] Methanol price list 2010, available at www.methanex.com

[8] Peter Diemer et al, "Potentials for utilization of COG in integrated iron and steel works", 2nd International meeting on ironmaking, Sep.2004, Brazil

[9] Francois Bollon - Total, "International DME standardization", presented at 6th Asian DME conference in Seoul, 2009

Table 1: Comparison of coking property of NS coal with typical coking coal

| Parameters | Typ. coking coal | NS coal |
|---|---|---|
| Volatile matter, dmmf | 19-35% | 31-37% |
| Reflectance of Vitrinite | 1.2-1.3% | 0.5-0.84% |
| FSI | | |
| weakly caking coal | 3 | 1-6 |
| moderately caking coal | 4-5 | |
| strongly caking coal | 6-7 | |
| RI | >45 | 60-75 |
| Sapozhnikov thickness of plastic layer | 14-17mm | 7-11mm |
| Maximum fluidity | 200-1000ddpm | 14ddpm |
| Fe2O3 in ash | <10% | 7.8-11.8% |
| CaO in ash | <3% | 6.4-12.7 % |
| CSR (predicted) | >80 | 53-68 |
| NKK window model | - | III |

Table 2: Experimental conditions

| | |
|---|---|
| Coal sample | Mongolian coal |
| Mass of coal sample | ~65 g |
| Carbonization temperature | ambient ~ 900 °C |
| Carbonization atmosphere | nitrogen |

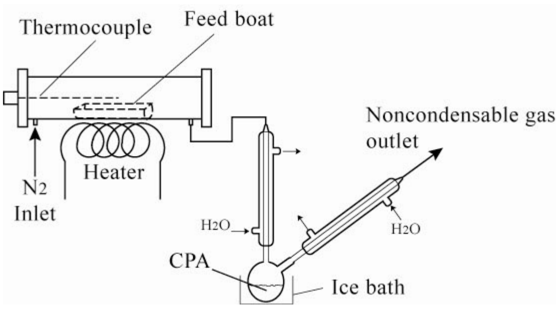


Fig.1: Schematic diagram of carbonization apparatus

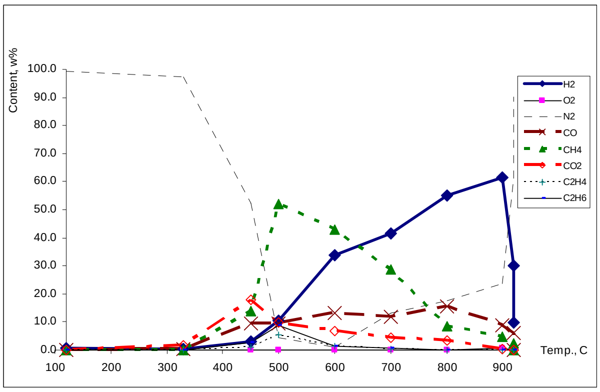


Fig.2: Change of off-gas composition from Mongolian NS coal at various temperatures of carbonization

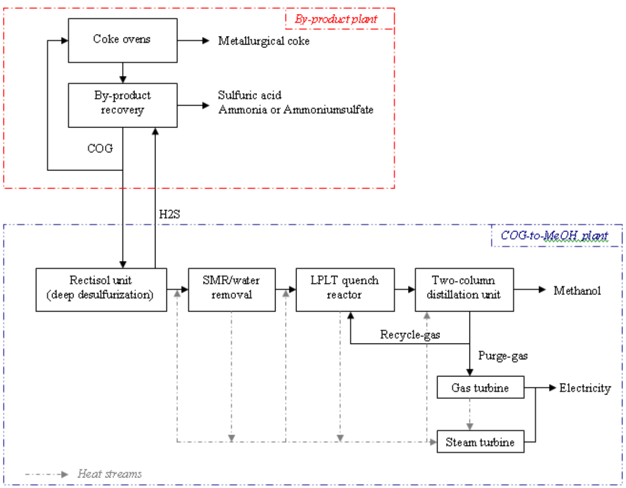


Fig.3: Process flow diagram for COG-to-Methanol plant

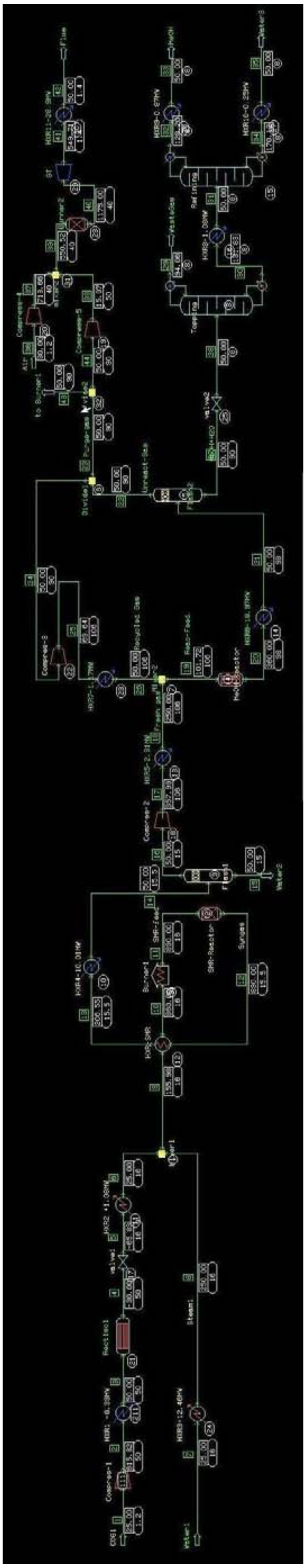

Fig.4: Process Flow Diagram of the COG-to-MeOH plant (Synthesized using ChemCAD III)

# CHARACTERIZATION OF GROUNDWATER DEVELOPMENT POTENTIAL IN AGUSAN DEL NORTE, PHILIPPINES

Student Number: 08M51539 Name: Pierre Anthony JOVEN Supervisor: Shinobu YAMAGUCHI
Jun-ichi TAKADA

## フィリピンのアグサンデルノルテ州における地下水開発潜在力の特徴

ピエル　アンソニー　フベン

Optimum groundwater utilization to augment agri-industrial water demand requires understanding of local hydrogeology. This study evaluates the groundwater development potential of Agusan del Norte, Philippines using Groundwater Resource Potential Index (GRPI) model. Geographic Information System (GIS) was utilized to manage, process and analyze existing data of well lithologic logs and to produce thematic maps of eight GRPI indicators. The provincial hydrostratigraphy shows that the study area is characterized by a shallow aquifer and a confined aquifer located at varying depths of 38-55m below ground surface. Further analysis delineated approximately 60%, 21% and 18% of the study area to have moderate, high and low groundwater development potential respectively. This study is expected to strengthen the provincial water management strategies in ensuring agri-industrial productivity.

# 1 Introduction

Growing population, increasing urbanization and emerging agri-industrial production are the major contributors to the unprecedented huge water demand for the province of Agusan del Norte, Philippines. Regarded as an under-valued resource, groundwater is one of the means to augment the provincial water demand.

Though 96% of the world's readily available freshwater is trap in groundwater aquifers; sufficient knowledge, awareness and understanding of the groundwater resources are still weak in many places especially in developing countries. One of the fundamental constraints of groundwater studies in developing countries is the lack of data and information of groundwater resource [1].

The advent of geographical information system (GIS) provides an opportunity of conducting cost-effective hydrogeologic studies. While well drilling requires significant amount of time, human and financial resources; GIS can utilize available data such as well lithologic logs without well drilling. With GIS analysis, organizations with limited financial resources such as local government units can play a significant role in managing its groundwater resource.

## 1.1 Problem Statement and Significance of Study

The province of Agusan del Norte has inadequate access to safe and potable water, including irrigation. Only about 70% of the households are connected to pipe water distribution system and only 15% of the farmlands are covered by an irrigation system [2]. People make necessary means to tap any available water source to have sufficient water supply in their households and businesses. Consequently, random well drilling and unregulated groundwater extraction to augment domestic, agricultural and industrial water demand eventually result to unproductive wells and deterioration of aquifer characteristics. Thus, in order to optimize groundwater utilization, it is necessary to understand the provincial hydrogeology, which requires the characterization of groundwater development potential.

## 1.2 Objectives of the Study

This study intends to contribute to the provincial government units' water management strategies by characterizing the provincial groundwater development potential. The specific objectives of the study include the following:

1. Establish a well geographic database by gathering all possible groundwater-related information for Agusan del Norte.
2. Understand the provincial aquifer characteristics by visualizing the provincial hydrostratigraphy.
3. Evaluate the groundwater development potential of the province and discuss its implications with policy recommendation.
4. Examine the capability of QGIS 1.4 as an alternative GIS platform to ArcGIS 9.3.

# 2 Characterization Framework and Methodology

Groundwater development potential (GDP) is the ability of an area to support present and future groundwater demand for domestic, agriculture and industry use. The characterization of GDP in Agusan del Norte, Philippines takes five steps: 1) data collection and revalidation, 2) identification of groundwater resource potential index (GRPI), 3) development of well geodatabase, 4) visualization of provincial hydrostratigraphy, and 5) analysis of groundwater development potential.

Hydraulic conductivity (K) of soil sample in the well lithologic log was utilized to differentiate the hydrostratigraphic units [3]. Subsequently, a model was formulated to evaluate the GDP. The GRPI model is composed of eight indicators, categorized in three sub-indices. Geographic information system (GIS), particularly ArcGIS 9.3, was utilized to manage, process and analyze existing data of well lithologic logs and to produce thematic maps of the eight GRPI indicators namely: 1) depth of confined aquifer, 2) thickness of confined aquifer, 3) static water level, 4) land use, 5) soil type, 6) slope, 7) effective rainfall and 8) rice consumptive use. The GRPI indicators and sub-indices were integrated using weighted multi-criteria overlay analysis to generate the GRPI map. Finally, the GRPI map was classified into five classes to create the GDP map. The GDP map delineated the study area as: 1) very high, 2) high, 3) moderate, 4) low, and 5) very low GDP.

## 2.1 Study Area

The study area comprises mainly of the Agusan Valley (Fig. 1). It is characterize by a low gradient alluvial floodplain with recent geology and lies between the longitudes from 125° 12' 50.4" to 125° 39' 21.6" and latitudes from 8° 42' 18.0" to 9° 27' 39.6". The study area has a total geographical area of about 1,121 km$^2$, which occupies about 40% of the province of Agusan del Norte. This areal extent constitutes 76% of all the settlement area wherein 95% of rice is being produced.

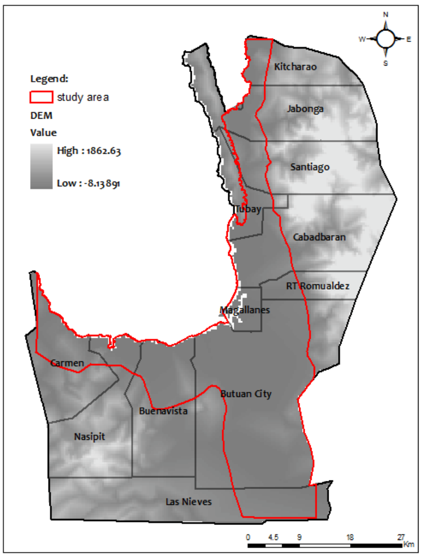


Figure 1. The study area (created by the author, April 2010)

## 2.2 Data Collection

A fieldwork in the Philippines was conducted in December 2009 until January 2010. The main objectives of the fieldwork were: 1) to gather existing data of well lithologic logs, 2) to revalidate gathered data, and 3) to rationalize the GRPI indicators and sub-indices.

### 2.2.1 Identification of Relevant Data

The researcher visited multiple national and local government agencies in Metro Manila and Agusan del Norte, Philippines to gather existing data. Relevant data collected include: lithologic logs or borehole logs of wells, geologic formations, soil type, land use, slope, rainfall, static water level, seismic faults, and rice production volume. The researcher had a consultation with local well professionals to discuss about the perceived location of deep confined aquifer within the province.

### 2.2.2 Local Seminar-Workshop

On January 2010, the researcher organized a provincial seminar-workshop, which was participated by local government planners and groundwater professionals. Specific objectives of the local seminar-workshop were: 1) to present the research proposal; 2) to revalidate collected data; 3) to rationalize the proposed GRPI indicators and indices; and 4) to discuss sustainability issues of the research outputs.

## 2.3 Groundwater Resource Potential Index (GRPI) Model

A model was developed for integrating the GDP indicators and sub-indices into a value called groundwater resource potential index (GRPI). GRPI is a combined statistic used to describe and differentiate areas by the level of GDP.

The GRPI model was rationalized and justified in a local seminar-workshop (Table 1). During the workshop, the proposed indicators and sub-indices were defined and their relationship relative to GDP was discussed. Then, worksheets were disseminated wherein each participant provided weight to the indicators and sub-indices based on their experiences and perception of the factors affecting groundwater availability, rechargeability and demand. Also, participants provided their justification behind the relative weights given to each indicator and sub-index.

Table 1. The GRPI Model

| | GPRI Sub-indices and Indicators | Weight (%) | |
|---|---|---|---|
| A. | Availability sub-index | 55 | |
| | 1. Depth of confined aquifer | | 37 |
| | 2. Thickness of confined aquifer | | 35 |
| | 3. Static water level | | 28 |
| B. | Rechargeability sub-index | 32 | |
| | 4. Land Use | | 36 |
| | 5. Soil type | | 26 |
| | 6. Slope | | 20 |
| | 7. Effective rainfall | | 18 |
| C. | Consumptive use sub-index | 13 | |
| | 8. Rice consumptive use | | 100 |

Source: Consolidated by the author, February 2010

Subsequently, all the responses were consolidated and the average weight of each indicator and sub-index was computed to create the GRPI model. The GDP was evaluated based on the GRPI model.

The GRPI sub-indices are: 1) availability, 2) rechargeability, and 3) consumptive use. The sub-index value is the summation of all indicators under each sub-index category multiplied by its respective indicator's weight, as shown in the model. This model utilized weighted multi-criteria overlay analysis. Literature supports that this analysis has been adopted recently in groundwater availability and groundwater recharge studies [4]. Similarly, GRPI was calculated by the summation of the three sub-index value multiplied by its respective sub-index weight. Clustering of indicators into categories or sub-index can be effective in analyzing the strengths and weaknesses of a certain area or locality.

# 3 Data Analysis and Findings

## 3.1 Well Geodatabase

In order to create a significant well geodatabase, two essential attributes of a database were examined. These are the reliability and content validity.

1) *Reliability of the thematic layers*. Reliability of the thematic layers in the well geodatabase is consistent with the data source. The vector and raster features classes in the well geodatabase are the same vector and raster data used by the Department of Environment and Natural Resources (DENR) and the Provincial Local Government of Agusan del Norte.

2) *Content validity of tabular data*. Content validity of general well database is based on the accuracy of data. Tabular data of general well database came from the authorized Philippine government agencies to collect and publish their specific data of concern and thus, all tabular data in the well geodatabase are considered authentic and accurate.

## 3.2 Provincial Hydrostratigraphy

The provincial hydrostratigraphy was visualized using three-dimensional cartography in ArcGIS 9.3 ArcScene application. The provincial hydrogeology shows the following major findings. First, the entire study area is characterized by a shallow aquifer, which is defined as water bearing formation of depth less than 20m. Second, the analysis found that another water bearing formation of deep confined aquifer is located below the shallow aquifer with depths ranging from 38 to 55 meters below the ground surface (Fig. 2). This can be interpreted that the shallow aquifer could be a satisfactory source of irrigation water whereas the deep confined aquifer is the suitable source of potable water.

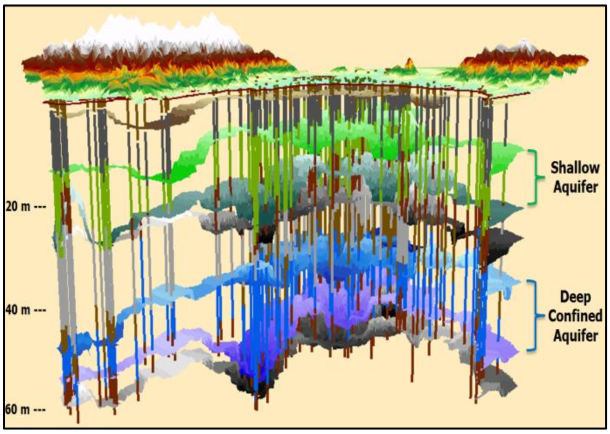


Figure 2. The provincial hydrostratigraphy (created by the author, April 2010)

These findings are particularly significant on the following two contexts. First, the presence of a shallow aquifer concurred with the previous reliable study of rapid assessment of water supply sources conducted by the National Water Resource Board in 1982. This extensive study using GIS further identified larger scale of shallow aquifer. The presence of shallow aquifer in the entire study area agreed with the previous study that most arable land in the Philippines is overlain with a shallow aquifer [5]. Second, there has been discussion among local professional well drillers that the area is exemplified with a deep confined aquifer. However, this study is the first to visualize its existence, supporting the argument of local professionals.

The three-dimensional cartography of the hydrostratigraphic layer was limited to a depth of 70m because most wells have lithologic log data until this depth. Although some wells have lithologic logs up to 150 meters, especially wells owned by water utility service providers, analysis results would be unreliable due to limited number of data points.

Understanding the provincial hydrostratigraphy will enable households and other groundwater users to determine the feasible location of wells, design well specifications and estimate construction cost of wells.

## 3.3 Groundwater Development Potential

Groundwater development potential (GDP) describes the ability of an area to support groundwater demand for domestic, agricultural and industrial use. GRPI value of 5 means that the area has abundant presence of groundwater and it requires minimal amount of power to pump groundwater whereas, GRPI value of 1 means that it is not feasible to extract groundwater in the area. Results showed that the lowest GRPI value is 1.7979 while the highest GRPI value is 4.5768. A large area of Butuan City has relatively low GRPI value whereas most areas of the municipalities of Magallanes and Tubay have relatively high GRPI value.

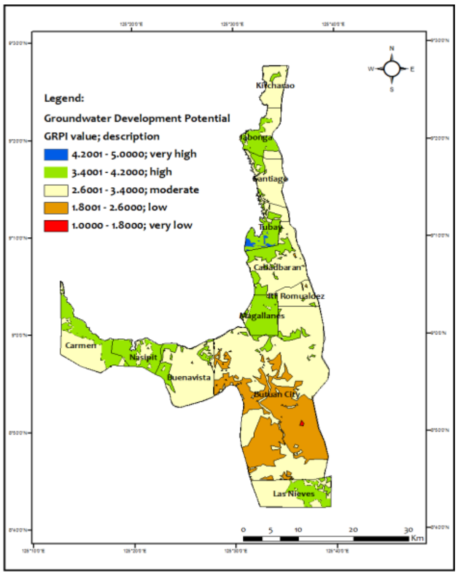


Figure 3. The groundwater development potential map (created by the author, June 2010)

In order to illustrate the GDP of Agusan del Norte, GRPI map was classified into five categories. This resulted in the GDP map (Fig. 3). The GDP map delineated approximately 60%, 21% and 18% of the study area to have moderate, high and low groundwater development potential respectively (Table 2).

Table 2. GRPI value range and area of each GDP class.

| GRPI value range | Description | Area in % of total area | Area, $Km^2$ |
|---|---|---|---|
| 4.2001 – 5.0000 | Very high | 0.38 | 4.23 |
| 3.4001 – 4.2000 | High | 21.22 | 237.86 |
| 2.6001 – 3.4000 | Moderate | 60.29 | 675.91 |
| 1.8001 – 2.6000 | Low | 18.07 | 202.53 |
| 1.0000 – 1.8000 | Very low | 0.04 | 0.46 |

Source: Summarized by the author, June 2010

The coastal zones of the municipalities of Jabonga, Nasipit and Carmen; and the entire area of Magallanes have high GDP. These areas can be considered as priority area for establishing agri-industrial and special economic zone. The southern part of Butuan City has low GDP, which can be inferred that the locality has difficulty of supporting current and future groundwater demand.

The municipalities of Kitcharao, Santiago, Buenavista and northern part of Butuan City have moderate GDP. This can be interpreted that the locality has the means of support current groundwater demand. However, unlike areas with high GDP, the ability of these localities to support future groundwater demand is uncertain. To ensure that the locality can augment future groundwater demand, groundwater management strategies must be implemented by the concerned local government unit.

# 4 Policy Recommendations

After careful considerations of the analyses and findings including the discussion during the local seminar-workshop, four over-arching policy themes persistently arises. These are: 1) prioritization of groundwater for potable water use; 2) improved efficiency of groundwater utilization; 3) regulation of groundwater pumping; and 4) rehabilitation of brush lands, grasslands and logged-over areas.

Groundwater for potable water use in households should be prioritized over agricultural and industrial use purposes. All local government units (LGUs) can widen agricultural irrigation coverage by taking advantage of the presence of shallow aquifer in their respective locality through shallow tube well irrigation. As much as possible, deep confined aquifer should be utilized exclusively for drinking water in households.

With high groundwater availability, the municipalities of Magallanes, Remedios T. Romualdez, Tubay and Cabadbaran City should be the key administration units to establish efficient groundwater utilization mechanism. LGUs should devise a system to store or divert surplus water coming from free-flowing wells. Establishment of local water utility service provider in these municipalities is urgently needed. This not only improves water use efficiency but also promotes equitable distribution and wider access to safe and affordable freshwater.

The municipalities of Kitcharao, Santiago, Buenavista and Butuan City have scarce groundwater availability. Groundwater pumping should be regulated in these localities. One approach of regulating groundwater pumping is limiting the density of deep wells in the area. Limiting the density of deep wells would stabilize pump flows and enable constant rate of groundwater recharge.

Extensive rehabilitation of brush lands, grasslands and logged-over areas should be considered as a provincial policy. All LGUs in the province are encouraged to increase investment in reforestation projects such as bio-fuels plantation in brush lands and watershed reforestation projects.

# 5 Evaluation of QGIS 1.4 as an Alternative GIS Platform

One of the constraints of GIS implement in local government units is the cost of commercial GIS software. To overcome this constraint; evaluation QGIS 1.4, which is a free and open source software for GIS, was pursued. This motivation would also avoid the illegal use of commercial GIS software.

QGIS 1.4 capability was evaluated by analyzing the groundwater development potential. After detailed investigation, it was recognized that QGIS 1.4 performs very well with vector and raster datasets through fTools, GRASS and other plugins. QGIS 1.4 is capable of performing standard geoprocessing and spatial analysis, with outputs comparable to ArcGIS. It can be inferred that QGIS 1.4 has a great potential to be deployed in local government units of Agusan del Norte, Philippines.

# 6 Conclusions

Reliable lithologic logs from various government agencies were identified in order to conduct a valid data analysis. The provincial hydrostratigraphy confirms that the study area is characterized by a shallow aquifer as well as deep confined aquifer. The GRPI model provided a holistic and comprehensive approach in evaluating the groundwater development potential of Agusan del Norte, Philippines. Further analysis delineated about 60%, 21% and 18% of the study area to have moderate, high and low GDP respectively.

These specific findings can assist the provincial government's decision to pursue water resources planning for sustainable groundwater utilization. Further, it is envisioned that this research will strengthening the provincial water management strategies.

# References


[1] M.K. Jha, A. Chowdhury, V.M. Chowdary, and S. Peiffer, "Groundwater management and development by integrated remote sensing and geographical information systems: Prospects and constraints," *Water Resource Management*, vol. 21, pp. 427-467, 2007.

[2] PGAN, Provincial Profile-Agusan del Norte. [Online], Available: http://www.agusandelnorte.gov.ph/index.php?option=com_content&task=view&id=20&Itemid=84. (accessed on February 12, 2010).

[3] K. O. Thomsen, C. Pokorny, and J. Agnoletti, "Groundwater resource planning – defining the shallow aquifer system," *Proc. 26th Annual ESRI Education User's Conference*, 2006.

[4] V. Madrucci, F. Taioli, and C. C. Araujo, C.C., "Groundwater favorability map using GIS multicriteria data analysis on crystalline terrain, Sao Paulo State, Brazil," *Journal of Hydrology*, vol. 357, pp. 153-173, 2008.

[5] W. David, "Constraints, opportunities and options in irrigation development," Philippine Institute of Developmental Studies, Discussion Paper Series No. 2000-39, 2000.

# FINANCIAL FEASIBILITY STUDY OF A NEW CEMENT PLANT IN MONGOLIA

Student number: 08M51551 Name: Binderiya DONDOV Supervisor: Shinya HANAOKA

モンゴルにおける新セメントプラント建設の財務的実行可能性分析

ドンドブ　ビンデリア

In order to successfully implement the project, financial feasibility study along with risk analysis is conducted for potential investment. The source of the project cash inflows is revenue from its sales. Therefore using the past 9 years time series observations on the total consumption of the country, the future years demand is forecasted applying Holt's linear exponential smoothing technique. To see if the project is worth more than it costs, both NPV and IRR are also estimated. Stochastic risk analysis is conducted based on the discounted cash flow modeling to determine the magnitude of consequence of important parameters like inflation rate and sales volume etc. to the total value of the project. The outputs illustrate that the cement plant project is worth undertaking an investment.

## 1 Introduction

The transition to a market economy and a series of severe winters (called 'Zhud') in Mongolia have resulted in the large scale migration of low-income families into the *gerr* areas[1] of Ulaanbaatar (UB) city [1]. Clearer policy directions, such as the "Compact City" concept of the UB city Master Plan 2030, have emerged in recent years to control spatial expansion and promote high-density development for the *gerr* areas [2]. Mongolia, on the other hand, imports approximately 70 percent of total cement consumption as the domestic cement producers are not being able to supply fast growing consumption needs. The residential market of Ulaanbaatar and provincial centers has consistently grown over the last few years, with supply of construction materials very much struggling to meet the high level of demand. With growing cement demand not only in Mongolia but in adjoining Siberian region as well, investments in new cement production capacity will yield good returns [3]. Thus it is vital to establish a new cement production facility to supply the growing needs to enhance economic activity as well as alleviate foreign trade balance deficit.

Hence the thesis is aimed at analyzing financial feasibility of a potential cement production facility for private investment when limited sources from the Government constrain the country. The most critical question is whether the revenue driven from the proposed project is worth more than investment made by the projects stakeholders. Given the annual net cash flows, both project owner and investor have to insure what is the probability that Net Present Value of the project reaches less than zero, what are the most influential economic factors to the total value of the project and risks that they must bear. On the other hand, question of whether market is capable of growing in the future is vital for project's revenue generation from its product sales. In order to answer these questions, the thesis aims to determine and analyze 1) Forecast of future cement demand derived from quantitative time series analysis 2) Estimation of annual cash flows, Net Present Value and Internal Rate of Return and 3) Risk analysis and modeling of uncertainty associated with future cash flows and NPV (Monte Carlo simulation using @Risk).

## 2 Proposed project

The new cement plant project owner is one of Mongolian private entities operating business in construction materials trade as well as mining exploration, extraction and prospecting works. It plans to implement processing facility to produce 1 million tons of Traditional Portland cement product per annum.

The cement plant location is planned to be within the area of '*Biluut*' limestone deposit in the Dalanjargalan soum of the Dornogobi province in Mongolia. The deposit is located about 17km north-west from 25th railway cross-roads in Dalanjargalan soum, 320km south-east from Ulaanbaatar city and 15km from Choir - Sainshand earth road. The '*Biluut*' deposit has approx. 30 million tons of limestone reserve as to be accessible to electricity, built

[1] The word 'gerr' refers to the felt tents used traditionally by Mongolian herdsmen. In this context, the 'gerr areas' refers to the periurban areas surrounding Ulaanbaatar and other provincial centers occupied by informal settlers.

infrastructure and auxiliary materials supply. The construction phase is estimated to be 2 years and operational phase will commence in 2013.The figure 1 below shows the location of the proposed project.

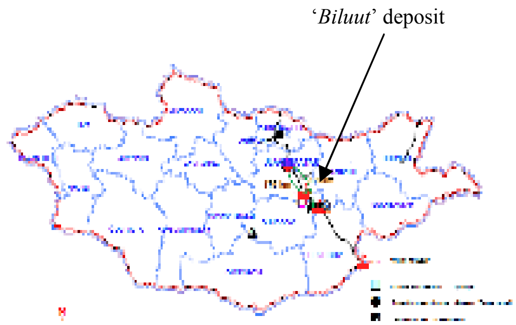


Figure1. Location of '*Biluut*' deposit

The two domestic producers: 'Erel' and 'Khutul' cement plants struggle to meet the present demand of 1 million tons per annum. The two cement plants produce approx. 100,000 tons and 170,000 tons of cement per annum, respectively.

# 3 Future Demand Forecasting

The main source of project cash inflows is the revenue from its sales. Thus it is important to answer to the question of whether the market is capable of growing in the future. Therefore using the past 9 years time series observations on the total consumption of the country, the future years demand is forecasted applying Holt's Linear Exponential smoothing technique. The total annual consumption of cement in 2001-2009 is shown in Table 1. Due to the Lehman shock hit the world market, Mongolia's cement consumption which increased gradually over past years fell dramatically in 2009.

Table 1. Annual consumption

| Year | Consumption, '000 tons |
|---|---|
| 2001 | 94.8 |
| 2002 | 200.2 |
| 2003 | 253.2 |
| 2004 | 275.7 |
| 2005 | 415.0 |
| 2006 | 450.7 |
| 2007 | 595.0 |
| 2008 | 978.7 |
| 2009 | 673.1 |

Fortunately, when historical sales data are available, some proven statistical forecasting methods have been developed for using these data to forecast future demand. Such a method assumes that historical trends will continue, so a company management then needs to make any adjustments to reflect current changes in the marketplace [4]. Thus the following algorithm (Holt's linear exponential smoothing) is applied based on the above yearly time series to generate future years' forecasts.

$S_t = \alpha y_t + (1+\alpha)(S_{t-1} + B_{t-1})$ , $S_t$ – the smoothed estimate
$B_t = \beta(S_t - S_{t-1}) + (1-\beta)B_{t-1}$, $B_t$ – the best estimate of the trend
where $0 \leq \alpha, \beta \leq 1$
$F_{t+1} = S_t + B_t$
$F_{t+m} = S_t + mB_t$, where m - number of period ahead to be forecasted

The smoothing parameter, α is optimized using *Solver* function on Excel spreadsheet and found to be 0.4 whereas trend smoothing constant, β is used as 0.2. The forecasted values up to 2015 as an example are shown together with actual consumption plots in the Figure 2 below. As a consequence of Double exponential smoothing method (Holt's linear), the forecasted values maintain monotonous rising trend in the upcoming years up to 2030. The demand of 2013, the first year of operation is estimated to be 1,149.0 thousand tons.

Another approach is utilized based on the quarterly time series. The forecasted values based on the quarterly time series do exhibit the rising trend as well and generate much closer data to the forecasts based on yearly time series. Quarterly time series reveals seasonal variation due to ceased constructions during winter period. Thus seasonal factor is estimated in order to measure how the period (quarter) compares to the overall average for an entire year. Hence seasonal effects are removed using estimated seasonal factors to generate forecasts applying exponential smoothing method. Since revenue from sales is a critical factor for the project to be viable, the yearly time series generated forecasts are market volume used as an uncertain parameter for Monte Carlo simulation in the stochastic risk analysis.

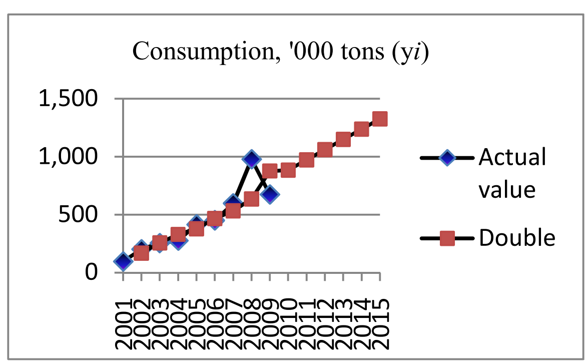

Figure 2. Scatter plot of forecasted values up to 2015

# 4 Financial evaluation

The economic viability of the project depends on the adequacy of the cash flows generated as compared to the cash flows that must be expended. Thus discounted cash flow (DCF) analysis is crucial in determining the economic viability of a proposed project and the adequacy of the rates of return that providers of capital to the project can expect to realize. Projecting the cash outflows and inflows is a critical part of the DCF analysis [5]. The proposed cement plant project's total cost was estimated on a basis of sound assumptions and current market data. Subsequently the project's total annual operating costs as well as capital expenditures are computed based on the Turnkey-Lump sum Engineering Procurement Construction contract established between the project owner and International Consulting firm.

## 4.1 Discounted cash flow analysis

Thus the total operating annual cash cost is estimated to be $US 20,122,753 which comprises of all direct and indirect costs, such as raw materials purchase, utilities (electricity, water), maintenance costs, transportation costs, wages and welfare of the plant employees, mining license fee, royalty and other costs.

The total capital cost is estimated to be $US 101,713,129 which includes investment costs for civil engineering, erection as well as plant machinery and equipment. In addition to the total annual cash outflows as well as total capital costs, revenue from the products sales is computed based on the forecasted values of demand and current market price. Consequently, the annual revenue from sales is estimated to be $US 83 million. Finally, net operating cash flows are estimated on an annual basis.

**Net Present Value**

The NPV of the proposed investment project is the present value of all of the after-tax cash flows (CF) connected with the project – all its costs and revenues, from now and the operational phases up to year 2030. The decision rule to follow: Undertake an investment to the project if NPV is positive (NPV>0). Previously in the thesis, it is assumed that the project's cost of capital; *r* is 9.9 percent on a basis of International Finance Corporation long-term loan interest rate. Then applying the formula of NPV, we have:

$$NPV = \sum_{t=o}^{n} \frac{CF_t}{(1+r)^t} = \sum_{t=2011}^{2030} \frac{CF_t}{(1.099)^t} = \$US\ 153,6\ million$$

**Internal Rate of Return**

Another method, Internal Rate of Return (IRR) for evaluating the proposed project is utilized. It is commonly referred as the capital investment project's expected rate of return. The IRR for the project is the discount rate that makes the NPV equals zero:

$$0 = \sum_{t=0}^{n} \frac{CF_t}{(1+IRR)^t} = CF_0 + \sum_{t=2013}^{2030} \frac{CF_t}{(1+IRR)^t}.$$

Thus we have IRR = 16% > 9.9%. As a result, expected rate of return, *IRR > r*.

## 4.2 Risk analysis of financial forecasting

Both the project owner and investor have to insure what is the probability that Net Present Value of the project reaches less than they expected and what are the most influential economic factors to the total value of the project. Monte Carlo simulation using @Risk is applied in order to model the uncertainty associated with the future cash flows estimated and answer to the above questions. In Monte Carlo simulation, uncertain inputs in a model are represented using ranges of possible values known as probability distributions. Probability distributions are much more realistic way of describing uncertainty in variables of a risk analysis. In business and government, one faces having to make decisions all the time where the outcome is uncertain. Understanding the uncertainty can help us a much better decision [6].

Thus discounted cash flow model is developed from the results of section 4.1 and uncertainty is described assigning probability distributions of input random variables: unit cost, inflation rate, no. of competitors, sales price, market volume, sales volume and overhead costs.

Output variables from the Monte Carlo simulation using @Risk are Net Present Value and Net Income during operational phase up to 2030. As a result, the average NPV equals $US 118.6 million. The probability that NPV<0 is about 2.5% as illustrated in the following figure 3. Monte Carlo simulation is ran using @Risk with 10,000 iterations – the spreadsheet is calculated repeatedly with a set of new possible values sampled from each distributions and each iteration.

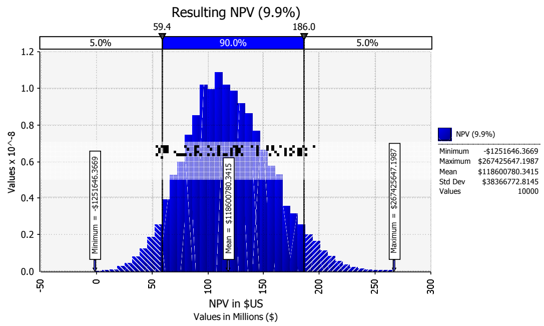


Figure 3. Histogram distribution of resulting NPV

@Risk Tornado graph – Regression mapped values shown in Figure 4 below displays the most influential factors affecting the NPV that are sales price of the year 2013 and no. of competitors entering the market in 2016 followed by unit cost of year 2013.

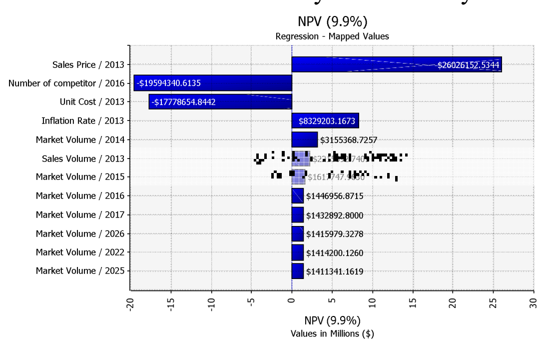


Figure 4. Tornado graph – regression mapped values

No. of competitor that enters the market is 2 at maximum and 1 at minimum values in the Uniform distribution assigned in the simulation. Though it is assumed there will be 3 plants in total over time to share the market, the Net income is expected to grow gradually, as a result. The summary trend graph below shows increasing risk over a range of outputs: Net Income/2013 to Net Income 2030. As the band gets wider, it illustrates increasing uncertainty in the Net income estimates over the years.

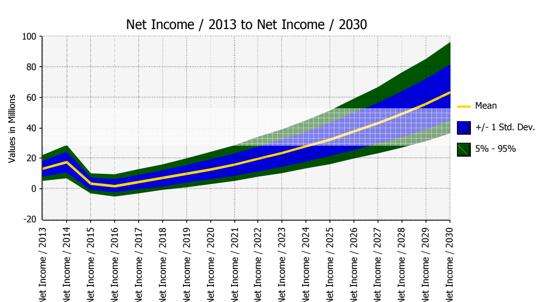


Figure 5. Summary trend graph

# 5 Conclusions

The project appears to generate significant economic return under sound assumptions. It is expected to contribute significantly to the economic development of Mongolia. Government of Mongolia aims to develop more and more infrastructure projects such that there is a necessity to ensure smooth supply of raw materials, in particular cement product for the those projects.

As a result of forecasting of future cement consumption in the country using Holt' linear exponential smoothing technique, it is estimated that the market volume will increase with monotonous rising trend in the upcoming years.

The DCF analysis involved estimating the amount of the initial investment, projection of after-tax-cash flows, estimating cost of capital, and then using the NPV and IRR method to determine whether the project is worth more than it will cost.

Financial forecasting model was developed for stochastic risk analysis to appraise the uncertainty attached to the project. If the project owner and investors are strongly risk averse, the project is the one to undertake an investment though the risk increases over time along with increase in the Net Income. There is a very low, i.e. 2.5% chance that Net Present Value will be negative. Thus the result illustrates that the project is expected to yield high expected future cash flows.

# References

[1] World Bank, Gerr area development report, Mongolia: Enhancing Policies and Practices for Gerr area Development in Ulaanbaatar, March 2010

[2] Asian Development Bank, Mongolia: Towards a Coherent Local Development Framework report, March, 2007

[3] Asian Development Bank, Mongolia: Private Sector Assessment report, April, 2009

[4] Hillier, F.S., and Lieberman, G.J., (2001) Introduction to Operations Research, Seventh edition, The McGraw-Hill Companies, Inc., USA

[5] Finnerty, J.D., (2007) Project Financing, Asset based Financial Engineering, Second edition, John Wiley & Sons Inc., USA

[6] Vose, D., (2009) Risk Analysis – A Quantitative guide, Third edition, John Wiley & Sons Ltd. England

# REASONABLE CONCESSION PERIOD FOR BUILD-OPERATE-AND-TRANSFER (BOT) ROAD PROJECTS IN THE PHILIPPINES

Student Number: 08M51568 Name: Hazel Perez PALAPUS Supervisor: Shinya HANAOKA

This research provides a methodology to determine the reasonable concession period that would be advantageous both to the government and the private sector with the effect of risks taken into consideration in the financial evaluation using Monte Carlo simulation and bargaining game theory. To demonstrate the applicability of the proposed methodology, two Build-Operate-and-Transfer (BOT) road projects in the Philippines were used as case studies. The results revealed that the resulting concession period of the case studies should have been longer than the actual concession period granted to the private sector indicating the impact of risks in the cash flow. With the proposed methodology, the government could further enhance its policies in processing BOT projects with the end in view of increasing private sector participation in infrastructure development.

## 1 Introduction

Concession period starts from the signing of the concession agreement between the government and the private sector indicating the span of time within which the private sector is responsible for the construction phase and operation phase of the Build-Operate-and-Transfer (BOT) project. In the Philippines, the length of concession period is usually decided by the infrastructure implementing/head agency. Currently, there are two BOT road projects implemented in the country. The Southern Tagalog Arterial Road (STAR) Tollway is currently operational with a 30- year concession period from 2000 to 2029 while the Tarlac-Pangasinan La Union Expressway (TPLEX) is under construction with a 35-year concession period from 2008-2043. Prior to the projects' submission to the evaluating agency to facilitate subsequent approval, the length of concession period is already defined and thus treated as an input parameter in project evaluation. Moreover, a quantitative risk analysis which considers the impact of variability in the concession parameters has not yet been put into practice. At present, the evaluating agency adopts a single point or deterministic modeling in project evaluation wherein a single best guess value of each variable is used to determine the financial indicators.

While Shen et al.'s [1, 2] studies offered an analytical deterministic method for determining the length of concession period to be granted to the private sector, they cannot be applied directly to the case studies used in this research. The cash flow structure generated for the case studies does not follow the cash flow trend of the hypothetical project used in previous studies. Likewise, the simulation model proposed by Shen and Wu [3] cannot be applied to the case studies as the same hypothetical project was utilized in the study. On the other hand, Ng et al.'s [4] proposed methodology was not used as it is believed that net present value (NPV) analysis is a more powerful method of project evaluation compared to internal rate of return (IRR) analysis used in the study. NEDA et al. [5] affirmed that the NPV criterion is widely accepted by accountants, financial analysts and economists as the only one that yields correct project choices in all circumstances.

This paper aims to provide a methodology to determine a reasonable concession period that considers the effect of risks on uncertain concession items in project evaluation. The proposed methodology generated a concession period interval within which a specific concession period could be agreed upon by the government and the private sector. Any point within the interval could be considered as the optimal concession period that would be advantageous to both BOT players. The results showed that the length of the concession period of the case studies should have longer than the actual concession period granted to the private sector.

## 2 Concession Terminologies

Terms related to the analysis of concession period were defined as follows. The relationship of these terminologies is shown in Figure 1.

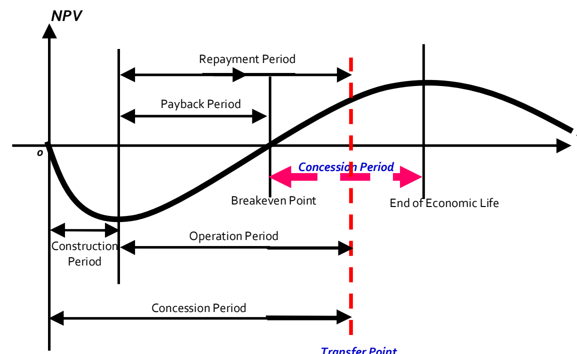


**Figure 1.** Typical NPV Structure of a BOT Project

- ❖ Concession Period – counts from the time when project owner and investor start signing the agreement [6] and includes construction and operation period.
- ❖ Breakeven Point – a point where net present value equals zero [7].
- ❖ Payback Period – time required to recover the cost of initial investment [8]. It ends when project reaches breakeven point.
- ❖ Repayment Period – the period which the debt obligation/loan is to be repaid [9].
- ❖ Transfer Point ($T_C$) – any time/year ($T$) between the breakeven point and the end of economic life; point where the project will be transferred back from the private sector to the government.
- ❖ Concession Interval/Concession Period Interval – interval/period starting from the project's breakeven point until the end of economic life, period where transfer point ($T_C$) decided based on the result of negotiation between the government and the private sector could occur.
- ❖ Economic Life – period over which the project would generate net gains [10].

## 3 Methodology

### 3.1 Concession Parameters

The case studies' concession parameters used as inputs to the financial model were categorized into *(i)* deterministic/certain and *(ii)* uncertain parameters.

### 3.1.1 Deterministic Parameters

Deterministic parameters are defined in this research as parameters of which values could be considered as stable over time.

a. Construction Period – The private sector would ensure that construction will be finished on time or even ahead of schedule to maximize generation of revenues by longer period of operation. Construction period (inclusive of the period for pre-construction activities) used in the model for STAR Tollway and TPLEX was year 2000 to 2007 and year 2008-2014, respectively.
b. Tax rates – Corporate tax and value-added tax imposed on the project are prescribed by law to be 32% of taxable income and 12% of revenues, respectively.
c. Other expenses during operation – This includes items such as insurance, rental fees and other management expenses apart from the regular annual operations and maintenance (O&M) cost spent for both projects.

### 3.1.2 Uncertain Parameters

Uncertain parameters, on the other hand, are those inputs which may be subject to change and high level of uncertainty over time since their future values are difficult to predict.

a. Investment cost – This includes expenditure items needed until the completion of the project. Quantity and cost of construction materials could change during the course of implementation. For TPLEX, *Program Evaluation and Review Technique* (PERT) distribution will be assigned for the cost components which are likely to be risky and prone to variation with distribution parameters of 120%, 100% and 90% of base cost. Since the construction of STAR Tollway was completed, its investment cost was considered deterministic in the financial evaluation. Base cost estimated for both cases was PhP3.4 billion in 2005 prices and PhP 16.8 billion in 2007 prices for STAR Tollway and TPLEX, respectively.
b. Macroeconomic variables – The fluctuations of the market variables such as inflation, interest rate and exchange rate maybe caused by the changes in the policies of the government and economic conditions. Normal distribution (*mean* ($\mu$)*=0, standard deviation* ($\sigma$)*=2.2%*) will be employed to model inflation variability with $\sigma$ computed using the historical inflation. As exchange rate is a function of inflation, its variability was already captured. For interest rates, normal distribution will be employed with $\mu=0$ and $\sigma=1\%$.
c. Expected rate of return – This was set equal to the weighted average cost of capital (WACC) determined by calculating the relative weights of the capital resources and multiplying them with the corresponding opportunity cost of capital (bank interest rate in the case of debt/loan) for each of the capital resource.
d. Traffic volume – As revenue of the case projects depends greatly on the realization of the assumed traffic projection, there is a great risk that the expected rate of return from the project may not be achieved if the assumed traffic is not realized. Normal distribution will be used to model the risk associated with traffic volume with $\sigma$=5% of estimate at a particular year.
e. Toll fee – Toll fees to be charged to the users both for STAR Tollway and TPLEX as well as periodic increases follow a parametric formula which is a function of macroeconomic variables.
f. O&M cost – Cost of labor and materials/ equipments needed for the annual O&M may vary over time. Uniform distribution with parameters *U[minimum= 100% of base O&M cost, maximum=110% of base O&M cost]* will be employed.
g. Revenue – This is determined by the toll fee and the traffic volume expected for the project which are uncertain parameters.
h. NPV – The net cash flow (NCF) calculated by obtaining the difference of revenue and cost was discounted by the WACC to obtain the NPV of the project.

## 3.2 Monte Carlo Simulation

After the financial model has been set-up with NCF and NPV set as the outputs, Monte Carlo simulation was performed using the software *@Risk 5.5.1 Industrial for Excel.* @Risk is a spreadsheet add-in to Excel that performs risk analysis to show possible outcomes and tell how likely these outcomes are to occur. @Risk was set to perform 10,000 iterations in each case study.

## 3.3 Proposed Methodology for Locating Concession Period Boundaries

The equations proposed by Shen et al. [1,2] were modified to consider the impact of loan repayment period while ensuring the expected rate of return from the project. The following equations will be used in the proposed methodology for determining the concession period:

$$NPV(T_{C\_L}) \leq NPV(T_C) \leq NPV(T_f) \quad (1)$$

$$NPV(T_{C\_U}) = NPV(T_f \quad (2)$$

$$T_{C\_L} \leq T_C \leq T_{C\_U} \quad (3)$$

*subject to the following conditions:*

$$NPV(T_{C\_L}) \geq 0 \text{ such that } T_{C\_L} \geq T_{PB} \quad (4)$$

$$T_{C\_L} \geq T_{RP} \quad (5)$$

*where:*

$T_{C\_L}$ – *lower boundary of concession interval where NPV= NPV(*$T_{C\_L}$*)*
$T_{C\_U}$ – *upper boundary of concession interval where NPV= NPV(*$T_{C\_U}$*)*
$T_f$ – *end of economic life where NPV= NPV(*$T_f$*)*
$T_{PB}$ – *end of payback period*
$T_{RP}$ – *end of loan repayment period*

Given an NCF and NPV resulting from the simulation as shown in Tables 1 and 2 and applying the principles of Equations 1 to 5, the following procedures are proposed for locating the concession boundaries.

❖ ***To locate*** $T_{C\_L}$***:***

a. Look for $T_{RP}$) and check whether $NPV(T_{RP}) \geq 0$.
b. If $NPV(T_{RP}) \geq 0$, this year will be considered as the $T_{C\_L}$.
c. If not, look for $T_{RP+n}$ where $NPV(T_{RP+n}) \geq 0$ to be considered as $T_{C\_L}$. $T_{RP+n}$ is the year following the $T_{RP}$ where n= 1,2..n.

❖ ***To locate*** $T_{C\_U}$ ***:***

a. Look for the last year where the net cash flow *(NCF)* $\geq 0$.
b. Consider that year as the end of economic life ($T_f$) and hence the $T_{C\_U}$.

## 3.4 Bargaining Game Theory

In an attempt to identify a specific concession, bargaining game theory was employed. The formulas proposed by Shen et al. [2] were likewise modified to consider the impact of repayment period and to employ the procedures proposed for locating the boundaries of concession interval.

As the BOT players behave rationally, they will not easily give up but bargain for a best deal during the negotiation. For the benefits that the private sector and government would have to share within the concession period interval, the proposed formula to be used is:

$$\text{Benefits generated between } [T_{C\_L}, T_{C\_U}] = NPV(T_f) - NPV(T_{C\_L}) \quad (6)$$

If the first round offer is initiated by the government, its best strategy is viewed as making the first round offer that can allow the investor to gain a similar range of payoffs to what the investor would gain from his possible counteroffer. If the first offer is rejected, the private sector is expected to make a counter offer. But in making a counteroffer, he would have to bear the bargaining cost $f_p$, and the cost of time value by applying the discount factor $\delta_p$, thus, the investor can get a minimum payoff, $\delta_p q_p$ - $f_p$ and maximum payoff, $\delta_p Q_p$ - $f_p$. Consequently, the strategy would allow the government to get a maximum payoff, $Q_g$ and minimum payoff, $q_g$ equivalent to:

$$Q_g \le [NPV(T_f) - NPV(T_{C\_L})] - (\delta_p q_p - f_p) \quad (7)$$
$$q_g \ge [NPV(T_f) - NPV(T_{C\_L})] - (\delta_p Q_p - f_p) \quad (8)$$

If indeed the investor makes a counteroffer, his best strategy is to make an offer that allows the government to gain a similar range of payoffs to what the government can gain if bargaining continues to the next round. At this point, the government will bear the bargaining cost of $2f_g$, for producing the first offer and the counteroffer, and the cost of time value by applying the discount factor $\delta_g$, thus, the government can get a minimum payoff, $\delta_g q_g$ - $2f_g$ and maximum payoff, $\delta_g Q_g - 2f_g$. This gives the investor a maximum payoff, $Q_p$ and minimum payoff, $q_p$ of:

$$Q_p \le [NPV(T_f) - NPV(T_{C\_L})] - (\delta_g q_g - 2f_g) \quad (9)$$
$$q_p \ge [NPV(T_f) - NPV(T_{C\_L})] - (\delta_g Q_g - 2f_g) \quad (10)$$

Transforming Eqs. 10 and 9 to Eqs. 7 and 8, resp:

$$Q_g = q_g = \frac{(1-\delta_p)[NPV(T_f) - NPV(T_{C\_L})] - 2\delta_p f_g + f_p}{1-\delta_p\delta_g} \quad (11)$$

The new upper concession boundary $(T'_{C\_U})$ is located at:

$$T'_{C\_U} = T[NPV = NPV(T_f) - Q_g] \quad (12)$$

Similar procedure is done when the private sector makes the first round offer. The modified equations are as follows:

$$Q'_p \le [NPV(T_f) - NPV(T_{C\_L})] - (\delta_p q'_g - f_g) \quad (13)$$
$$q'_p \ge [NPV(T_f) - NPV(T_{C\_L})] - (\delta_g Q'_g - f_g) \quad (14)$$
$$Q'_g \le [NPV(T_f) - NPV(T_{C\_L})] - (\delta_p q'_p - 2f_p) \quad (15)$$
$$q'_g \ge [NPV(T_f) - NPV(T_{C\_L})] - (\delta_p Q'_p - 2f_p) \quad (16)$$
$$Q'_p = q'_p = \frac{(1-\delta_g)[NPV(T_f) - NPV(T_{C\_L})] - 2\delta_g f_p + f_g}{1-\delta_p\delta_g} \quad (17)$$

The new lower concession boundary $(T'_{C\_L})$ is located at:

$$T'_{C\_L} = T[NPV = NPV(T_{C\_L}) + Q'_p] \quad (18)$$

# 4 Results and Discussion

## 4.1 Simulation Results

The resulting NPV and NCF with risk factors denoted by $rNCF_i$ and $rNPV_{Tc}$, respectively, are shown in Tables 1 and 2.

## 4.2 Concession Period Boundaries

With $T_{RP}$ of 2023 and 2017 for TPLEX and STAR respectively, and applying the procedures prescribed in Section 3.3, the concession period could occur at the following interval:

$$2043 \le T_C \le 2062 \quad \text{for TPLEX}$$
$$2035 \le T_C \le 2057 \quad \text{for STAR Tollway}$$

**Table 1.** NCF and NPV of TPLEX

| Year | $rNCF_i$ | $rNPV_{Tc}$ | Year | $rNCF_i$ | $rNPV_{Tc}$ |
|---|---|---|---|---|---|
| 2009 | -1004.66 | -816.21 | 2050 | 3801.10 | 455.03 |
| ... | ... | ... | 2051 | 3484.43 | 491.63 |
| 2013 | -4324.51 | -10342.50 | 2052 | 3585.16 | 525.43 |
| 2014 | 1543.04 | -9596.48 | 2053 | 3200.95 | 552.84 |
| ... | ... | ... | 2054 | 3268.19 | 578.19 |
| 2023 | 2012.65 | -4829.24 | 2055 | 2812.32 | 597.75 |
| ... | ... | ... | 2056 | 2826.81 | 615.46 |
| 2042 | 4065.83 | -83.16 | 2057 | 2291.72 | 628.49 |
| 2043 | 3901.68 | 10.71 | 2058 | 2245.88 | 639.99 |
| 2044 | 4069.64 | 98.80 | 2059 | 1605.76 | 647.21 |
| 2045 | 3873.81 | 174.56 | 2060 | 1486.14 | 653.32 |
| 2046 | 4032.69 | 245.75 | 2061 | 726.49 | 655.96 |
| 2047 | 3805.16 | 306.39 | 2062 | 427.13 | 657.35 |
| 2048 | 3948.50 | 363.02 | 2063 | -515.69 | 655.97 |
| 2049 | 3676.79 | 410.64 | 2064 | -1527.50 | 651.73 |

**Table 2.** NCF and NPV of STAR Tollway

| Year | $rNCF_i$ | $rNPV_{Tc}$ | Year | $rNCF_i$ | $rNPV_{Tc}$ |
|---|---|---|---|---|---|
| 2005 | -1019.57 | 0 | 2045 | 1240.32 | 387.17 |
| 2006 | -654.16 | -1817.67 | 2046 | 1192.06 | 409.38 |
| ... | ... | ... | 2047 | 1135.92 | 428.61 |
| 2017 | 357.33 | -1407.03 | 2048 | 1177.03 | 446.7 |
| ... | ... | ... | 2049 | 1104.59 | 462.12 |
| 2035 | 944.61 | 20.36 | 2050 | 1021.23 | 475.07 |
| 2036 | 1021.02 | 70.46 | 2051 | 1040.6 | 487.07 |
| 2037 | 1033.92 | 116.5 | 2052 | 931.25 | 496.83 |
| 2038 | 1045.25 | 158.74 | 2053 | 806.44 | 504.53 |
| 2039 | 1128.28 | 200.13 | 2054 | 785.62 | 511.36 |
| 2040 | 1131.3 | 237.8 | 2055 | 620.82 | 516.29 |
| 2041 | 1129.82 | 271.94 | 2056 | 420.18 | 519.37 |
| 2042 | 1210.18 | 305.14 | 2057 | 199.77 | 520.78 |
| 2043 | 1200.07 | 335.03 | 2058 | -53.95 | 520.61 |
| 2044 | 1180.04 | 361.71 | 2059 | -348.11 | 518.93 |

## 4.3 Narrowed Concession Period Boundaries

To narrow down the resulting concession interval, bargaining game theory was employed. With a cost of money of the government of *10%* and cost of money of the private sector equal to *10%* and *13%* for TPLEX and STAR Tollway, respectively, the BOT player's discount factor *(δ)* can be computed using Gibbon's formula [11] *(r=cost of money of BOT player)*:

$$\delta = \frac{1}{1+r} \quad (19)$$

Bargaining costs $f_g$ and $f_p$ for the government (G) and the private sector (P), respectively, could be in the form of losses due to costly delayed agreement. If the length of concession period is not agreed at once, the benefits that will be generated on $T_{C\_L}$ could be considered losses to both BOT players. With various combination of $f_g$ and $f_p$ as percentage of $NPV(T_{C\_L})$, NPV at the concession boundaries, and the computed $\delta_p$ and $\delta_g$ plug into the equations in Section 3.4, the new concession boundaries $[T'_{C\_L}, T'_{C\_U}]$ are shown in Table 3.

Since it is difficult to find a perfect converging point of concession period, tolerance level, α is used to indicate that any point within the concession interval would be an agreeable concession period if the following criterion can be met:

$$\alpha \ge \frac{T'_{C\_U} - T'_{C\_L}}{T_{C\_U} - T_{C\_L}} \quad (20)$$

For a tolerance level of *10%,* the range at various scenarios is acceptable as the computed α for both case studies as shown in Table 3 is smaller than the assumed level. Consider the scenario where BOT players would have a 50-50 % share of $NPV(T_{C\_L})$. As shown in Figure 2, there is about 54% probability that TPLEX's NPV at year 2047 will be equal or less to the mean computed by the simulation. In other words, there is about 46% chance that the NPV at year 2047 would further exceed the mean. This indicates that the private sector is secured of its return until the end of concession period should year 2047 be decided as the transfer point. For STAR Tollway, if year 2040 is selected as the transfer point, there is a 53% chance that the NPV at this point will be equal or less to the resulting mean NPV as shown in Figure 3. This indicates that an NPV greater than the mean at year 2040 could still be expected with 47% probability.

**Table 3.** Sensitivity Analysis with Bargaining Cost Scenarios

| | % Share to Bargaining Cost | | | | | | |
|---|---|---|---|---|---|---|---|
| G | 10% | 20% | 40% | 50% | 60% | 80% | 90% |
| P | 90% | 80% | 60% | 50% | 40% | 20% | 10% |
| **TPLEX** | | | | | | | |
| $T'_{C\_L}$ | 2046.1 | 2046.4 | 2047.0 | 2047.3 | 2047.6 | 2048.3 | 2048.7 |
| $T'_{C\_U}$ | 2046.5 | 2046.8 | 2047.4 | 2047.7 | 2048.0 | 2048.7 | 2049.1 |
| α | 1.71% | 1.71% | 1.83% | 1.83% | 1.83% | 2.18% | 2.25% |
| **STAR Tollway** | | | | | | | |
| $T'_{C\_L}$ | 2036.5 | 2037.2 | 2038.6 | 2039.3 | 2040.1 | 2041.9 | 2042.8 |
| $T'_{C\_U}$ | 2037.8 | 2038.5 | 2040.0 | 2040.8 | 2041.7 | 2043.7 | 2044.8 |
| α | 5.97% | 6.24% | 6.49% | 7.08% | 7.48% | 8.27% | 8.96% |

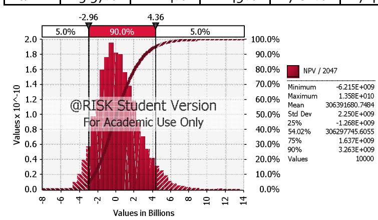


**Figure 2.** NPV of TPLEX at Year 2047

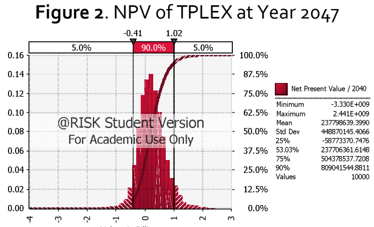


**Figure 3.** NPV of STAR Tollway at Year 2040

# 5 Conclusion and Recommendation

The proposed methodology will enable the evaluating agency to analytically determine the reasonable concession period to be granted to the private sector taking into account the uncertainties associated with various concession parameters in the financial evaluation. The analysis of NPV results generated by the simulation provided a range of concession period for the government and the private sector to negotiate. The negotiation to arrive at a specific concession period is considered as a bargaining situation and thus bargaining game theory was utilized in this research. While a perfect converging point of concession period was not achieved, it can be inferred that any point chosen on the resulting concession interval is a reasonable concession period that would be advantageous both to the government and the private sector.

The concession period of the case studies were found to be longer using the proposed methodology indicating the impact of risks in the cash flow with the use of Monte Carlo simulation. Longer concession period would give private sector a greater chance to exceed the expected return from its investment. Granting a longer but reasonable concession period is also one way of ensuring that the government is protecting the interest of the private sector, thus, giving more confidence to the private sector to invest in government infrastructure projects through BOT. The resulting concession period also protects the interest of the government as it ensures that the project is still profitable for the government to operate before reaching the end of its economic life.

The proposed methodology is envisaged to help the government in further enhancing its policies in processing BOT projects. With the concession period treated as an output parameter, chances of eliminating potential BOT project will be avoided. The evaluating agency may find a BOT project not feasible at a pre-set concession period and may recommend disapproval thereof. With the analysis of concession period, a BOT project maybe found feasible at a longer concession period with a confidence of achieving the expected returns indicated by the statistics resulting from the simulation. This broadens the current deterministic evaluation criteria which focus on NPV and IRR results as viability indicators.

The proposed methodology should also be tested on other BOT infrastructure projects which may have different cash flow structure to establish its effectiveness. Future works may also focus on further refinement of the simulation model by gathering more information on key variables to accurately assign their probability distribution. Further, it is recommended that the evaluating agency should already shift from using the current deterministic model to the use of simulation model in the financial evaluation of future BOT projects. While it is recognized that the software used for Monte Carlo simulation is quite expensive, the government should invest in acquiring this tool to improve its evaluation techniques and properly manage risks taking into account the likelihood of occurrence resulting from the simulation.

# References

[1] Shen, L.Y., Li, H. and Li, Q.M., Alternative Concession Model for Build Operate Transfer Contract Projects, Journal of Construction Engineering and Management, ASCE, 2002
[2] Shen, L.Y., Bao, H.J., Wu, Y.Z. and Lu, W.S., Using Bargaining-Game Theory for Negotiating Concession Period for BOT-Type Contract, Journal of Construction Engineering and Management, ASCE, 2007
[3] Shen, L.Y. and Wu, Y.Z., Risk Concession Model for Build/Operate/Transfer Contract Projects, Journal of Construction Engineering and Management, ASCE, 2005
[4] Ng, S.T., Xie, J., Cheung Y.K., and Jefferies, M., A simulation model for optimizing the concession period of public-private partnerships schemes, International Journal of Project Management, 2007
[5] National Economic and Development Authority, Canadian International Development Agency, and United Nations Development Programme, Reference Manual on Project Development and Evaluation, Volume 1, Philippines, 2005
[6] Xie, L. and Xu, W., Calculation of the Concession Period for Generalized BOT Project, IEEE Xplore, 2008
[7] Fragniere, E. and Sullivan G., Risk Management: Safeguarding Company Assets, Thomson Netg, Crisp Fifty-Minute™ Series, 2007
[8] Schniederjans, M., Schniederjans, A., and Schniederjans D., Outsourcing and Insourcing in an International Context, M.E. Sharpe, Inc., 2005
[9] Organisation for Economic Co-operation and Development (OECD) Publishing, OECD Glossary of Statistical Terms, 2008
[10] UNIDO, Guidelines for Infrastructure Development through Build-Operate- Transfer (BOT) Projects, 1996
[11] Gibbons, R., Game Theory for Applied Economists, Princeton University Press, USA, 1992

# Representation of the Double-Directional Channel by using Spherical Wave Expansions

Student Number: 08M18111 Name: Kenji Nakai Supervisor: Jun-ichi Takada

# 球波動関数を用いた双角度チャネルモデルの表現

中井 健二

本研究では，アンテナの電磁界を球波動関数で表せるように，従来平面波モデルで表されてきた双角度チャネルモデルに対しても球波動関数を使って構築することを試みる．もっとも単純な例として，半波長ダイポールアンテナと自由空間見通し（Line Of Sight:LoS）伝搬路を取り上げ，従来の平面波を用いたモデルとの比較を通じて球波動関数を用いたチャネルモデルの導出を試みる．

## I. Introduction

There is an approach that extracts or de-embeds the transmitting (Tx) and receiving (Rx) antennas from the multipath radio channels, as they are parts of communication devices of the channel in particular in the state-of-art Multiple-Input Multiple-Output (MIMO) technology. This approach is called double-directional channel, since it constructs a radio propagation model independent of antennas. This approach enables the comparison of performances of different antennas in the same propagation environment by embedding the antennas into the double-directional channel.

Conventionally, the double directional channel is expressed as a superposition of local plane waves at both Tx and Rx antennas. Although the radio wave emitted from an antenna propagates as a spherical wave, Rx antenna is very far from Tx antenna, so that this spherical wave is modeled as a plane wave locally. Moreover, in the scattering processes such as reflection and diffraction, image source and diffraction point are also very far from both Tx and Rx, so that they are also modeled as plane waves.

This thesis tries to express the double-directional channel by the spherical wave expansions (SWE). Not only the antennas, but also the propagation channel is expressed by SWE as shown in Fig.1. The advantage of the use of SWE is that the resolution in angular domain is automatically determined by the size of the antenna. In contrast, the required angular resolution of the plane wave is infinite regardless of the antenna size.

This thesis reviews the basic spherical wave theory [2−3] at first. Next, how to find the unknown coefficients for the spherical harmonics expansion of the antenna pattern is explained. A new modeling approach of the double-directional channel using the spherical harmonics is finally proposed by using the electric dipole. Finally, by utilizing the measured antenna pattern, the convergence property of the finite sum of the spherical harmonics is discussed.

## II. Spherical Wave Theory

In this thesis, time dependence of $\exp(\mathrm{j}\omega t)$ is assumed. By using a separation of variables and solving the free space homogeneous vector Helmholtz equation in the spherical coordinates, the vector spherical wave functions

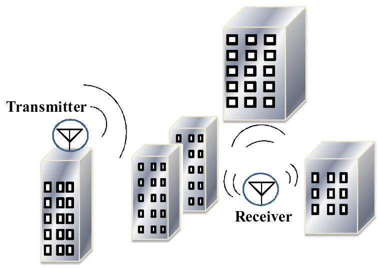


Fig. 1. Double-directional channel expressed by spherical wave

are obtained. Their components of travelling wave represented by using the spherical Hunkel function $\mathrm{h}_n^{(2)}(kr)$ of the second kind can be expressed as [2]

$$\boldsymbol{F}_{1mn}(r,\theta,\phi) = \frac{1}{\sqrt{2\pi}}\frac{1}{\sqrt{n(n+1)}}\left(-\frac{m}{|m|}\right)^m \mathrm{e}^{-\mathrm{j}m\phi} \left(\mathrm{h}_n^{(2)}(kr)\frac{-\mathrm{j}m\bar{P}_n^{|m|}(\cos\theta)}{\sin\theta}\hat{\boldsymbol{\theta}} - \mathrm{h}_n^{(2)}(kr)\frac{\mathrm{d}\bar{P}_n^{|m|}(\cos\theta)}{\mathrm{d}\theta}\hat{\boldsymbol{\phi}}\right) \tag{1}$$

$$\begin{aligned}\boldsymbol{F}_{2mn}(r,\theta,\phi) = &\frac{1}{\sqrt{2\pi}}\frac{1}{\sqrt{n(n+1)}}\left(-\frac{m}{|m|}\right)^m \mathrm{e}^{-\mathrm{j}m\phi} \\ &\left(\frac{n(n+1)}{kr}\mathrm{h}_n^{(2)}(kr)\bar{P}_n^{|m|}\hat{\boldsymbol{r}}\right. \\ &+\frac{1}{kr}\frac{\mathrm{d}}{\mathrm{d}(kr)}\left(kr\mathrm{h}_n^{(2)}(kr)\right)\frac{\mathrm{d}\bar{P}_n^{|m|}(\cos\theta)}{\mathrm{d}\theta}\hat{\boldsymbol{\theta}} \\ &\left.+\frac{1}{kr}\frac{\mathrm{d}}{\mathrm{d}(kr)}\left(kr\mathrm{h}_n^{(2)}(kr)\right)\frac{-\mathrm{j}m\bar{P}_n^{|m|}(\cos\theta)}{\sin\theta}\hat{\boldsymbol{\phi}}\right)\end{aligned} \tag{2}$$

where $n = 1,2,3,...$ and $m = -n, -n+1, ..., 0, ..., n-1, n$, and $\bar{P}_n^{|m|}(\cos\theta)$ is the normalized associated Legendre function. In general, $n$ and $m$ represent the mode indices in $\theta$ and $\phi$. Equations (1) and equation (2) can be rewritten by using the vector spherical harmnonics $\boldsymbol{Y}^m_{(1,2,3),n}$ which are orthogonal mode functions of the electromagnetic field in spherical coordinates as follows.

$$\boldsymbol{F}_{1mn}(r,\theta,\phi) = \mathrm{h}_n^{(2)}(kr)\boldsymbol{Y}^m_{1,n}(r,\theta,\phi) \tag{3}$$

$$\begin{aligned}\boldsymbol{F}_{2mn}(r,\theta,\phi) = &\frac{1}{kr}\frac{\mathrm{d}}{\mathrm{d}(kr)}\left(kr\mathrm{h}_n^{(2)}(kr)\right)\boldsymbol{Y}^m_{2,n}(r,\theta,\phi) \\ &+\frac{\sqrt{n(n+1)}}{kr}\mathrm{h}_n^{(2)}(kr)\boldsymbol{Y}^m_{3,n}(r,\theta,\phi)\end{aligned} \tag{4}$$

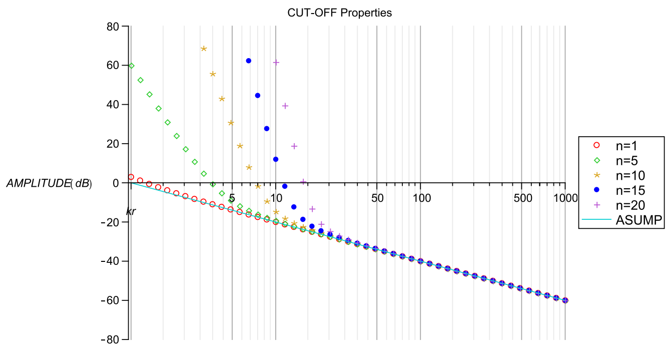


Fig. 2. Amplitude of spherical Hunkel function of the second kind vs phase

Here, the spherical vector harmonics are the orthonormal mode functions, therefore the following relation can be willingly defined.

$$\int_{\phi=0}^{2\pi}\int_{\theta=0}^{\pi} \boldsymbol{Y}_{s,n}^{m}(\hat{\boldsymbol{r}})\boldsymbol{Y}_{s',n'}^{m'*}(\hat{\boldsymbol{r}})\sin\theta \mathrm{d}\theta\mathrm{d}\phi = \delta_{ss'}\delta_{nn'}\delta_{mm'} \tag{5}$$

Here, some weighted coefficients of arbitrary radiation patterns (see Eq.(6)) can be derived by using this orthogonality afterwards.

By using SWE, the outward propagating electric field from the source in angular domain can be expressed as

$$\boldsymbol{E}(r,\theta,\phi) = k\sqrt{\eta}\sum_{s=1}^{2}\sum_{n=1}^{N}\sum_{m=-n}^{n} Q_{smn}\boldsymbol{F}_{smn}(r,\theta,\phi) \tag{6}$$

where $\eta$ is the wave impedance given by $\eta = \sqrt{\mu_0/\epsilon_0} \simeq 120\pi \simeq 377[\Omega]$, $k$ is the propagation constant given by $k = 2\pi/\lambda = \omega\sqrt{\mu_0\epsilon_0}$ is the wavelength. Regarding the index $s$, $s = 1$ indicates TE-wave, while $s = 2$ indicates TM-wave. Moreover, the spherical wave series can be truncated at a sufficient value of $n = N$ determined by the size of the antennas due to cut off property as Eq.(6) not an infinite number of spherical wave modes that would be required to exactly characterise the radiated field of a general source, as shown in Fig.2. This graph can be separated into the two regions. One is the far field or propagation region following $1/r$ is emvelop attenuation. The other one is the near-field or evanescent region where the field attenuate exponentially. Even a strong field is generated within the region, it is attenuated exponentially and does rarely contribute to radiation field.

*1) The derivation of $Q$ coefficients:* Here, from the simulated radiation pattern, the coefficients $Q$ in eq.(6) can be derived by solving the following set of linear equations, although the orthonormality of vector spherical harmonics which is eq.(5) that is usually used to derive the coefficients. That is because all spherical pattern can not be obtained in experiment data. By substituting Eq.(11) and Eq.(12) into the left-hand side of eq.(6), the outward electric field can be expressed as matrix form as

$$\boldsymbol{E} = \boldsymbol{Q}\boldsymbol{F} \tag{7}$$

where $\boldsymbol{E}$ is the simulated electric field column vector, $\boldsymbol{F}$ is the matrix of the spherical wave functions and column vector $\boldsymbol{Q}$ is the weight vector. Usually, Eq.(7) is overdetermined and $\boldsymbol{E}$ is derived as the least square

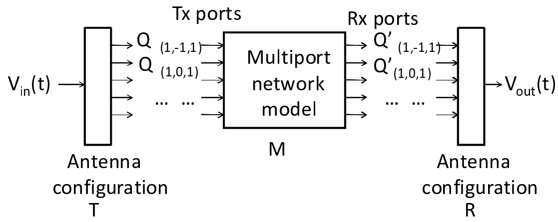


Fig. 3. Equivalent circuit model

solution, i.e.

$$\boldsymbol{Q} = \boldsymbol{F}^{-}\boldsymbol{E} \tag{8}$$

where $\boldsymbol{F}^{-}$ is the Moore-Penrose pseudo inverse of $\boldsymbol{F}$. Therefore, the vector radiation pattern is reconstructed since the unknown coefficient $Q$ is found by solving the simultaneous equation as the Eq.(8).

## III. For Channel Model by using SWE

By representing antennas using Eq.(6), the double-directional channel can also be expressed as an equivalent multiport circuit. Multipath environment such as Fig.1 can be represented as Fig.3, where each individual port corresponds to a mode of spherical harmonics. In my research, it is assumed that Tx antenna is connected to the matched generator and Rx antenna is terminated by the matched load.

Here, $\boldsymbol{Q}$ of the outward propagating modes at Tx antenna, and is mapped into $\boldsymbol{Q}$ of the inward propagating modes at Rx antenna, through the propagation channel $\boldsymbol{H}_{\text{prop}}$ are determined as follows.

$$\boldsymbol{Q}' = \boldsymbol{H}_{\text{prop}}\boldsymbol{Q} \tag{9}$$

where $\boldsymbol{H}_{\text{prop}}$ is a propagation channel matrix determined for the spherical harmonics. In the similar manner, Tx antenna and Rx antenna are also mapped into their signals $v_{\text{in}}(t)$ and $v_{\text{out}}(t)$, through the antenna transmitting coefficients and the antenna receiving coefficients as follows.

$$\begin{aligned}\boldsymbol{Q}(t) &= \boldsymbol{T}v_{\text{in}}(t),\\ v_{\text{out}}(t) &= \boldsymbol{R}\boldsymbol{Q}'.\end{aligned} \tag{10}$$

where $\boldsymbol{T}$ is a $SMN \times 1$ column matrix with elements, $\boldsymbol{R}$ is a $1 \times S'M'N'$ row matrix with elements. Therefore, it is clear that $\boldsymbol{T} \propto \boldsymbol{Q}_{\text{smn}}$ and its reciprocal ($\boldsymbol{R}_{smn} = (-1)^m\boldsymbol{T}_{s,-m,n}$) at Rx as $\boldsymbol{R} \propto \boldsymbol{Q}'_{\text{s'm'n'}}$. Rgardeing, the complex amplitudes of incoming and outgoing waves on guide, the nomalization is chosen such that the power carried by these waves are $\frac{1}{2}|v_{\text{in}}|^2$ (The incident power) and $\frac{1}{2}|v_{\text{out}}|^2$ (the radiated power), respectively. By using spherical harmonics, the equivalent circuit of the channel can be derived. In my thesis Tx antenna was represented by using SWE first. And then, Rx antenna was also represented by using SWE. Finally, the channel matrix was also obtained by SWE. Each of the propagating mode coefficients is finite due to cut off property so that the channel can be also finite by SWE ($S'M'N' \times SMN$). Data size is reducted remarkably compared to the plane wave modeling, therefore, we can deal with discrete data due to the SWE model.

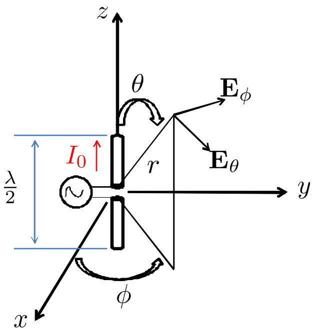


Fig. 4. half-wave dipole

## IV. Simulation of Antenna Pattern Representation

### A. Tx Antenna Side

A simulation is conducted by a simple antenna which is a half-wave dipole to verify the theoretical concept. As an example, in case of the far field of electric half-wave dipole in z-polarization (see Fig.4) where the dipole is located in the origin of the coordinate system, the equation for vertical positioned half-wave dipole is as follows

$$\boldsymbol{E}_\theta(r,\theta,\phi) = \frac{\mathrm{j}\eta I_0}{2\pi r}\exp[-\mathrm{j}kr_0]\frac{\cos(\frac{\pi}{2}\cos(\theta))}{\sin(\theta)} \tag{11}$$

$$\boldsymbol{E}_\phi(r,\theta,\phi) = 0 \tag{12}$$

Then, simulated conditions are determined by.

- $\lambda = 0.1m$ is assumed.
- Conducted for whole sphere to get the radiation pattern in whole solid angle (Angle steps of $\theta$, $\phi$ are every 1 degree.)
- $r = \infty$ is assumed.

*1) Pattern Reconstruction using Finite Spherical Harmonics:* Now, the question is how to select the appropriate $N$. Here, the relative error $\epsilon$ is considered as a function of $N$, which is defined as

$$\epsilon = \frac{\sum_R\sum_S\left(|\Delta E_\theta(\theta_R,\phi_S)|^2 + |\Delta E_\phi(\theta_R,\phi_S)|^2\right)\sin\theta_R}{\sum_R\sum_S\left(|E_\theta(\theta_R,\phi_S)|^2 + |E_\phi(\theta_R,\phi_S)|^2\right)\sin\theta_R}, \tag{13}$$

where, the error at individual angle, $\sin\theta$ is weighted considering the density of the point and $\Delta$ means the difference of reconstructed the electric field and simulated the field simulated at each index $(R, S)$, that are also the numbers of samples in elevation angle and azimuth angle. In this case, $N$ in Eq.(6) is predicted as $N \simeq 2$.

Fig.5 shows the relative error as function of $N$ for the simulated antenna. For example, to suppress the error lower than $1\%$, $N$ should be at least 1. Fig.6 compares the simulated and the reconstructed pattern for $N = 2$. It is quite similar to the simulated pattern.

### B. Rx Antenna Side

Rx antenna can be modeled in the same manner as Tx antenna. To derive the inward propagating modes $Q'_{s'm'n'}$, it is needed that plane waves arriving at the Rx antenna are expressed by using SWE since on the far-field the waves is arriving there. This is owing to fact that we suppose that a plane wave is arriving at Rx antenna to simplify the model. Then, around the Rx antenna the

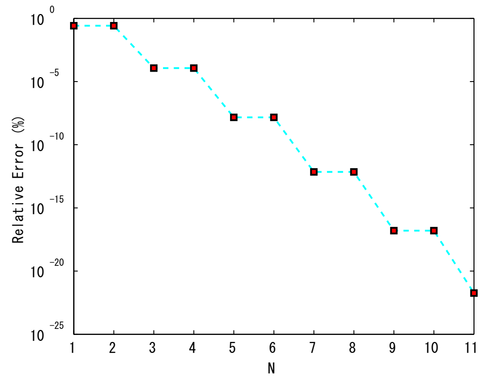


Fig. 5. Relative error of z-polarization

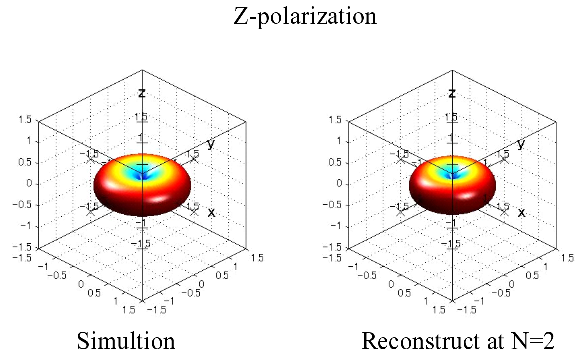


Fig. 6. Pattern comparizon

electric field includes the origin, so that in the field the spherical Bessel function is used as the solution of radial function in place of the spherical Hunkel function of the second kind in Eq.(6) since the Bessel function is not divergent at the position.

Now, a plane wave $\boldsymbol{E}(\boldsymbol{r}) = \boldsymbol{E}_0\exp(-\mathrm{j}k\hat{\boldsymbol{k}}\cdot\boldsymbol{r})$ ($\boldsymbol{E}_0$ is a plane wave spectrum) with $\hat{\boldsymbol{k}}$ means the unit vector of propagation direction of plane waves, which is observed at the position $\boldsymbol{r}$ measured from the origin. Then, it can be expanded into regular spherical vector waves $\boldsymbol{F}'_{s'm'n'}$ using spherical Bessel function in place of the spherical Hunkel function of the second kind of $\boldsymbol{F}_{smn}$ used in the eq.(6) as follows [2], [3]

$$\boldsymbol{E}_0\exp(-\mathrm{j}k\hat{\boldsymbol{k}}\cdot\boldsymbol{r}) = k\sqrt{\eta}\sum_{s'=1}^{2}\sum_{m'=-n'}^{n'}\sum_{n'=1}^{N'} q'_{s'm'n'}\boldsymbol{F}'_{s'm'n'} \tag{14}$$

Then, it can be shown that the unknown expansion coefficients of the electric field in the Rx antenna can be derived by using the orthonomalization of vector spherical harmonics of eq.(5) as

$$q'_{s'm'n'} = \frac{4\pi(-\mathrm{j})^{n'-s'+1}}{k\sqrt{\eta}}\int_{\theta=0}^{\pi}\int_{\phi=0}^{2\pi}\boldsymbol{E}_0\cdot\boldsymbol{Y}^{m'*}_{s',n'}(\hat{\boldsymbol{k}})d\Omega \tag{15}$$

where, for deriving eq.(15), the relation $\exp(-\mathrm{j}k\hat{\boldsymbol{k}}\cdot\boldsymbol{r})$ is represented by SWE and used [4].

$$\exp(-\mathrm{j}k\hat{\boldsymbol{k}}\cdot\boldsymbol{r}) = 4\pi\sum_{s=1}^{2}\sum_{n=1}^{\infty}\sum_{m=-n}^{n}(-\mathrm{j})^n \mathrm{j}_n(kr)\boldsymbol{Y}^{m'*}_{s',n'}(\hat{\boldsymbol{k}})\boldsymbol{Y}^{m'}_{s',n'}(\boldsymbol{r}) \tag{16}$$

Here, for empty space we have $\boldsymbol{Q} = \boldsymbol{Q}'$. If there is no dipole present, the total field is

$$\begin{aligned}\boldsymbol{E}(r,\theta,\phi) &= k\sqrt{\eta}\sum_{smn}\{Q'_{smn}\boldsymbol{F}^{(1)}_{smn}(r,\theta,\phi) \\ &\qquad + Q_{smn}\boldsymbol{F}_{smn}(r,\theta,\phi)\} \\ &= 2k\sqrt{\eta}\sum_{smn} Q'_{smn}\boldsymbol{F}'_{smn}(r,\theta,\phi) \qquad (17)\end{aligned}$$

where $\boldsymbol{F}^{(1)}_{smn}$ means the vector spherical wave functions using the spherical Hunkel function of the first kind which is the inward propagating wave, and the relation of the spherical Bessel function and Hunkel function is used. The expansion coefficients $Q'_{smn}$, of the inward propagating modes are related to the expansion coefficients $q_{s'm'n'}$ of the regular waves as $2Q'_{smn} = q_{smn}$.
The both antennas model were derived. In the next step, the double-directional propagation channel will be modeled by using the eq.(9)

## V. Double-directional Channel Model using Spherical Harmonics

Now, we consider the same electric dipole antennas at both stations are used and they are polarized in $+z$-direction at the origin. Then, the dipole field has only one term in the summations, i.e. $s = 2, m = 0$ and $n = 1$ [2]. So there are only six spherical modes altogether with $n = 1$. Moreover, for a lossless antenna, $\boldsymbol{T}$ and $\boldsymbol{R}$ explained in the section 3 are satisfying the unitary condition which implies that the norm, the sum of the elements absolute squared, of every column and every row. Therefore, $|\boldsymbol{T}|^2 = 1$. Since $\boldsymbol{T}v_{\text{in}} = \boldsymbol{Q}$, and $|v_{\text{in}}|^2 = |\boldsymbol{Q}|^2$ due to power conservation. In case of our modeling, $T_{201} = R_{201}$ holds due to the reciprocal theorem, which shows that only one mode of the incoming field will transfer power to the load. So we have $v_{out} = Q'_{201}$ as it is explained in the section 3. Hence, all the energy of the incoming mode is received by the dipole and absorbed in the load.
Here, $\boldsymbol{F}'_{smn} = \boldsymbol{F}'_{201}$ is the only mode to have a $z$-component at the origin. Setting $r = 0$ in eq.(17) therefore yields by using the caluculation result of $\boldsymbol{F}'_{201}$

$$v_{\text{out}} = Q'_{201} = \frac{\sqrt{6\pi}}{2}\frac{1}{k\sqrt{\eta}}E_z(0,\theta,\phi) \qquad (18)$$

Equation (18) expresses the received signal in the dipole in terms of the electric field component parallel to the dipole.

### A. Numerical Example

Here, the plane wave spectrum $\boldsymbol{E}_0$ in the eq.(15) is given by using the reconstructed electric field obtained in the section 2

$$\boldsymbol{E}_0 = \lim_{kr\to\infty}\boldsymbol{E}(r,\theta,\phi)\sqrt{4\pi}\frac{\mathrm{e}^{-jkr_d}}{kr_d} \qquad (19)$$

where an additional factor $\sqrt{4\pi}$ implies that expressions for gain and directivity become simpler, and $r_d$ is the distance between the Rx and Tx antennas. Finally, by combining them, it is confirmed that the power received the prove when aligned parallel to the electric field of the test antenna is the same compared to the plane wave modeling.

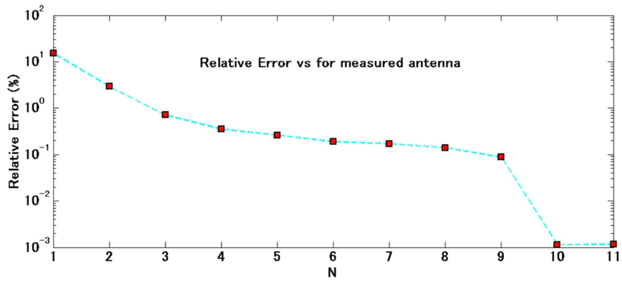


Fig. 7. Relative error of measured and reconstructed pattern

## VI. Appendix

### A. Experimental result of antenna pattern

The antenna pattern measurement has been conducted by using SATIMO Stargate [5], which is a spherical near field measurement system. The measurement is conducted for the whole sphere to get the radiation pattern in the whole solid angle. A biconical antenna ($0.345\lambda \times 0.60\lambda$) was measured at $2.385$ GHz. Obviously this measurement system itself may use the same spherical harmonics approach inside the system and it just outputs far field vector antenna pattern in whole sphere.

Fig.7 shows the relative error as function of $N$ for the measured antenna. For example, to suppress the error to $1\%$, $N$ should be at least 3. The question is why the behavior decays rapidly when N changes at 10 from 9 about above figure. The answer is because this system cut off at the $N = 10$

## VII. Conclusinon and Future Works

This thesis presented how to express the double-directional channel modeling. By using measured or simulated antenna pattern, the antenna model can be derived. And, a plane wave is expressed by using SWE in Rx antenna. And, by using the electric dipole at both stations, it is confirmed that the power received the prove when aligned parallel to the electric field of the test antenna is the same compared to the plane wave modeling. In the next step, our taget is the MIMO technology. Before multiplexing a channel, antenna offset should be considered since in the spherical coordinate system the vector cannot define parallel shift. Therefore, first the $x-$shift and $z-$shift may be a good commencing point to validate it. If the shift is allowed, for MIMO channel by augmenting both Tx and Rx. By comparing the conventionally modeling, if new information is obtained, this is a way to ameliorate the quality of wireless communication system and save frequencies.

## References

[1]K. Araki, T. Ohira and J. Takada, "Eigen mode expansion of free space and its application to an expression for antenna equivalent circuit", IEICE Tech.Rep, A.P2006-128, Jan.

[2]J.E.Hansen, Spherical Near-Field Antenna Measurement, IEE Electromagnetic waves series 26, London, U.K, 1988

[3]A.A.Glazunov, On the Antenna-Channel Interactions: A Spherical Vector Wave Expansion Approach, Doctoral Thesis, Lund University, Lund, Sweden, February, 2009.

[4]J.D.Jackson, Classical Electrodynamics−second edition−, Wiley & Sons, 1975

[5]SATIMO,"Antenna Measuremnt", http://www.satimo.com/content/products/sg-24

# Effects of Power Sector Reform in China - A case study of Liaoning province

Student Number: 08M51545 Name: ZHENG Mingyue Supervisor: Naoya ABE

# 中国における電力部門改革の影響 ～遼寧省に着目して～

鄭 明月

本研究は、2002 年中国における電力部門改革の影響を評価するため、イギリスおよび日本における電力部門改革の影響と比較分析を行った。その際、中国の経済規模の巨大さなどを踏まえ、遼寧省の事例研究を行った。国レベルでの比較する上で、遼寧省の事例研究を行った。具体的には、①電力価格制度の定性的比較の後、②各国および省における電力発電部門における競争状況の創出の有無に着目し、市場集中度、ハーフィンダールハーシュマン指数及びジニ係数による三つの数値を算出・比較を行い、③さらに Chow テストにより、中国の電力発電部門に対して構造的影響を与えているか否か確認した。

## 1. Introduction

Since the establishment of the People's Republic of China (RPC) in 1949, the electricity industry had been controlled by the central government until 1985. The Ministry of Electric Power Industry managed both administration and the single power utility enterprise.

To meet the rapidly growing electricity demand, the Chinese government conducted the drastic reform of the power sector in 2002, resulting in that the power generation assets were allocated to five national power companies and the power grid assets was reorganized into national power grids respectively in 2002. The sector reform resulted in the division between power generation and power transmission. State Electricity Regulatory Commission of China (SERC) also was established to manage and monitor electricity market.

The total capacity of China power generation has indicated very high rates of growth. In 1952, the total capacity was only 0.19GW, in 1987, it reached to 103GW, and then in 2009, it had raised to 874GW. The electricity generation in China depended on fire power, which has 80% share of the total capacity in 2009.

## 2. Objective

The first objective is to access the competitive market conditions of the electricity generation market in China with comparison with those in both UK and Japan, after reviewing the electricity price mechanism in those three countries. The second is to figure out whether or not there is a structural change in the Chinese power sector after the reform.

In China, which is a broad and vast country, there are 23 provinces, 5 autonomous region and 4 municipalities. There is a huge gap among them in terms of economy scale, distribution of natural resource, and population size. In this research, Liaoning province, which is on one of the economically rapidly growing provinces in China, is selected as a case study region because there were two pilot projects for new electricity pricing policy.

## 3. Approaches

### 3.1 Concentration Ratio (CRn)

To assess the competition conditions of the electricity generation sectors in China, the concentration ratio is calculated. It indicates the percentage of market share owned by the largest n firms,

$$\mathrm{CR}_n = \sum \mathrm{R}_n, \quad n = 4 \text{ or } n = 8 \qquad \text{(Ep.1)}$$

where R: market share of company

In general, if CR4 <30%, there is a competition market. If 30%<CR4<65%, there is a middle level monopoly market. If CR4>65%, there is a high level monopoly market.

### 3.2. Herfindahl-Hirschman index (HHI )

The U.S. Department of Justice uses HHI to measure market concentration for purposes of antitrust enforcement. HHI is also used by the Japan Fair Trade Commission to check the consequence of monopoly level when there is a proposed

M&A proposal between companies.

HHI uses the market shares of all the firms in an industry and the corresponding HHI value of the industry is the total squared values of each firm share. It gives more weight on those firms which occupy the larger portion of the industry.

$$\mathrm{HHI} = \mathrm{S1}^2 + \mathrm{S2}^2 + \mathrm{S3}^2 + \cdots + \mathrm{Sn}^2 \quad \text{---- (Ep.2)}$$

Range of HHI value is from 0 to 10,000. If HHI<1,000, there is a competition market. If 1,000<HHI<1,800, there is a middle level monopoly market. If HHI>1,800, there is a high level monopoly market.

### 3.3 Gini Coefficients

Gini Coefficients are calculated to measure the equality or distribution of power generation capacities of the power companies as shown in Eq.3.

$$G = \left(\frac{1}{T}\right)\left\{T + 2\left[1 - \frac{\sum_{t=0}^{T}(T + 2 - \mathrm{Rank}C_t)C_t}{\sum_{t=0}^{T} C_t}\right]\right\} \quad \text{(Eq. 3)}$$

T : numbers of samples
Ct: electricity generation capacity
Rank Ct : rank of sample
G : Gini Coefficient value

When the value of Gini Coefficient is approaching to 0, the distribution is approaching to fair situation. When the value of Gini Coefficient is approaching to 1, it means the distribution has a huge differential.

In addition to the three approaches above, qualitative analysis is adopted to compare Chinese pricing policy with those in both UK and Japan.

### 3.4 Chow test

Chow test, which is an application of F-test, is a method to assess whether the expected values of a quantitative variable within several pre-defined groups differ from each other.

For example, the Chow test is adopted to examine if there is a structural change in 2002 for the relationship between Chinese electricity generation amount and its GDP from 1979 to 2009. Three regression runs are then necessary as below.

<u>**Regression for the total period:**</u>

$$Y_{EP(1979\sim2009)} = X_{GDP(1979\sim2009)}\beta_{total} + u_{total} \quad \text{---(Eq. 5)}$$

<u>**Regression for the period before change**</u>

$$Y_{EP(1979\sim2001)} = X_{GDP(1979\sim2001)}\beta_{2001} + u_{2001} \quad \text{---(Eq. 6)}$$

<u>**Regression for the period after change**</u>

$$Y_{EP(2002\sim2009)} = X_{GDP(2002\sim2009)}\beta_{2002} + u_{2002} \quad \text{---(Eq. 7)}$$

Then Chow test is required to compute the following statistics, which follows the F distribution. The null hypothesis is that there is no change in 2002.

$$F = \frac{\text{explained squares sum of Y on X}}{\text{residual squares sum of Y on X}} = \frac{\left(\frac{RSS_{total} - RSS_{After} - RSS_{Before}}{k}\right)}{\left(\frac{RSS_{After} + RSS_{before}}{n_1 + n_2 - 2k}\right)} \quad \text{--- (Eq. 8)}$$

where k: number of variables, N: total sample numbers, $RRS_{total}$: Residual sum of square from (Eq.5), $RRS_{before}$: Residual sum of square from (Eq.6), $RRS_{after}$: Residual sum of square from (Eq.7)

Calculated F value will follow the distribution with α (k, N-2k) degree of freedom. In the example above, $F_{critical(2,58)} = 3.1$ if the significance level is at 5 % (p=0.05)

The computed F value is:

$$F_{computed} = \frac{\left(\frac{RSS_{total} - RSS_{(2002\sim2009)} - RSS_{(1979\sim2001)}}{2}\right)}{\left(\frac{RSS_{(2002\sim2009)} + RSS_{(1979\sim2001)}}{31+31-4}\right)} = 1.3 \quad \text{--- (Eq. 9)}$$

Because computed F value is smaller than the critical F value, hypothesis was not be rejected; that is, there is no structure change happened in 2002.

## 4. Data

As for the necessary data sets for China, interview survey was conducted in China in November, 2010 to visit State Electricity Regulatory Commission of China (SERC) in Beijing and Northeast Grid company in Shenyang. By this survey, the following data sets were collected; they are (1) total capacity of all generation companies in China 2002~2009, (2) total production of electricity, (3) GDP 1996~2009 and total capacity of all generation companies in Liaoning province 2002~2009.

As for the data of the total

generation capacity of the electricity companies in both UK and Japan, it was obtained from each generation company homepage.

## 5. Results

### 5.1. Price system

In UK, there are two pricing systems. One is Contracts Market which generators make contract directly with electricity suppliers to sell a fixed amount of electricity at a point in the future. The other is Balancing Market where generators resolve difference between their contracted amount and amount of electricity they actually delivered.

Electricity price in Japan is determined by the electricity companies under the regulations of the government.

The Electricity price in China is controlled by NDRC (National Development and reform Commission). NRDC adjusts the price several times one year according to coal price fluctuation. The pricing system in Liaoning province is consistent with the national regulator which is decided by NDRC.

### 5.2 Concentration Ratio (CR4)

The concentration Ratio results of UK, Japan, China and Liaoning are shown in Figure1.

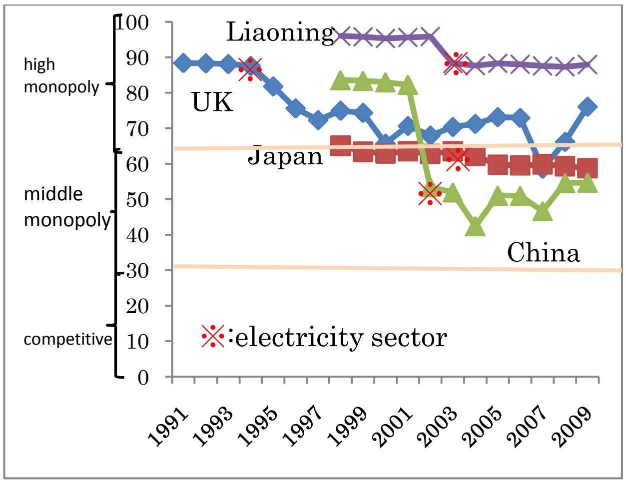


Figure1. Concentration Ratio results of UK, Japan, China and Liaoning province

In UK, before and after the reform, CR4 >65%, so there is a high level monopoly market. In Japan, before and after the reform, 30%<CR4<65%, so there is a middle level monopoly market. In China, before the reform, CR4>65%, there is a high level monopoly market. But after the reform, 30%<CR4<65%, it turned to middle level monopoly market. In Liaoning, before and after the reform, CR4 >65%, so there is a high level monopoly market.

### 5.3 HHI

The HHI results of UK, Japan, China and Liaoning are shown in Figure2. In UK, before the reform, HHI>1,800, there so was a high level monopoly market. However 1,000<HHI <1,800, it turned to middle level monopoly market. In Japan, both before and after the reform, 1,000<HHI<1,800, there is a middle level monopoly market.

In China, before the reform, HHI>1,800, there was a high level monopoly market. After the reform, HHI<1,000, it turned to competition market.

In Liaoning, both before and after the reform, HHI>1,800, there was a high level monopoly market.

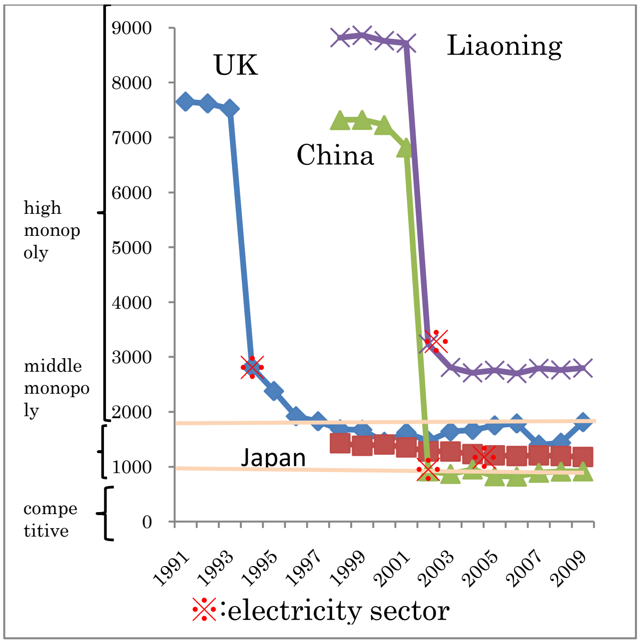


Figure2. Herfindahl-Hirschman index results of UK, Japan, China and Liaoning province

Numbers of generation companies in China is much more than UK and Japan, so the HHI value of China is lower than UK and Japan. However, in the provincial level, in Liaoning province, the number of generation companies close to UK and Japan. But the HHI value is much larger than UK and

Japan. In the province area, monopoly level of China is higher than UK and Japan.

Table1. Number of electricity generation companies in 3 countries and Liaoning province

| UK | Japan | China | Liaoning |
|---|---|---|---|
| 8 | 10 | 33 | 6 |

### 5.4 Gini Coefficients

The Gini Coefficients results of UK, Japan, China and Liaoning are shown in Figure3. In UK, after the reform, Gini value is getting smaller, reaching to much less value compared to others. It means the scale of generation companies is close to each other. In Japan, Gini value has not changed much, it similar to Liaoning. Japan and Liaoning are between UK and China. In China, after the reform, it has the highest Gini value, it means the capacities of China concentrated in several companies.

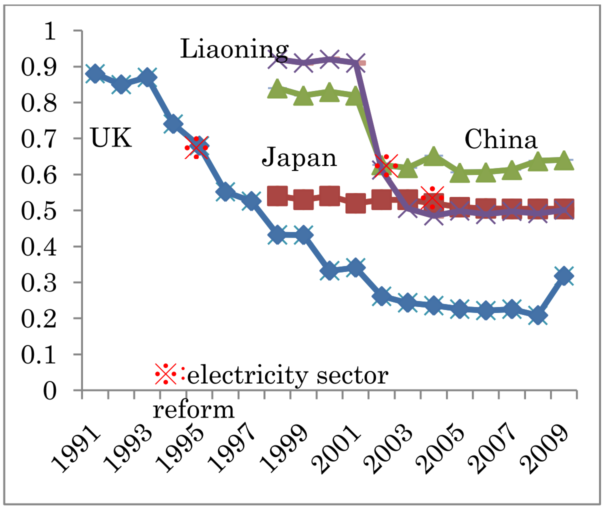


Figure3. Gini Coefficients results of UK, Japan, China and Liaoning province

### 5.5 Chow test

The result of Chow test for the possible structural change which can be found in the simple relationship between electricity generation and GDP in China from 1996 to 2009 is shown in Table 2. The results indicate that there are structural changes from 1998 to 2001 (4 consecutive years), implying that this study could not find a structural change after the Power sector reform in 2002. Some structural change could occur before the Power sector reform in 2002, possibly due to massive investment for the augmentation of electricity generation capacity. As hindsight, the unbundling of the power sector, especially the generation sub-sector, could be possible only after the total size of electricity generation capacity became large enough.

Table 2 result of Chow test on generation production & GDP of China 1996~2009

| Year | Comouted F value | Critical F value | Hypothesis |
|---|---|---|---|
| 1996 | 1.3 | 3.1 | can not reject |
| 1997 | 2.3 | 3.1 | can not reject |
| 1998 | 4.1 | 3.1 | rejected |
| 1999 | 7.7 | 3.1 | rejected |
| 2000 | 16.3 | 3.1 | rejected |
| 2001 | 5.9 | 3.1 | rejected |
| 2002 | 1.3 | 3.1 | can not reject |
| 2003 | 0.9 | 3.1 | can not reject |
| 2004 | 0.6 | 3.1 | can not reject |
| 2005 | 0.4 | 3.1 | can not reject |
| 2006 | 0.3 | 3.1 | can not reject |
| 2007 | 0.2 | 3.1 | can not reject |
| 2008 | 0.1 | 3.1 | can not reject |

## 6. Conclusion

The conclusion of this study is summarized as the following. As for the first goal, it is confirmed that electricity price system in China has not been formed through a competition market comparing with UK and Japan. Then, based on the results of the 3 methods for the assessment of market competitiveness in China, the study found that the electricity generation market in China cannot be regarded as competitive. At Liaoning province, the number of generation companies is limited and its state is close to monopoly. As for the second goal, according to the result of Chow test, it could not confirm that power sector reform induces obvious effect on the structure change of generation production and GDP at the national level.

## References

[1]Asgari, Mohammad Hssein. Market power analysisi for the electricity market. Energy Policy, 2010, 38(2010)5582-5599.

[2]Colella, Whitney. Implications of electricity liberalization for combined heat and power fuel cell systems: a case study of the United Kingdom. Journal of Power Sources106, 2002, 397-404.

[3]H.W.Ngan. Electricity regulation and electricity market reforms in China. Energy Policy, 2010, 38(2010)2142-2148.

# EXPERIMENTAL STUDY ON THERMAL BOUNDARY LAYER ALONG A BUILDING WALL

Student Number: 09M18019 Name: Shiho ONOMURA Supervisor: Manabu KANDA

建物の鉛直壁面に発達する熱境界層の観測研究

小野村　史穂

本研究では，建物鉛直壁面に発達する熱境界層の観測を行った．壁面近傍には，法線方向に，複数の熱電対と超音波風速計を配置し，熱駆動上昇流の詳細な温度分布と速度情報を取得した．壁面近傍の温度及び温度変動強度の分布から，壁面近傍の上昇流が温度差による乱れと大気中の擾乱との影響により，三層に分類できることが明らかとなった．自然対流とは異なり，壁面からの対流熱伝達は，大気の乱れにより促進されていた．

## 1. Introduction

In the field of urban meteorology, it is important to know the temperature and velocity distribution within urban canopy layers. Nakamura and Oke [1] and Kanda et al. [2] obtained the overall temperature/wind patterns within street canyons. An alternative way to predict temperature and velocity fields within urban canopy layers is numerical models. In numerical approaches, the parameterization of boundary conditions is important. Monin-Obukhov similarity (MOS) is applied to thermal boundary layers along horizontal surfaces, whereas such theoretical frameworks have not been established for vertical walls. Thus, the measurements of the thermal boundary layer developed along the vertical walls of buildings are very important to know the mechanism of heat transfer process near walls and formulate the parameterization. However, the previous field studies did not focus on thermal boundary layers very close to vertical walls.

Thermal boundary layers along a vertical heated plate have been investigated well in the field of mechanical engineering. Tsuji and Nagano [3] and Hattori et al. [4, 5] have precisely measured temperature and velocity profiles normal to vertical heated plates using vertical wind tunnels. However, the studies were based on natural convection or combined convection with laminar flow in the outer layer and the fetch scale of the heat plates was much smaller than that of building walls. Therefore, it is unclear that those results can be applied to the thermal boundary layers along building walls which have the overwhelmingly long fetch of building walls and high $Re$ number.

In the present study, the measurements of thermal boundary layers developed along a building wall were conducted to provide better understandings of thermal exchange process along vertical walls and to lead to the better modeling of the process.

## 2. Experimental setup

The measurements were conducted on the dates written in Table 1. The south-southwest oriented wall of Ishikawadai 3rd Building, Ookayama campus, Tokyo Institute of Technology was selected for the thermal boundary layer observation (Fig.1 (a)). The wall is constructed by concrete and the surface was covered by beige tiles. The weather was almost fine through the observation. A thermocouples rake was set perpendicularly to the wall at a height of 22.16 m from the ground and at the lateral center of the wall (Fig.2). On the rake, the thermocouples were installed more densely with shorter distance from the wall. The diameter of thermocouples is only 0.05 m on the edges to reduce the influence of directly radiation heat. Three ultrasonic anemometers were set at 2m above the roof top (S1), 35 mm away from the wall (S2), and 2 m away from the wall (S3). For Case4, part of the wall was covered by black-painted Styrofoam boards to make large temperature differences and to amplify the wall temperature fluctuations, so that they can be captured by an infrared camera (Fig.1 (b)).

Table 1. Dates and measurement heights

| No. | Case 1 | Case 2 | Case 3 | Case 4 |
|---|---|---|---|---|
| Date | 1st Aug. | 28th Aug. | 3rd Sep. | 16th Dec. |
| Measurement height | 2.87 m | 22.16 m | 22.16 m | 22.16 m |

(a) Case 1-3 (b) Case 4

Figure 1 Wall of Ishikawadai 3rd building

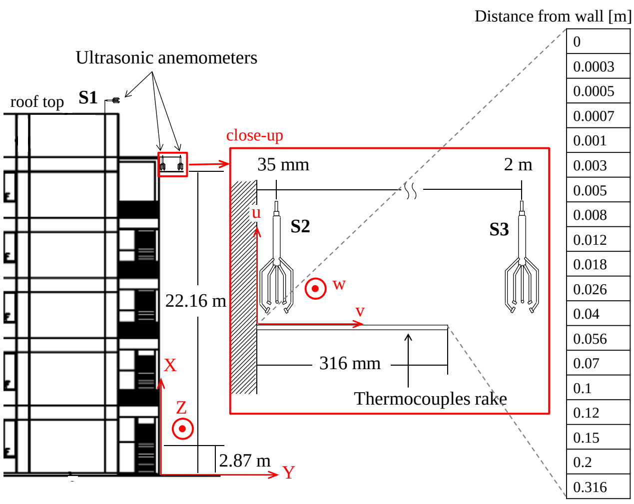


Figure 2 Experimental setup

## 3. Result

### 3.1. Mean temperature profiles

The shapes of mean temperature profiles normalized by temperature difference, $\Delta T = (T_w - T_\infty)$, almost agree with each other. However, as observed in Fig.3, the profiles of $3 \le \Delta T$ are shifted to higher temperature compared with that of $1 \le \Delta T < 3$. This detail will be discussed in chapter 3.5.

### 3.2. Intensity of temperature fluctuation

Profiles of the intensity of temperature fluctuation, $\sigma_t$, in Case 3 are shown in Fig.4. Three layers can be recognized. The ranges of each layer are (1) the nearest layer (y ≤ 0.001 m), (2) the middle layer (0.001 m < y < 0.04 m), and (3) the farthest layer (0.04 m ≤ y). The characteristics of each layer can be explained by using two main elements which generate temperature fluctuation. One is natural convection resulted from temperature difference, and the other is forced convection contained in the outer layer. Although some surrounding factors like heat from the ground and winds blowing through buildings can affect thermal boundary layers, it can be assumed that they are included into natural or forced convection. At the nearest layer, the former is dominant and the latter is very small, since $\sigma_t$ can be normalized by $\Delta T$. The value of $\sigma_t$ is small because viscosity suppresses it. That means the influence of forced convection is small. At the farthest layer, the profiles are independent of $\Delta T$. Turbulence in forced convection mainly induces the temperature fluctuation.

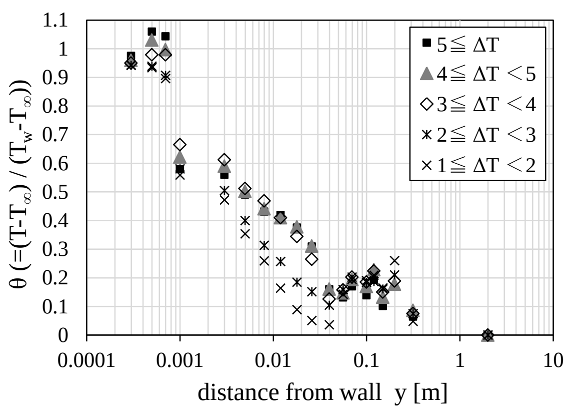


Figure 3 Mean temperature profile

The absolute value of $\sigma_t$ seems to be related to the intensity of disturbance in the outer layer. The reason why $\sigma_t$ gets smaller with $y$ is the effect of heat from the wall decreases as the measurement point is farther from the wall. The middle layer includes both influences because the value of $\sigma_t$ is largest. In this layer, natural convection generated by the temperature difference and forced convection in the outer layer can be intermittently mixed.

For investigating the influence of forced convection from the outer layer on temperature fluctuation, the profiles in the range of $3 \leq \Delta T < 4$ in Fig. 4 is further classified into each range of turbulence kinetic energy, $e$. As seen in Fig.5, the intensities of temperature fluctuation are larger, as $e$ is higher. A profile satisfying the condition of $3 \leq \Delta T < 4$ and $e < 0.3$ from Case 2 is also plotted by plus signs. It agrees well with that taking the same condition in Case 3. This agreement indicates the result that the intensity of temperature fluctuation depends on mainly $\Delta T$ and $e$.

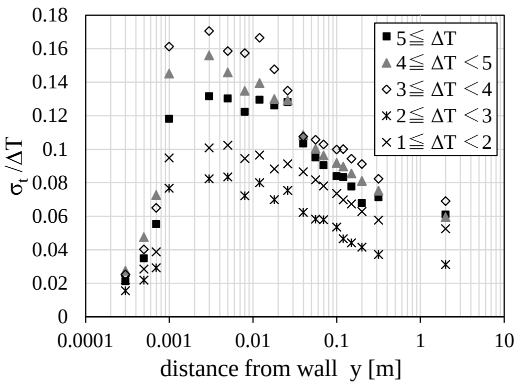


Figure 4 Intensity of temperature fluctuation (Case 3)

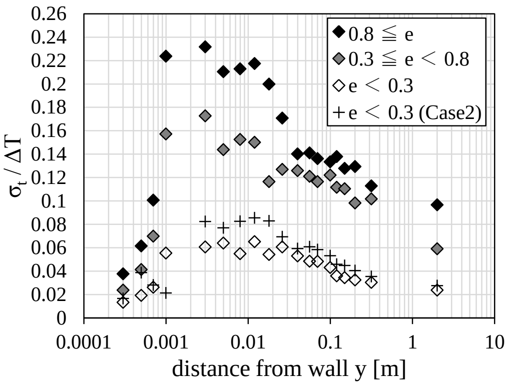


Figure 5 Intensity of temperature fluctuation
(3< $\Delta T$ <4, in Fig.4) classified into the range of $e$

## 3.3. Instantaneous phenomenon

Time variations of temperature at all the measurement points and velocities measured near wall are shown in Fig.6. The three layers as mentioned above also can be recognized in this time series. The characteristics of each layer can be explained as described in the chapter 3.2. Focusing on the middle layer (0.001 m < y < 0.04 m), the patterns of the flow close to the wall are discussed. In the time range of 1 - 3 s, temperature in the middle layer rapidly dropped with strong upward wind coming from the outer layer. In the time range of 3 - 6 s, velocities decrease and the temperature of the middle layer increases. This observation suggests that forced convection is dominant in the former time period (1 - 3 s), and natural convection is dominant and the thermal boundary layer is established near the wall in the latter time period (3 - 6 s).

## 3.4. Heat transfer

Fig.7 shows heat transfer rates in Case 4. $Nux$ number decreases as $Rax$ number increases. This result is different from the relationship that $Nux$ increases with $Rax$ under natural convection in the wind tunnel experiments (Tsuji and Nagano (1988) and Hattori et al. (2006)). It is because heat transfer rate is related to not only natural convection but also forced convection. As

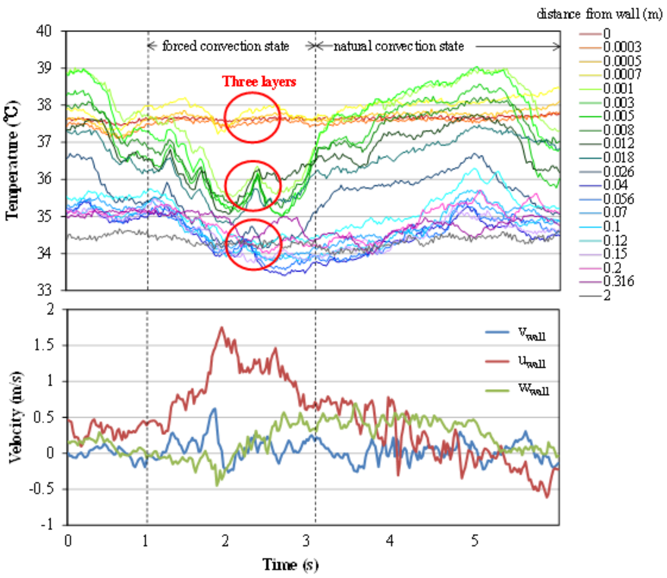


Figure 6 Time variations of temperature at all points
and velocity components of the anemometer (S2)

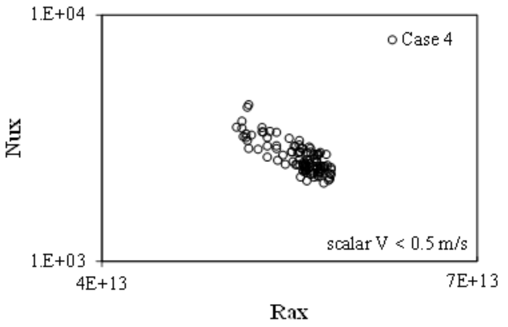


Figure 7 Relationship between *Nux* and *Rax*

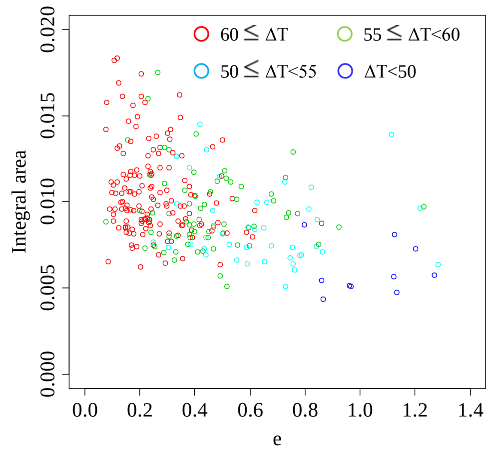


Figure 8 Relationship between integral area versus $e$

the forced convection gets stronger, $\Delta T$ becomes smaller. Since $\Delta T$ is almost equivalent to $Rax$, it leads to larger heat flux.

## 3.5. Thickness of thermal boundary layers

The integral area of a temperature profile was introduced as an index of thickness of thermal boundary layer. The relationship between the integral area and $e$ can be categorized with color coding of the data for each range of $\Delta T$. As seen in Fig.8, the integral area increases with $\Delta T$, whereas it decreases by $e$. In addition, $\Delta T$ and $e$ have a strong correlation. Therefore, this figure will be useful for roughly modeling the normalized temperature profiles in terms of $e$ and just one measured $\Delta T$.

## 3.6. Images of thermal boundary layers

Through consecutive thermal images captured by the infrared camera, it was observed that the scale of the development of thermal boundary layers is very various. Thermal driven flows were locally developed everywhere on the wall and some of them merge to become longer while others were dispersed due to the disturbances of forced convection.

## 3.7. Conclusion

The thermal boundary layers developed along a building wall were measured with thermocouples, ultrasonic anemometers, and an infrared camera. The remarkable results are summarized as follows:

(a) In thermal driven flow, three layers can be characterized by the influence from natural convection from temperature difference and forced convection from the outer layer.

(b) Heat transfer rate, $Nux$, decreases with $Rax$ due to forced convection in the outer layer.

(c) The thickness of temperature profiles depends on $e$ and just one measured $\Delta T$.

## Reference

[1] Nakamura, Y. and Oke, T. R. : Wind temperature and stability conditions in an east-west oriented urban canyon, *Atmos.Environ.*, Vol122, No12, pp. 2691-2700, 1988

[2] Kanda, M., Kasamatsu, F., and Moriwaki, R. : Spatial variability of turbulent fluxes and temperature profiles in an urban roughness layer, *Boundary-Layer Meteorology*, Vol.121, pp.339-350, 2006

[3] Tsuji, T. and Nagano, Y. : Characteristics of a turbulence natural convection boundary layer along a vertical flat plate, *Int. J. Heat and Fluid flow*, Vol.31, No8, pp. 1723-1734, 1988

[4] Hattori, Y., Tsuji, T., Nagano, Y., Tanaka, N. : Characteristics of turbulent combined-convection boundary layer along a vertical heated plate, *Int. J. Heat and Fluid flow*, Vol.21, pp.520-525, 2000

[5] Hattori, Y., Tsuji, T., Nagano, Y., Tanaka, N.: Turbulence characteristics of natural-convection boundary layer in air along a vertical plate heated at high temperatures , *Int. J. Heat and Fluid flow*, Vol. 27, pp.445-455, 2006

# Analysis of International Freight Transportation Characteristics of Landlocked Countries

**Student Number: 09M18025 Name: Hironori KAWAI Supervisor: Shinya HANAOKA**

# 国際貨物輸送における内陸国の特性分析

河合　弘則

本研究は内陸国間に存在する差異に着目し、貿易と内陸貨物輸送において存在するボトルネックの特性を抽出する事を目的としている。貿易に関しては、貨物が内陸国に隣接する沿岸国の港湾を出るまでのプロセスにおける問題点を取り扱い、内陸貨物輸送に関しては、内陸国の輸送時間を決定づけている要因の分析を行った。さらに、そこで明らかとなった要因をもとに、各内陸国の輸送環境の特性について考察を行った。

## 1. INTRODUCTION

There are 43 landlocked countries (LLCs) in the world. And United Nations reported 31 of them are being called Landlocked Developing Countries (LLDCs). One of the factors of their harsh economic conditions is considered to be difficulty in trade. As LLCs have no their own seaport, they have to cross at least one border when they trade by maritime transport and their access to the seaports of transit neighbor countries (TC). In case that TC doesn't have efficient transit trade facilities or doesn't allow LLC to conduct cross-border trade without frequent cargo inspection or cumbersome procedures, in addition to inland transportation with long distance to the seaport, LLC suffers from long transportation time, high transportation cost. Consequently some LLCs suffer from high trade cost and slow economic development.

Although LLCs have a lot of disadvantages regarding trade and economic development, some LLCs in Europe such as Andorra, Austria, Czech Republic, Hungary, Liechtenstein, Luxemburg, San Marino, Slovakia and Switzerland, are classified into high income countries and Azerbaijan, Belarus, Kosovo, Macedonia, Moldova, Serbia and Kazakhstan are upper middle income countries (definition of World Bank). This fact can prove that LLCs have chance to realize economic development, if they are under certain environment. And from the fact that some LLCs are high income countries and others LLCs are developing country, homogeneity among LLCs cannot be claimed. In fact, each LLC has characteristics.

As also will be noted from Figure.1, although LLCs basically suffer from high export cost and long export time, but data of LLCs are quite variable, stated differently, trade environment are quite different from LLCs to LLCs. And some other conditions such as GDP per capita and trading partners are quite different in each LLC.

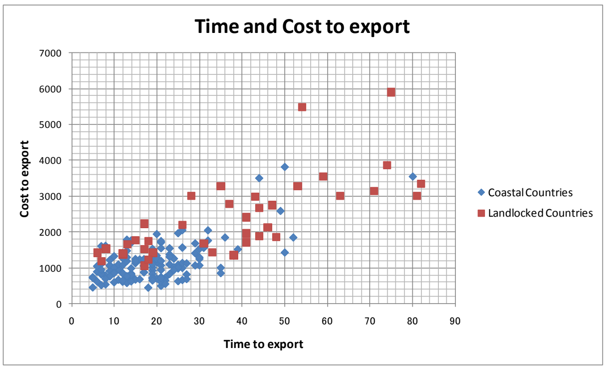


Fig. 1 Total Cost and Time to Trade

*Source: World Bank, Trading across border 2011*

## 2. RESEARCH OBJECTIVE AND FRAMEWORK

Some researches have proved disadvantages of LLCs. For instance, Limao and Venables (2001) stated that being landlocked raises transport costs by around 50% (for the median landlocked country compared to the median coastal economy). Radelet and Sachs (1998) proved that transport and insurance costs are twice as high for landlocked countries as coastal countries and they demonstrate that there is a link between transport costs and economic growth. And some other papers have demonstrated the impact of being landlocked on trade, transport cost and economic growth. But there is no previous research which focuses on disparity among LLCs. So this paper analyses characteristics of each LLC.

This thesis focuses on disparity among landlocked countries (LLC) and analyzes the characteristics of them. Analyses are conducted related to international trade and freight transportation of LLC by using Doing business data 2011 (World bank) covering the process between the vessel's arrival at the port of LLC's transit neighbor countries (TC) and the cargo's delivery at the warehouse in LLCs (for import). And this study consists of four analyses.

I. Characteristics analysis of bottlenecks of LLCs' trade procedures
II. Determinants of inland transportation of LLCs
III. Characteristics analysis of inland transportation of LLCs
IV. Case study focus on Bhutan, Nepal, Chad and Central African Republic

## 3. CHARACTERISTICS OF BOTTLENECKS OF LLCs' TRADE PROCEDURES

By using cluster analysis (Ward method), bottlenecks of procedures required for trade such as documents preparation, customs clearance and technical control, and ports and terminal handling are extracted to define which processes have significant problems for each LLC. Although this analysis focused on export time and cost, import time and cost data, now the result using export time are shown in Table 1 and Table 2.

Table 1.Result of classification

| | |
|---|---|
| Cluster 1 | Botswana, Mali, Lesotho, Kosovo, Swaziland, Hungary, Macedonia, Serbia |
| Cluster 2 | Burundi, Nepal, Paraguay, Uganda |
| Cluster 3 | Belarus, Slovakia, Bolivia, Czech Republic, Armenia, Austria, Luxembourg, Switzerland |
| Cluster 4 | Bhutan, Rwanda, Malawi, Zambia, Moldova, Azerbaijan, Ethiopia, Burkina Faso, Laos, Mongolia |
| Cluster 5 | Niger, Uzbekistan |
| Cluster 6 | Central African Republic, Zimbabwe, Chad, Kyrgyzstan |

Table 2.Characteristics of each cluster

| | Good condition | Bottlenecks |
|---|---|---|
| Cluster1 | Documents, Inland, Customs | |
| Cluster2 | Document | |
| Cluster3 | All | |
| Cluster4 | Port | Document |
| Cluster5 | | Document, Port, Inland |
| Cluster6 | | Document, Inland |

LLCs in Cluster 3 have few bottlenecks in trade procedures. Bolivia is exceptional of this group where mostly European countries occupy. Cluster 2 is the group in the second best condition among LLCs. Botswana, Mali Lesotho, and Swaziland in Sub Saharan Region are classified into this group except for European countries. Countries in Cluster 2, Burundi, Nepal, Paraguay, and Uganda suffer from long inland transportation time but documentation is relatively efficient. Cluster 4 consists of African countries and Asian countries, and their bottleneck is documentation.. LLCs in Cluster 5,6 and Afghanistan, Kazakhstan, Tajikistan (outlier in this analysis). These African and Central Asian countries have a lot of bottlenecks. Their trade procedures are most inefficient among LLCs. Especially time to documents preparation and Inland transportation are serious problems. Many of Central Asian countries have to cross more than two borders and are far from the seaport, so they cannot avoid long inland transportation and are enforced to have cumbersome documentation. Although Central African Republic, Zimbabwe, Chad, Niger (in Cluster 5, 6) don't have physical constraint, inefficient bureaucracy, poor infrastructure, conflict in neighbor countries and other factors make them in the difficult condition.

## 4. DETERMINANTS OF INLAND TRANSPORTATION TIME OF LLCs

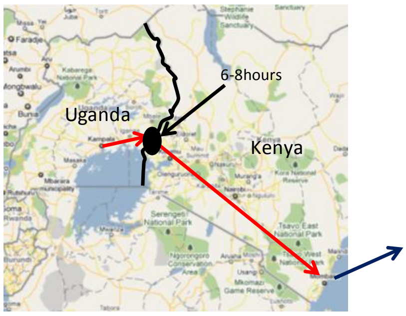


Fig. 2 Sketch map of access to seaport (e.g Uganda→Kenya)

Inland transportation is one of the most serious bottlenecks for LLCs. Take Uganda for example, inland transportation time from its capital, Kampala to Kenyan seaport, Mombasa (1187 km) takes 18 days, while Austria, needs only 2 days to complete the transport to the German port of Hamburg despite the distance of 900 km. This difference is made by border-crossing time (Uganda needs 6-8 hours to cross the border), infrastructure quality, and some other factors.

Now factors which contribute to inland transportation time (*TT*) for LLCs' access to seaport is analyzed using multiple regression analysis. Transport infrastructure (road and railway), country risk, distance to seaport, and land form of LLCs and TCs are incorporated in regression models as explanatory variable and their impact on freight transport are measured.

### 4.1 EXPLANATORY VARIABLES

1) Transport infrastructure

As LLCs depend on more than one TC for their overseas exports and imports by maritime transportation, in the process of their access to seaport, transport infrastructure quality of LLCs (*LLCInfra*) and TC (TC*Infra*) can be significant. Each LLCs' and TCs' Infrastructure quality are measured by composite variables constructed from three variables (kilometers of road, kilometers of paved road, kilometers of rail (each per square kilometer of country data)) by Principal Component Analysis (PCA), because these measures are highly correlated among themselves.

2) Country risk

Efficiency in bureaucracies of LLCs and TCs are considered to exert an influence on border-crossing time and frequency of cargo inspection.

This analysis uses data named “Euromoney Country Risk” which shows efficiency of bureaucracies. In this database, economists and heads of researchers worldwide were asked to rate each country across six categories: government stability, regulatory environment, non-payment of loans / dividends / trade-related finance, non-preparation of capital, corruption perception and information access / transparency. And higher the scores, more efficient bureaucracies the countries have.

3) Geographical features

Distance to seaport from the capitals of LLCs to seaport (*Dist*) data of which are quoted from “Landlocked Developing Countries Fact and Figures” (by United Nations) are incorporated into regression models, since importance of distance for transport time is obvious.

And as many of LLCs are located in mountainous areas, there is a possibility that some LLCs’ freight transportation suffer from difficulty in land form. Latitude of capitals in LLCs (*Latitude*) and Forest area (percentage of land area) (*LLC forest*, *TC forest*) are selected.

### 4.2 REGRESSION MODELS

The variables of *LLCInfra*, *TCInfra*, *LLCCR*, *TCCR* are highly correlated among themselves, so these variables are separately incorporated into regression models to avoid multicollinearity.

Table 3. Coefficient of correlation

| | *LLCInfra* | *TCInfra* | *LLCCR* | *TCCR* |
|---|---|---|---|---|
| *LLCInfra* | *1* | | | |
| *TCInfra* | 0.925718 | 1 | | |
| *LLCCR* | 0.795664 | 0.769989 | 1 | |
| *TCCR* | 0.679597 | 0.744667 | 0.644349 | 1 |

1) *TT* = *f* (*Dist*, *LLCInfra*, *Latitude*, *LLCforest*, *TCforest*)
2) *TT* = *f* (*Dist*, *TCInfra*, *Latitude*, *LLCforest*, *TCforest*)
3) *TT* = *f* (*Dist*, *LLCCR*, *Latitude*, *LLCforest*, *TCforest*)
4) *TT* = *f* (*Dist*, *TCCR*, *Latitude*, *LLCforest*, *TCforest*)

*TT*: Inland transportation time from the capital of LLCs to seaports of TCs at the average of transportation time for exporting and importing
*Dist*: Closest distance from the capital of LLCs to seaports of TCs
*LLC Infra*: Infrastructure index of LLCs
*TC Infra*: Infrastructure index of TCs
*LLCCR*: Country risk of LLCs
*TCCR*: Country risk of TCs
*Latitude*: Latitude of LLC’s capitals
*LLC forest*: Percentage of forest area in total land area of LLCs
*TC forest*: Percentage of forest area in total land area of TCs

### 4.3 ESTIMATION RESULT

Table 4. Estimation results

| Dependent Variable: Inland transportation time (*TT*) | | | | | | | | | | |
|---|---|---|---|---|---|---|---|---|---|---|
| | 1) | | 2) | | 3) | | 4) | | 5) | |
| | Coefficient | t-value | Coefficient | t-value | Coefficient | t-value | Coefficient | t-value | Coefficient | t-value |
| *Constant* | 4.062 | 0.773 | 5.031 | 0.971 | 14.100 | 2.432 | 11.950 | 1.345 | 12.05 | 3.39 |
| *Dist* | 0.009 | 4.889 | 0.008 | 4.787 | 0.007 | 4.620 | 0.008 | 3.944 | 0.01 | 5.53 |
| *LLC Infra* | −2.572 | −1.559 | | | | | | | | |
| *TC Infra* | | | −3.299 | −1.994 | | | | | | |
| *LLC CR* | | | | | −0.733 | −3.390 | | | −0.71 | −3.62 |
| *TC CR* | | | | | | | −0.487 | −1.472 | | |
| *Latitude* | −0.001 | −0.347 | −0.001 | −0.558 | −0.001 | −0.001 | 0.000 | 0.067 | | |
| *LLC forest* | −0.037 | −0.456 | −0.017 | −0.203 | −0.023 | −0.325 | −0.028 | −0.331 | | |
| *TC forest* | 0.006 | 0.049 | −0.026 | −0.197 | −0.004 | −0.039 | 0.002 | 0.012 | | |
| | | | | | | | | | | |
| *Adjusted R2* | 0.512 | | 0.534 | | 0.616 | | 0.508 | | 0.644850906 | |
| *Observations* | 37 | | 37 | | 37 | | 37 | | 37 | |

From the result, Distance to seaport from the capitals of LLCs to seaport in TCs (*Dist*), transport infrastructure quality of LLCs (*LLCInfra*) and TC (*TCInfra*), country risk of LLCs (*LLCCR*) and TCs (*TCCR*) are confirmed to be the factors influencing on inland transportation of LLCs. But Latitude of capitals in LLCs (*Latitude*), Forest area (*LLC forest*, *TC forest*) could not be significant variables. This result assumes that data used for land form were not appropriate or land form doesn’t affect transportation time.

## 5. CHARACTERISTICS OF INLAND TRANSPORTATION OF LLCs

Based on the factors confirmed by regression analysis in the last part, characteristics of inland transportation environment are extracted by cluster analysis again. Transport infrastructure, country risk of LLC and TC and distance to seaport are used as variables.

Table 5. Result of classification

| | |
|---|---|
| Cluster1 | BurkinaFaso, Mali, Niger, Uganda, Ethiopia, Malawi, Paraguay, Afghanistan, Mongolia, Zambia, Burundi, CentralAfricanRepublic, Chad, Rwanda |
| Cluster2 | Armenia, Azerbaijan, Bhutan, Belarus, Macedonia, Moldova |
| Cluster3 | Laos, Nepal, Zimbabwe, Lesotho, Swaziland, Bolivia, Botswana |
| Cluster4 | Kyrgyzstan, Tajikistan, Uzbekistan, Kazakhstan |
| Cluster5 | Austria, Switzerland, CzechRepublic, Luxembourg, Hungary, Slovakia |

Table 6. Characteristics of each claster

| | Good condition | Bottleneck |
|---|---|---|
| Cluster1 | | *LLCInfra, TCInfra, LLCCR,TCCR* |
| Cluster2 | *Dist,* | |
| Cluster3 | *Dist, TCCR* | *LLCInfra, TCInfra, LLCCR* |
| Cluster4 | | *Dist,LLCInfra, TCInfra, LLCCR,TCCR* |
| Cluster5 | *LLCInfra, TCInfra, LLCCR,TCCR* | |

Cluster 1 and 4 are in difficult condition among LLCs. Cluster 1 consists of African and Asian countries, especially infrastructure developments of them are the worst. In Cluster 4, all countries are Central Asian countries. They suffer from long distance to seaport, bad condition of TCs and have poor infrastructure and inefficient bureaucracies.

Countries in Cluster 5 are in the best condition among LLCs. They all are high income European countries and have few bottlenecks on freight transportation. Cluster 2 consists of second best LLCs. Except for Bhutan, middle income European countries are in this group. Cluster 3 is exceptional considering region and their transport environment are relatively in good condition among landlocked developing countries.

Basically LLCs are classified by region in this analysis, but there are some exceptions. Difference between Paraguay (Cluster 1) and Bolivia (Cluster3) in South America is due to the distance to seaport and country risk of their TCs. These factors also make East Asian countries, Mongolia (Cluster 1) and Laos (Cluster 2) classified in different clusters. The reason why Bhutan (Cluster 2) and Nepal (Cluster 3) are in the different group is their own country risk.

## 6. CASE STUDY

As analyses above-mentioned are based on secondary data of each country, actual conditions of freight transportation are hard to be seen. Therefore case study has to be conducted. This study covers Bhutan, Nepal, Chad, Central African Republic and now focuses on agreement with TCs.

### 6.1 BHUTAN, NEPAL

Although both Bhutan and Nepal are located in South Asia and have common transit country, India, transport environment of Bhutan is better than that of Nepal according to the analysis in the last part. And in fact, inland transportation time for exporting of Bhutan is 13days, while that of Nepal is 19days. Now their disparity is analyzed.

There is difference in their own country risk and distance to Kolkata (Indian seaport), but in detail major difference is linked to each transit agreement with India. Although they both signed transit trade agreement with India, there is difference of its history and content. India allows Bhutanese transit trade to be conducted under the supervision of Bhutanese customs, yielding little administrative hassle. In contrast, Nepal's relations with India have frequently been strained, with India often seen to have more influence in the negotiation of treaties and disputes. (Faye et al (2004))

This case shows relationship between LLCs and TCs influences on inland transportation especially in case LLCs don't have more than one transit country.

### 6.2 CHAD, CENTRAL AFRICAN REPUBLIC

Chad and Central African Republic (CAR) are one of the poorest countries in the world. Their international transit transport costs are the highest. (CAR:3900$/TEU,24days, Chad:4405$/TEU, 30days) It's because of their poor domestic infrastructure and political conditions and they suffer from civil wars in major transit countries.

Chad has no choice but to go through Cameroon even when transit seaport is in Nigeria due to geographical restriction. Although CAR has two transit countries, Cameroon and Congo Republic, transit route through Congo Republic is time-consuming. So they mainly depend on Cameroon when they conduct transit trade. But even in Cameroon, transport environment has a lot of problems such as frequent cargo inspection, lacking of efficient border facilities and customs procedure system and another problem is that railway of Cameroon are not linked to the border with Chad and CAR. In addition to the problems of inland transportation, long dwelling time at Douala port in Cameroon is serious. They need approximately 30days until the cargo left the Douala.

## 7. CONCLUSION

This paper showed characteristics of bottlenecks of LLC's trade procedures and inland transportation, determinants of long inland transportation time and actual condition of some LLCs. Characteristics of each LLC are not only determined by region they are located in but also by each infrastructure level, bureaucracy efficiency, distance to seaport, relationship and agreement with neighbors, conditions of TCs and other factors.

## Reference

1) Euromoney Country Risk Onlineavailable:http://www.euromoney.com/Article/2675673/Country-risk-Methodology.html
2) Limao, N, and Venables AJ. (2001) " Infrastructure, geographical disadvantage and traosport costs. "World Bank Economic Review 15(3): 451-479.
3) Michael L. Faye; John W. McArthur; Jeffrey D. Sachs; Thomas Snow(2004), "The Challenges Facing Landlocked Developing Countries", Journal of Human Development and Capabilities, Volume 5, Issue Number 1 March 2004 , pages 31 - 68
4) Raballand, G., (2003) "Determinants of the negative impact of being landlocked on trade: an empirical investigation through the Central Asian case", Comparative Economic Studies 45: 520–536.
5) World Bank Doing Business 2011 Online available: http://www.doingbusiness.org/

# OPERATION AND MANAGEMENT OF WIND POWER PLANTS UNDER RISK OF FAILURE

Student Number: 09M18048 Name: Yoshihiro Sato Supervisor: Naoya Abe

故障リスク下にある風力発電設備の運用と管理

佐藤 好浩

本論文では、風力発電運営に伴う不確実性を考慮にいれた運営シミュレーションを行い、予想される事業収益の分布を示した。想定した不確実性として、ワイブル分布による風速の出現、1 基当たり年間故障事故回数、1 回あたり稼働停止時間を入力した。シミュレーションでは、故障リスク、稼働停止の長期化、包括契約の利点についてシミュレーション結果を基に考察した。

## 1. Introduction

Suttsu-town, a local municipality in Hokkaido with the population size 3,744 (2005 Census), earns 85 million yen from wind power plants annually, partially due to the preferable wind conditions there. They pay back the profit to citizens in the forms of scholarship to local students and subsidies to local community activities. By contrast, Jyoetsu-city, another local government in Niigata prefecture, loses about 35 million yen from wind power plants annually. According to NHK, about 60% of wind power plants operated by Japanese local government are suffering budget deficit.

The reasons for the latter case can be: (1) longer downtime of plants than they planned, (2) inadequate maintenance works, and/or (3) less generation of electricity than initially expected, partially due to inadequate feasibility study.

A maintenance expert from NEIC Japan, which is a wind turbine parts providing company, pointed out that some small wind power plant operators cannot arrange adequate maintenance services because those expenses are too expensive and those operators are often in deficient[1]. On the other hand, Suttsu-town is currently operating five 1,990 kW class turbines and has paid serious attentions to the maintenance of the plants by making a package-deal type contact with a private engineering firm. It is becoming clear that maintenance works are crucial for the operation of wind power plants.

## 2. Review of existing studies

Milborrow (1994) studied economic potential of wind power [1]. It mentioned that costs such as capital, land, O&M (Operation and Management), and decommission are required to calculate the cost of generation of electricity also mentioned that international costs of generation of electricity of wind power plants are different from country by country, due to wind condition, transportation cost and subsidies. Khalfallah et al (2007) suggested that theoretical method by assuming power curve as a linear function [2]. NEDO (New Energy Development Organization), one of the Japanese government research funding agencies, conducted a comprehensive wind speed survey in Japan from 1997 to 2000 [3].

To examine the profitability of wind power plants under risk of failures, their failure data are indispensable. However, these data have been only available qualitatively and not accumulated enough quantitatively in Japan, making the statistical study of failure events associated with wind power plants difficult.

In this area, Abe and Sato (2009)[4] studied the relationship between failure events and its properties statistically for the first time based on the failure data from METI (Minister of Economy, Trade and Industry) Hokkaido questionnaire survey [5] and NEDO (New Energy Development Organization) research[6]. Its results demonstrate that the larger the output size is, the smaller the failure risk is. Wind power plants located in coastal area face higher risk than the ones located in inland area. The present study is the extension of the previous study and simulated profitability of wind power plants based on the failure data with Monte Carlo simulation.

[1] Interview to a NEIC Japan expert was held on Oct, 28, 2010.

# 3. The Study Framework

### 3.1 Weibull distribution

The present study applied Weibull distribution to simulate wind speed. In probability theory and statistics, the Weibull distribution is a continuous probability distribution. The probability density function of a Weibull random variable v is

$$f(v) = \left(\frac{k}{c}\right)\left(\frac{v}{c}\right)^{k-1} \exp\left[-\left(\frac{v}{c}\right)^{k}\right] \quad (3.1)$$

,where v is wind speed, k is shape parameter and c is scale parameter. The mean of a Weibull random variable can be expressed as follow

$$\tilde{v} = c\Gamma\left(1+\frac{1}{k}\right) \quad (3.2)$$

$\Gamma$ is gamma function. NEDO had researched about wind speed in Japan. The present study referenced the report to decide the shape parameter and mean of wind speed. Scale parameter is calculated by expression (3.2).

### 3.2 Generating electricity estimates

The output of a wind turbine is a function of wind speed. Because of mechanical friction, wind turbine cannot generate electricity when wind speed is too slow. Minimum wind speed which generates electricity is called as cut-in wind speed. If wind speed is too fast, the turbine cannot also generate electricity because of the limitation of the turbine. Maximum wind speed which generates electricity is called as cut-out wind speed. Minimum wind speed which generates rated power called rated wind speed. Power curve, a relationship between wind speed and output, was assumed a simple linear power curve suggested by Khalfallah (2007) [2] as follow:

$$P = \frac{P_r}{v_r - v_{in}}(v - v_{in}) \quad (v_{in} \le v \le v_r) \quad (3.3)$$

,where $P_r$ is rated power, v is wind speed, $v_{in}$ is cut-in wind speed and $v_r$ is rated wind speed.

The present study assumed that Weibull distribution provided an average wind speed per day, and power curve is estimated one day generating electricity. Annual generating electricity ignoring failure is the sum of one day generating electricity. To consider generation loss, annual generating electricity is the product of annual generating electricity ignoring failure and availability ratio as follow expression

$$P_{annual} = P(1 - \frac{t}{365}) \quad (3.4)$$

,where $P_{annual}$ is annual generating electricity considering failures, P is annual generating electricity ignoring failures and t is annual downtime of the plant.

### 3.3 Discount Cash Flow analysis

Discounted cash flow (DCF) analysis is a method of valuing a project, company, or asset using the concepts of the time value of money. All future cash flows are estimated and discounted to give their present values (PVs) – The sum of all the future cash flows, indicating both incoming and outgoing, indicated that the net present value (NPV), which represented the value of the cash flows.

$$NPV = \sum_{n=1}^{N} \frac{NB_n}{(1+r)^{n-1}} \quad (3.4)$$

,where NPV is net present value, N is the project term, $NB_n$ is net benefit in $n_{th}$ year and r is discount rate. The present study assumed the discount rate to be 2%, which thought to be the same as interest rate of local government bond. The rate of the profitability of wind power business should be more preferable at least than the interest rate of the bond. Indeed Suttsu-town issued local bonds when they constructed the wind power plants to finance the plants.

### 3.4 Monte Carlo methods

Monte Carlo method is a class of computational algorithms that rely on repeated random sampling to compute their results. Monte Carlo method results in the distribution of the calculated value. The present study input Weibull distribution, frequency distribution of ANA (Annual Numbers of Accident per turbine) and frequency distribution of DPA ( Downtime Per Accident) as random variables. Weibull parameters are based on NEDO research [3]. Summary of ANA and DPA data are presented in Table.1. Constant parameters are introduced in Table.2.Project period are indicated in Table.3.

**Table.1 Summary of random variables**

| | ANA(annual numbers per turbine) | DPA(days) |
|---|---|---|
| Sample size | 277 turbines | |
| Term | From 2004 to 2008 | |
| Mean | 0.15 | 22.4 |
| Std.Dev | 0.25 | 59.0 |
| Min | 0 | 3 |
| Max | 5 | 365 |

The present study considered fitting the frequency distribution of ANA to probability distribution such as Poisson distribution. But the frequency distribution cannot be fitted.

**Table.2 list of constant parameters**

| | |
|---|---|
| Numbers of Periodic Check | 2 times per year |
| Days of Periodic check | 5 days per year |
| Cost of Periodic check | 2.5 million yen per check |
| Construction cost | |
| Over 1000kW | 200 thousand yen per kW |
| Less than1000kW | 300 thousand yen per kW |
| Numbers of Labors | 1 person per 4 turbines |
| Annual salary | 6 million yen |
| Price of electricity | 9 yen/kWh |
| Subsidies | 30% of total construction cost |
| Cost to recovery | 1.5 million yen per accident |
| Discount rate/ Debt service term | 2% / 10 years |
| Decommission cost | 100 million yen |

**Table.3 Project period of wind power plants**

| Period (total 19 years) | Incoming | Outgoing |
|---|---|---|
| Construction (1st year ) | Subsidies | Construction |
| Operation (2nd ~18th year) | Electricity selling | Debt service<br>Maintenance<br>Labor |
| Decommission (19th year) | | Decommission |

# 4. Results

### 4.1 Evaluation of model reliability

To evaluate the reliability of the model, simulated values of the model were compared with three operational results such as Suttsu town, Tomamae-town and Jyoetsu-city. Suttsu-town case is a one profitable case. While, Jyoetsu-city case is an unprofitable one. Tomamae town is break even case. The results are shown in Fig.1.

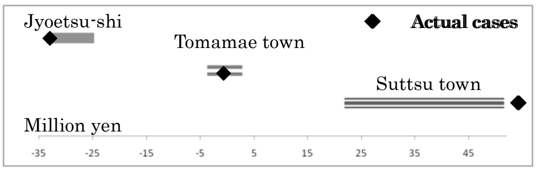


**Fig.1 a range of simulated annual profit**

Although Suttsu-town actual result was more profitable than a range of simulated values, the simulated results and actual cases are always same order of magnitude. It was confirmed that the model can simulate both success case and failure case.

### 4.2 Evaluation in condition of risk

The present study simulated the profitability by categorized risk factors, output size, locations and local region. Output size is categorized as large (1,000kW-), middle (500-1,000kW) and small (-500kW). Location is categorized as coastal area and inland area. Aomori prefecture and Koushinetsu area were chosen as local region. As a result, large wind power plants are more profitable than small plants. Especially, the fact that the maintenance cost rate of the small plants always supposed to be higher than the large ones was demonstrated. (Fig.2)

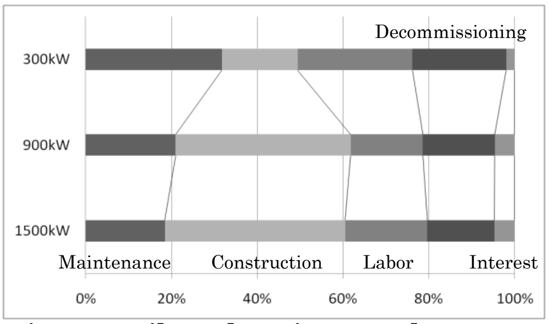


**Fig.2 Detail total project cost by output size.**

The present study cannot confirm the difference of profitability of locations and local region.

### 4.3 Evaluation of maintenance costs

The plants operating more than one turbine will reduce deficient risks because single wind turbine plants cannot earn revenues when an accident occurred. The simulation revealed relationship between numbers of turbines and the profitability. As a consequence, the more numbers of turbines are, the more profitable wind power plants are. Four 900kW turbines should be constructed at least with Probability to gain positive profit over 90%.

Longer downtime will also be supposed to be a critical issue of the operation. The simulation revealed relationship between downtime per accident and the profitability. (Fig.4)

The simulation supposed that every accident interval to recovery is constant. Horizontal axis indicates the numbers of days to recovery. Vertical axis indicates the probability of annual benefit in surplus. If downtime is longer than 3 months, eight 900kW turbines should be constructed to earn profit with probability over 90%.

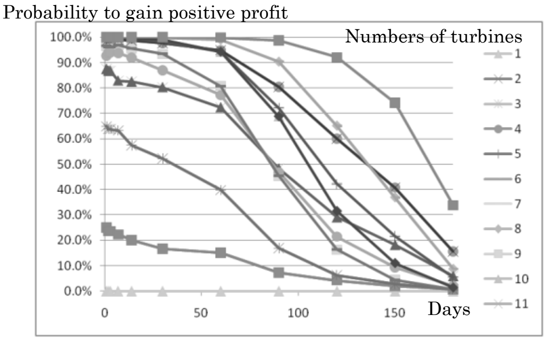


**Fig.4 Relationship between downtime and the Probability to gain positive profit.**

Package contract is a maintenance contract adapted by Suttsu-town case, which pay average maintenance cost annually. This contract is beneficial because maintenance cost is always constant regardless of the numbers of accident. Maintenance companies are given an incentive for short recovery time. Commonly, package contract determine upper limit of recovery time with backup fee. The simulation revealed an advantage of the package contract. The simulation supposed that every downtime is two days and maintenance cost replace average maintenance cost. As a result, Package contract increase about 105 thousand yen of average annual profit and 3% of the Probability to gain positive profit.

### 4.4 Sensitivity analysis

In the present study, cost parameters are qualitatively determined by hearing research and case studies. It remains possible that the model cannot simulate correct impact of the maintenance cost. Thus sensitivity analysis was implemented by changing recovery cost per accident (Fig.5).

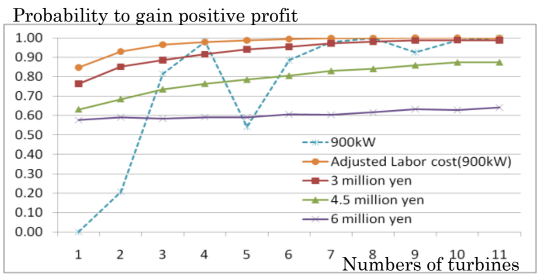


**Fig.5 Profitability impact of recovery cost**

As a result, the profitability is decreased with an increase in recovery cost.

## 5. Conclusions

The present study simulated profit and loss of wind power plants considering failure risks. The following conclusions were confirmed.

(a) Large wind power plants are more profitable than small ones. It was proven that small plants' maintenance cost has a higher rate than the large ones.
(b) When downtime is always longer than 3 months, eight 900kW turbines are necessary at least to earn profit with probability over 90%.
(c) Package contract can increase about 105 thousand yen of average annual profit and 3% of the Probability to gain positive profit respectively.

The results suggests that local governments are required several wind turbines of mega watt class at least to earn profit stably. In addition, long downtime more than several months reduces the profitability at impermissible level. Small wind power plants have great risk to gain profit. Those local governments that are operating wind power plants can need to have both adequate number and size of the plants as well as suitable maintenance system; otherwise they may need to consider shutting down their plants to minimize the loses.

## References

[1] D. Milborrow, ECONOMICS OF WIND POWER AND COMPARISON, Renewable Energy, Volume 5, pp.692-699, 1994

[2] M. G. Khalfallah, Aboelyazied M. Koliub, Suggestions for improving wind turbines power curves, The Ninth Arab International Conference on Solar Energy, 2007

[3] NEDO, *Huuryoku Kaihatsu Field test* (Field test for wind energy development, the research of wind speed), 2000

[4] N. Abe. Y. Sato, "Survival Analysis of Wind Power Plants", Journal of JWEA, vol.92, pp-98-103, 2009

[5] METI Hokkaido, *Hokkaido ni okeru Huuryoku Hatsuden no Genjyo to Kadai* (Current situation and issue of wind power in Hokkaido), 2004 -2008.

[6]NEDO, *Huuryoku Hatsuden Riyouritsu Koujyou Iinkai oyobi Koshou Jiko tou Chousa Iinkai* (upgrading availability of wind power council and research report of the accident), 2004-2008

# Adhesion between elastic beam and rigid body

Student Number：09M18054　Name：Yu SEKIGUCHI　Supervisor：Kunio TAKAHASHI

# 弾性梁と剛体の間に働く凝着力

関口 悠

弾性梁側面が剛体に凝着する際に、弾性梁に働く凝着力を理論的に求め、実験により検証した。弾性梁の剛体への接触を線接触と面接触の二つに分け、弾性梁の変形と系全体のエネルギーを考慮することで、弾性梁に働く力を求めた。また凝着力が凝着仕事に関するパラメータにより変化することを示した。静的条件と動的条件を仮定した実験を行い、理論に沿う結果を得るとともに、理論に沿わない範囲における原因について考察をした。

## 1. Introduction

Adhesion is used by some insects like gecko to grip and climb walls or move on ceiling. Gecko has a lot of micro-nano-hair on its foot, which are called seta and spatula. These micro-nano-hairs enable the gecko to grip surface in order for the hairs to adhere to the surface [1]. The hairs deform to adhere to the surface even if it has some surface roughness. And also they can be detached from the surface easily because of the hairs' structural feature.

An elastic beam with an adhesive tip is used to express a mechanism of gecko's foot hair [2]. This model has a limited adhesive area. Gecko's foot hair is also assumed to be a tape and Kendall's theory of thin-film peeling [3] is used to express the adhesion mechanism [4].This theory considers the change of the adhered area but not the deformation of the hair.

In the present study, an elastic beam, which has adhesive beam side, is assumed. Therefore both the flexible adhered area and the deformation are considered. The adhesion force between the elastic beam and a rigid body is obtained theoretically and experimentally.

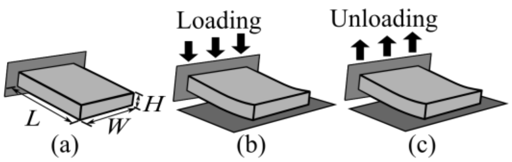


Fig.1 Schematic illustration of the elastic beam

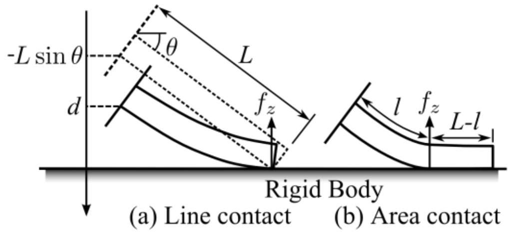


Fig.2 Model of adhesion between the elastic beam and rigid body.

## 2. Model

Figure 1 shows a model of adhesion between an elastic beam and a rigid body considered in this study. The elastic cantilever beam, which has the dimension of length $L$, thickness $H$ and width $W$, contacts to the rigid body at angle $\theta$ (see Fig.2).

When approaching the rigid body, the elastic beam firstly contacts to the rigid body at the edge of the elastic beam. This contact is called line contact. In loading process, the rigid body presses the edge and the elastic beam starts deforming. Consequently, the side surface of the elastic beam adheres to the rigid body. This contact is called area contact. During unloading process, the adhered area keeps decreasing until the separation occurs.

## 3. Force between elastic beam and rigid body

When the elastic beam contacts to the rigid body, the force occurs between the elastic beam and the rigid body. As for the calculation, $x$-$y$ axis is fixed as shown in Fig. 3. The force is applied to the elastic beam with the strength, $-f_z \cos\theta$, in $y$-direction. The force and the deformation in $x$-direction are considered as negligibly small. The deformation in $y$-direction is considered as small enough to neglect the effect of bending for the moment. The force is considered as concentrated load at $x=L$ for line contact and at $x=l$ for area contact.

### 3.1 Line Contact

At line contact, shear force and moment are considered to obtain the deformation of the beam at $x=L$. By considering the relation among the displacement, the deformation and the length, the force is obtained as

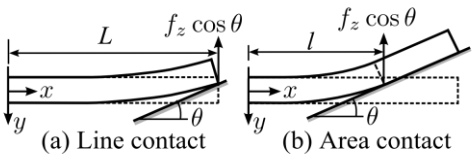


Fig.3 Deformation of the elastic beam.

$$\tilde{f}_z \frac{\cos^2\theta}{\sin\theta} = \frac{1}{4}\left(\frac{\tilde{d}}{\sin\theta} + 1\right), \tag{1}$$

where the force and the displacement are normalized as $\tilde{f}_z = f_z/(12EI/L^2)$ and $\tilde{d} = d/L$.

The contact changes into area contact when the gradient of the elastic beam at $x$=$L$ becomes equal to that of the rigid body (i.e. $\tilde{d}/\sin\theta = -1/3$).

## 3.2 Area Contact

At area contact, the force occurs at $x$=$l$ and the elastic beam for $l$<$x$<$L$ adheres to the rigid body. Therefore shear force and moment for this range is considered as 0. As the same manner with the line contact, the deformation at $x$=$l$ is obtained and the force is expressed as

$$\tilde{f}_z = \frac{\sin\theta}{\tilde{l}^3\cos^2\theta}\left(\frac{\tilde{d}}{\sin\theta} + \frac{\tilde{l}}{2}\right), \tag{2}$$

where the length is normalized as $\tilde{l} = l/L$.

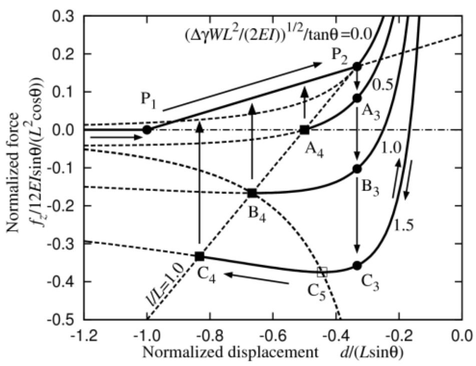


Fig.4 Relation between force and displacement.

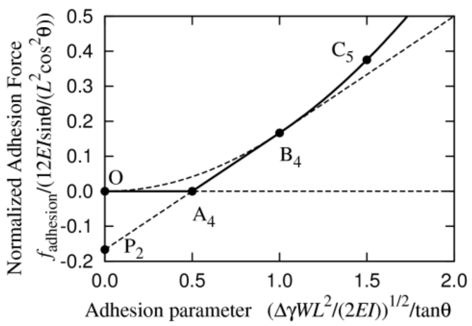


Fig.5 Relation between adhesion force and adhesion parameter.

The adhered area is equilibrium at the lowest energy condition. Therefore the total energy is considered to obtain the stable length $\tilde{l}$. Total energy can be expressed as a sum of the elastic energy and the loss in surface energy. From the minimal point of the total energy, the stable length is obtained and the force is expressed as

$$\tilde{f}_z \frac{\cos^2\theta}{\sin\theta} = \frac{8\left(\dfrac{\sqrt{3\Delta\tilde{\gamma}\tilde{W}}}{\tan\theta}\right)^3 \dfrac{\tilde{d}}{\sin\theta}}{\left(\sqrt{1 - 12\dfrac{\sqrt{3\Delta\tilde{\gamma}\tilde{W}}}{\tan\theta}\dfrac{\tilde{d}}{\sin\theta}} - 1\right)^3} + \frac{2\left(\dfrac{\sqrt{3\Delta\tilde{\gamma}\tilde{W}}}{\tan\theta}\right)^2}{\left(\sqrt{1 - 12\dfrac{\sqrt{3\Delta\tilde{\gamma}\tilde{W}}}{\tan\theta}\dfrac{\tilde{d}}{\sin\theta}} - 1\right)^2} \tag{3}$$

for $\sqrt{3\Delta\tilde{\gamma}\tilde{W}}/\tan\theta > 0$ and

$$\tilde{f}_z \frac{\cos^2\theta}{\sin\theta} = \frac{1}{54\left(\dfrac{\tilde{d}}{\sin\theta}\right)^2} \tag{4}$$

for $\sqrt{3\Delta\tilde{\gamma}\tilde{W}}/\tan\theta = 0$, where $\Delta\gamma$ is the work of adhesion, which is required to separate a unit area of adhered surfaces. $\Delta\gamma$ and $W$ are normalized as $\Delta\tilde{\gamma} = \Delta\gamma/(6EI/L^3)$ and $\tilde{W} = W/L$.

## 4. Adhesion Force

The relation between the force and the displacement is shown in Fig. 4. During the loading process, the force moves from $P_1$ to $P_2$. At $P_2$, the contact changes into area contact. During the unloading process, the force moves following the curve $A_3A_4$ ($B_3B_4$ or $C_3C_4$). The curve $A_3A_4$, $B_3B_4$ and $C_3C_4$ are plotted with different $\Delta\gamma$.

The adhesion force is the minimal force, i.e. the maximum tensile force. Therefore it is obtained as

$$\tilde{f}_{\text{adhesion}} \frac{\cos^2\theta}{\sin\theta} = \frac{1}{6}\left(\frac{\sqrt{3\Delta\tilde{\gamma}\tilde{W}}}{\tan\theta}\right)^2 \tag{5}$$

for $\sqrt{3\Delta\tilde{\gamma}\tilde{W}}/\tan\theta > 1$,

$$\tilde{f}_{\text{adhesion}} \frac{\cos^2\theta}{\sin\theta} = \frac{\sqrt{3\Delta\tilde{\gamma}\tilde{W}}}{3\tan\theta} - \frac{1}{6} \tag{6}$$

for $0.5 < \sqrt{3\Delta\tilde{\gamma}\tilde{W}}/\tan\theta < 1$

and 0 for $\sqrt{3\Delta\tilde{\gamma}\tilde{W}}/\tan\theta < 0.5$.

The relation between adhesion force and the adhesion parameter is plotted in Fig.5.

## 5. Experiment

Experiments to measure the force between the elastic beam and the rigid body were carried out by controlling the displacement using the equipments as shown in Fig.6. Two experiments, dynamic condition and static condition, were considered. In the theory, the static condition is assumed. But the dynamic condition has to be discussed for the applications. Therefore, both conditions were considered. As for the elastic beam, shock absorbing gel and silicone rubber were used. As for the rigid body, aluminum alloy with polished surface and glass plat were used. To minimize the effect of friction between the elastic beam and the rigid body, steal balls were set under the rigid body. In the experiment, the force, which was measured using electric scale, was considered as the concentrated force $f_z$ in Fig. 2. Young's modulus of Gel and Silicone rubber were measured using tensile testing machine for the elastic range and obtained as 1.3*10$^5$[Pa] and 2.9*10$^5$[Pa]. Results of the dynamic condition are shown in Figs. 7 and 8. Those of the static condition are shown in Fig. 9.

Under the dynamic condition, the results partially predicted the theory (Fig. 7(a) and (b), Fig. 8(a) and (b)). But also some differences exited as well. One of them was observed at the initial unloading part. In the first part of the unloading process, the adhered area was constant whereas it decreases theoretically. Another difference is observed at the releasing part. Theoretically releasing occurs when the adhered area becomes zero. But experimentally it occurred before it

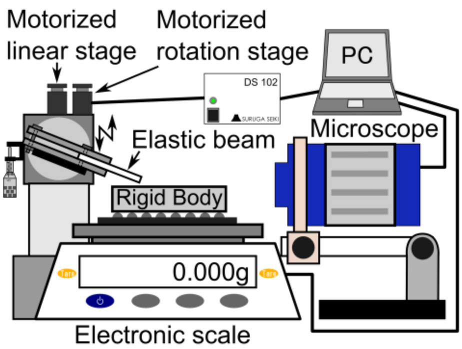


Fig.6 Equipments for the experiment.

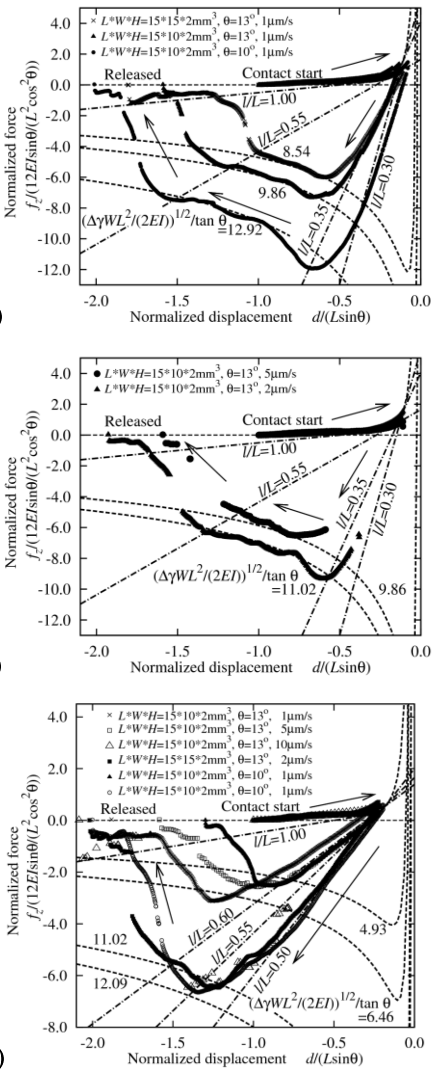


(a)

(b)

(c)

Fig.7 Experimental results under the dynamic condition using gel.

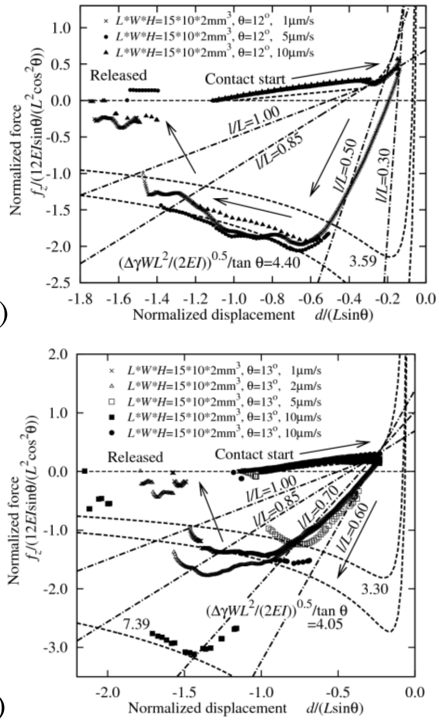


(a)

(b)

Fig.8 Experimental results under the dynamic condition using rubber.

became zero. It is considered that the assumption of elastic beam is one of the reasons. Three dimensional effect or the effect of large deformation would exist. Therefore other mechanisms for the initial unloading part and the releasing part were suggested in the experiment.

Figure 7 (c) shows the different result of dynamic condition using gel. In this figure, the force was changed as V-shape. This change was caused by the difference of the initial unloading part. With large non-adhered length $\tilde{l}$ (i. e. small adhered area), the force was changed like V-shape. This large length was related to the displacement at the start point of the unloading process. With smaller displacement, the larger length was obtained.

Figure 8 shows the result of dynamic condition

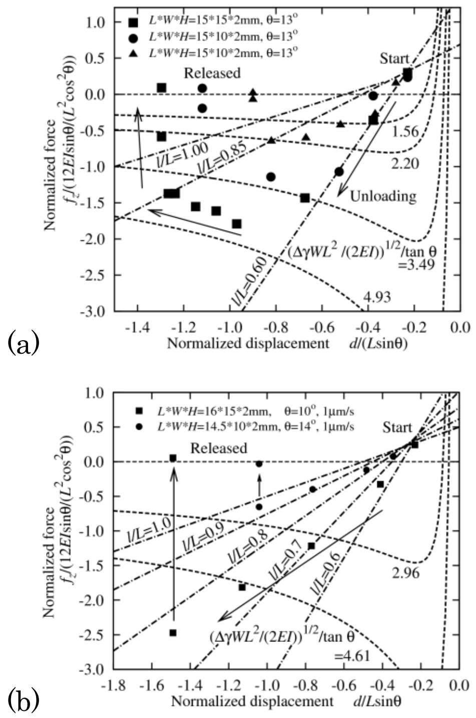


Fig.9 Experimental results under the static condition using (a)gel and (b) rubber.

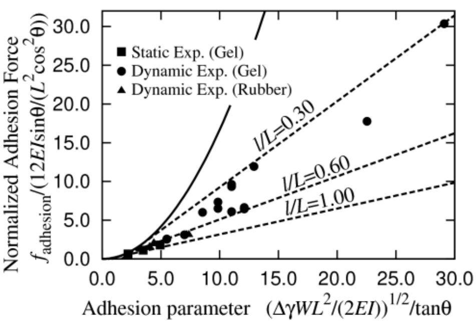


Fig.10 Experimental results of the adhesion force.

using silicone rubber. The change of the force was almost same as the one using gel. But at initial unloading part and at releasing part, there are some differences. At initial unloading part, the length changed whereas it was constant with the results using gel. At releasing part, the releasing occurred with smaller adhered area than that using gel. These differences are considered to be caused by the material properties.

Under the static condition, the same tendency as the dynamic condition was observed. But the work of adhesion $\Delta\gamma$ was different from that of the dynamic condition. At the dynamic condition, $\Delta\gamma$ was larger. Also there were differences between gel and silicone rubber. This is considered to be caused by the material properties.

The maximum force at each experiment is plotted in Fig. 10 against the adhesion parameter. Because $\tilde{l}$ is constant at the first part of the unloading process, the maximum tensile force observed near the cross point of the theoretical force curve and the line of the constant $\tilde{l}$ . Therefore the result doesn't follow the theoretical adhesion force curve. Instead, it almost follows the adhesion force which expresses the force at the cross point and includes the constant non-adhered length $\tilde{l}_{\text{const.}}$. It can be expressed as

$$\tilde{f}_{\text{adhesion}}\frac{\cos^2\theta}{\sin\theta} = \frac{\sqrt{3\Delta\tilde{\gamma}\tilde{W}}}{3\tilde{l}_{\text{const.}}\tan\theta} - \frac{1}{6\tilde{l}_{\text{const.}}^2} \tag{7}$$

and this is shown as the broken line in Fig.10.

## 6. Conclusion

The model of the adhesion between the elastic beam and the rigid body is proposed to obtain the adhesion force theoretically. The line contact and the area contact are introduced to obtain the relation between the force and the displacement. Experiments to verify the relation between the force and the displacement were carried out and the results partially predicted the theory. The different mechanisms were suggested at the initial unloading part and the releasing part.

*References*


[1] K. Autumn, et al., *Nature*, **405**, 681-685, 2000

[2] K.Takahashi, et al., *J. adhesion adhesive*, **26**, 639-643, 2006

[3]K.Kendall, *J. Phys. D : Appl. Phys.*, **8**, 1449-1452, 1975

[4] N. S. Pesika, et al., *J. Adhesion*, **83**, 383-401, 2007

# System to make teaching materials based on collective intelligence

Student number : 09M18060 Name : Yuhei Negishi Supervisor : Yukihiko Yamashita

# 集合知に基づく教材作成システム

根岸 侑平

教育の不均衡の問題を解消するため，e ラーニングの重要性が増している。しかしながら，e ラーニング教材の作成にコストがかかるという問題を抱えている。tobe システムは教材をテキストベースで記述することで教材作成コストを削減したが，XML の知識が必要なため容易に作成できない。また，教材を他のクリエイタと共同で作成することができず，１人あたりの作業負荷が大きい。一方，Wikipedia に代表される Wiki は世界中の多数の人々が参加することによって 1 人当たりの作業負荷を抑え，広範囲の情報を持続的に提供している。本研究では tobe システムに集合知の概念を取り入れ，ネットワーク上で多数の人々が XML の知識を使わずに１つの教材の作成に参加することを可能にするシステムの構築を行う。

## 1. Introduction

After 1990, due to the innovations of Information Technology, utilization of equipments like PC has become widespread among general households.

Then nowadays, according to development of the Internet and WWW, we can exchange information regardless of time and place. And utilization of e-Learning system gives a chance to everyone to learn by using PC anytime and anywhere. However the problem is that to make teaching materials for e-Learning, not only teaching methodology skill but also IT skill are necessary. Furthermore, correction and modification of materials are difficult. Therefore, making materials costs very much. On the other hand, Wiki systems give an opportunity to people around the world to exchange their information. According to Wiki philosophy, applying Wiki does not need any especial skill, and making materials by a group is possible. However, Wikis are static pages, thus Wikis cannot be an effective learning system.

Then in this research, I propose a new system, combining the tobe (Text Oriented Bi-Stream Explanation) system and Wiki system. The tobe system is a text-base learning system that makes animation from tobeML (XML based markup language) document. Then, its combination with Wiki enables to create a tobeML document easily by a group via a network.

## 2. e-Learning

Electronic Learning (e-Learning) [1] is a type of technology supported education. E-Learning is used interchangeably in a wide variety of contexts. In companies, it refers to the strategies that use the company network to deliver training courses to employees. Lately in some universities, e-Learning is used to define a specific mode to attend a course or programs of study where the students rarely attend face-to-face for on-campus access to educational facilities.

## 3. tobe system

The tobe system [2] is a system to

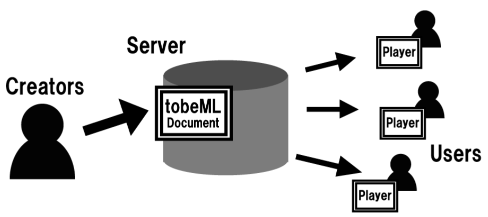


Fig-1 tobe System

change the text-base data to animation for e-learning (Fig-1). In the tobe system, the program named “Expositor” does this conversion. In this system all the data are written in text, therefore the cost of make teaching materials has been reduced. Expositor makes a situation similar to real classroom on the PC screen. Expositor just can read the text which is written in the tobeML language defined originally for this system.

When a learner runs Expositor, a window (Fig-2) appears on the screen. As you can see in Fig.2, the tobe system includes three main parts, a board, a professor with pointer, and a talk part (the part that professor explains by voice).

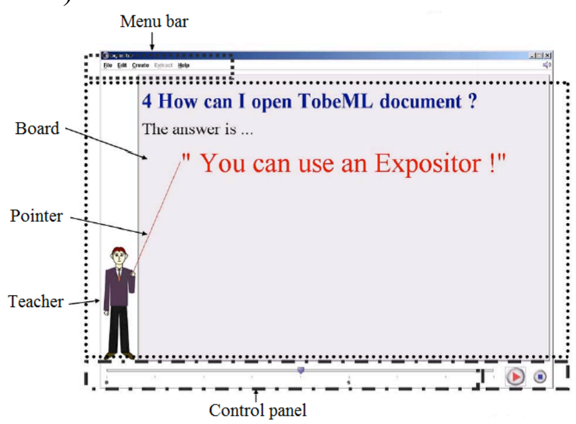


Fig-2 Expositor

## 4. Collective intelligence

Collective intelligence (CI) [3] is a shared or group intelligence that emerges from the collaboration and competition of many individuals. CI can also be defined as a form of networking enabled by the rise of communications technology, namely the Internet. Web 2.0 has enabled interactivity and thus, users are able to generate their own contents. CI draws on this to enhance the social pool of existing knowledge. Communication tools enable humans to interact, share, and collaborate with both ease and speed. With the development of the Internet and its widespread use, the opportunity to contribute to community-based knowledge forums, such as Wiki systems becomes possible.

### 4.1 Wiki

Wiki [4] comes from a Hawaiian word “WikiWiki” for "fast". A wiki is a web page or collection of web pages designed to enable anyone who accesses it to contribute or modify the content using a simplified markup language. Wikis are often used to create collaborative websites and to power community websites. The collaborative encyclopedia Wikipedia is one of the best-known wikis. Wikis are used in business to provide networks and knowledge management systems. Ward Cunningham, the developer of the first wiki software, Wiki-Wiki Web, originally described it as "the simplest online database that could possibly works". Wiki is a piece of server software that allows users to freely create and edit Web page content using any Web browser. And Wikis have simple text syntax for creating new pages.

## 5. tobe system 2.0

The tobe system enabled to make teaching materials based on text and reduced the cost of making teaching materials. But to make the tobeML documents, the knowledge of XML is necessary. Therefore making teaching materials is a bit difficult.

So I propose the tobe system 2.0. The tobe system 2.0 is the tobe system based on CI. In this system, creators can edit the tobeML documents without the knowledge of XML using the tobeML

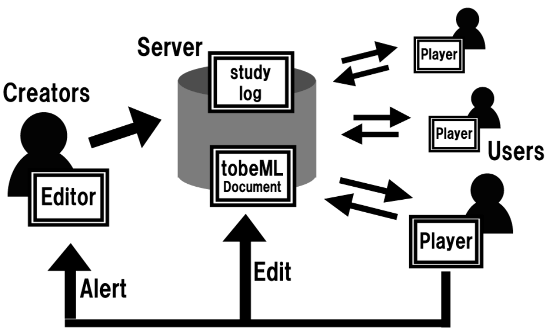


Fig-3 tobe system 2.0

editor. Also, they can edit one tobeML document in corporate with other creators. Fig.3 illustrates the tobe system 2.0.

### 5.2 tobeML editor

The tobeML editor will enable to make teaching materials without the knowledge of XML. Furthermore, many people can edit a teaching material because the editor can be used on the web. The tobeML editor is composed of two parts: the board part and the talk part.

The board part is to edit the contents of the board. To describe the board part, the editor has two modes. One is the explanation mode, and the other is the question mode.

The explanation mode (Fig-5) is to describe the explanation. Creators can set the font size or color, and layout of text or images easily. The question mode (Fig-6) is to describe the question. When creators describe the question and its choices, tobeML text is generated automatically.

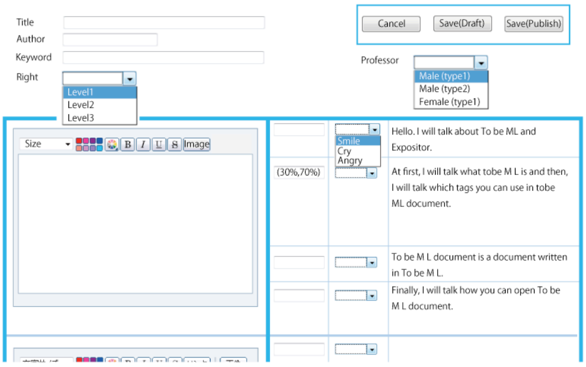


Fig-4 tobeML editor

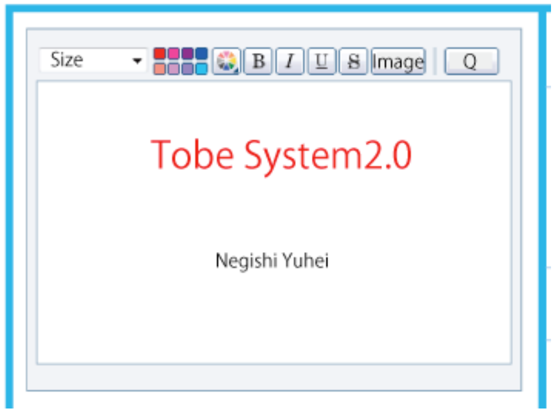


Fig-5 Explanation mode

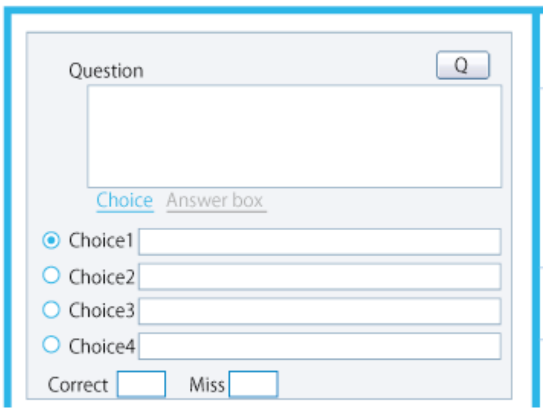


Fig-6 Question mode

The talk part is to describe the talk and action of the professor and the coordinate of his pointer.

Creators can determine the professor's action by choosing from the pull down menu (Fig-7), and the coordinate of his pointer by clicking the point of the board (Fig-8).

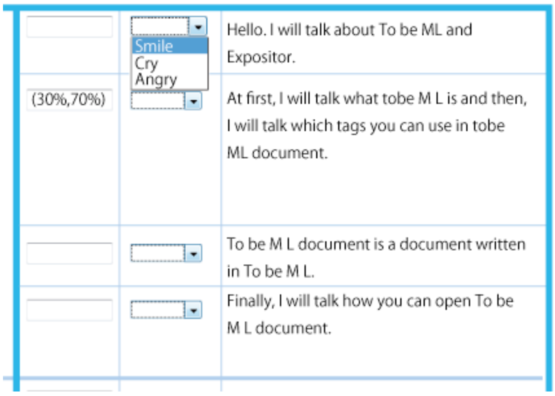


Fig-7 Selecting action

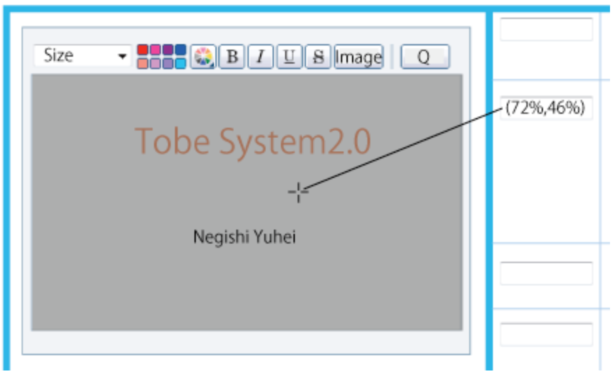


Fig-8 Selecting the coordinate of the pointer

## 6. Experiment

To evaluate the tobeML editor, I conducted an experiment. I compared the time for the subjects to describe a tobeML document using the tobeML editor and using only a text editor. Fig-9 shows the teaching material to be described.

Table-2 shows the result of this experiment. Using the tobeML editor, the time to create tobeML documents was reduced.

Table-2 Result of experiment

| tobeML editor | Averaged time |
|---|---|
| Use | 238.8 sec |
| Not use | 538.2 sec |

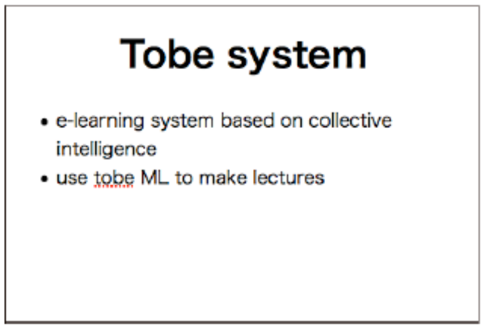


(Smile and say) Today, I'll introduce to be system. (Point at (10.15, 41.23) and say) To be system is (Point at (10.15, 41.23) and say) To be system is an e-learning system based on collective intelligence. Everyone can make its contents. (Point at (10.15, 61.53) and say) To make

Fig-9 Teaching material for experiment

## 7. Conclusion

In this research, I proposed the tobe system 2.0 to make teaching materials using CI. Also I developed the tobeML editor and conducted an experiment to prove that creators can edit tobeML document easily using the developed tobeML editor.

As future works, I have to improve the interface of tobeML editor for creators to use it more effectively, and develop the expositor which corresponds to tobeML 2.0.

## References

[1] What is e-Learning, http://satt.jp/tech/e-learning.htm. (in Japanese)

[2] Shoko Tobe: Explanation markup language based on XML and the expositor (Master thesis, Tokyo Institute of technology, in Japanese)

[3] Wikipeida: http://en.wikipedia.org/wiki/

[4] e-words: wiki, http://e-words.jp/w/Wiki.html

# THE CHARACTERISTICS OF RAINFALL IN TOKYO WITH DETAILED URBAN GEOMETRIC DATA

Student Number: 09M18077 Name: Eriko FUKUMOTO Supervisor: Manabu KANDA

詳細な都市幾何形状を考慮した東京都における降雨特性の把握

福本恵梨子

本論文の目的は東京都における①都市幾何形状の変遷の把握，②夏季における雨量の空間偏差の把握，および③上記①②の因果関係の把握である．詳細な 3 次元幾何形状データベースより，東京都心部における幾何形状がここ十数年で顕著に変化したことを示した．また，9 年間の雨量データからは，夏季における雨量の空間偏差が 23 区内で増加したことを示した．空間解像度の高い雨量データからは，これまで明らかにされていなかった 23 区中心部での正の空間偏差を指摘し，都市化や海風収束との因果関係を示唆した．

## 1. Introduction

In cities, unusual weather, such as localized heavy rain, has become a serious problem. Urbanization is thought to be one of the causes for this unusual weather. Past studies have shown that urban cities indeed have some kind of an effect to the characteristics of precipitation. Fujibe [1] used AMeDAS data from 1979 to 1994 to show that positive anomaly of rainfall frequency lays in the urban central area. In addition, the possibility of urban buildings causing upward flow, enhancing the heavy rainfall was presented [2]. Moreover, a numerical simulation supported the effects of urban configuration on localized heavy rainfall [3].

Due to the economic change and new land policy at around year 2000, Tokyo Metropolis has undergone a major transformation. The construction of high-rise buildings accelerated in the central urban area complicating the city’s land surface. It is extremely crucial to clarify this transition and its effects on localized heavy rain. Although urbanization includes other factors, such as anthropogenic heat, the very basis of them is the urban structure, and was the main focus in this research.

The objectives of this study were: 1) to observe the transition of urban geometry, 2) to observe the spatial anomaly of rainfall during summer, and 3) to find some relationship between 1) and 2). The greatest strength of this research is analyzing data that has not been considered that much, until now, which could lead to the possible causes of localized heavy rain.

## 2. Transition of Urban Geometric Parameters

The change in surface geometry was discussed in terms of data obtained from a 3-dimensional urban geometric database for years 1996, 2001, and 2009. Data for 1996 were based on data sources of the Land Use Survey Results from the Bureau of Urban Development and data for 2001 and 2009 were made by CAD Center Corp. Validation was done to prove that comparing the two different sources is acceptable. Using these sources, building height $H$ was averaged for a mesh of 1/360° and other parameters, such as displacement height $d$, were calculated. $d$ represents a virtual surface due to buildings and was calculated based on Macdonald et al. [4], where

$$\frac{d}{H} = 1 + A^{-\lambda_p}(\lambda_p - 1) \quad (1)$$

and $A$ (= 4.43) is a constant. Affective elevation was defined by adding $d$ to the actual elevation. This affective elevation incorporates the urban effects and was used throughout this research.

The difference between results from 1996 to 2009 for $d$ is shown in Fig. 1. Figures for the other parameters are not shown here. However, all values showed positive difference in the urban central areas such as in Chuo ward, near Shinjuku station, and along the bay. This clearly shows the accelerated growth of high-rise buildings in the urban central area and not throughout the Tokyo Metropolis.

The actual elevation in the east side of the 23 wards showed values of less than 4 m, as in Fig. 2; whereas in the west area the values are larger up to 50 m. When $d$ was added to this (Fig. 3), affective elevation at the central areas increased. However, the elevation gap in the middle of the 23 wards remained.

## 3. Spatial Anomaly of Rainfall

The information on the amount of rainfall was obtained from point precipitation data measured by the River Bureau and from Radar Rainfall Information System called Amesh managed by the Bureau of Sewerage. Compared to the 10 observation points of AMeDAS, the River Department has 118 observation points and Amesh has a spatial resolution of 250 m. All rainfall data are shown in the form of anomaly calculated from the mean annual/daily cumulative amount of rainfall from 12:00 to 24:00 during summer time.

### 3.1. Transition of Rainfall Anomaly

The transition of the rainfall characteristics was observed by dividing the 9-year data from the River Department into first and second halves (Fig. 4). In the first half there was a relatively clear division between positive and negative anomaly at the middle of the Tokyo Metropolis. Meanwhile, in the second half the border became unclear and positive anomaly increased in the 23 wards. The possible causes of this transition will be discussed further on.

### 3.2. Rainfall Anomaly with High Spatial Resolution

It is crucially important to use Amesh data to see the spatial anomaly at areas where River Department data could not cover due to its sparse distribution. The spatial anomaly for all rainfall events in 2008, shown in Fig. 8, displayed negative anomaly along the shore and positive anomaly in the western side. In addition, strong positive anomaly at the center of the 23 wards and also in Setagaya ward was observed.

### 3.3. Spatial Anomaly of Localized Heavy Rainfall

The extraction conditions of localized heavy rain were based on Shimoju et al. [3]: 1) hourly precipitation exceeds 15 mm within the 23 wards, 2) maximum temperature exceeds 30 degree-C, 3) starting time of strong rain is between 12:00 and 21:00, 4) end time of strong rain is before 24:00, and 5) are not affected by synoptic weather according to weather maps and weather satellites.

Using the River Department data localized heavy rainfall days within the 9 years were analyzed (Fig. 5). The northwest area of the 23 wards obviously had large positive anomaly. It is where localized heavy rain events are commonly featured by the media and corresponds with the area where positive anomaly increased in Fig. 4.

The spatial anomaly of localized heavy rainfall events in 2008 to 2010 was obtained by using the new Amesh data (Fig. 9).There was strong positive anomaly in Nerima ward and negative anomaly along the shore and in the old town area, which agrees with the other results formerly presented.

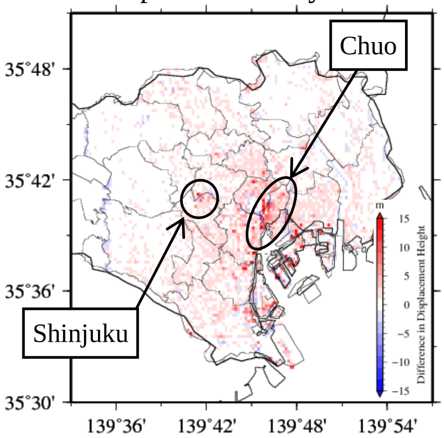


Figure 1: Change in Displacement Height

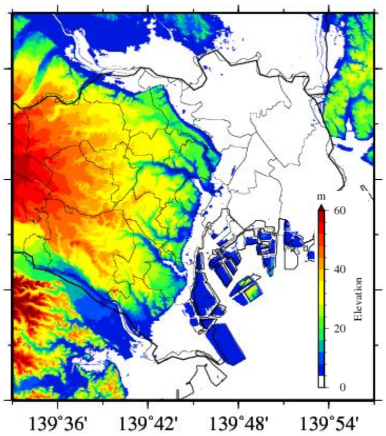


Figure 2: Elevation

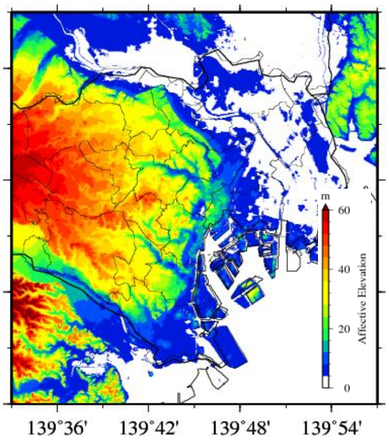


Figure 3: Affective Elevation for 2009

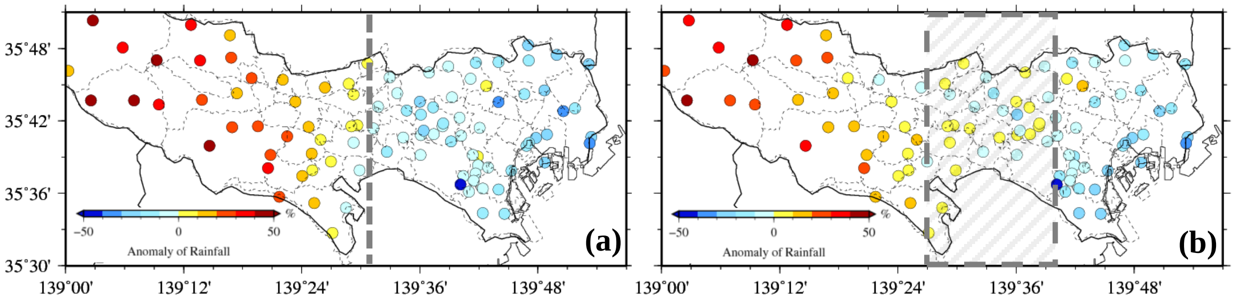


Figure 4: Transition of the Anomaly of Rainfall; (a) 2000-2003 and (b) 2004-2008

However, Suginami ward was covered with negative anomaly, which was not apparent until now.

# 4. Relationship Between Urbanization and Rainfall Distribution

The spatial anomaly of rainfall was compared with affective elevation and other urban characteristics.

## 4.1. Affective Elevation and Anomaly of Rainfall from the River Department

As shown in Fig. 6, an exponential curve approximated the relationship between rainfall anomaly and affective elevation for the first and second half of the whole Tokyo Metropolis, which implies that the higher the affective elevation the more positive the anomaly of rainfall. The slope became steeper in the second half, which corresponds with Fig.4, where the positive anomalies decreased in high-elevation regions and increased in low-elevated urban areas.

Next, the same operation was done for the results of only the 23 wards (Fig.7) in addition with the anomaly of localized heavy rainfall. No curve was found to fit well with the distribution. However, there was a clear gap at around 10 to 20 m high, which divided the rainfall characteristic into two types: positive anomaly at high affective elevation and negative anomaly at low affective elevation. The variability of the anomaly of localized heavy rainfall was larger than normal rainfalls, which designates the complexity of localized heavy rain.

## 4.2. Affective Elevation and Anomaly of Rainfall from Amesh

Dependency on the elevation gap at around 10 to 20 m high was observed for the anomaly of all rainfall days in 2008 (Fig. 8 (a)) as well, where positive anomalies in the western and central areas were located at the high affective elevation region.

For the anomaly of localized heavy rainfalls in years 2008 to 2010, an obvious relationship with affective elevation was not found (Fig.9). However, the positive anomaly in Nerima ward was located in the leeward region of where affective elevation increased drastically (red circle). This could be due to the convergense of sea breeze at the leeward region of increased *d* enforcing the amount of rainfall. This mechanism has been observed through numerical simulation as well [3].

## 4.3. Urban Characteristics and Anomaly of Rainfall

Fig. 8 (b) showed several interesting facts when compared with other urban affects. First, the strong positive anomaly in the center of the 23 wards fitted right inside the Yamanote Line railway (red line). This is due to the extreme increase in urban geometric parameters at the area below, causing this area to become a stagnant zone of sea breeze. Next, positive anomaly in the southern area seemed to lie at the region circled in green, where Kampachi clouds frequently form [5].

One definite fact which can be said in comparison with urban geometric parameters is that large positive anomaly did not occur where average building height or displacement height increased.

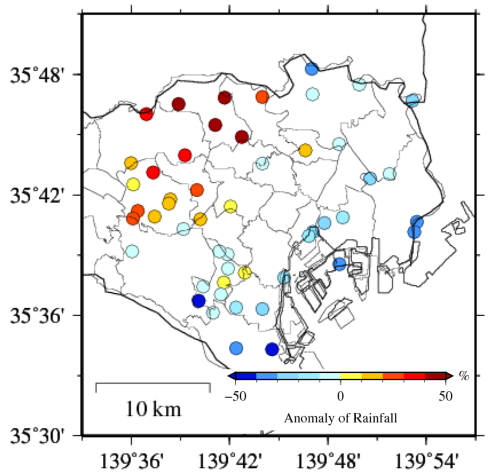


Figure 5: Spatial Distribution of Localized Heavy Rainfall Anomaly

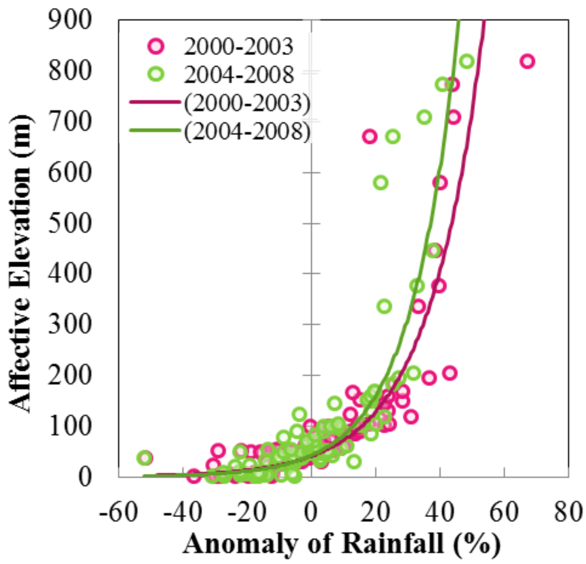


Figure 6: Relationship between Anomaly and Affective Elevation (Tokyo Metropolis)

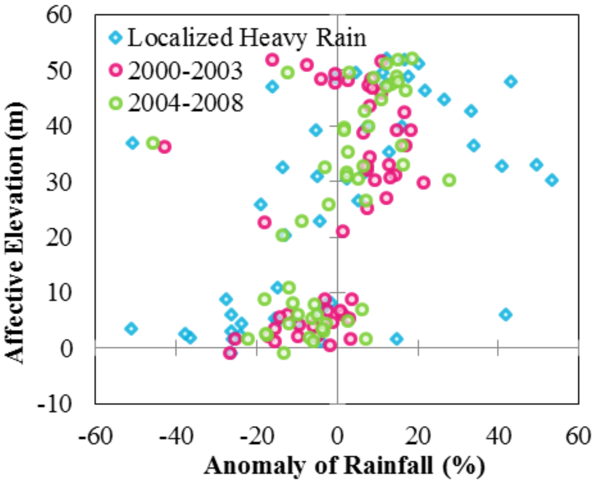


Figure 7: Relationship between Anomaly and Affective Elevation (23 Wards)

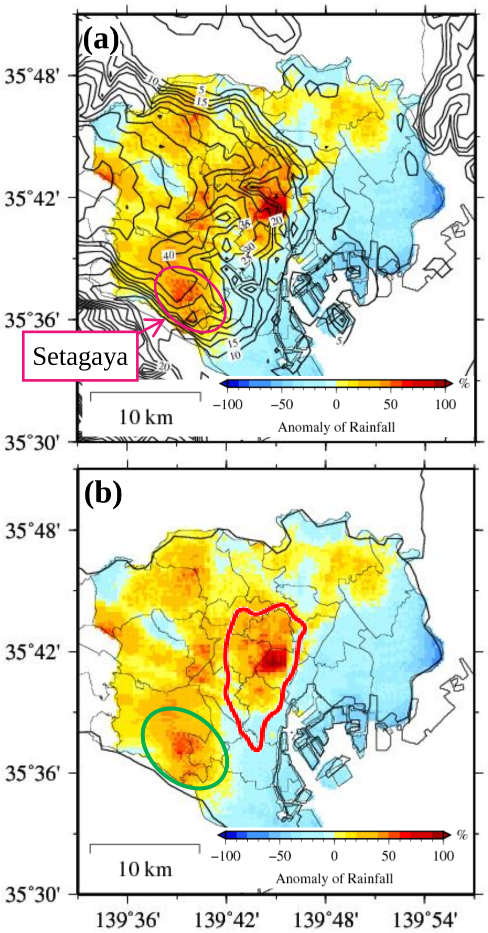


Figure 8: Spatial Anomaly of Rainfall with (a) Affective Elevation and (b) Urban Characteristics

## 5. Conclusion

1) The urban geometry of Tokyo Metropolis changed drastically from 1996 to 2009.
2) The "affective elevation" increased at the central areas of the 23 wards, resulting into an elevation gap between the east and west regions.

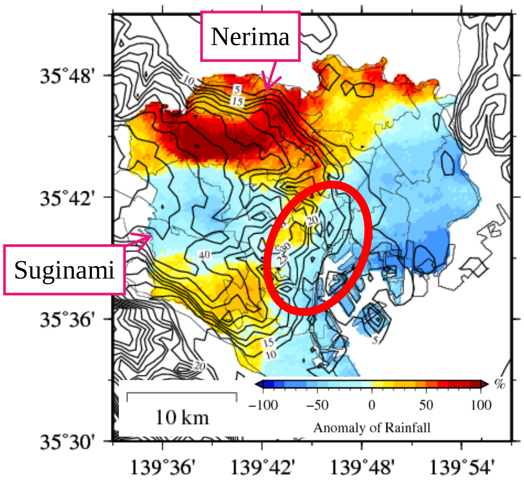


Figure 9: Spatial Anomaly of Localized Heavy Rainfall with Affective Elevation

3) Using the 9-year data of the River Department, positive anomaly found in the Tama region during the first 4 years shifted into the 23 wards during the remaining years.
4) The radar rainfall data with high spatial resolution, called Amesh, showed that summertime rainfall in 2008 had strong positive anomaly inside the Yamanote Line.
5) Nerima ward showed strong anomaly of rainfall in cases of localized heavy rain due to urbanization at the central areas.
6) Anomaly of rainfall was not positive in areas where urban geometry increased.

## Reference


[1] Fujibe, F., 1998, Spatial Anomalies and Long-Term Changes of Precipitation in Tokyo, *Tenki*, **45**, 7-18.

[2] Takahashi, H., Nakamura, Y., and Suzuki, H., 2008, Relation Between the Distribution of Summertime Intense Rainfall Frequency and the High-Rise Buildings in Tokyo Metropolitan Area, *Abstract of Japan Geoscience Union Meeting*, X156-002.

[3] Shimoju, R., Nakayoshi, M., and Kanda, M., 2009, The Effects of Sea Breeze Convergence Caused by Urban Geometry on Localized Heavy Rainfall in Summer in Tokyo, *Annual Journal of Hydraulic Engineering, JSCE*, **53**, 277-282.

[4] Macdonald, R. W., Griffiths, R. F., and Hall, D. J., 1998, An Improved Method for the Estimation of Surface Roughness of Obstacle Arrays, *Atmospheric Environment*, **32**, 1857-1864.

[5] Kanda, M., Inoue, Y., and Uno, I., 2000, Numerical Study on Kanpachi Street Cloud, *Tenki*, **47**, 11-24.

# A STUDY ON THE EFFECTS OF SEAWATER AS MIXING/CURING WATER ON THE HYDRATION CHARACTERISTICS OF BLAST-FURNACE SLAG CEMENT

Student Number: 09M18083 Name: Daisuke FURUYA Supervisor: Nobuaki OTSUKI

# 高炉セメントに対する海水練り・海水養生の影響

古谷　大輔

本研究は高炉セメントを海水で練混ぜ・養生した影響を、水和・空隙・強度・拡散係数・鉄筋腐食について調査、関連付けて比較・検討を行ったものである。高炉セメントを海水で練混ぜた場合、スラグの反応率が増加し、空隙が緻密化、初期の圧縮強度が増加した。海水で養生した場合、28 日までの圧縮強度はわずかに増加した。鉄筋腐食はスラグ置換率 50%が最も腐食抵抗性が高く、これは細孔溶液の Cl/OH 比を抑えられた事が原因であると考えられる。

## 1. Introduction

The use of blast furnace slag cement (BFS) is advantageous from the viewpoint of the $CO_2$ reduction. Blast furnace slag is generated from the steel manufacturing process as a by-product. Especially, BFS is used for construction of the port and offshore structures because of its good resistance against chloride attack. In such locations, obtaining pure water is difficult. Moreover, the demand for fresh water as drinking water will be increased as population increases in the future. These make it difficult to use pure water as construction material. Therefore, there is a demand to use seawater as mixing/curing water for BFS, and the demand will be growing. However, the corrosion of steel in reinforced concrete is a threat when using seawater due to a lot of chloride ion content in seawater.

The influence of an inorganic ion to the hydration of the ordinary portland cement (OPC) has been studied. Also, the influence of alkali (ex : calcium hydroxide) as activator to BFS hydration has been researched. However, researches about effect of seawater as mixed inorganic compounds are scarce.

In this paper, the author explains the relationship between following effects of mixing/curing with seawater

1. Effect to hydration characteristics
2. Effect to micropore structure
3. Effect to properties of cement composites
4. Effect to rebar corrosion

## 2. Overview of the experiment

The experiment compares the effect on paste and mortar specimens of mixing with seawater or distilled water and curing with seawater or distilled water. The mixing / curing patterns are shown table 1.

**Table 1 Mixing/curing pattern and symbol**

| | | Curing | | |
|---|---|---|---|---|
| | | distilled Water | Seawater | sealed (Fukan) |
| Mixing | distilled Water | WW | WS | WF |
| | Seawater | SW | SS | SF |

The replacement ratio of BFS to OPC are 50%, 70% and 90% that named as B50, B70 and B90 respectively.

Table 2 show the chemical composition of cement and BFS respectively. Blaine specific surface areas of BFS is 4200 $cm^2 \cdot g^{-1}$ .

**Table 2 Chemical composition of OPC and BFS (mass%)**

| | CaO | $SiO_2$ | $Al_2O_3$ | FeO | MgO | $SO_3$ |
|---|---|---|---|---|---|---|
| OPC | 63.96 | 20.38 | 5.18 | 3.37 | 1.88 | 1.97 |
| BFS | 43.9 | 32.4 | 13.9 | - | 6.4 | 1.6 |

The paste specimens of 10mm ×10mm × 4mm were cured with water in bottle or sealed curing with wrap after 24 hours pre-curing. At a set time, the specimens were crushed to prepare the powder specimens passing through the 150μm sieve for the each chemical analysis.

Measurement items are XRD, TG-DTA and DSC for hydration characteristics, mercury intrusion porosimetry for micropore structure, compressive strength test, salt meter, pH meter for properties and corrosion monitor for rebar corrosion. Hydration and micropore structure analysis use paste specimen. While properties and corrosion analysis use mortal specimen.

In the case of reaction ratio of BFS, crystallization heat of Melilite with DSC at a heating rate of 20°C/min. was utilized[1]. The crystallization heat at approximately 950°C was calculated with DSC, as shown in Fig. 1.

Thermogravimetric analysis (TGA, Mac Science WS002) of the samples was performed at a heating rate of 10°C/min. under nitrogen from 20°C and 1000°C.

The cumulative pore volume was measured using a mercury porosimeter (CE INSTRUMENTS Pascal240, pressure range: 0.1-200 MPa).

Pore solution for measurement of pH and Cl content was prepared by JIS A 1154-2003 "Method of test for chloride ion content in hardened concrete using hot-water extraction." The pH of pore solution was measured using a handy pH meter (Toko chemical laboratories TPX-999). The Chloride ion content was measured by SALMATE－100V, Asahi life science.

The mortar specimens of 40mm × 40mm × 160mm were prepared for the measurement of compressive strength. The compressive strength test (AYC-500P (500kN, load: 0.6±0.4 N•mm-2/sec.)), following JIS A1108 "Concrete compression examination", was carried out.

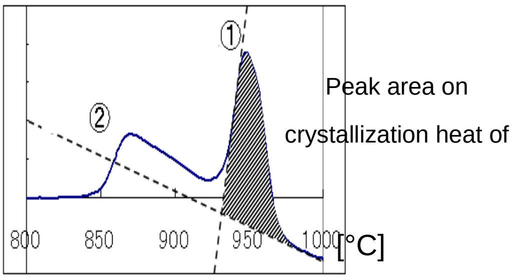


**Fig. 1 Quantitative determination of the residual BFS (Peak area on crystallization heat of Melilite)**

## 3. Experimental Results

### 3.1 Effect of mixing with seawater to cement

The results of slag reaction ratio tests of B70 are shown in Fig. 2. Mixing with seawater raises the BFS reaction ratio compared to mixing with distilled water for the entire period. The increasing has the largest value at day 1, since then, reduced and remain.

The results of mercury intrusion porosimetry of B70 are shown in Fig. 3. The amount of pores is decreased by mixing with seawater compared to data of 1st day. As hydration advances, products fill the space of BFS cement particles. Therefore pores of BFS cement become little in amount and fine in size.

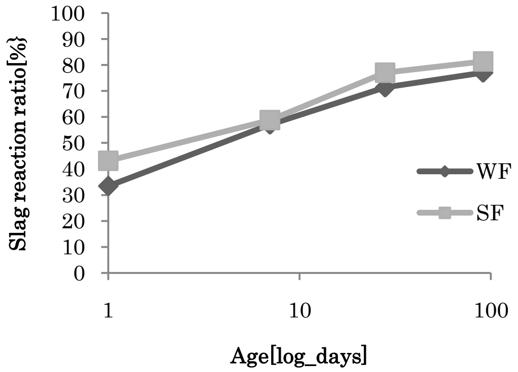


**Fig. 2 Influence of mixing with seawater on slag reaction ratio on B70**

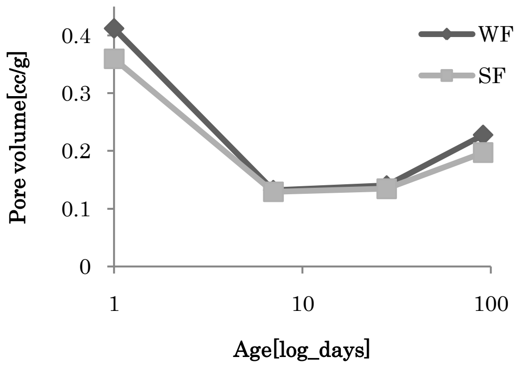


**Fig. 3 Influence of mixing with seawater on pore volume on B70**

The results of compressive strength tests of B70 are shown in Fig. 4. BFS cement is strengthened in entire period by mixing with seawater. Strength depends on the micropore structure; accordingly, the representative index is the amount of pore and the pore diameter. Mixing with seawater decreases the amount of pores. Therefore BFS cement is strengthened.

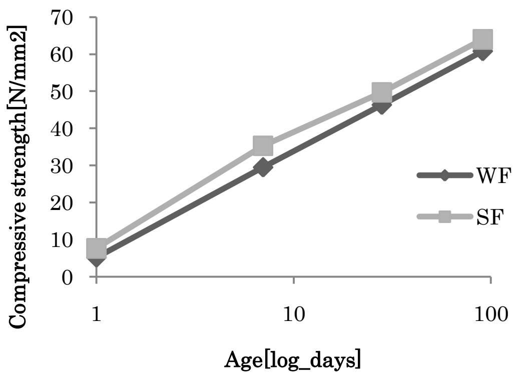


**Fig. 4 Influence of mixing with seawater on compressive strength on B70**

### 3.2 Effect of curing with seawater to cement

The results of slag reaction ratio tests of B70 are shown in Fig. 5. Difference between specimen mixing distilled water and mixing seawater has the largest value at day 28th. Curing influence effects cement paste from surface. Hence, the effect of curing with seawater retards.

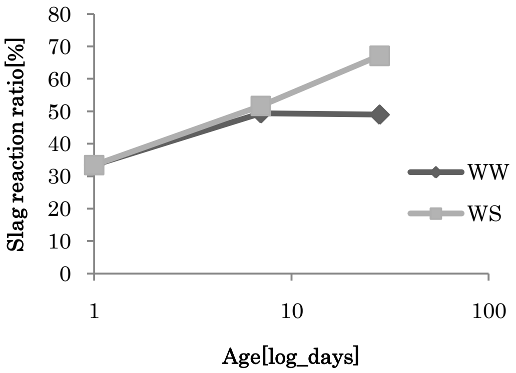


**Fig. 5 Influence of curing with seawater on slag reaction ratio on B70**

The results of mercury intrusion porosimetry of B70 are shown in Fig. 6. Amount of pore decreases from day 7. The Influence effects earlier than the influence on slag hydration ratio. This happens because Pores are filled by not only increased hydration products but also precipitate from seawater.

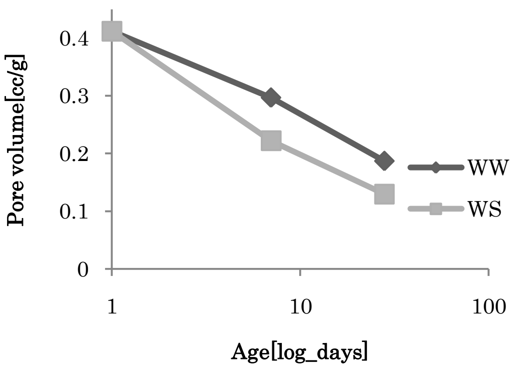


**Fig. 6 Influence of curing with seawater on pore volume on B70**

The results of compressive strength tests of B70 are shown in Fig. 7. Specimen is strengthen slightly by curing with seawater until 28th day. The smaller effect than paste specimens is caused by size effect.

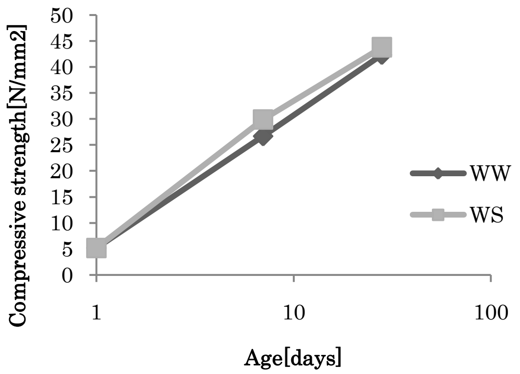


**Fig. 7 Influence of curing with seawater on compressive strength on B70**

### 3.3 Effect to rebar corrosion

The results of rebar corrosion test are shown in Fig. 8.

In case of mixing with distilled water and curing with seawater(Fig. 8-(a)), curing with seawater causes rebar to corrode in OPC specimen. It suggests that BFS cement has high-resistance for rebar corrosion by salt attack even if it is exposed to seawater at extreme early stage.

In case of mixing with seawater and sealed curing(Fig. 8-(b)), mixing with seawater does not cause corrosion except for B90.

In case of mixing and curing with seawater(Fig. 8-(c)), there is similar trend to case of mixing distilled water and curing seawater, OPC specimens corroded significantly compared to BFS specimens at day 91. corrosion rate trend is in order of OPC > B70 ≥ B90 > B50. The results is uncorrelated with replacement ratio. Because corrosion ratio determines the balance between chloride content and pH of pore solution[2].

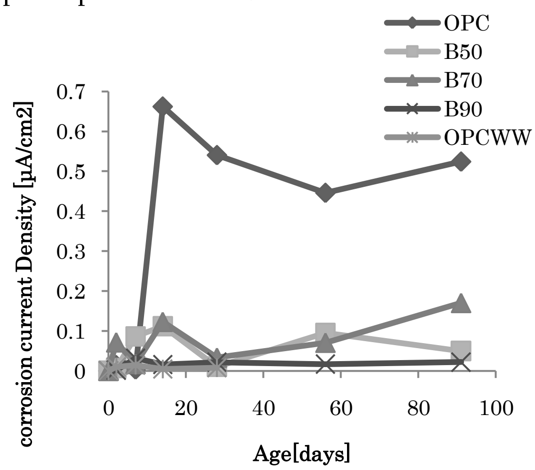


(a) Mixing with distilled water / Curing with seawater

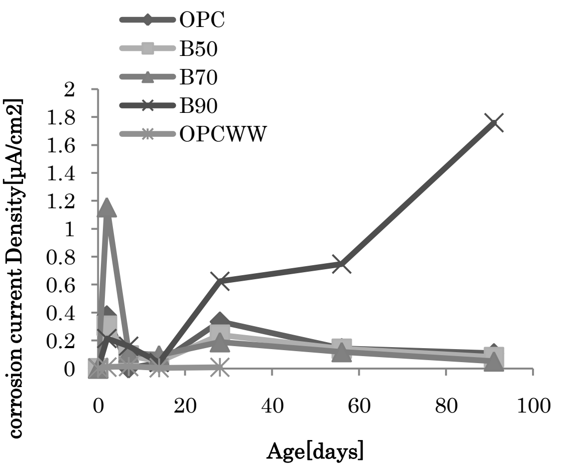


(b) Mixing with seawater / Sealed curing

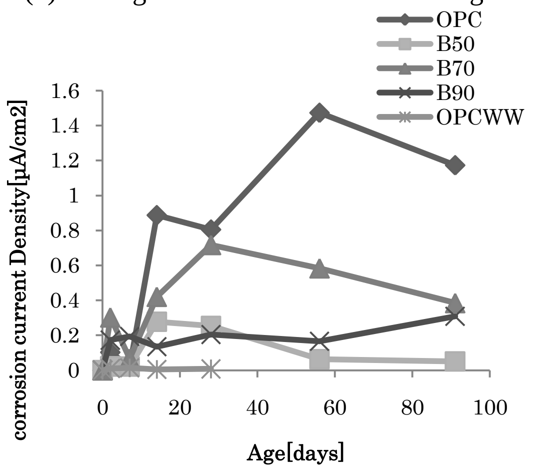


(c) Mixing with seawater / Curing with seawater

**Fig. 8 Influence of mixing/ curing water on corrosion rate**

The results of pH and fusible chloride content measurements are shown in Fig. 9. Rings on the graph express markedly corroded cases. The rings are grouped in a low hydroxide ion content area. OH amount has heavy influence to corrosion rate. Case of B50 show higher OH amount. This is the reason why B50 has good resistance for salt attack. The main alkali source of cement is $Ca(OH)_2$, Ability of $Ca(OH)_2$ generation is lower BFS than OPC. However, seawater causes Ca leaching in case of OPC shown Fig. 10. $Ca(OH)_2$ reacts with $MgCl_2$ in seawater and produce $Mg(OH)_2$ and $CaCl_2$. The $CaCl_2$ dissolves in water.

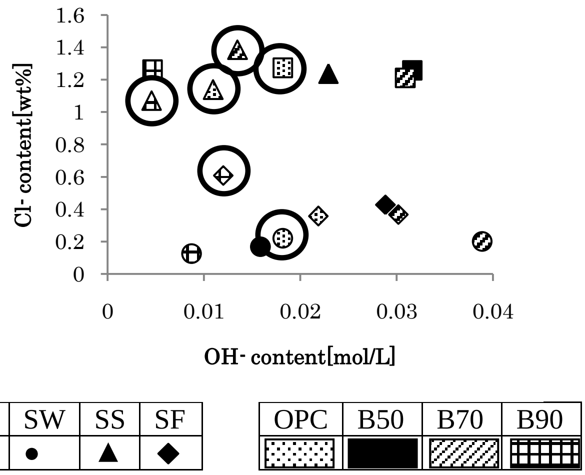


**Fig. 9 Relationship between corrosion and Cl/OH**

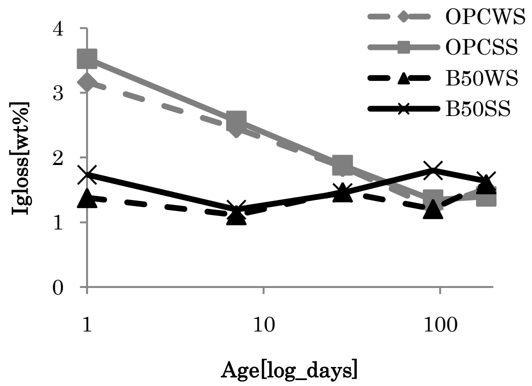


**Fig. 10 Influence of curing water on $Ca(OH)_2$ (OPC, B50)**

## 4. Conclusions

The following conclusions are derived from the investigations of this study:

(1) Mixing with seawater with sealed curing raises the strength in BFS cement specimens by accelerated slag hydration.

(2) Cured with seawater raises the strength in BFS cement specimens until 28th by accelerated slag hydration.

(3) 50% replacement BFS has good resistance for chloride corrosion for both cases of mixing and curing with seawater.

It is recommended to use high-replacement ratio BFS (about 50%) if there is no choice but to mix / cure with seawater.

## Reference

1. Imoto, H., Concrete engineering annual thesis collection, 28 [1], pp. 29-34, 2006.
2. Erlin, Bernard; Verbeck, George J : CORROSION OF METALS IN CONCRETE NEEDED RESEACH , Corros of Met in Concrete, p39-46

# Identification of main compound in Lao medicinal plant-Kiderm

Student Number: 09M18090 Name: Nariaki Maeshibu Supervisor: Sachio Hirose,

# ラオス薬用植物キデムに含まれる成分の同定

前澁 成昭

ラオスの糖尿病患者が長年服用してきた伝統薬がある。キデムと呼ばれる薬用植物の根を熱水で抽出したものには血糖値を下げる効果があり、過度に摂取しても血糖値が下がりすぎないといわれている。しかし、キデムは慣用名で学名や成分についての報告はない。本研究では分離、定性、定量の同時分析が可能な LCMS によって成分の解析を行った。主成分については、NMR による分子構造の決定を行うことを目的とした。主成分は分子量が 722 でありフラボノイドでコーヒー酸に置換基が２個ついていると推定された。

## 1. Introduction

Herbal medicine has a history of several thousand years and their worldwide utilization has been increased recently in both developing and developed countries. The World Health Organization estimated that 65-80% of the world population used herbal medicines as the primary form of healthcare [1]. In addition, adding value to local medicinal plants and agricultural products to produce herbal medicine or finding new lead compounds for medication is a way to improve the living standard in the developing countries. However, there are many medicinal plants that have not been studied.

In Lao P. D. R., Kiderm is one of the medicinal plants that have been used for the treatment of diabetes mellitus. A blood glucose level lowering was observed when a tea form from this plant was applied to patients who have Type 2 diabetes. It is said that glucose concentration in blood does not fall even if it is consumed in excess. However, the scientific name and the compounds in Kiderm have not been identified yet.

In herbal medicine, it has been generally accepted that the efficacy of herbal medicines can be attributed to the synergistic activity of various major and minor compounds of the herbs [3][4]. Therefore, it is essential to develop a method for online analysis of the compounds in Kiderm in order to understand better the pharmacological effect and ensure the quality control of the herb in the future.

The aim of this study is to elucidate the medicinal compounds in Kiderm using liquid chromatography hybrid ion trap time-of-flight mass spectrometry (LC/IT-TOF MS) and to identify the molecular structure of the main fraction in ingredients using nuclear magnetic resonance (NMR).

## 2. Materials and Methods

### 2.1 Materials

Roots of Kiderm were purchased from a herbal medicine shop in Vientiane province, Laos in November 2008 and dried at room temperature. All chemicals were purchased from Wako Chemical Industries, Ltd. (Tokyo, Japan). Ultrapure water produced by the Milli-Q Advantage vessel (Millipore, USA) was used for liquid chromatography mass spectrometry (LCMS) analysis.

### 2.2 Extraction of Kiderm roots

#### 2.2.1 Extraction solvent

To investigate the effect of the solvent for extraction, Kiderm roots were crushed to pieces under 500 µm. 1 g of roots powder was extracted 40 mL of water or methanol in water bath at 60˚C for 2 hours. The extracted liquid was filtered with 0.45 µm membrane filter. The filtrate was transferred into 1.5 mL vial for LCMS analysis. The area of each peak from chromatogram at 279 nm was compared.

#### 2.2.2 Compounds in skin and core

To compare the compound from skin and core of Kiderm roots, 5 g powder was of each samplewas extracted with 200 ml methanol by soxhlet extractor for 24h.

### 2.2.3 Extraction temperature

1 g of Kiderm roots powder was extracted using 40 mL methanol in water bath at temperature 15℃ 30℃ 45℃ 60℃.

## 2.3 LCMS-IT-TOF analysis

Optimal condition for separation was studied by using a Shimadzu LCMS 2010EV system. The separation was performed on ZORBAX Eclipse XDB-C18 column (150 mm x 2.1 mm, 3.5 µm, Agilent technologies, CA, USA). The mobile phase consisted of 0.1% formic acid aqueous solution (A) and methanol (B). The elution was performed at 0.2 mL $min^{-1}$. The column temperature was kept at 40˚C. UV spectra were scanned from 200 to 470 nm.

For LC/IT-TOF MS analysis, 500 g Kiderm roots were extracted with 1.5 L methanol at 60˚C for 7 hours. The extracted liquid was filtered through filter paper No.101 (Toyo Roshi Kaisha, Japan) and evaporated by rotary evaporator. A total of 10 g of residual extract was obtained. An amount of 16 mg was dissolve in 1.6 mL methanol and filtered with 0.45 µm membrane filter. The filtrate was transferred into 1.5 mL vial for LC/IT-TOF MS analysis using Shimadzu LC/IT-TOF MS system couple with electrospray ionization source (ESI). ESI-$MS^n$ experiments were conducted in both positive and negative modes. The following instrumental parameters were used: interface voltage, +4.5 kV (positive mode), -3.5 kV (negative mode); heat-block temperature, 200˚C; curved desolvation line (CDL) temperature, 200˚C; flow rate of nebulizing gas ($N_2$), 1.5 L $min^{-1}$; and pressure of driving gas ($N_2$), 100 kPa. Mass spectrometry was performed in the full-scan mode ($MS^1$) and automatic multiple-stage fragmentation-scan modes ($MS^2$-$MS^4$) over an *m/z* scan range of 100-1000.

## 2.4 NMR

### 2.4.1 Separation for NMR

Pure compound is needed for identification of the molecular structure by NMR. To separate main compound efficiently, liquid-liquid extraction was done on extract of Kiderm using chloroform and water. Water phase was freeze dried because the target was in it. The extract was dissolved with 0.1% formic acid and filtered for LC. The main ingredient was separated and collected by LC on ZORBAX Eclipse XDB-C18 column (250 mm x 9.4 mm, 5 µm, Agilent technologies, CA, USA).

### 2.4.2 Stability of the main compound

Stability of the main compound was tested on 55℃ and room temperature.

### 2.4.3 NMR analysis

Purified main compound was dissolved in methanol-d4 99.8%. $^{1}$H, $^{13}$C, HH-COSY and HSQC was measured.

## 3. Results and discussion

### 3.1 Extraction solvent

Almost all of the peak area from methanol extracted samples were smaller than those extracted with water. The main peak area decreased 47%. However, one peak was detected only by methanol. Methanol was used as extraction solvent further experiments because the extracted samples did not decay easily.

### 3.2 Skin and Core

319 mg of extract was obtained from 5 g core and 374 mg was obtained from 5 g skin. PDA suggested that the skin contained much more main compound than the core. Beside the main compound, skin and core also contain several different minor compounds. LCMS analysis for the extract was done without skin and core separation due to less information about the location of useful compound.

### 3.3 Effects of extraction temperature

The amounts of the extraction were compared based on the main peak area (Fig. 1). The amount of the extract increased as the temperature rose. The most effective temperature was 60℃.

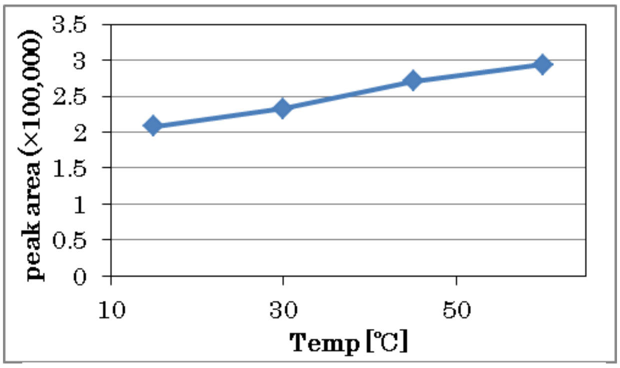


Fig. 1 Effect of temperature on extraction

### 3.4 LC/IT-TOF MS

The optimum condition for analysis was investigated by using isocratic elution and gradient elution using 20% to 70% methanol in water. Figure 2 shows the chromatogram of Kiderm extract at UV 279 nm and the total ion chromatogram (TIC) obtained by LC/IT-TOF MS in negative mode using optimum condition. Maximum UV absorption and mass data of each peak were summarized in Table 1. Most of the peaks were observed when using mobile phase consisted of 20% to 40% methanol. Main peak and other several PDA peaks showed the maximum UV absorption in the range of 270–280 nm. This indicated that the compounds could be flavonoid compounds in the group of flavones, flavonols, dihydrochalcones, catechins and flavan-3-ols.

Water and 60% ethanol gave higher peak area than those extractions by pure methanol and ethanol (data not shown). This result suggested that the compounds in Kiderm were hydrophilic and supported the above hypothesis. Although water gave higher peak area than other solvents, water could also easily extract unwanted components such as sugar and amino acid. For analytical purpose, we chose methanol as the extraction solvent because it gave a higher ratio of the main peak and also it is easier for evaporation in separation process.

In negative mode (Table1), the main peak (peak No 11) gave ion at *m/z* 721.1783 in $MS^1$, which indicated the deprotonated molecule $[M – H]^–$. In positive mode, sodium adducted ion $[M+Na]^+$ at *m/z* 745.1707 was observed. This result indicates that the molecular weight of the compound is 722.18. Fragmentation of ion at *m/z* 721.1783 gave ion at *m/z* 541.1340 which was 180.0443 lower than the precursor ion (721.1783). The loss of 180 Da from a molecular ion could be due to the loss of glucoside ($C_6H_{12}O_6$). However, calculation of $C_6H_{12}O_6$ gave exact mass at 180.0634 which shows 106 ppm higher than 180.0443. The IT-TOF mass spectrometer provided an accuracy of about 10 ppm at *m/z* 1000 in $MS^2$. This mass difference indicates that there is low possibility that the molecule has glucosides. Instead, $C_9H_8O_4$ (exact mass 180.0423, 11 ppm) was proposed as potential fragment which was lost from the molecular structure. This lost fragment could be caffeic acid. Ion at *m/z* 361.0883 also indicated the cleavage of caffeic acid from the molecule. The strong intensity of ion at *m/z* 299.0861 may be the skeleton structure of the compounds. From this result, the main compound in Kiderm was considered to be a flavonoid compound with two molecules of caffeic acid. The fragment pathway of the main peak is proposed in Scheme 1. Compounds 5, 6, 11, and 15 could have similar basic structure, since they produced similar fragment ions (Table 1). The compounds could be similar to flavonoids that were reported to have efficacy in lowering blood glucose, and aldose reductase inhibitory activity [2][5][6]. However, the accurate position of functional group of the flavonoids can not be determined by mass spectrometry.

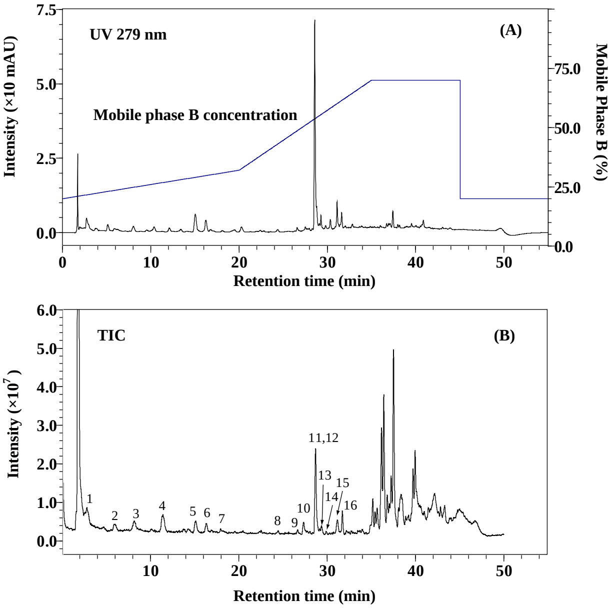


Fig. 2 UV chromatogram and TIC

Table 1 Retention time, UV (λ max) and MS data from the Kiderm root extract

| Peak No | Rt min | UV $\lambda_{max}$ | $MS^1$ *m/z* | $MS^2$ *m/z* / $MS^3$ *m/z* (% base peak) |
|---|---|---|---|---|
| 1 | 2.82 | 281 | 359.0993 | - |
| 2 | 5.90 | 273 | 443.1904 | - |
| 3 | 8.23 | 221, 251 | 373.1143 | - |
| 4 | 11.35 | 247 | 403.1241 | - |
| 5 | 15.16 | 279 | 541.1352 | 361.0889(8), 317.1048(14), 299.0899(63), 281.0791(13), 273.1132(38), 237.0930(13), 197.0452(30), 179.0375(17) |
| 6 | 16.41 | 275 | 541.1342 | 361.0918(43.54), 343.0765(16), 317.1041(25), 299.0936(8), 273.1116(100), 255.0968(10), 197.0476(16), 179.0361(7) |
| 7 | 17.94 | 251 | 403.1249 | - |
| 8 | 24.39 | 281 | 525.1380 | - |
| 9 | 26.59 | 273 | 555.1487 | - |
| 10 | 27.32 | 282, 328 | 389.0853 | - |
| 11 | 28.58 | 279 | 721.1783 | 541.1340 / 361.0936(12), 343.0863(7.58), 317.1019(15), 299.0918 (83), 281.0817(18),273.1111(35), 255.0982(7), 237.0908(19),197.0441(35), 179.0347(15) |
| 12 | 28.79 | 279 | 721.1775 | - |
| 13 | 29.34 | 276 | 719.1644 | - |
| 14 | 29.84 | 282 | 717.1436 | - |
| 15 | 31.16 | 279 | 705.1811 | 541.1351 / 361.0884(8), 343.0783(8), 317.1046(23), 299.0914(100), 281.0835(31), 273.1119(68), 255.0969(13), 237.0923(16), 197.0447(51), 179.0357(26) |
| 16 | 31.70 | 329 | 343.0823 | - |

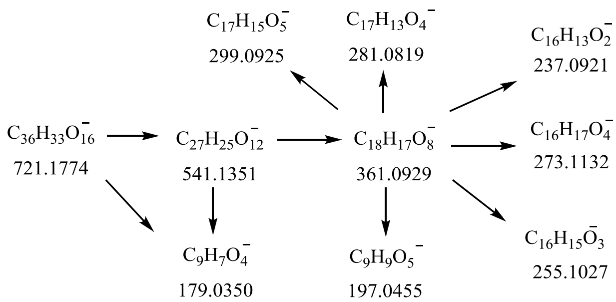


Scheme 1 Proposed fragment pathway of the main compound in Kiderm

### 3.5 Purification of main compound

The extract did not dissolve in water and chloroform so much therefore it was often dissolved in the methanol. The 1iquid-liquid extraction was done with precipitate. Over 90% of main compound was collected and over 80% of the weight of the extract was removed. On LC purification method, good separation of main compound was obtained by 35% methanol on isocratic flow (Fig. 3). Figure 4 shows the chromatogram of the main compound fraction after LC fraction collection. Unexpectedly a few peaks with shorter retention time than the main compound were detected. It took one month to isolate and purify the compound.

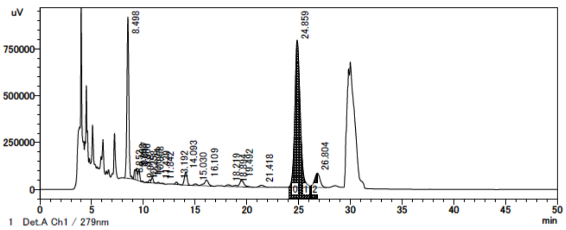

Fig. 3 Purification of main compound by LC

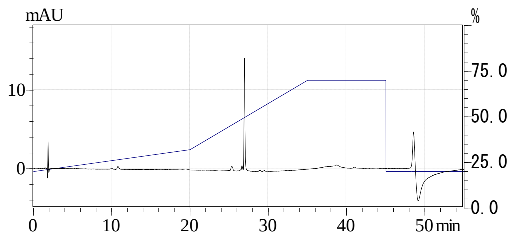


Fig. 4 PDA chromatogram of purified main compound

### 3.6 Stability of the main compound

The peak of the main compound of the fraction left in constant temperature reservoir (55℃) degraded completely after one week. The peak area of the main compound decreased 20% at room temperature after one week. It is necessary to keep the fraction in the refrigerator (4℃).

### 3.7 NMR analysis

Figure 5 shows $^{1}$H of the main compound. Count number was 480. But the peaks from compound were too weak to identify molecular structure. Results of $^{13}$C (Fig. 6), HH-COSY and HSQC were also useless of identification.

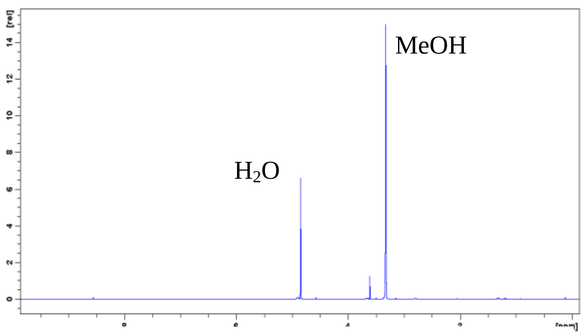


Fig. 5 $^{1}$H of main compound

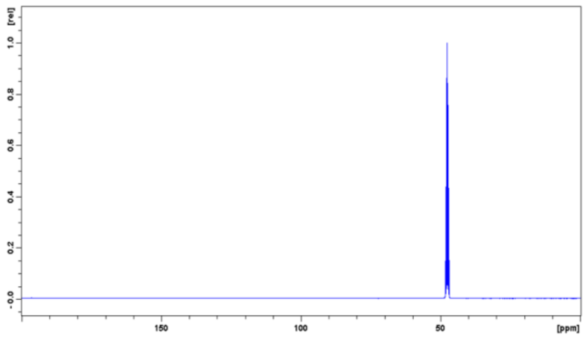

Fig. 6 $^{13}$C of the main compound

## 4. Conclusion

The compounds in Kiderm were effectively extracted by using polar solvent such as water and methanol. Most of the compounds were found to be hydrophilic. They show maximum UV absorption at 270-280 nm and may be flavonoid compounds. At least 4 compounds could be flavoinoid with two molecules of caffeic acid. Figure 7 shows proposed molecular structure of the main compound. The glucose level lowering effect of Kiderm could be due to the effect of the compounds similar to those of flavonoids reported previously.

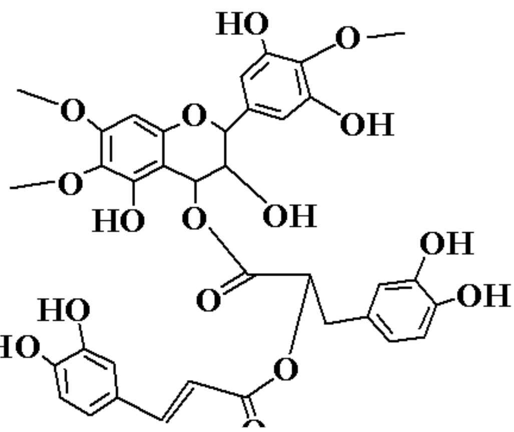

Fig. 7 Proposed molecular structure of main compound

## Reference

[1] Hao, H. P., et al., Anal. Chem. 80, 8187-8194 (2008)

[2] Igarashi, K., et al., J. nutr. sci. & vita. 58, 496-500 (2007)

[3] Liang, X. M., et al., J. Chro. A 1216, 2033-2044 (2009)

[4] Liang, Y. Z., et al., J. Chro. B 812, 63-70 (2004)

[5] Matsuda, H., et al., Chem & Pharm. Bull. 50, 788-795 (2002)

[6] Yoshikawa, M., et al., J. Chem. & Pharm. Bull. 46, 113-119 (1998)

# Wastewater Treatment by Adsorption with Activated Carbon from Wood Residues in Rubberwood Sawmilling Process

Student Number: 09M18108 Name: Saori MITANI Supervisor: Ryuichi EGASHIRA

# ゴム木材製材プロセスにおける残材由来活性炭を用いた吸着による排水処理

三谷　沙織

残材の熱処理生成物である木酢液を木材の防腐剤，活性炭を防腐剤の混入した排水を処理するための吸着剤として利用することにより，東南アジア等における本プロセスの改善を計る方法に対して，実用上重要である固定床型吸着装置の適用を試みた。ゴム木材おが屑を熱処理して得られた活性炭によるフェノールを含むモデル排水の吸着実験を撹拌槽，固定床吸着装置を用いて行い，吸着平衡と粒子内有効拡散係数を実測した。活性炭粒子内部の拡散係数が小さく，外部のそれは大きいことが推測された。実験結果に基づくシュミレーション計算より，木酢液は全て同時に得られた活性炭により処理できることが分かった。

## 1. Introduction

In Southeast Asian countries, rubberwood (RW) furniture manufacturing is an important industry. Sawmilling provides the processed wood for the industry. The current sawmilling process is shown in the black part of Fig. 1. Rubberwood logs are cut, preserved and dried, and molded into products. The problems from the process are to use toxic preservatives and to generate large amount of wood residues. The preservatives contain the harmful compounds such as boric acid and mixture of borax pentahydrate and the workers are exposed to the harmful environment. In addition, the wastewater, containing the preservatives, is discharged without any treatment, which causes soil and water contaminations. The large amount of wood residues with the preservatives are dumped or thrown away in rural sites and burned illegally, causing soil contamination, accidental forest burning and generation of hazardous gases.

To solve these problems in the sawmilling process, we proposed the utilization of the products from thermal treatment of RW residues. The proposed process is shown in Fig. 1, as well. A portion of residues from the cutting and molding process are thermally treated under steam atmosphere to produce the pyroligneous acid (PA), activated carbon (AC) and off-gas. PA is used as preservative, replacing the current purchased preservative because it contains the components useful as preservatives. Table 1 shows the some components in PA which we identified. The concentrations of these toxic components such as phenolic compounds are very low compared with current harmful preservatives, but they need to be removed from the wastewater. So, it is treated by adsorption with the AC. The remaining wood residues and off-gas are used for heat generation. We conducted the thermal treatment of RW sawdust under various conditions, studied the characteristics of the products, and evaluate the feasibility by simple calculation based on these experimental results. These studies showed that the improvement of the process by the proposed method was feasible in terms of material and heat balances [1].

In order to put this method to practical use, more detailed studies of the individual operations in this process should be carried out. For wastewater treatment, it is necessary to study not only adsorption isotherms but also kinetics.

This study aims to design the fixed bed adsorption column for the wastewater treatment in this process. Firstly, thermal treatments of RW sawdust were conducted to obtain the AC. With this AC, the adsorption of phenol, a representative pollutant in PA, from the aqueous solution with stirring vessel and fixed bed column were conducted to measure the adsorption equilibrium and rate parameters.

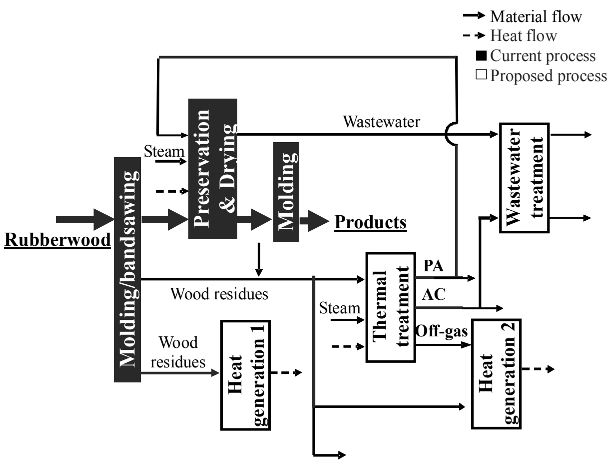


Fig. 1 Current and proposed process of sawmilling: material and heat flows

Table 1 Components in PA

| Components | Mass fraction [%] |
|---|---|
| Water | 92 |
| Acetic acid | 0.89 |
| Acetone | 0.22 |
| Phenolic compounds | 0.06 |
| Methanol | 0.02 |

## 2. Experimental

### 2.1 Preparation of AC by thermal treatment of RW sawdust

RW sawdust was thermally treated under steam atmosphere in a stainless steel tube heated by an electric furnace to obtain the AC. The experimental equipment is shown in Fig. 2, the same as previous study [1]. The tube was heated from room temperature until the specified treatment temperature, 873K, and the temperature was kept for 1 hour, defined as holding time. Table 2 shows the principal conditions of thermal treatment. The water content in obtained crude PA was measured by Karl Fischer Instruments (758KFD Titrino) from Metrohm company.

### 2.2 Adsorption with stirring vessel

AC was washed, dried, grounded and sieved before adsorption experiments. The schematic diagram of the vessel is shown in Fig. 3. The experimental conditions are shown in Table 3. A specified amount of AC was mixed with the model wastewater containing phenol in the stirring vessel. The stirring velocity was 500 rpm, which is reported to be high enough for external mass transfer resistance to be negligible under such systems and conditions [2]. The temperature of the material system in vessel was kept at 303 K in an isothermal bath. The samples were intermittently collected until the system reached adsorption equilibrium. The samples were analyzed by gas chromatograph (GC-14B with FID, Shimadzu Co., Ltd.; ULBON HR-20M column I.D. 0.00053 m × 30 m).

### 2.3 Adsorption with fixed bed

Based on the results of batch adsorption in the stirring vessel, fixed bed adsorption was conducted with the small column which was made of acrylic resin. The column size was 2.1 cm in I.D. and 4 cm in length. Pretreated AC was soaked with deionized water under vacuum condition to remove air in the pores. Then it was packed in the column. The model wastewater containing phenol was supplied to the column in an upward flow direction at a desired flow rate by a delivery pump. Samples were taken from the effluent on the top of the column and phenol concentration was determined by gas chromatograph. Figure 4 shows the apparatus for fixed bed adsorption. Principal conditions of the experiment are shown in Table 4.

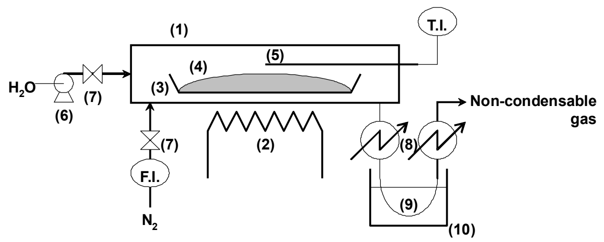


Fig. 2 Schematic diagram of thermal treatment apparatus: (1) tubular reactor; (2) electric tubular furnace; (3) sample holder; (4) feed/solid product; (5) NiCr-Constantan thermocouple; (6) micro-plunger pump; (7) valves; (8) condensers; (9) liquid product trap; (10) iced bath (275~277 K); F.I. flow indicator; T.I. temperature indicator

Table 2 Principal conditions for thermal treatment

| Feed | | RW sawdust |
|---|---|---|
| Mass of feed | [g] | 25 ± 5 |
| Atmosphere | | $H_2O$ |
| Flow rate | [$m^3 \cdot h^{-1}$] | |
| | < 473K | 0.003($N_2$) |
| | > 473K | 0.0012($N_2$) |
| | | 0.003($H_2O$) |
| Temperature | [K] | 873 |
| Holding time | [h] | 1 |

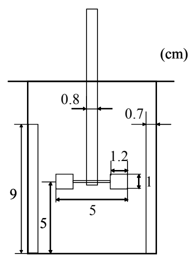


Fig. 3 Schematic diagram of stirring vessel

Table 3 Principal conditions for adsorption with stirring vessel

| Feed solution | Phenol solution |
|---|---|
| Volume of feed solution [$m^3$] | 500 × $10^{-6}$ |
| Concentration of phenol in feed solution,, $C_0$ [$g \cdot m^{-3}$] | 100–400 |
| Adsorbent | AC |
| Particle radius AC, $R_p \times 10^3$ [m] | 0.21−0.85, 0.08−0.18 |
| Concentration of adsorbent, $C_{AC}$ [$g \cdot m^{-3}$] | 200–2000 |
| Stirring speed [rpm] | 500 |
| Sampling size [$m^3$] | 3 × $10^{-6}$ |
| Contacting time [h] | 75, 200 |
| Contacting temperature [K] | 303 |

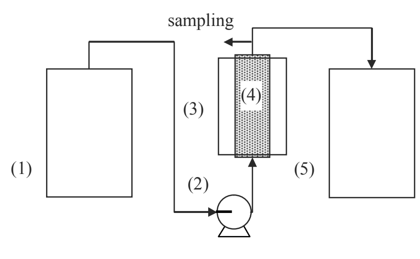


Fig. 4 Schematic diagram of fixed bed apparatus:
(1) Feed tank; (2) Solution delivery pump; (3) Heating water tube; (4) Fixed bed column; (5) Reservoir

Table 4 Principal conditions for fixed bed adsorption

| | |
|---|---|
| Feed solution | Phenol solution |
| Fluid velocity, $u \times 10$ [m·h$^{-1}$] | 2.6–5.4 |
| Concentration of phenol in feed solution, $C_0$ [g·m$^{-3}$] | 230–300 |
| Adsorbent | AC |
| Particle radius of AC, $R_p \times 10^3$ [m] | 0.08–0.18 |
| Mass of adsorbent [g] | 2.5 ± 0.5 |
| Sampling size [m$^3$] | $3 \times 10^{-6}$ |
| Contacting temperature [K] | 303 |

## 3 Results and discussion

### 3.1 Preparation of AC by thermal treatment of RW sawdust

Thermal treatment of RW sawdust produced crude PA, AC and off-gas. The color of crude PA was dark brown and water content was 83 %. It was because it contained a lot of tar components, which we proposed to be removed by distillation. All sawdust was evenly treated to AC. AC was black in color and lighter in mass if compared with feed sawdust. Off-gas was non-colored gas and had a bad smell. Mass of obtained crude PA, AC and off-gas were about 30 %, 20 % and 50 % of the feed sawdust, respectively. Mass of off-gas was derived based on material balance.

### 3.2 Adsorption with stirring vessel

The basic equation of adsorption rate into the particle is written as Eq. (1)

$$\partial q/\partial t = D_e \cdot (\partial^2 q/\partial r^2 + (2/r)\,(\partial q/\partial r)) \quad (1)$$

with boundary conditions

$r = R_p$ ; $\rho_s \cdot D_e \cdot \partial q/\partial t = -(V_L/S)\cdot(\partial C/\partial t)$, $q = f(C)$

$r = 0$ ; $\partial q/\partial r = 0$

and initial conditions $q = 0$ for $0 \le r \le R_p$

and $C = C_0$ at $t = 0$

where $q$ is amount adsorbed, $D_e$ is effective intraparticle diffusivity, $r$ is radial position in the particle, $\rho_s$ is particle density, $V_L$ is volume of solution, $S$ is external surface area, $C$ is concentration of phenol in the solution. The measured concentration change allows to estimate the value of $D_e$.

The time course of the dimensionless concentration, $C/C_0$, of phenol in the solution are presented in Fig. 5. The concentration decreased over time, which shows that the phenol in the solution could be removed by AC.

$C_1/C_0$ is shown in table in Fig. 5, where $C_1$ is the final concentration of phenol. When $C_0$ was low, $C_1/C_0$ was low. When the mass fraction of AC in the solution, $C_{AC}$ was low, $C_1/C_0$ was high.

The adsorption isotherm fitted Henry's type well from $C_1$ of each run. Theoretical curves by analytical solution of Eq. (1) are also drawn in Fig. 5 [3](dotted lines). $D_e$ was measured by fitting to theoretical curves. However, it was difficult to fit all data with this theoretical curve. Compared with the curve, experimental concentration decreased quickly in early stage and then gradually decreased. Theoretical curves, which are obtained by numerical solution of Eq. (1) with using the different values of $D_e$ for inner part of AC, $D_{e,i}$, and outer part of one, $D_{e,o}$, are also drawn in Fig. 5(solid lines). They fitted the experimental results better than former lines. This suggests that $D_e$ of inner part of AC was smaller than outer part of it and it controlled the overall adsorption rate in later period of time.

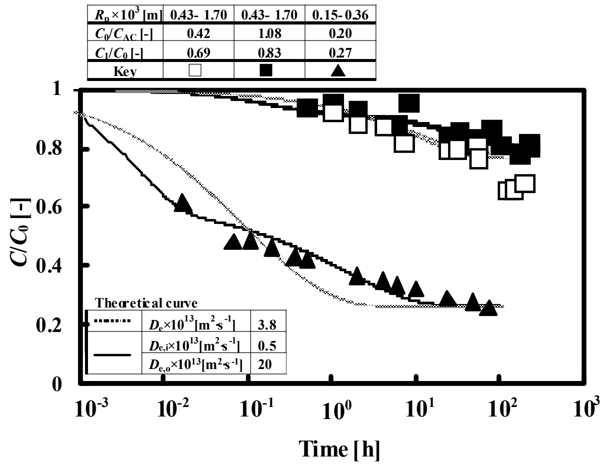


Fig. 5 Concentration change in stirring vessel

### 3.3 Adsorption with fixed bed

Material balance equation in fixed bed is written as Eq. (2)

$$u \cdot \partial C/\partial z + \rho_b \cdot \partial q_{ave}/\partial \theta = 0 \quad (2)$$

with boundary conditions

$r = R_p$ ; $\rho_b \cdot \partial q_{ave}/\partial \theta = k_f a_v \cdot (C - C_s)$,

$\rho_b \cdot \partial q_{ave}/\partial \theta = D_e \cdot a_v \cdot \rho_p \cdot (\partial q/\partial r)$, $q = f(C)$

$r = 0$ ; $\partial q/\partial r = 0$

and initial conditions $q = 0$ for $0 \le r \le R_p$

and $C = C_0$ for $t = 0$, $z = 0$

where, $u$ is flow rate, $C$ is bulk concentration of phenol in the bed, $z$ is axial location in the column, $\rho_b$ is bed density, $q_{ave}$ is average amount adsorbed, $\theta$ is time, $\rho_p$ is particle density, $k_f a_v$ is fluid phase mass transfer coefficient, and $C_s$ is concentration at interface. Eq. (1) and (2) can be solved numerically to obtain the breakthrough curve.

Fixed bed adsorption runs were conducted under three different conditions. $u$ and $C_0$ were varied. The breakthrough curve was measured for each run shown in Fig. 6. Breakthrough concentration, $C_B$, was fixed 10% of $C_0$.

From the results, effluence concentration of phenol, $C$, was 0 at first. This is because whole phenolic compound was adsorbed by AC which was packed in the column during the solution flowing in the column. Then, $C/C_0$ gradually increased with time. Breakthrough time, $t_B$, showed increasing tendency with decreasing $u$.

The shapes of the curves spread widely at high concentration field. Probably, the intraparticle mass transfer might dominate in this adsorption. Some researchers reported that for rate control in the mobile phase, the wave "fronts" has a sharp tail; for rate control in the stationary phase, the wave "tails" has a sharp front [4].

Theoretical breakthrough curves were estimated by same method as before. Similarly to stirring vessel, model of smaller $D_{e,i}$ than $D_{e,o}$, which are shown by solid lines in Fig. 6, fitted better to experimental results better than model of uniform $D_e$ values in the particle, which are shown by dotted lines. Appropriate values of $D_{e,i}$ was small compared with that of stirring vessel. Possible reason was difference of adsorption operation. For example, channeling might occur in the column. If so, flow rate became inconstant and it caused earlier increase of concentration. But decisive reason was not clear.

Then, simulation calculation for industrial adsorption column operation was conducted. Figure 7 shows the process flow for simulation calculation. The yield and other characteristics of products were based on experimental results. Toxic component in wastewater was assumed to be only phenol and the concentration was 1500 ppm, which is sum of phenolic compounds in obtained PA. $C_B$ was fixed 1 ppm, which is the permissible level in Malaysia. Simulation was done to meet following conditions, which all of PA is treated by $t_B$ within unit of time and excess amount of AC is discharged. Then, relations were obtained as follows to satisfy these conditions.

$$u \cdot t_B \cdot \xi / L \geq 1,\ 1 \geq t_B$$

In this equation, ξ is yield and density parameter obtained by experiment and $L$ is column length. Table 5 shows the example of simulation calculation. All of PA could be treated by AC and excess amount of AC could be treated.

## 4. Conclusion

AC which posses the adsorption ability of phenol was sufficiently obtained by thermal treatment of RW sawdust.

In adsorption with stirring vessel, it was found that mass transfer rate of inner part of AC particle was much smaller than outer part.

In adsorption with fixed bed, mass transfer rate in inner part of AC particle was small similarly to stirring vessel. Based on the results, simulation calculation showed that all of PA obtained by thermal treatment could be treated by AC.

Therefore, it is concluded that application of fixed bed operation for wastewater treatment in proposed sawmilling process will be feasible.

**Nomenclature**

$C_0$: feed concentration [g·m$^{-3}$], $R_p$: particle radius [m], $C_{AC}$: concentration of AC [g·m$^{-3}$], $u$: velocity of the fluid [m·h$^{-1}$], $D_e$: effective intraparticle diffusivity [m$^2$·s$^{-1}$], $q$: amount adsorbed [g·(g-AC)$^{-1}$], $t$: time [s], $r$: radial position within a particle [m], $\rho_s$: particle density [g·m$^{-3}$], $V_L$: volume of solution [m$^3$], $S$: external surface area [m$^2$], $C$: concentration in the fluid phase [g·m$^{-3}$], $C_1$: final concentration [g·m$^{-3}$], $D_{e,o}$: effective intraparticle diffusivity of outer part in AC [m$^2$·s$^{-1}$], $D_{e,i}$: effective intraparticle diffusivity of inner part in AC [m$^2$·s$^{-1}$], $z$: axial location in the column [m], $\rho_b$: bed density [g·m$^{-3}$], $q_{ave}$: average amount adsorbed [g·(g-AC)$^{-1}$], $\theta$: adjusted time [s](= $t$-$\varepsilon$·$z/u$), $\rho_p$: particle density [g·m$^{-3}$], $k_f a_v$: fluid phase mass transfer coefficient [s$^{-1}$], $C_s$: concentration at interface [g·m$^{-3}$], $a_v$: specific surface area [m$^2$], $C_B$: breakthrough concentration [g·m$^{-3}$], $t_B$: breakthrough time [h], $\xi$ : yield and density parameter [-]($\xi = \rho_{PA} Y_{AC} / \rho_b Y_{PA}$ ), $L$ : column length [m], $R$: mass of RW residues [kg·h$^{-1}$], $Y_{PA}$ : yield of PA [-], $Y_{AC}$ : yield of AC [-], $M_{AC,Column}$ : amount of AC for column [kg], $M_{AC,Exit}$ : excess amount of AC [kg]


**References**

[1] Rizafizah Othaman, et al. *J. Chem. Eng.Japan*, Vol. 41, No. 12, pp. 1149-1158 (2008)

[2] Suzuki Motoyuki, et.al. *J.Chem. Eng. Japan*, Vol. 8, No. 1, pp. 79-81 (1975A)

[3] Crank, "Mathematical diffusion", Oxford (1956)

[4] Friedrich G. Helfferich. *J. Chromatography*, 629, pp. 97-122, (1993)


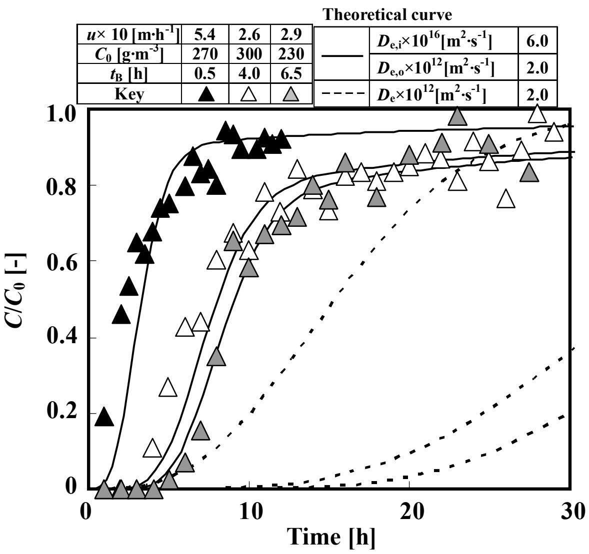


Fig. 6 Breakthrough curves of phenol

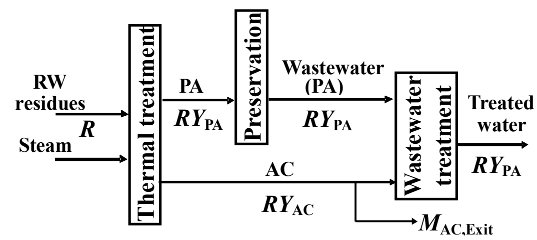


Fig. 7 Process flow for simulation calculation

Table 5 Example of simulation calculation

| | |
|---|---|
| Mass of RW residues, $R$ [kg·h$^{-1}$] | 10000 |
| Mass of obtained PA, $RY_{PA}$ [kg·h$^{-1}$] | 14000 |
| Mass of obtained AC, $RY_{AC}$ [kg·h$^{-1}$] | 2080 |
| Volumetric flow rate of waste water to column [kg·h$^{-1}$] | 14 |
| Column length, $L$ [m] | 3.0 |
| Fluid velocity, $u$ [m·h$^{-1}$] | 98 |
| Breakthrough time, $t_B$ [h] | 1.0 |
| Amount of AC for column, $M_{AC,Column}$ [kg] | 90 |
| Excess amount of AC, $M_{AC,Exit}$ [kg] | 1990 |

# Quadratically Constrained Criterion based on Maximum a Posteriori Estimation for Binary Classifier

Student Number: 09M18114 Name: Tatsuya Yokota Supervisor: Yukihiko Yamashita

二値識別のための MAP 推定に基づく二次制約評価基準

横田 達也

本論文では，MAP 識別器を構成するための新しい二次制約評価基準を提案する．一般の MAP 識別では，事後確率の推定を伴うが，本手法では事後確率の推定をせずに，直接，MAP 識別と同じ結果を与える識別関数を推定する．本評価基準に基づく識別器は，重み関数を選択することで，最小二乗回帰やサポートベクターマシンとして特徴づけることができる．さらに，計算機実験の結果，既存の従来手法と比べて有意な差を得ることができた．

## 1 Introduction

Maximum a posteriori (MAP) based methods play an important role in machine learning and pattern recognition. In this paper I propose a new classification criterion based on the MAP estimation for a binary problem. In our method, I do not estimate the posteriori probability; instead I construct a discriminant function that provides the same result.

I show that the least square regression (LSR) and the support vector machine (SVM) can be derived from the criterion. Furthermore I propose novel classifiers based on the criterion and conduct experiments to demonstrate their advantages.

## 2 Model Formalization

Let $y \in \{+1, -1\}$ be the category to be estimated from a pattern $\boldsymbol{x} \in \mathbb{R}^M$. The training samples are given by

$$\{\boldsymbol{x}_n, y_n\}_{n=1}^N. \tag{1}$$

And the classifier is given by

$$\hat{y} = \begin{cases} +1 & D(\boldsymbol{x}) > 0 \\ -1 & D(\boldsymbol{x}) < 0, \end{cases} \tag{2}$$

where $D(\boldsymbol{x})$ is a discriminant function. The goal of this research is to optimize the discriminant function based on the MAP estimation.

### 2.1 MAP based Classifier

In the MAP classification, when an unlearned patten $\boldsymbol{x}$ is given, its category $\hat{y}$ is estimated by finding the maximum *a posteriori* probability, $P(y|\boldsymbol{x})$ :

$$\hat{y} = \underset{y}{\operatorname{argmax}}\, P(y|\boldsymbol{x}). \tag{3}$$

In our approach [4], it is necessary and sufficient that

$$D(\boldsymbol{x}) \begin{cases} > 0 & P(+1|\boldsymbol{x}) > P(-1|\boldsymbol{x}) \\ < 0 & P(-1|\boldsymbol{x}) > P(+1|\boldsymbol{x}). \end{cases} \tag{4}$$

## 3 Proposed Method

In this section, I define a new criterion for the discriminant function $D(\boldsymbol{x})$ based on MAP estimation and explain its properties.

Let a weighting function $Q(\boldsymbol{x})$ satisfy

$$\int_{\mathcal{D}} Q(\boldsymbol{x}) \mathrm{d}\boldsymbol{x} = 1, \quad Q(\boldsymbol{z}) > 0 \tag{5}$$

for all $\boldsymbol{z} \in \mathcal{D}$, where $\mathcal{D}$ describes the data domain. The new MAP classifier is called the *quadratically constrained MAP* (QCMAP) classifier and is defined as follows:

$$\text{maximize} \quad \sum_{y \in \{+1,-1\}} \int_{\mathcal{D}} P(\boldsymbol{x}, y) \min(yD(\boldsymbol{x}), 1) \mathrm{d}\boldsymbol{x}, \tag{6}$$

$$\text{subject to} \quad \int_{\mathcal{D}} Q(\boldsymbol{x}) |D(\boldsymbol{x})|^2 \mathrm{d}\boldsymbol{x} \le 1. \tag{7}$$

To optimize the criterion, I maximize the expectation of $\min(yD(\boldsymbol{x}), 1)$. Since we have $P(\boldsymbol{x}, y) = P(\boldsymbol{x})P(y|\boldsymbol{x})$, we can write the objective function in (6) as

$$\int_{\mathcal{D}} P(\boldsymbol{x}) \{P(+1|\boldsymbol{x}) \min(D(\boldsymbol{x}), 1) + P(-1|\boldsymbol{x}) \min(-D(\boldsymbol{x}), 1)\} \mathrm{d}\boldsymbol{x}. \tag{8}$$

If the measure of $\{x|P(+1|x) = P(-1|x)\}$ is zero (a condition that is satisfied in almost all classification problems), then $D(\boldsymbol{x})$ is given by

$$D(\boldsymbol{x}) = \begin{cases} +1 & \text{if } P(+1|\boldsymbol{x}) > P(-1|\boldsymbol{x}) \\ -1 & \text{if } P(+1|\boldsymbol{x}) < P(-1|\boldsymbol{x}) \end{cases} . \tag{9}$$

$D(\boldsymbol{x})$ yields the same results as the MAP classifier.

### 3.1 Training method

I define $D(\boldsymbol{x}|\boldsymbol{w})$ using a linear model function as

$$D(\boldsymbol{x}|\boldsymbol{w}) := \sum_{i=1}^M w_i x_i = \langle \boldsymbol{w}, \boldsymbol{x} \rangle . \tag{10}$$

And the criterion of QCMAP estimation can be transformed by replacing the ensemble mean by the sample mean, and substituting (10) as follows:

$$\text{maximize} \quad \sum_{n=1}^{N} \min\left(y_n \langle \boldsymbol{w}, \boldsymbol{x}_n \rangle, 1\right) \tag{11}$$

$$\text{subject to} \quad \boldsymbol{w}^T H \boldsymbol{w} \le 1, \tag{12}$$

where

$$H(i,j) := \int_{\mathcal{D}} Q(\boldsymbol{x}) x_i x_j \mathrm{d}\boldsymbol{x}, \tag{13}$$

Here objective function (11) is piecewise linear function because of the min function. But it can be linearized by using slack variables $\xi_n$:

$$\text{minimize} \quad \sum_{n=1}^{N} \xi_n \tag{14}$$

$$\text{subject to} \quad y_n \langle \boldsymbol{w}, \boldsymbol{x}_n \rangle \ge 1 - \xi_n \tag{15}$$

$$\xi_n \ge 0, \quad n = 1, \ldots, N \tag{16}$$

$$\boldsymbol{w}^T H \boldsymbol{w} \le 1. \tag{17}$$

This optimization problem is a quadratically constrained linear programming (QCLP) problem. QCLP is a second-order cone programming (SOCP) [2] problem and many solvers are available. QCMAP problems can also be solved (i.e., trained) by the primal-dual interior point method. [6]

## 3.2 Construction of Constraints

In this section, I consider four types of constraint for QCMAP estimation by choosing four weighting functions.

First, I choose $P(\boldsymbol{x})$ as the weighting function

$$Q_1(\boldsymbol{x}) := P(\boldsymbol{x}), \tag{18}$$

so it satisfies condition (5). Then, the matrix $H_1$ can be calculated analytically by replacing the ensemble mean by the sample mean:

$$H(i,j) = \int_{\mathcal{D}} P(\boldsymbol{x}) x_i x_j \mathrm{d}\boldsymbol{x} \simeq \frac{1}{N} \sum_{n=1}^{N} \boldsymbol{x}_n^{(i)} \boldsymbol{x}_n^{(j)} =: H_1(i,j) \tag{19}$$

where $\boldsymbol{x}_n^{(i)}$ denotes the $i$th element of vector $\boldsymbol{x}_n$. So we have

$$H_1 = \frac{1}{N} X^T X, \quad \text{where} \quad X := \begin{pmatrix} \boldsymbol{x}_1 & \boldsymbol{x}_2 & \cdots & \boldsymbol{x}_N \end{pmatrix}^T. \tag{20}$$

This constraint is given by

$$\boldsymbol{w}^T X^T X \boldsymbol{w} \le N. \tag{21}$$

In this case, *QCMAP estimation is equivalent to LSR.*

Now let me assume that $||\boldsymbol{x}||^2 = 1$ and the data domain $\mathcal{D}$ is equal to the $M-1$ dimensional hyperspherical surface $S^{M-1}$. This assumption holds in the Gaussian kernel model. I choose the weighting function to be

$$Q_2(\boldsymbol{x}) := \frac{1}{S_{M-1}}, \tag{22}$$

where $S_{M-1}$ is the surface area of $S^{M-1}$. This constraint is given by

$$||\boldsymbol{w}||^2 \le M. \tag{23}$$

We can see that the constraint matrix is defined as $H_2 := \frac{1}{M} I_M$. In this case, *QCMAP estimation is equivalent to the SVM method.*

If the training samples are distributed normally, $P(\boldsymbol{x})$ should be similar to a normal distribution. In this case the regularization of QCMAP estimation may be achieved by choosing a normal distribution as the weighting function. So, I propose to use the weighting function

$$Q_3(\boldsymbol{x}|\boldsymbol{\mu}, \Sigma) := \frac{1}{(\sqrt{2\pi})^M \sqrt{|\Sigma|}} e^{-\frac{1}{2}(\boldsymbol{x}-\boldsymbol{\mu})^T \Sigma^{-1} (\boldsymbol{x}-\boldsymbol{\mu})}. \tag{24}$$

Then constraint matrix $H_3$ is given by

$$H_3(i,j) := \int_{\mathcal{D}} \frac{x_i x_j}{(\sqrt{2\pi})^M \sqrt{|\Sigma|}} e^{-\frac{1}{2}(\boldsymbol{x}-\boldsymbol{\mu})^T \Sigma^{-1} (\boldsymbol{x}-\boldsymbol{\mu})} \mathrm{d}\boldsymbol{x}. \tag{25}$$

QCMAP estimation with Eq. (25) provides a novel classifier, which we call the “Gaussian QCMAP” (GQCM) classifier. If we use the Gaussian kernel model as basis function and still use a normal distribution in the original space for $Q(\boldsymbol{x})$, then I can calculate $H_3$ analytically.

When I consider the robustness for outliers, the weighing function should have small value in massed area and large value in sparse area, since the value controls the strength of regularization. So, I propose a following weighting function

$$Q_4(\boldsymbol{x}) := \left(1 + \frac{\lambda}{\nu^M - 1}\right) Q_3(\boldsymbol{x}|\boldsymbol{\mu}, \nu^2\Sigma) - \frac{\lambda}{\nu^M - 1} Q_3(\boldsymbol{x}|\boldsymbol{\mu}, \Sigma), \tag{26}$$

where $0 < \lambda < 1$ and $\nu > 1$. If we assume $\Sigma$ is diagonal matrix, then this weighting function always satisfy Eq.(5). Basically, $\lambda$ should be nearly 1. Fig.1 depicts examples of this weighting function. If $\nu$ increases, the weighting function becomes smooth and wider. Then, we have

$$H_4 = \left(1 + \frac{\lambda}{\nu^M - 1}\right) H_3' - \frac{\lambda}{\nu^M - 1} H_3, \tag{27}$$

where $H_3'(i,j) := \int_{\mathcal{D}} Q_3(\boldsymbol{x}|\boldsymbol{\mu}, \nu^2\Sigma) x_i x_j \mathrm{d}\boldsymbol{x}$. *It's classifier can be characterized as a robust classifier for peripheral area,* because the values of its weighting function is large in peripheral area. I call its classifier the “robust QCMAP” (RQCM) classifier.

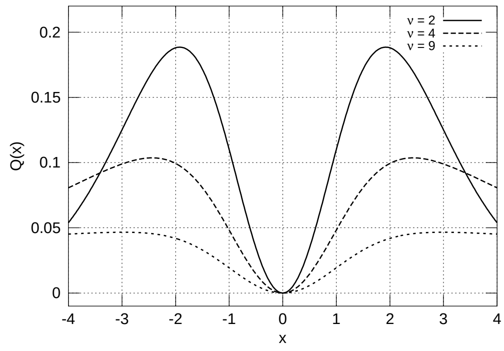


Figure 1: $Q_4(\boldsymbol{x})$

## 3.3 Construction of Classifiers

Actually, I define a discriminant function as

$$D(\boldsymbol{x}|\boldsymbol{\alpha}, \beta) = \sum_{n=1}^{N} \alpha_n k(\boldsymbol{x}_n, \boldsymbol{x}) + \beta, \tag{28}$$

where $k(\boldsymbol{x}, \boldsymbol{y}) = \exp(-\gamma||\boldsymbol{x} - \boldsymbol{y}||^2)$. In other words,

$$D(\boldsymbol{x}|\boldsymbol{w}) = \langle \boldsymbol{w}, \boldsymbol{\phi}(\boldsymbol{x}) \rangle, \tag{29}$$

where

$$\boldsymbol{w} = \begin{pmatrix} \alpha_1 & \cdots & \alpha_N & \beta \end{pmatrix}^T, \tag{30}$$

$$\boldsymbol{\phi}(\boldsymbol{x}) = \begin{pmatrix} k(\boldsymbol{x}_1, \boldsymbol{x}) & \cdots & k(\boldsymbol{x}_N, \boldsymbol{x}) & 1 \end{pmatrix}^T. \tag{31}$$

GQCM and RQCM are trained by

$$\text{maximize} \quad \frac{1}{N} \sum_{n=1}^{N} \min\left(y_n \langle \boldsymbol{w}, \boldsymbol{\phi}(\boldsymbol{x}_n) \rangle, 1\right) \tag{32}$$

$$\text{subject to} \quad \boldsymbol{w}^T H \boldsymbol{w} \leq 1, \tag{33}$$

where if $H = H_3$ then the classifier is GQCM, and if $H = H_4$ then the classifier is RQCM.

# 4 Experiments

The experiments with respect to two classifiers of GQCM and RQCM were done with following sample sets:

- Artificial samples,
- 13th UCI Data sets.

## 4.1 Artificial samples

Fig.2(a) shows the discriminant functions of GQCM, LSR and SVM. If I focus on the two outliers of (-5,1) and (5,-1), LSR fits the outliers and the SVM ignores them. The GQCM approach occupies an intermediate position. Fig.2(b) shows the discriminant functions of RQCM and GQCM. When the value of weighting function is large, constraint is strong. Then it is contemplated that RQCM becomes robust for peripheral area.

## 4.2 Performance with UCI data sets

In this experiment, I compared the GQCM and RQCM approaches with existing typical classifiers using thirteen UCI data sets for binary problem. The parameters of weighting function $Q_3(\boldsymbol{x}|\boldsymbol{\mu}, \Sigma)$ are

$$\boldsymbol{\mu}(i) = \mathrm{E}[x_i], \quad \Sigma(i,j) = \begin{cases} \mathrm{Var}[x_i] & i = j \\ 0 & i \neq j. \end{cases} \tag{34}$$

And I set $\lambda = 0.99$ and $\nu = 5$ for $Q_4(\boldsymbol{x})$.

Table 1 contains the results of this experiment. The values in the table are the "average $\pm$ standard deviation" of the error rate for all realizations, and the minimum values for all classifiers are underlined. Columns $\mathrm{S}_1$, $\mathrm{A}_1$, $\mathrm{S}_2$ and $\mathrm{A}_2$ show the results of a significance test (t-test with $\alpha = 5\%$) for differences between GQCM/SVM, GQCM/$\mathrm{AB_R}$, RQCM/SVM and RQCM/$\mathrm{AB_R}$, respectively. A "+" means that the QCMAP error is significantly smaller while a "$-$" means the QCMAP error is significantly larger. The penultimate line for "Mean%", is computed by using the average values of Table 1 as follows. First I normalize the error rates by

$$\left\{ \frac{\text{(particular value)}}{\text{(minimum value)}} - 1 \right\} \times 100[\%] \tag{35}$$

for each data set. Next the "average" values are computed for each classifier. This evaluation method is taken from [5]. The last line shows the average of p-value between "particular" and "minimum" (i.e., minimum p-value is 50%).

# 5 Discussions

I have shown that the QCMAP approach includes both LSR and the SVM, and two novel classifiers GQCM and RQCM. GQCM is characterized not only as regularized LSR, but also as an intermediate classifier between LSR and SVM. If we make the variance parameter $\Sigma$ in $Q_3(\boldsymbol{x}|\mu, \Sigma)$ very large, the weighting function becomes uniform and the classifier tends towards the SVM. On the other hand, when training samples are distributed normally, if we set $\mu$ and $\Sigma$ to be their maximum likelihood estimators, the GQCM classifier becomes similar to LSR.

RQCM is characterized as a robust classifier for peripheral area. According to Mean% and p-value, the RQCM classifier is the best of all the classifiers considered.

It should be noted that the QCMAP classifiers produce excellent results despite not having a regularization parameter. In general, the QCMAP constraint can be regarded as a special case of $\boldsymbol{w}^T H \boldsymbol{w} < \rho$, with regularization parameter $\rho$. If I adjust $\rho$ to optimize, its classifier could be better. However, in terms of the clarity of the theory, a classifier without a regularization

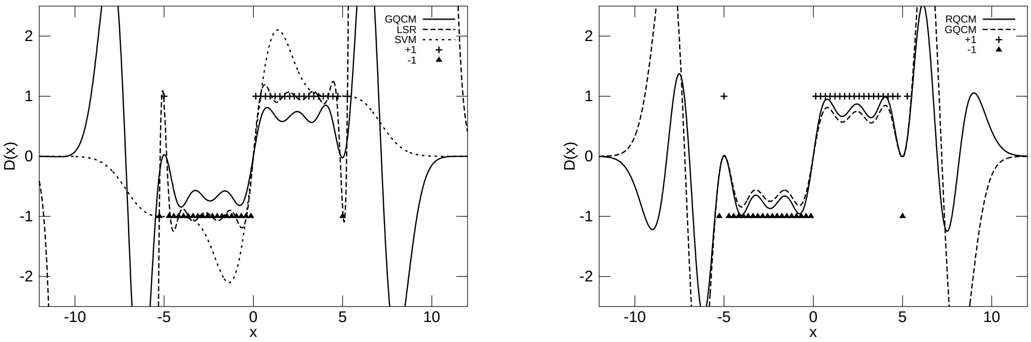


(a) LSR, SVM, and GQCM (b) GQCM and RQCM

Figure 2: Artificial experiments: the lines depict discriminant functions of each classifiers. '+' and black triangles depict the training samples of each categories +1 and −1, respectively

Table 1: Experimental result

| | GQCM | $S_1$ | $A_1$ | RQCM | $S_2$ | $A_2$ | LSSVM | SVM | KFD | AB | $AB_R$ |
|---|---|---|---|---|---|---|---|---|---|---|---|
| Banana | $10.5 \pm 0.5$ | + | + | $10.4 \pm 0.4$ | + | + | $10.6 \pm 0.5$ | $11.5 \pm 0.7$ | $10.8 \pm 0.5$ | $12.3 \pm 0.4$ | $10.9 \pm 0.4$ |
| B.Cancer | $25.6 \pm 4.1$ | | | $24.6 \pm 4.3$ | + | + | $26.7 \pm 4.7$ | $26.0 \pm 4.7$ | $25.8 \pm 4.6$ | $30.4 \pm 4.7$ | $26.5 \pm 4.5$ |
| Diabetes | $23.0 \pm 2.0$ | + | + | $22.7 \pm 2.1$ | + | + | $23.3 \pm 1.7$ | $23.5 \pm 1.7$ | $23.2 \pm 1.6$ | $26.5 \pm 2.3$ | $23.8 \pm 1.8$ |
| F.Solar | $33.5 \pm 1.5$ | − | + | $33.3 \pm 1.8$ | − | + | $34.2 \pm 1.7$ | $32.4 \pm 1.8$ | $33.2 \pm 1.7$ | $35.7 \pm 1.8$ | $34.2 \pm 2.2$ |
| German | $23.9 \pm 2.3$ | | | $23.9 \pm 2.1$ | | | $23.6 \pm 2.2$ | $23.6 \pm 2.1$ | $23.7 \pm 2.2$ | $27.5 \pm 2.5$ | $24.3 \pm 2.1$ |
| Heart | $15.5 \pm 2.8$ | | + | $15.1 \pm 3.1$ | + | + | $16.6 \pm 3.6$ | $16.0 \pm 3.3$ | $16.1 \pm 3.4$ | $20.3 \pm 3.4$ | $16.5 \pm 3.5$ |
| Image | $3.4 \pm 0.7$ | − | − | $3.1 \pm 0.5$ | | − | $3.0 \pm 1.6$ | $3.0 \pm 0.6$ | $4.8 \pm 0.6$ | $2.7 \pm 0.7$ | $2.7 \pm 0.6$ |
| Ringnorm | $1.9 \pm 0.1$ | − | − | $1.7 \pm 0.2$ | − | − | $1.6 \pm 0.2$ | $1.7 \pm 0.1$ | $1.5 \pm 0.1$ | $1.9 \pm 0.3$ | $1.6 \pm 0.1$ |
| Splice | $10.4 \pm 0.7$ | + | − | $10.5 \pm 0.5$ | + | − | $11.0 \pm 1.6$ | $10.9 \pm 0.7$ | $10.5 \pm 0.6$ | $10.1 \pm 0.5$ | $9.5 \pm 0.7$ |
| Thyroid | $4.2 \pm 2.4$ | + | | $4.1 \pm 2.1$ | + | | $4.7 \pm 2.3$ | $4.8 \pm 2.2$ | $4.2 \pm 2.1$ | $4.4 \pm 2.2$ | $4.6 \pm 2.2$ |
| Titanic | $22.1 \pm 1.0$ | + | + | $22.1 \pm 0.9$ | + | + | $22.5 \pm 0.9$ | $22.4 \pm 1.0$ | $23.2 \pm 2.0$ | $22.6 \pm 1.2$ | $22.6 \pm 1.2$ |
| Twonorm | $2.6 \pm 0.2$ | + | + | $2.6 \pm 0.2$ | + | + | $2.8 \pm 0.2$ | $3.0 \pm 0.2$ | $2.6 \pm 0.2$ | $3.0 \pm 0.3$ | $2.7 \pm 0.2$ |
| Waveform | $9.7 \pm 0.4$ | + | | $9.8 \pm 0.4$ | | | $9.8 \pm 0.5$ | $9.9 \pm 0.4$ | $9.9 \pm 0.4$ | $10.8 \pm 0.6$ | $9.8 \pm 0.8$ |
| Mean% | 6.0 | | | 3.4 | | | 6.7 | 7.8 | 9.1 | 14.5 | 4.7 |
| P-value | 80.9 | | | 71.3 | | | 93.6 | 91.1 | 86.0 | 94.8 | 90.8 |

parameter that has theoretical grounding is superior to a classifier with an unknown regularization parameter.

# 6 Conclusions

In this research, I have proposed a "quadratically constrained maximum a posteriori" (QCMAP) estimation procedure and proven that it reduces to LSR and the SVM upon choosing appropriate weighting functions.

Furthermore, I have proposed two novel classifiers "Gaussian QCMAP" (GQCM) classifier and "robust QCMAP" (RQCM) classifier. As the experimental results, the usefulness and significance of QCMAP classifiers have been demonstrated.

# References

[1] Gavin C. Cawley and Nicola L. C. Talbot. Preventing over-fitting during model selection via Bayesian regularisation of the hyper-parameters. *J. Mach. Learn. Res.*, 8:841–861, May 2007.

[2] M. Lobo, L. Vandenberghe, S. Boyd, and H. Lebret. Applications of second-order cone programming, Nov. 1998.

[3] S. Mika, G. Ratsch, J. Weston, B. Scholkopf, and K.R. Mullers. Fisher discriminant analysis with kernels. In *Neural Networks for Signal Processing IX, 1999. Proceedings of the 1999 IEEE Signal Processing Society Workshop*, pages 41 –48, August 1999.

[4] Nopriadi and Y. Yamashita. Maximum a posteriori based kernel classifier trained by linear programming. *LNCS*, 6218:493–502, 2010.

[5] G. Rätsch, T. Onoda, and K.R. Müller. Soft margins for adaboost. *Tech. Rep. NC-TR-1998-021, Royal Holloway College, University of London, UK*, 42(3):287–320, 1998.

[6] 小島政和, 水野真治, 土谷隆, and 矢部博. **内点法**. 朝倉書店, 2001.

# Selective catalytic reduction of NO over $TiO_2$-$ZrO_2$ supported metal catalysts

Student Number: 09M18137 Name: Yang WANG Supervisor: Hirofumi HINODE

# $TiO_2$-$ZrO_2$ 担持金属触媒による NO 選択還元

王 楊

本研究では、$TiO_2$-$ZrO_2$ 担持金属触媒を用い、過剰酸素存在下でプロペンを還元剤とする NO の選択還元反応の活性について検討した。$TiO_2$-$ZrO_2$ へ $Mn_2O_3$ を機械的に混合したところ、活性が向上し、250℃付近で NO を $N_2$ への転化率が 71%であった。反応系に水蒸気が存在する条件で同様な実験を行ったところ、水蒸気存在下での失活は観測されなかった。そこで、NO が生成した $NO_2$ とプロペンが反応して $N_2$ を生じる反応機構が推定できる。

## 1. Introduction

Nitrogen oxides (NO, $NO_2$ and $N_2O$) are the major sources of air pollution and can cause photochemical smog, acid rain and ozone depletion. About 50% of these nitrogen oxides are emitted from automobiles [1]. In automobiles, three-way catalysts are used to elimate HC, CO and NOx simultaneously at stoichiometric condition. However, it requires specific air-fuel ratio and cannot work in lean-burn condition. Therefore, it is necessary to develop new catalysts to reduce nitrogen oxides in lean-burn condition. Among all treatment methods, selective catalytic reduction by unburned hydrocarbons existing in exhaust gas (HC-SCR) is gaining attention, because of its potential ability to remove NO from oxygen-rich exhaust. However, there is still no practical catalyst that has been discovered so far.

$TiO_2$-$ZrO_2$ is known of its high BET surface area and strong mechanical strength, and is widely used in many reactions as catalyst [2]. A study on the performance of Cu-supported $TiO_2$-$ZrO_2$ in HC-SCR reported catalytic activity [3]. On the other hand, Nb-supported $TiO_2$ and Mn-supported $TiO_2$ were also investigated [4] [5] [6].

It was also suggested that NO reduction is carried out by the reaction to generate $NO_2$ followed by the reaction of $NO_2$ with hydrocarbons [4].Metal oxide was thought to accelerate the formation of $NO_2$ [5][6][7].Therefore, researchers are aiming at increasing activity of the catalyst further by adding metal oxide to catalyst. M. Misono et al. showed that addition of $Mn_2O_3$ to Ce-ZSM-5 was enhanced the oxidation of NO to $NO_2$ and oxidative decomposition of organic intermediates containing nitrogen and oxygen[8].

Based on these reports, $Mn_2O_3$ was selected as metal oxide that would be added to the catalyst, and the activity of developed catalyst was tested.

Therefore, in this study, the catalytic activity of Nb-supported $TiO_2$-$ZrO_2$ (Nb/$TiO_2$-$ZrO_2$) catalyst and Mn-supported $TiO_2$-$ZrO_2$ (Mn/$TiO_2$-$ZrO_2$) for the reduction of NO with propene in the presence of $O_2$ was investigated.

## 2. Experimental

### 2.1 Materials

First, $TiO_2$-$ZrO_2$ composite support was prepared by co-precipitation method [9]. And then M/$TiO_2$-$ZrO_2$(M=Nb,Mn)) was prepared by impregnation method using the following procedures:

The $NH_4[NbO(C_2O_4)_2(H_2O)_2](H_2O)_7$ or $MnCO_3$・$H_2O$ was added into 300 mL of ion-exchanged water and then the $TiO_2$-$ZrO_2$ was added to the mixture followed by stirring at room temperature for 24 hours. After that, the mixture was dried up at about 100°C for 24 hours, and calcined at 550°C for 4 hours under air flow.

(Mn+Nb)/$TiO_2$-$ZrO_2$ was prepared by co-impregnation method by impregnating $TiO_2$-$ZrO_2$ with Nb and Mn simultaneously. (Mn-Nb)/$TiO_2$-$ZrO_2$ was prepared by consecutive impregnation method from $TiO_2$-$ZrO_2$ with Nb/$TiO_2$-$ZrO_2$ prepared firstly followed by impregnation with Mn using $MnCO_3$・$H_2O$ as precursor.

$Mn_2O_3$+($TiO_2$-$ZrO_2$) was prepared by mixing $Mn_2O_3$ and $TiO_2$-$ZrO_2$ mechanically. $Mn_2O_3$ was prepared by calcination of $MnCO_3 \cdot H_2O$ at 600°C for 3 hours under air flow. The mechanically mixed sample was then calcined at 550 °C for 4 hours under air flow.

Finally, all catalysts were pelletized, crushed and sieved into particles with diameter between 0.71~1.00 mm.

## 2.2 Catalytic Activity Measurement

The catalytic activity measurement was carried out in a fixed-bed flow reactor. The reactant gas composition was as followed:1500 ppm of NO, 1500 ppm of $C_3H_6$, 10% of $O_2$, and helium as a balance gas with a total space velocity of 13000 $h^{-1}$ over 0.8 g of catalyst. The reaction temperature was increased stepwise at intervals of 50°C starting from 150°C.

The concentrations of NO and $NO_2$ were measured by NOx analyzer (NOA-7000, Shimadzu Corp.). $N_2O$ and $CO_2$ were analyzed by gas chromatographs (GC-8A, Shimadzu Corp. and GC-390, GL Science CO.) respectively. Catalysts were characterized by TG-DTA, XRD and BET.

The influence of water vapor on the activity of catalyst was investigated by introducing 10 vol. % of water vapor during the reaction. Gas composition and analysis apparatus were the same as stated above.

## 3. Results and Discussion

### 3.1 Catalytic Activity of M/$TiO_2$-$ZrO_2$(M=Nb, Mn)

Figure 1 shows the conversion of NO to $N_2$ over Nb/$TiO_2$-$ZrO_2$ catalysts with Nb loading levels from 0-20wt.%.Every Nb loaded catalyst showed lower catalytic activity than that of bare $TiO_2$-$ZrO_2$.It can be thought that Nb participated in the NO reduction and the optimal loading level of Nb was 15wt.%.

Figure 2 shows the effect of Mn loading levels on the catalyst activity of Mn/$TiO_2$-$ZrO_2$. The loading level of Mn was 0-15wt.%.The conversion of each Mn loaded catalyst decreased. However, the peak temperature of each Mn loaded catalyst shifted to lower temperature. The optimal loading level of Mn was 1wt.%.

### 3.2 Catalytic Activity of (Mn+Nb)/$TiO_2$-$ZrO_2$ and (Mn-Nb)/$TiO_2$-$ZrO_2$

Influence of Mn loading levels on the catalytic activities were also investigated for co-impregnated (Mn+Nb)/$TiO_2$-$ZrO_2$ and consecutively impregnated (Mn-Nb)/$TiO_2$-$ZrO_2$ catalysts. The results were shown in Figure 3 .The loading levels of Nb and Mn were 15wt.% and 1wt.%,respectively.The catalytic activities of both catalysts decreased. For consecutively impregnated catalyst, it is possible that Mn covered Nb active site by impregnation and oxidized $C_3H_6$ to $CO_2$ before $C_3H_6$ could function as reducing agent. This could lead to the decrease of catalytic activity.

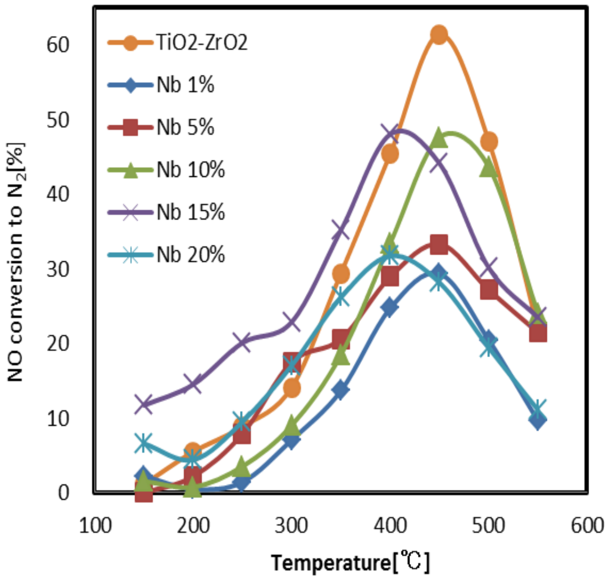


Fig.1 Influence of Nb loading levels on Nb/$TiO_2$-$ZrO_2$for the reduction of NO to N2.

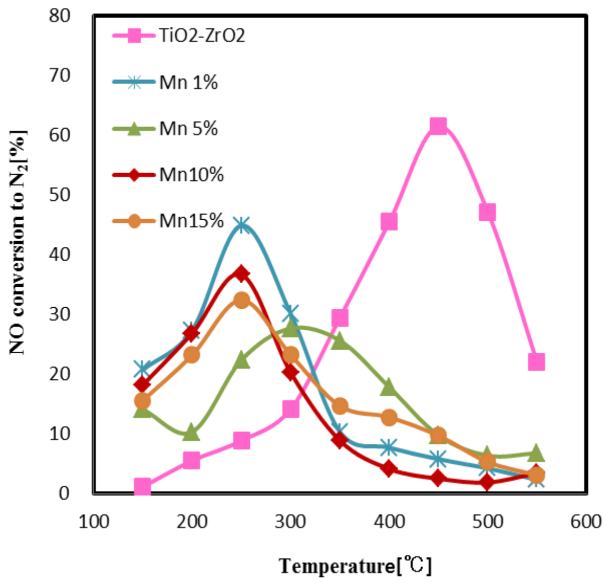


Fig.2 Influence of Mn loading levels on Mn/$TiO_2$-$ZrO_2$ for the reduction of NO to N2.

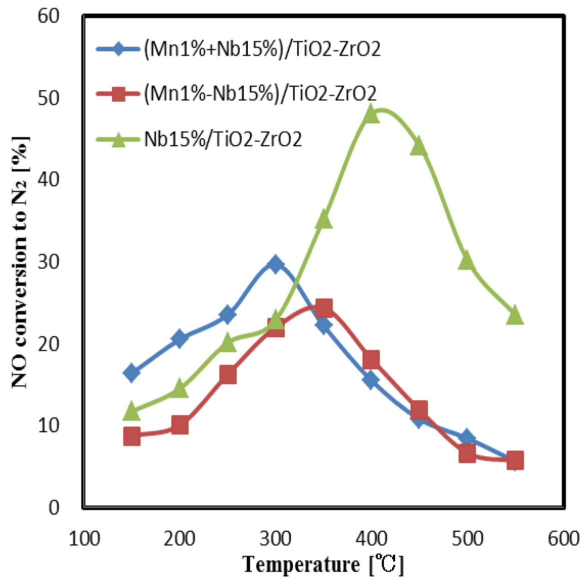


Fig.3 Comparision of (Mn+Nb)/$TiO_2$-$ZrO_2$, (Mn-Nb)/$TiO_2$-$ZrO_2$ and Nb catalyst activities

### 3.3 Catalytic Activity of $Mn_2O_3$+($TiO_2$-$ZrO_2$)

Figure 4 shows the conversion of NO to $N_2$ over mechanically mixed $Mn_2O_3$+($TiO_2$-$ZrO_2$) catalyst using $C_3H_6$ as a reducing agent .For all mechanically mixed catalysts, the maximum conversion of each catalyst shifted to lower temperature. Mechanically mixed $Mn_2O_3$ + ($TiO_2$-$ZrO_2$) with ratio of (1:4) and (1:9) showed higher catalytic activity than that of $TiO_2$-$ZrO_2$. The conversion of NO to $N_2$ over $Mn_2O_3$+ ($TiO_2$-$ZrO_2$)(1:9)catalysts showed maximum conversion of NO to $N_2$ reached 71% at 250°C.

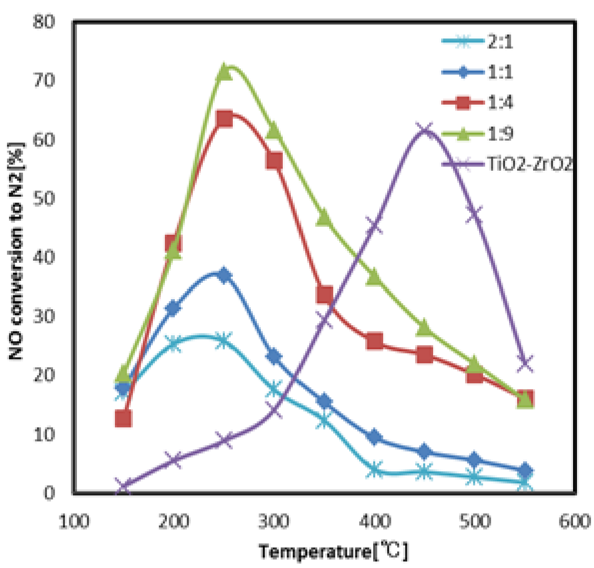


Fig.4 Influence of $Mn_2O_3$:($TiO_2$-$ZrO_2$) ratio on mechanically mixed $Mn_2O_3$+($TiO_2$-$ZrO_2$) catalyst

The conversion of NO to $N_2$, $NO_2$ and $N_2O$, and oxidation of $C_3H_6$ to $CO_2$ over mechanically mixed $Mn_2O_3$+($TiO_2$-$ZrO_2$)(1:9) catalyst are shown in Figure 5. The activities of NO conversion to $N_2$ and $C_3H_6$ conversion to $CO_2$ were improved at low temperature . Small amount of $N_2O$ was produced in the low temperature region below 350°C. $NO_2$ formation decreased in the temperature region where the conversion of NO to $N_2$ was high, and increased again in the temperature region where the conversion of NO to $N_2$ decreased. This result confirmed the reaction mechanism that NO was oxidized to $NO_2$ before it was subsequently reduced to $N_2$. $NO_2$ formation was accelerated at higher temperature because of the oxidation. This indicated that addition of $Mn_2O_3$ enhanced formation of $NO_2$ and activation of propene. Up to 250°C, the conversion of $C_3H_6$ to $CO_2$ showed similar tendency with the conversion of NO to $N_2$ in which the conversion increased with increasing temperature. It means $C_3H_6$ was used as reducing agent to produce $N_2$. At temperature higher than 250°C, the conversion of $C_3H_6$ to $CO_2$ increased until it reached at 100%.In this region, $C_3H_6$ was probably just oxidized by reaction with $O_2$.

Catalyst should be resistant to water vapor for practical use because exhaust gas normally contains water vapor. Figure 6 shows comparison of mechanically mixed $Mn_2O_3$+($TiO_2$-$ZrO_2$)(1:9) catalyst activity with or without the presence of water vapor. Because of the water vapor, the conversion of NO to $N_2$ shifted to higher temperature slightly although no activity inhibition was observed. The reason is considered that the high catalytic activation under high temperature condition. Another is that the active sites for the NO reduction to $N_2$ are activated by water vapor. On the other hand, in this experiment, the water vapor did not show obvious effect on the $C_3H_6$ combustion. NO conversions to $N_2O$ and $NO_2$ profile (not shown in the figure) were similar regardless of the existence of water vapor.

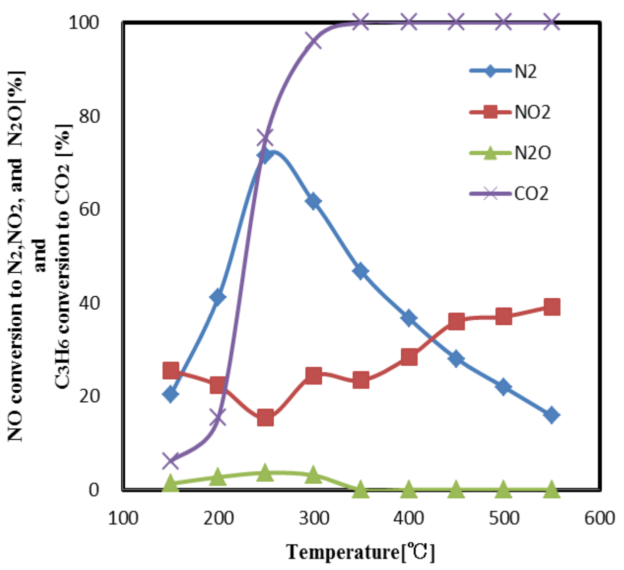


Fig.5 Catalytic activity of $Mn_2O_3$+($TiO_2$-$ZrO_2$)(1:9)

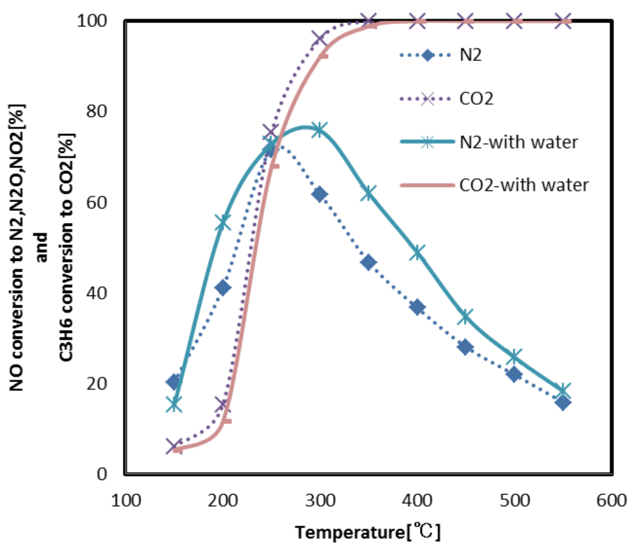


Fig.6 Catalytic activity of $Mn_2O_3$+ ($TiO_2$-$ZrO_2$) (1:9) with water vapor.

### 3.4 Characterization of Catalyst

The BET surface areas of Nb catalysts and Mn catalysts are summarized in Table 1.

| *Catalysts (After calcination)* | *Specific Surface Area [m2/g]* |
|---|---|
| $TiO_2$-$ZrO_2$ | 252.6 |
| Mn1%/($TiO_2$-$ZrO_2$) | 45.6 |
| Nb15%/($TiO_2$-$ZrO_2$) | 67.4 |
| $Mn_2O_3$+($TiO_2$-$ZrO_2$)(1:9) | 42.0 |
| (Mn1%+Nb15%)/($TiO_2$-$ZrO_2$) | 50.1 |

The surface area of $TiO_2$-$ZrO_2$ catalyst after calcination was 252.6$m^2$/g. After impregnation with Nb or Mn, the surface area decreased. It was suggested that no obvious relationship between BET and NO activity by many researchers [3] [5] [6].And this was also confirmed in this experiment.

## 4. Conclusion

Enhancements of $C_3H_6$-SCR activity were observed when $TiO_2$-$ZrO_2$ was mechanically mixed with $Mn_2O_3$.The maximum conversion of NO to $N_2$ was 71% at 250°C. The effect of $Mn_2O_3$ addition to Nb/$TiO_2$-$ZrO_2$ catalyst depends on the preparation method. $Mn_2O_3$ added by impregnation was thought to cover the active site of Nb/$TiO_2$-$ZrO_2$.

Mechanically mixed $Mn_2O_3$+($TiO_2$-$ZrO_2$)(1:9) catalyst did not show the deactivation caused by water vapor. As for the reaction mechanism, it is proposed that NO is oxidized to $NO_2$ and then reacts with $C_3H_6$ to $N_2$.

## References

[1] H.Schneider, U.Scharf, A.Wokaun, A.Baiker, J.Catal.147, 545 (1994)

[2] B.M.Reddy, P.M.Sreekanth, Y .Yamada, Q.Xu. T.Kobayashi, Appl.Catal. A 228(2002) 269-278.

[3] N.Sakata: Master Thesis, Tokyo Institute of Technology (2003)

[4] H.Kawai: Master Thesis, Tokyo Institute of Technology (2004)

[5] C.Tang: Master Thesis, Tokyo Institute of Technology(2006)

[6] M.Makii: Master Thesis, Tokyo Institute of Technology(2006)

[7] H.Hamada, Y.Kintaichi, M.Sasaki and T.Ito and M.Tabata, Appl. Catal,70,L15(1991)

[8] M.Misono, et al,Catal.Today,38 (1997)157

[9] Kazuhiro Ito, Shuichi Kakino, Keita Ikeue, Masato Machida, "NO adsorption/desorption property of $TiO_2$-$ZrO_2$ having tolerance to $SO_2$ poisioning,"Appl. Catal. B 74 pp.137-143, February 2007

# Applicable condition of linear approximation for boost switching regulator ～For charging tiny electric energy to capacitor～

Student Number: 09M18143 Name: HUANG Shu Supervisor: TAKAHASHI Kunio

# 昇圧スイッチングレギュレータ回路に対する線形近似解の適用可能条件 ～些末電力のキャパシタに対する蓄積のための研究～

黄 舒

スイッチングレギュレータの昇圧回路方式を用いて，キャパシタにエネルギーを蓄積するシステムを設計するため，解析解が有用である．本研究では，解析解を求めるために，スイッチングレギュレータの昇圧回路の線形近似モデルを構築し，そのモデルに対する解析解の適用可能条件を理論的および実験的に検討した．

## 1 Introduction

Though there is a lot of tiny electric energy around us such as light, winds, water flow and so on, the energy has not been used yet. If it is possible to charge the renewable energy around us, the anxiety to the future of humanity can be reduced. But it is necessary to design an efficient charge system to use it, because the renewable energy is so tiny. At present, in the use of renewable energy, the provide of steady energy has been required [1]. But it is worth designing from the viewpoint of charge the renewable with a high energy efficiency, even if the provide of steady energy is unsteady.

As a charge device, compared with storage battery,capacitor is used for high energy efficiency. For charging tiny electric energy, a booster is needed because the capacitor can efficiently charge energy with high voltage.The switching regulator is used for boosting the voltage [2].

For charging the energy with high efficiency with switching regulator,it is necessary to design a switching regulator and analytical solution is important. Therefore, a linear approximation model is necessary to obtain analytical solution and it is useful to examine the applicable condition of the approximation model.

Therefore, In order to design an efficient charge system for charging TEE to capacitor, it is necessary to introduce the linear approximation model of switching regulator and verify the applicable condition of the linear approximation model theoretically and experimentally.

## 2 Theory

### 2.1 Linear approximation model

Figure 1 shows the switching regulator.

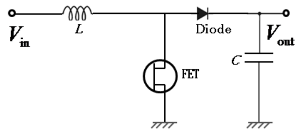


Fig. 1: switching regulator

In the switching regulator, the inductor, FET and diode are nonlinear, it is difficult to obtain analytical solution by using the nonlinear parameters. Therefore, considering the internal resistance of the inductor, FET and diode, a linear approximation model is showed as Figure 2.

Then, as the input voltage from the tiny electric energy, there are a variety of power supplies. In order to design the optimum parameters of the switching regulator,the input voltage $V_{in}$ is assumed to be a simple power supply, a constant-voltage DC power supply, showed as Figure 2.

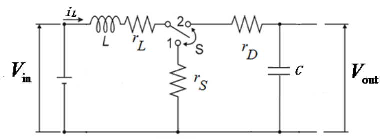


Fig. 2: Linear approximation model-1

In the model, $L$ is the inductance of the inductor, inductor, FET and diode are approximated as the resistances $r_L, r_D, r_S$ for considering the energy loss of the inductor, FET, diode. $T_1$ is the time interval when the switch on 1, $T_2$ is the time interval when the switch on 2, $T$ is the switching period, $T = T_1 + T_2$, $D$ is the duty ratio, $D = \frac{T_2}{T}$.

$L, r_L, r_D, r_S$ are the circuit parameters, $T$ and $D$ are the control parameters. For charging the tiny electric energy, it is necessary to determine the control parameters.

Then, in order to determine the control parameters, the voltage of capacitor is assumed to be a constant voltage, for assuming the capacitor with large enough capacity as the voltage of the capacitor does not change in one period.

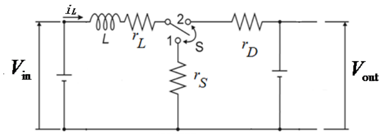


Fig. 3: Linear approximation model-2

$i_1$ is the inductor current when the switch on 1 and $i_2$ is the inductor current when the switch on 2. The positive direction of $i_L$ is showed in Figure 2.

When the switch is on 1,

$$V_{in} = (r_L + r_S)i_1 + L\frac{di_1}{dt} \tag{1}$$

When the switch is on 2,

$$V_{in} - V_{out} = (r_L + r_D)i_2 + L\frac{di_2}{dt} \tag{2}$$

From the condition of continuity of current, showed as eq.(3) and eq.(4).

$$i_1(t=0) = i_2(t=T_2) \tag{3}$$

$$i_1(t=T_1) = i_2(t=0) \tag{4}$$

The inductor current $i_1$ and $i_2$ can be expressed as eq.(5) and eq.(6).

$$i_1 = \frac{(1-e^{\frac{-R_2T_2}{L}})(\frac{V_{in}-V_{out}}{R_2} - \frac{V_{in}}{R_1})}{1-e^{\frac{-(R_1T_1+R_2T_2)}{L}}} e^{\frac{-R_1}{L}t} + \frac{V_{in}}{R_1} \tag{5}$$

$$i_2 = \frac{(1-e^{\frac{-R_1T_1}{L}})(\frac{V_{in}}{R_1} - \frac{V_{in}-V_{out}}{R_2})}{1-e^{\frac{-(R_1T_1+R_2T_2)}{L}}} e^{\frac{-R_2}{L}t} + \frac{V_{in}-V_{out}}{R_2} \tag{6}$$

Where,

$$R_1 = r_L + r_S, R_2 = r_L + r_D, T = T_1 + T_2$$

The electric charge per a unit time of the capacitor can be expressed as eq.(7).

$$\begin{aligned} q &= \frac{Q}{T} = \frac{\int_0^{T_2} i_2 d_t}{T} \\ &= \frac{1}{R_2T}[L\frac{(1-e^{\frac{-R_1T_1}{L}})(\frac{V_{in}}{R_1} - \frac{V_{in}-V_{out}}{R_2})}{1-e^{\frac{-(R_1T_1+R_2T_2)}{L}}}(1-e^{\frac{-R_2T_2}{L}}) \\ &+ (V_{in}-V_{out})T_2] \end{aligned} \tag{7}$$

Where,

$$\tilde{T_1} = \frac{R_1T_1}{L}, \tilde{T_2} = \frac{R_1T_2}{L}, \tilde{a} = \frac{V_{out}}{V_{in}}$$

$$D = \frac{\tilde{T_2}}{\tilde{T}}, \tilde{T} = \tilde{T_1} + \tilde{T_2}, \tilde{r} = \frac{R_2}{R_1}$$

$\tilde{r} = \frac{R_2}{R_1}$ is approximated as 1, because the internal resistance of inductor is larger than FET and diode.

The electric charge can be expressed by normalized parameters as eq.(8).

$$q = \frac{V_{in}}{R_1}\left[\frac{\tilde{a}}{\tilde{T}}\frac{(1-e^{-(1-D)\tilde{T}})(1-e^{-D\tilde{T}})}{(1-e^{-\tilde{T}})} - (\tilde{a}-1)D\right] \tag{8}$$

From $\tilde{a} = \frac{V_{out}}{V_{in}}$, $\tilde{a}$ is larger than 1. Therefore, $(\tilde{a}-1)D$ is positive. When $f(D,\tilde{T})$ as eq.(9) is large, The electric charge will be large.

$$f(D,\tilde{T}) = \frac{1}{\tilde{T}}\frac{(1-e^{-(1-D)\tilde{T}})(1-e^{-D\tilde{T}})}{(1-e^{-\tilde{T}})} \tag{9}$$

Figure 4 shows the relation between $\tilde{T}$ and $f(D,\tilde{T})$. The horizontal axis is $\tilde{T}$, the vertical axis is $f(D,\tilde{T})$. From figure 4, when $\tilde{T}$ is small, $f(D,\tilde{T})$ will be large. From $\tilde{T} = \frac{R_1T}{L}$, the inductance of the inductor should be large.

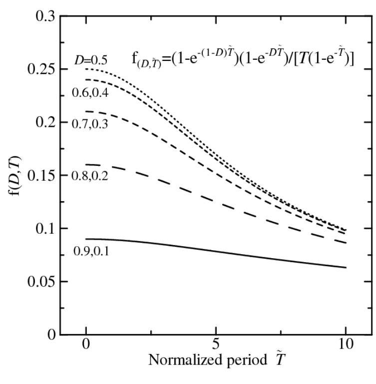


Fig. 4: The relation between $\tilde{T}$ and $f(D,\tilde{T})$

When $\tilde{T}$ is small, the electric charge per a unit of the capacitor approaches $\frac{V_{in}}{R_1}[-\tilde{a}(D-\frac{1}{2\tilde{a}})^2 + \frac{1}{4\tilde{a}}]$, when $D = \frac{1}{2\tilde{a}}$.

Therefore, as control parameters, the duty ratio can be controlled by $D = \frac{1}{2\tilde{a}} = \frac{V_{in}}{2V_{out}}$.

## 2.2 Applicable condition of linear approximation

In the linear approximation model, The diode is approximated to resistance. The reverse current might flow to the inductor when the voltage of the capacitor grows. In the experiment, the diode is used, the reverse current can not flow to the inductor. The inductor current in the model should be positive.

When $t = nT(n > 0)$,

$$i_1 = \frac{(1 - e^{\frac{-R_2 T_2}{L}})(\frac{V_{in} - V_{out}}{R_2} - \frac{V_{in}}{R_1})}{1 - e^{\frac{-(R_1 T_1 + R_2 T_2)}{L}}} e^{\frac{-R_1}{L}t} + \frac{V_{in}}{R_1} > 0 \tag{10}$$

$$D < -\frac{ln(1 - \frac{1 - e^{-\tilde{T}}}{\tilde{a}})}{\tilde{T}} \tag{11}$$

$$\tilde{T} = \frac{R_1 T}{L}, \tilde{a} = \frac{V_{out}}{V_{in}}$$

From eq.(11) and $D = \frac{1}{2\tilde{a}}$, the applicable condition of linear approximation can be showed by figure 5.

From figure 5, when$V_{in} = 0.5$V, $V_{out} = 500$V, the input voltage is boosted to 1000 times, the duty ratio can be controlled by $D = \frac{1}{2\tilde{a}}$ when $\tilde{T} = 0.5, 1$. But when $\tilde{T} = 2, 4, 6$, the reverse current flows to the inductor. When the reverse current flows to the inductor, the duty ratio can not be controlled by $D = \frac{1}{2\tilde{a}}$.

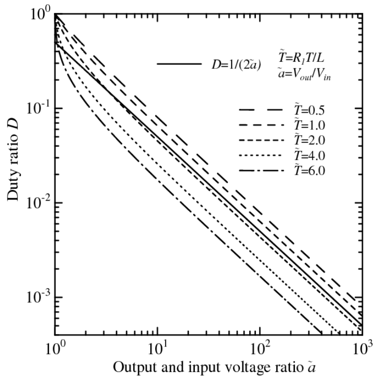


Fig. 5: Applicable condition of linear approximation

$D = \frac{1}{2\tilde{a}} = -\frac{ln(1 - \frac{1 - e^{-\tilde{T}}}{\tilde{a}})}{\tilde{T}}$ is the boundary condition of linear approximation.

Then, the duty ratio $D$ can be controlled by $D = \frac{1}{2\tilde{a}}$ from $\tilde{a} = 0$ to the boundary condition.

# 3 Experiments

## 3.1 Experimental method

In the experiment, in order to examine the applicable condition of the linear approximation, the inductor current and the booster voltage are measured at 3 kinds of conditions, in the range of applicable condition, the boundary condition of linear approximation and out of the applicable condition..

A function generator is used to control the switching frequency of the FET.

At $\tilde{T} = 3.67$, the experiment is done at $A_{11}, D = 0.48, \tilde{a} = 0.7$, $A_{12}, D = 0.48, \tilde{a} = 1.04$ and $A_{13}, D = 0.48, \tilde{a} = 1.28$.

In the same way, at $\tilde{T} = 1.83$, the experiment is done at $A_{21}, D = 0.37, \tilde{a} = 0.96$, $A_{22}, D = 0.37, \tilde{a} = 1.35$ and $A_{23}, D = 0.37, \tilde{a} = 1.7$. At$\tilde{T} = 1.22$, the experiment is done at $A_{31}, D = 0.21, \tilde{a} = 1.9$, $A_{32} D = 0.21, \tilde{a} = 2.36$ and $A_{33} D = 0.21, \tilde{a} = 2.74$.

The experiment result of 9 points showed as figure 6.

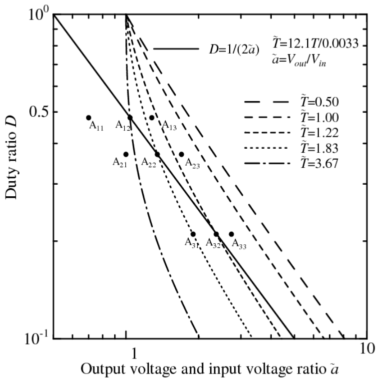


Fig. 6: Applicable condition of linear approximation at $\tilde{T} = 3.67, 1.83, 1.22$

In order to measure the inductor current, a 10Ω resistance is placed between power supply and inductor. The voltages are measured by oscilloscope. In the experiment, the voltage of the resistance and capacitor, and the switching frequency are measured as figure 7.

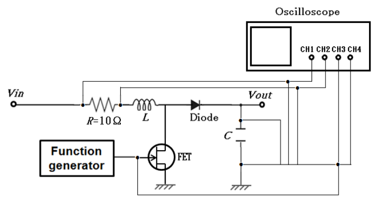


Fig. 7: Experimental method

## 3.2 Experimental equipments

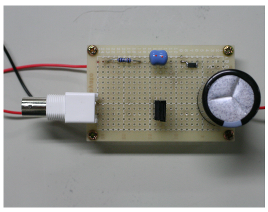

Fig. 8: Experimental equipments

According to section 2.1, the circuit parameters have been determined, FET is N channel MOSFET, K2232, diode is CMS01, inductor is SLF10145, capacitor is SMG series. The internal resistances of inductor, FET are $12.1\Omega, 0.05\Omega$ and the internal resistance of diode is changed between $5\Omega$ and $15\Omega$ because it is nonlinear. The inductance of inductor is $3300\mu$H and the capacity of capacitor is $22000\mu$F.

Figure8 shows the experiment equipments, by the inductor, FET, diode and capacitor.

### 3.3 Experimental results

In the experiment, the inductor current and the booster voltage at 9 points are measured. Here, the experimental results of points $A_{21}, A_{22}, A_{23}$ are showed when $\tilde{T} = 1.83$.

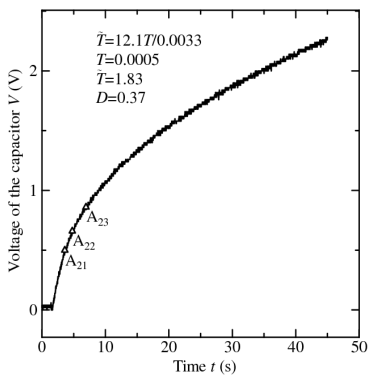


Fig. 9: Booster voltage when $\tilde{T} = 1.83, D = 0.37$

Figure 9 shows the booster voltage when $\tilde{T} = 1.83, D = 0.37$.

Figure 10, Figure 11, Figure 12 shows the inductor current and the booster voltage at the point $A_{21}$, $A_{22}$, $A_{23}$. The horizontal axis is time, the left of the vertical axis is the inductor current and the right of the vertical axis is the booster voltage.

From the results, at $A_{21}, A_{22}, A_{23}$, the booster voltages agree with the theoretical booster voltage, $v = 0.48V, v = 0.63V, v = 0.86V$, are almost constant.

The theory and the experiment of inductor currents almost agree at$A_{21}, A_{22}$. At $A_{22}$ the inductor current is $0A$, when $t = 0.0005$s. But the inductor current does not agree at $A_{23}$ because of the diode. The experimental result shows that the linear approximation is applicable at point $A_{21}$, the point $A_{22}$ is the boundary condition of linear approximation and the point $A_{23}$ is the condition can not be linear approximated.

From the results, the applicable condition of the model has been examined experimentally.

# 4 Conclusion

To design the system to charge the tiny electric energy in the capacitor by using the boost switching regulator, the applicable condition of linear approximation has been examined in the linear approximation model theoretically and experimentally and the applicable condition of linear approximation has been clarified.

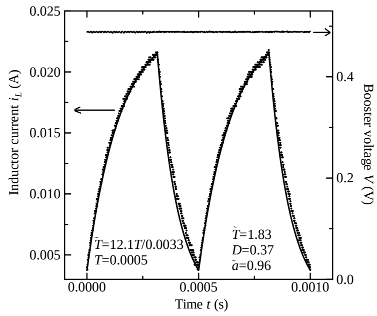


Fig. 10: The inductor current and the booster voltage at $A_{21}$

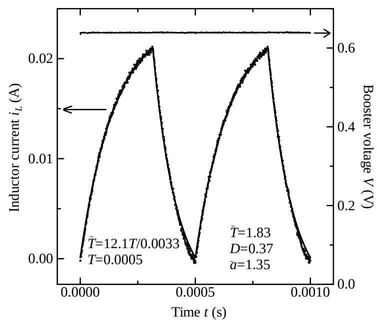


Fig. 11: The inductor current and the booster voltage at $A_{22}$

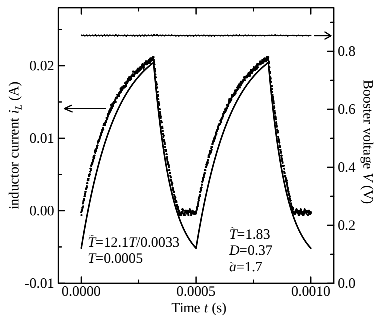


Fig. 12: The inductor current and the booster voltage at $A_{23}$

# References


[1] Jonathan W.Kimball, Theresa L.Flowers,Patrick L.Chapman, Low-Input-Voltage,Low-Power Boost Converter Design Issues, *IEEE POWER ELECTRONICS LETTERS*, **Vol. 2,NO. 3**,(2004)

[2] Otome Keisuke, Effects of conditions of use on the energy efficiency of boost switching regulator, *master thesis*, (2010)

# Decomposition of nitrous oxide over rutile structure titania supported metal catalysts

Student Number : 09M18185 Name : Peng GAO Supervisor : Hirofumi HINODE

# ルチル型チタニア担持金属触媒による $N_2O$ 分解

高 鵬

本研究では、３種類のルチル型チタニア担持金属触媒（鉄、コバルト、ニッケル、バリウム）の $N_2O$ 分解活性について検討した。ルチル型チタニア(602X03)担持コバルト(10%)触媒は最大活性を示し、酸素がない場合で 550℃において $N_2O$ を完全に分解した。10%存在下では $N_2O$ の 100%分解温度は高温側にシフトし、触媒活性を抑制することを確認した。触媒のキャラクタリゼーションは触媒のキャラクタリゼーションはＸ線回折に結晶構造解析、ＢＥＴ比表面積測定などにより行った。

## 1. Introduction

Nitrous oxide ($N_2O$) is a greenhouse gas that greatly contributes to the green house effect and severely destructs the ozone layer in the stratosphere. The major stationary sources of nitrous oxide are the adipic acid and $HNO_3$ processing units, which are responsible for about a quarter of worldwide emissions. Agriculture and fluidized bed combustion processes also contribute to $N_2O$ emission. Vehicles equipped with three-way catalysts contribute as the mobile emission sources when the three-way catalysts deteriorate due to prolonged use. With the increase in concern for environmental protection, efforts have been made to convert $N_2O$ into $N_2$ and $O_2$ before it is released into the atmosphere.

Previous study showed that rutile structure titania had better activity than anatase structure on $N_2O$ decomposition during activity test using $Cu/TiO_2$ catalysts [1].

In this study, the decomposition of $N_2O$ over rutile structure $TiO_2$ supported Fe, Co, Ni and Ba catalysts was investigated.

## 2. Experimental

### 2.1 Catalyst preparation

$M/TiO_2$ (M=Fe, Co, Ni, Ba) catalysts were prepared by impregnation method. $TiO_2$ (602X03, 602X05, 603X03; TohoTitanium co.,LTD.) were used as supports.

In the preparation of $Fe/TiO_2$(example), $TiO_2$ was impregnated in an aqueous solution of $Fe(NO_3)_3{\cdot}9H_2O$ (99.9%, Wako Co.). Each of the solution was stirred at room temperature for one day followed by 12 hours drying up at 70℃. Then the catalyst were calcined at 600℃ for 5 hours under air flow. In order to reduce pressure drop, the catalysts were pelletized, crushed and sieved to between 0.71mm to 1.00mm. The following nomenclatures for the catalyst samples are used: Fe(x wt%)/$TiO_2$ (y) where x means Fe loading levels, and y means $TiO_2$.

The sources of Co, Ni and Ba were $Co(NO_3)_2{\cdot}6H_2O$ (99.5%, Wako Co.), $Ni(NO_3)_2 \cdot 6H_2O$ (99.9%, Wako Co.) and $Ba(NO_3)_2$ (99.9%, Wako Co.), respectively.

### 2.2 Catalytic activity experiment

The catalytic reaction was carried out in a fixed-bed flow reactor under atmospheric pressure, and the reactant gas was prepared by mixing $N_2O$, $O_2$ and He as a balance gas. Then the mixed gas of 1000ppm $N_2O$, 0%/10% $O_2$ and He was fed to the catalyst at flow rate of 5.0-6.0ml/s, which correspond to $16000h^{-1}$ of space velocity.

Gas chromatography (GC323w; GL Science Co., with Porapak N, Porapak Q and Molecular Sieve 13X column) was used to analyze $N_2O$, $N_2$ and $O_2$.

### 2.3 Catalyst characterization

Characterizations of catalysts were performed by TG(TG8120), XRD(MultiFlex), BET(SA3100) and SEM(JSM-5310LV) -EDS(JED-2140).

## 3. Result and discussion

### 3.1 The activity for the decomposition of $N_2O$ over $M/TiO_2$(602X03) (M = Fe, Co, Ni, Ba)

Figure 1 shows the catalytic activity of $M/TiO_2$(602X03) (M= Fe, Co, Ni, Ba) catalysts for $N_2O$ decomposition. The axis is the reaction temperature. The shift to lower temperature region means high activity. The loading level for each sample here was selected from the loading level of the sample with the best performance result.

NO and $NO_2$ were not detected in all condition.

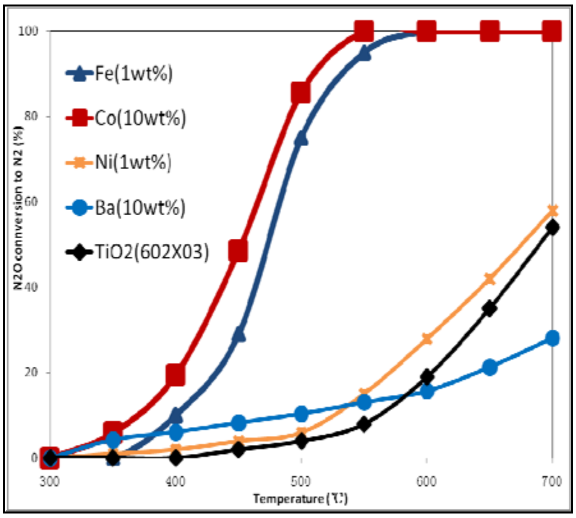


Fig.1 Comparison of the catalytic activity for the decomposition of $N_2O$ over each catalyst without oxygen

Parent $TiO_2$(602X03) calcined at 600℃ decomposed only 58% of $N_2O$ to $N_2$ even at 700℃. When iron or cobalt was supported on $TiO_2$, the catalytic activity was promoted. When Co loading level was 10wt%, the highest catalytic activity for the decomposition of $N_2O$ was achieved. Decomposition of $N_2O$ to $N_2$ over Co(10wt%)/$TiO_2$(602X03) catalysts began at 350℃, and the conversion of $N_2O$ to $N_2$ reached 100% at 550 ℃ without $O_2$. Fe(1wt%)/$TiO_2$(602X03) completely decomposed $N_2O$ at 600℃ without $O_2$.

Ni(10wt%)/$TiO_2$(602X03) decomposed 60% of $N_2O$ at 700 ℃ , and Ba(10wt%)/$TiO_2$(602X03) decomposed only approximately 30% of $N_2O$ even at 700℃. According to XRD results, there was only $NiTiO_3$ or $BaTi_2O_5$ peaks in the catalyst after calcinations while no NiO or BaO peaks appeared. The reason was that the precursor $Ni(NO_3)_2$ and $Ba(NO_3)_2$ reacted with $TiO_2$ during 600 ℃ calcinations, and catalyst activity was inhibited.

### 3.2 The optimum Metal loading level and the effect of $TiO_2$ as support

Figures 2 showed the catalytic activity of Fe/$TiO_2$ for $N_2O$ decomposition prepared from $TiO_2$ (602X03). Fe loading levels(1wt%, 5wt%, 10wt%) of Fe/$TiO_2$(602X03) showed almost the same activities for $N_2O$ decomposition. Therefore the optimum Fe loading levels of Fe/$TiO_2$(602X03) was 1wt%.

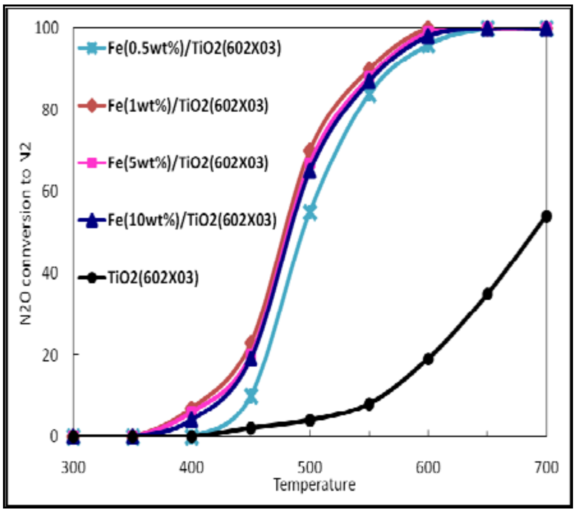


Fig.2 The catalytic activity for the decomposition of $N_2O$ over Fe/$TiO_2$(602X03)

Figures 3 showed the catalytic activity of Co/$TiO_2$ for $N_2O$ decomposition prepared from $TiO_2$ (602X03). The optimum Co loading levels of Co/$TiO_2$(602X03) was 10wt%.

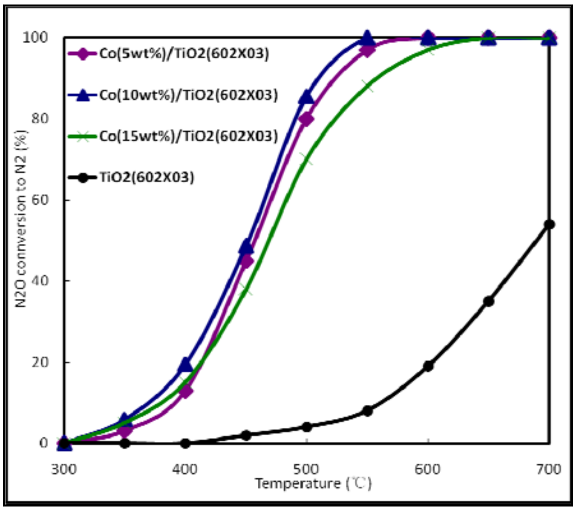


Fig.3 The catalytic activity for the decomposition of $N_2O$ over Co/$TiO_2$(602X03)

Table 1 shows the relationship between the BET specific surface area of $TiO_2$ and the optimum metal loading level of M/$TiO_2$(M=Fe, Co) from the catalytic activity experiments for $N_2O$ decomposition and geometrical calculation from $M_xO_y$ and $M(NO_3)_x$ projected area.

Table 1 Relationship between specific surface area of $TiO_2$ and optimum Fe and Co loading level for the decomposition of $N_2O$

| Support (metal) | Specific surface area ($m^2/g$) before/after | Optimum Metal loading level from experiment | Optimum Metal loading level from geometrical calculation of active site | Optimum Metal loading level from geometrical calculation of precursor |
|---|---|---|---|---|
| 602X03(Fe) | 73.80/32.85 | 1wt% | 2.89wt% ($Fe_2O_3$) | 0.93wt% ($Fe(NO_3)_3$) |
| 602X03(Co) | | 10wt% | 12.56wt% ($Co_3O_4$) | 7.71wt% ($Co(NO_3)_2$) |

The results from Table 1 indicate that the optimum Fe and Co loading level obtained from the catalytic activity experiments was agreed well with on the calculated value from the projected area of precursor($Fe(NO_3)_3$ and $Co(NO_3)_2$). Therefore, when the $TiO_2$ surface was covered with $Fe(NO_3)_3$ or $Co(NO_3)_2$ molecule completely, the catalytic activity for the decomposition of $N_2O$ reached the highest value. If the amount of $Fe(NO_3)_3$ or $Co(NO_3)_2$ loaded exceeded the optimum loading, the catalytic activity remained the same or declined because of sintering of Fe or Co.

Table.2 The optimum metal loading level of M/ $TiO_2$

| Catalyst | Optimum Metal loading level | $T_{100}$(℃) |
|---|---|---|
| Fe/$TiO_2$(602X05) | 1wt% | 600 |
| Fe/$TiO_2$(603X03) | 1wt% | 600 |
| Co/$TiO_2$(602X05) | 5wt% | 600 |
| Co/$TiO_2$(603X03) | 5wt% | 600 |

*$T_{100}$ means the temperature of 100% $N_2O$ conversion.

The optimum metal loading level of the other M/$TiO_2$ were shown in Table 2. The difference of the optimum Co loading level was considered to be related with the difference of the specific surface area of each $TiO_2$.

### 3.3 The effect of calcination temperature

Figures 4 show the catalytic activity of Co(10wt%)/$TiO_2$, Ni(10wt%)/$TiO_2$ and Ba(10wt%)/$TiO_2$ for $N_2O$ decomposition prepared from 602X03 with different calcination temperatures. On the Co(10wt%)/$TiO_2$, the calcination temperatures 400℃ and 600℃ showed the same activity, but 700℃ showed the worse activity than the others. The reason is that $CoTiO_3$ was appeared in the catalyst at higher calcination temperatures. On the Ni(10wt%)/$TiO_2$ and Ba(10wt%)/$TiO_2$, even if on the lower calcination temperature 400℃, the better activity was not showed.

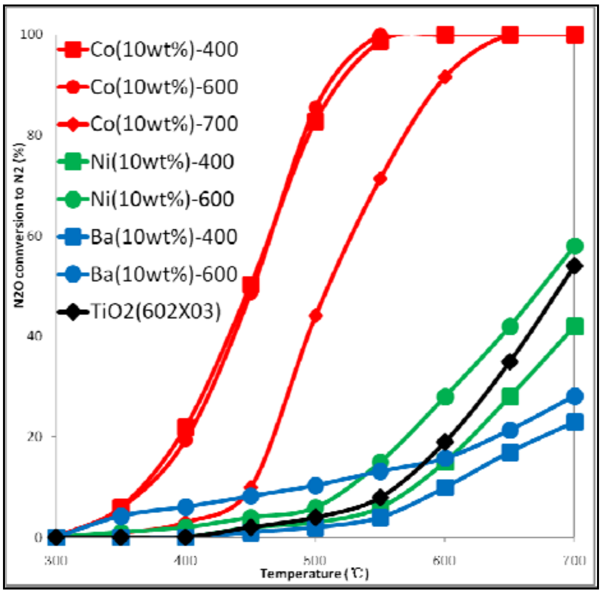


Fig.4 The catalytic activity for the decomposition of $N_2O$ over each catalyst with different calcination temperatures.

### 3.4 The influence of oxygen

Figures 5 shows the catalytic activity of Fe(1wt%)/$TiO_2$ and Co(10wt%)/$TiO_2$ for $N_2O$ decomposition prepared from 602X03 with oxygen(10%). The decomposition of $N_2O$ shifted to the higher temperature by the introduction of oxygen (10%). This result indicated that conversion of $N_2O$ was inhibited by the existence of $O_2$. The reason was that $O_2$ compete with $N_2O$ in the process of adsorption on active site[2].

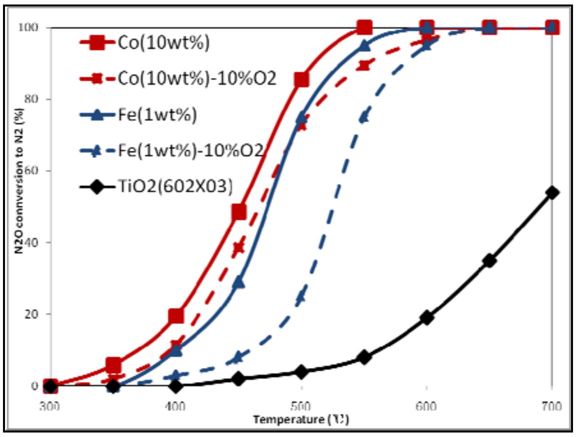


Fig.5 The catalytic activity for the decomposition of $N_2O$ over Fe(1wt%)/$TiO_2$(602X03) and Co(10wt%)/$TiO_2$(602X03) with oxygen(10%)

### 3.5 Characterization of catalysts

Figure 6 shows the results of XRD patterns of each catalyst after calcinations. In Fe(1wt%)/$TiO_2$ and Co(10wt%)/$TiO_2$, $Fe_2O_3$ and $Co_3O_4$ peaks ware appeared, that was confirmed the activity site. $NiTiO_3$ and $BaTi_2O_5$ peaks in the Ni(10wt%)/$TiO_2$ and Ba(10wt%)/$TiO_2$, were not the activity site for $N_2O$ decomposition.

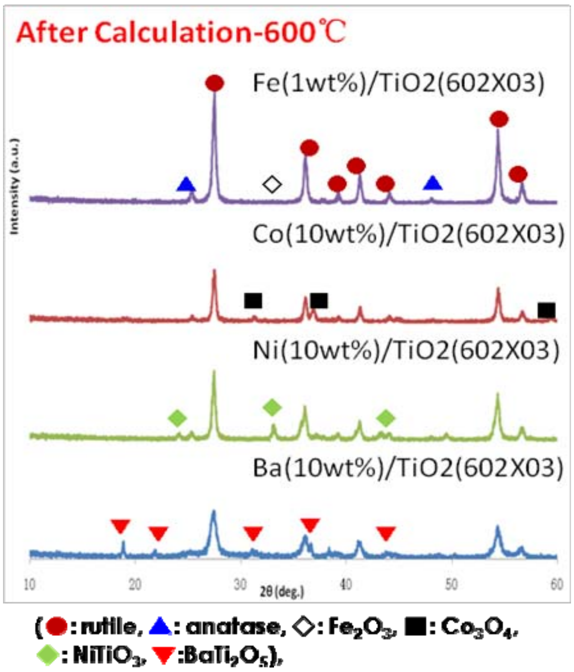


Fig.6 XRD patterns of each catalyst

Figure 7 shows the results of XRD patterns of each catalyst with different calcination temperatures. In Co(10wt%)/$TiO_2$ with 700 ℃ calcination temperatures, $CoTiO_3$ peaks was appeared, and the activity was inhibited. In the Ni(10wt%)/$TiO_2$ and Ba(10wt%)/$TiO_2$ with different calcination temperatures, show the same XRD result.

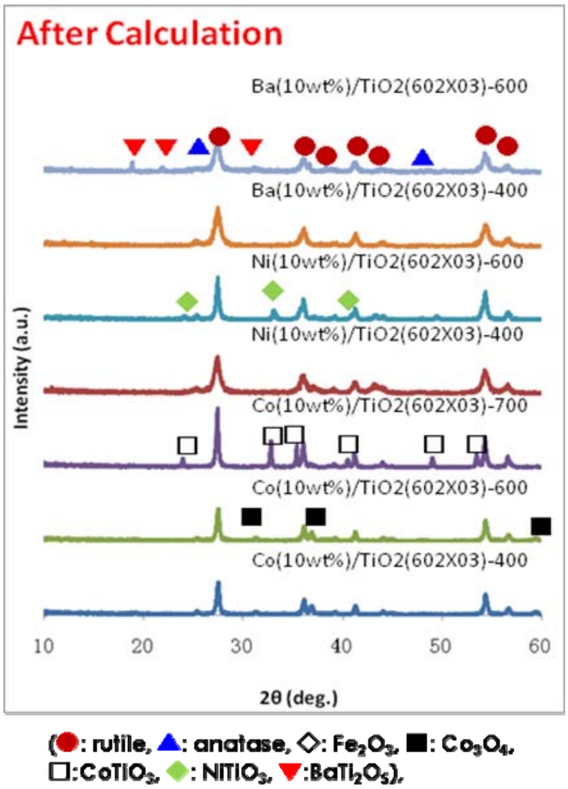


Fig.7 XRD patterns of each catalyst with different calcination temperatures

## 4. Conclusion

Fe/$TiO_2$ and Co/$TiO_2$ exhibited the catalytic activity for $N_2O$ decomposition. Co(10wt%)/$TiO_2$(602X03) showed the best catalytic activity, $N_2O$ was decomposed completely at 550℃ without $O_2$. Ni/$TiO_2$ and Ba/$TiO_2$ did not show the activity, because during the calcinations the precursors reacted with $TiO_2$, and catalyst activity was inhibited.

$N_2O$ decomposition was inhibited by the existence of $O_2$. In Co(10wt%)/$TiO_2$(602X03), the 100% $N_2O$ conversion was showed at 600℃.

## Reference

[1] K.Yanagida, Master thesis, "The decomposition of nitrous oxide over titania supported metal catalysts" Tokyo Institute of Technology (2006).

[2] S. Suarez, M. Yates, A.L. Petre, J.A. Martin, P. Avila and J. Blanco, "Development of a new Rh/$TiO_2$–sepiolite monolithic catalyst for $N_2O$ decomposition" Appl. Catal. B 64 (2006), p. 302.

# Heavy Metal Adsorption by Zeolite from Lake Sludge as Raw Material

Student Number: 09M18172 Name: Yan Shao
Supervisor: Hirofumi Hinode co-supervisor: Nakasaki Kiyohiko

# 湖沼汚泥を原料とした合成ゼオライトによる重金属吸着

邵 妍

閉鎖水域である湖沼に汚染物質が汚泥とともに容易に蓄積され、悪臭や富栄養化等の様々な環境問題を引き起こす。一般的な処理方法として汚泥の浚渫が行われる。しかし浚渫汚泥の埋め立て処理は軟弱地盤の形成や高コスト等の問題点が伴っているため、汚泥の再資源化技術の開発が必要である。本研究では、シリカおよびアルミナに富んだ浚渫汚泥を吸着剤として利用できるゼオライトに転換する技術の開発を行った。種々の反応条件（アルカリ濃度、反応時間、反応温度、Si/Al のモル比およびアルカリ水溶液/固体汚泥質量比）におけるアルカリ水熱合成によってゼオライト Na-P1 やゼオライト Analcime-C 等が生成できた。合成したゼオライトの吸着能力を比較するために陽イオン交換容量(CEC)の測定および重金属吸着実験を行った。

## 1. Introduction

Nowadays, water pollution is becoming a serious environmental problem. Some of the water sources are river, lake and groundwater. Here, we focused on lake because it is a closed water system where pollutants could be accumulated easily. Generally, the sludge in the bottom of a lake is dredged to remove the pollutants and then it is disposed by landfilling. However, there are some problems such as the formation of soft-ground and the shortage of landfilling site. Therefore, an effective use of the dredged lake sludge must be considered.

The main components of lake sludge are silica and alumina, which are the same as the main components of zeolites. Previous studies reported that coal fly ash containing silica and alumina could be converted into zeolites[1-2].

Other studies also reported that zeolites could be synthesized from lake sludge using hydrothermal treatment in sodium hydroxide solution medium[3].

In this study, the hydrothermal syntheses of zeolite from lake sludge in alkali solutions at various Si/Al ratios were carried out and the effect of reaction conditions were investigated. Furthermore, the application of the synthesized zeolites was also investigated.

## 2. Experimental

### 2.1 Synthesis of zeolite

Lake sludge from Kasumigaura was used in this study. After being crushed to particle size less than 150 μm, the sludge was dried at 105°C for 24 hours and sieved. Prior to hydrothermal treatment, lake sludge was mixed with sodium hydroxide (NaOH) solutions with different concentrations and was shaken for 24 hours in a 23 ml Teflon reaction vessel. Molar ratio of silicon to aluminum (Si/Al) was adjusted by adding $Na_2SiO_3$ solution and/or $Al(OH)_3$. The vessel was then put inside an autoclave and incubated at a temperature of 90 to 150°C in an oven for the hydrothermal treatment. After the reaction, the slurry was filtered and the solid phase was washed several times with distilled water to eliminate the excess sodium hydroxide solution.

### 2.2 Characterization

The identifications of crystalline materials in sludge and synthesized zeolite products were carried out by X-ray diffraction analysis (XRD). The surface structure was observed by scanning electron microscopy, energy dispersive X-ray spectroscopy (SEM-EDS).

### 2.3 Cation exchange capacity (CEC) measurement

The cation exchange capacity of zeolite product was determined by sodium acetate method. The sample was saturated with NaOAc solution, and then the $Na^+$ was extracted by $NH_4OAc$ solution. The amounts of released $Na^+$ were measured using Inductively Coupled Plasma – Atomic Emission Spectorometry (ICP-AES).

### 2.4 Heavy metal adsorption

The synthesized zeolites were evaluated on their capability to remove heavy metal in aqueous solutions. 50ml of solution containing different concentrations of $Pb^{2+}$ or $Cd^{2+}$ were poured into a glass bottle with 0.5g sample and were shaken at 150rpm. After equilibration period, solid and liquid were separated by centrifugation and filtration (0.45μm membrane filter). The concentrations of $Pb^{2+}$ or $Cd^{2+}$ in solution were determined by ICP.

## 3. Results and discussion

### 3.1 XRD patterns of zeolite products

**Figure 1** shows XRD patterns of zeolite products obtained at different concentrations of NaOH solutions. Si/Al was 1.9 which is the molar ratio of Si to Al in the raw lake sludge (no adjusting by $Na_2SiO_3$ or $Al(OH)_3$) and heating temperature (T) was 120°C. At NaOH concentrations of 1 to 2 M, zeolite NaP1 phase was observed. Quartz phase that is the main component of sludge was still present. At NaOH concentration of 4 M, Sodium Aluminum Silicate Hydrate phase was detected. Hydrothermal treatments in alkali mediums with different NaOH concentrations could yield different types of zeolite phases.

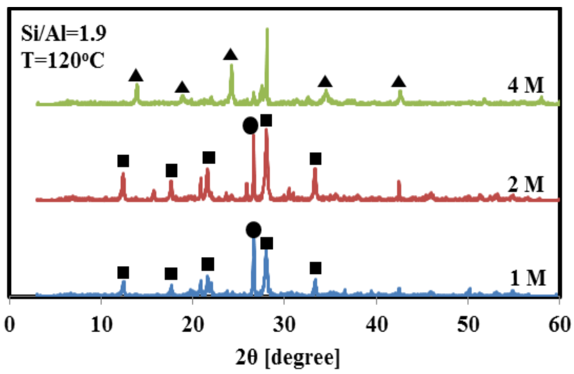


Figure 1 XRD patterns of products prepared with different NaOH concentrations

▲: Sodium Aluminum Silicate Hydrate ($1.08Na_2O!Al_2O_3!1.68SiO_2!1.8H_2O$);

●:Quartz ($SiO_2$); ■:Zeolite Na-P1 ($Na_6Al_6Si_{10}O_{32}.12H_2O$)

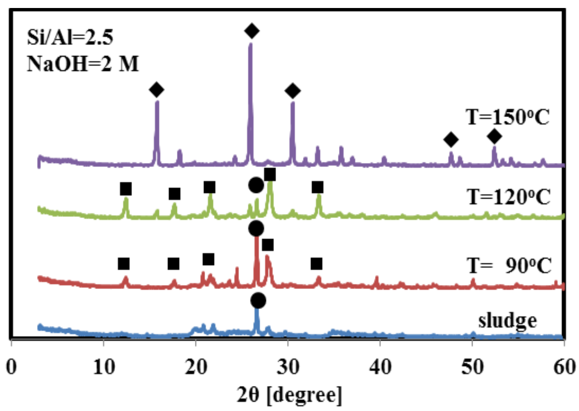


Figure 2 XRD patterns of products prepared at different heating temperatures (T)

◆: Zeolite Analcime-C ($Na(Si_2Al)O_6.H_2O$)

XRD patterns of the products synthesized by hydrothermal treatments at different heating temperatures were shown in **Figure 2**. The amount of quartz was reduced with increasing temperature which indicated that Si was dissolve at higher treatment temperature. The dissolved elements (Si and Al) then formed zeolite Na-P1 type phase at 90-120°C and transformed into zeolite Analcime-C at 150°C.

The liquid to solid ratio (L/S), which was the ratio of the volume of NaOH solution to the weight of raw sludge in Teflon reaction vessel, was changed from 2 to 8 ml/g. The XRD patterns of the products were shown in **Figure 3**. Only zeolite Na-P1 and quartz could be observed at all L/S values. Because the shape of all graphs almost the same, so the reaction temperature is still low could be considered. The L/S ratio showed no effect on the type of zeolite formed.

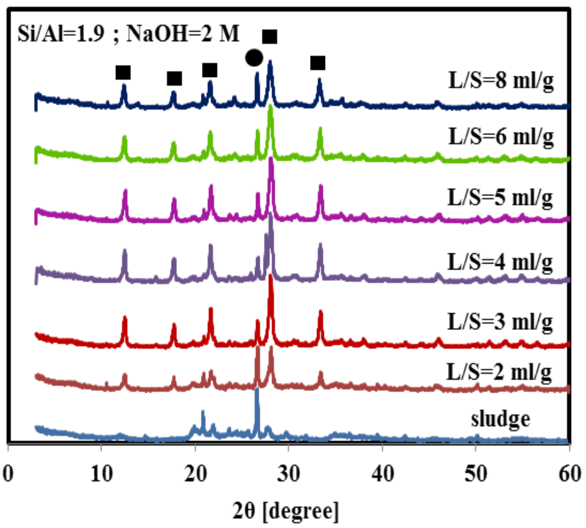


Figure 3 XRD patterns of products prepared with different liquid to solid ratio (L/S)

### 3.2 Cation Exchange Capacity (CEC) of zeolite products

**Figure 4** shows the CEC values of zeolite products obtained at various Si/Al ratios with different treatment temperatures.

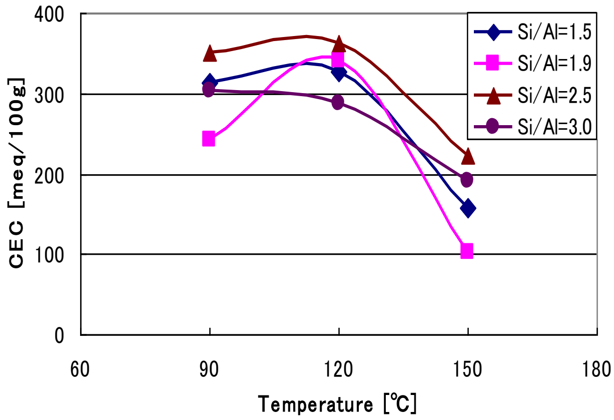


Figure 4 CEC of products obtained on various Si/Al ratios and temperatures

CEC of products reached optimum values at 120°C as the treatment temperature was increased from 90 to 150°C. The change in Si/Al ratios from 1.5 to 3.0 also showed an optimum at Si/Al=2.5. From XRD patterns of the products, it was thought that decrease of the CEC values from 120-150°C was due to the transformation of zeolite Na-P1 into Analcime-C. By hydrothermal treatment, raw sludge (CEC value=19 meq/100g) could be converted into zeolites with high potential use as ion exchange materials for heavy metals contaminants in aqueous solution.

Table 1. CEC and major phases observed by XRD at various Si/Al ratios and different temperature

| Si/Al | T(℃) | Major phase | CEC (meq/100g) |
|---|---|---|---|
| 1.5 | 90 | Na-P1 | 313 |
| | 120 | Unnamed Zeolite | 328 |
| | 150 | Na-P1, Unnamed Zeolite | 158 |
| 2.5 | 90 | Na-P1 | 350 |
| | 120 | Na-P1,Species-P | 362 |
| | 150 | Analcime-C | 223 |
| 3.0 | 90 | Na-P1 | 304 |
| | 120 | Analcime-C ,Species-P | 288 |
| | 150 | Analcime-C | 190 |

### 3.3 Heavy metal adsorption

The adsorption capacities of $Pb^{2+}$ and $Cd^{2+}$ were measured at various conditions. The zeolite product synthesized at 120 °C, Si/Al=2.5 (Z-1) showed $Pb^{2+}$ adsorption of 55.3 mg/g and $Cd^{2+}$ adsorption of 40.9 mg/g. The zeolite product synthesized at 150 °C, Si/Al=1.5 (Z-3) showed $Pb^{2+}$ adsorption of 37.3 mg/g and $Cd^{2+}$ adsorption of 24.0 mg/g.

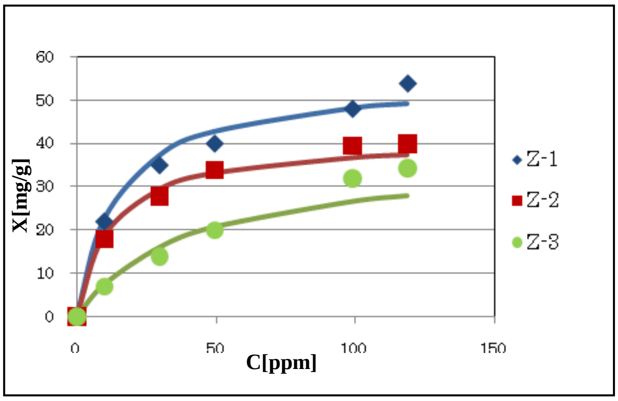


Figure 5 Langmuir adsorption isotherm of the $Pb^{2+}$ ion

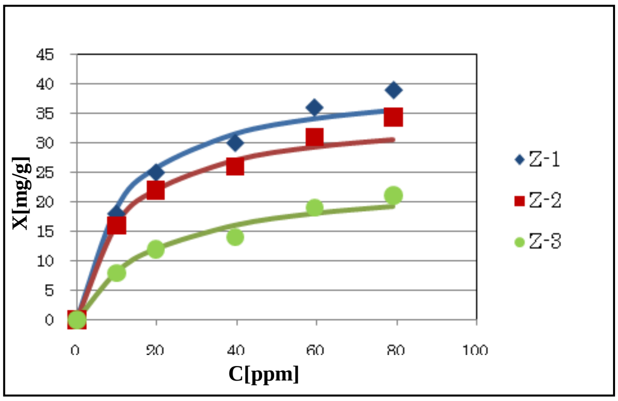


Figure 6 Langmuir adsorption isotherm of the $Cd^{2+}$ ion

### 4. Conclusions

From lake sludge, several types of zeolites were successfully synthesized by hydrothermal reaction in alkali solution. Soluble elements in sludge such as Si and Al tend to dissolve at higher temperature and form zeolites. Zeolite Na-P1 and zeolite Species-P which were synthesized at Si/Al ratio of 2.5 and reaction temperature of 120°C showed the highest value of CEC (362meq/100g). The L/S ratio showed no effect on the type of zeolite formed. Obtained zeolites also have adsorptive capability toward $Pb^{2+}$ (Xm=55.3mg/g) and $Cd^{2+}$ (Xm=40.9mg/g) ions. These values were higher than those reported on previous study. (Activated carbon $Xm(Pb^{2+})$=35.7mg/g and artificial zeolite $Xm(Cd^{2+})$=38.55mg/g). The zeolite synthesized from lake sludge in this study could be applied for several applications such as soil improvement or water purification.

### References

1) X. Querol et al., "Synthesis of zeolites from coal fly ash: a overview", Int. J. Miner. Process, p.413-423, May 2002

2) M. Inada et al., "Synthesis of zeolite from coal fly ashes with different silica–alumina composition", Int. J. Miner. Process, p.299-304, 2005

3) Y. Shao et al., "Synthesis of zeolites from lake sludge", Water and Environment Tech. Conference, 25-1B-06, June 2010

Table 2. CEC and adsorption capacity of $Pb^{2+}$ and $Cd^{2+}$ forvarious synthesis conditions.

| Zeolite product | Synthesis condition | CEC (meq/100g) | Xm(mg/g) for $Pb^{2+}$ | Xm(mg/g) for $Cd^{2+}$ | Major phase |
|---|---|---|---|---|---|
| **Z-1** | **Si/Al=2.5, 120℃, L/S=5ml/g, 2M NaOH** | **362** | **55.3** | **40.9** | **NaP1, Species-P** |
| **Z-2** | **Si/Al=1.5, 90℃, L/S=5ml/g, 2M NaOH** | **313** | **41.1** | **35.2** | **NaP1** |
| **Z-3** | **Si/Al=1.5, 150℃, L/S=5ml/g, 2M NaOH** | **158** | **37.3** | **24.0** | **Analcime-C** |

# Sulfate resistance of cementitious materials with blast furnace slag, lime stone powder and anhydrite

Student Number: 09M18189 Name: Jeong-Gook Jang Supervisor: Nobuaki Otsuki

# 高炉スラグ微粉末，石灰石微粉末および無水石膏を混和したセメント系材料の耐硫酸塩性

張正菊

本研究は，1．セメント系材料おける硫酸マグネシウム劣化機構を明らかにすること，2．高炉スラグ微粉末，石灰石微粉末および無水石膏のそれぞれの材料が耐硫酸塩性に与える影響を明らかにし，耐硫酸塩性を向上させるための材料設計を提案することを目的とした．

その結果，1．セメント系材料の硫酸マグネシウム劣化機構は，劣化初期に収縮し，その後，膨張することが明らかになった．初期の収縮は，浸漬初期に水酸化カルシウム量が減少して水酸化マグネシウム量が増加したことに起因し，その後の膨張は，二水石膏またはエトリンガイト量が大きく増加したことに起因したものと結論付けた．また，2．高炉スラグ微粉末の混和率を高めることで水和初期の水酸化カルシウム量を減らすこと，無水石膏の混和率を高めることで水和初期に多量のエトリンガイトを生成させモノサルフェートの生成を抑制すること，石灰石微粉末の混和率を高めることで水和初期にモノカーボネートを生成させモノサルフェートの生成を抑制することが耐硫酸塩性の向上に有効であることが明らかになった．

## 1. Introduction

Sulfate attack is one of the major deterioration problems for cement based materials, such as concrete, mortars and cement paste. This has been reported in Middle East Asia, North America and worldwide [1], [2]. Our research group has been conducting experiments improve the sulfate resistance by mixing admixtures such as blast furnace slag (BFS), limestone powder (LSP), and anhydrite (AH) to ordinary Portland cement (OPC) [3]. However, the previous researches considered only $Na_2SO_4$ attack conforming to ASTM-C1012. In the Middle East and so on where there is a lot of $MgSO_4$ in soil, it is expected that the deterioration mechanism is different from that of $Na_2SO_4$ attack. Also, $MgSO_4$ deterioration mechanism has not been clarified and material design to improve $MgSO_4$ resistance has not been conducted. Therefore, this research focuses on the deterioration of cementitious materials with OPC-BFS-AH-LSP due to $MgSO_4$. Also, the purpose of this study is to clarify $MgSO_4$ deterioration mechanism and to propose material design to improve $MgSO_4$ resistance using BFS-LSP-AH.

## 2. Experimental procedure

### 2.1 Specimens

The materials used in this study were OPC, BFS, AH and LSP. Table.1 shows chemical composition and physical properties of the materials used. Mix proportion of each materials are OPC:BFS=60:40, 45:55, 30:70% and AH=0, 3, 5, 7, 10% and LSP=0, 5, 10, 20%. Specimens were prepared with water-binder ratio w/b=0.5 and dimension of paste specimens is 1×1×8cm. Specimens were cured in the mold for 24 hours. And then, specimens were cured in water for 6 days. After water curing, the specimens were submerged in 5 mass% $MgSO_4$ solution at 23℃.

### 2.2 Method

Sulfate resistance was evaluated based on length and mass change tests conforming to the ASTM standards. Also, all specimens were photographed with the use of digital camera. Compressive strength were measured based on JIS R 5201.

In order to clarify the importance of understanding $MgSO_4$ deterioration and $MgSO_4$ resistance of cementitious materials with OPC-BFS-LSP-AH,

Table.1 Chemical composition and physical properties of materials used

| Material | Ig.loss (mass%) | Chemical composition (mass%) | | | | | | Specific surface area($cm^2/g$) |
|---|---|---|---|---|---|---|---|---|
| | | $SiO_2$ | $Al_2O_3$ | $Fe_2O_3$ | CaO | MgO | $SO_3$ | |
| OPC | 1.07 | 20.37 | 5.57 | 3.38 | 63.17 | 2.04 | 2.48 | 3300 |
| BFS | 0.49 | 33.60 | 14.26 | 0.41 | 43.13 | 6.05 | - | 4550 |
| LSP | 43.20 | 0.33 | 0.10 | 0.05 | 55.80 | 0.19 | - | 7610 |
| AH | 0.85 | 1.00 | 0.30 | 0.10 | 40.50 | 0.10 | 56.80 | 3990 |

hydration products of the cement pastes were examined using X-ray diffraction test (XRD), thermal analysis (TG/DTA), and scanning electron microscope (SEM).

## 3. $MgSO_4$ deterioration mechanism

### 3.1 Change of length and external appearance

Fig.1 shows the experimental result of length change test and Fig.2 shows the external appearance of specimens after exposure to 5 mass% $Na_2SO_4$ and $MgSO_4$ solutions. In the case of (a) $Na_2SO_4$ solution exposure, specimens expanded from early ages and some specimens got destroyed. On the other hand, in the case of (b) $MgSO_4$ solution exposure, specimens shrank in early ages and then it expanded. Moreover, in the case of (b) $MgSO_4$ solution exposure, disintegration of specimen surface was observed.

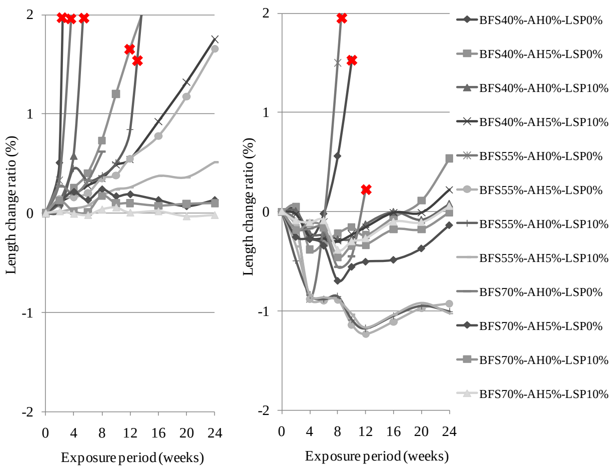


(a) $Na_2SO_4$ solution (b) $MgSO_4$ solution

Fig.1 Length change after exposure to 5 mass% $Na_2SO_4$ and $MgSO_4$ solutions

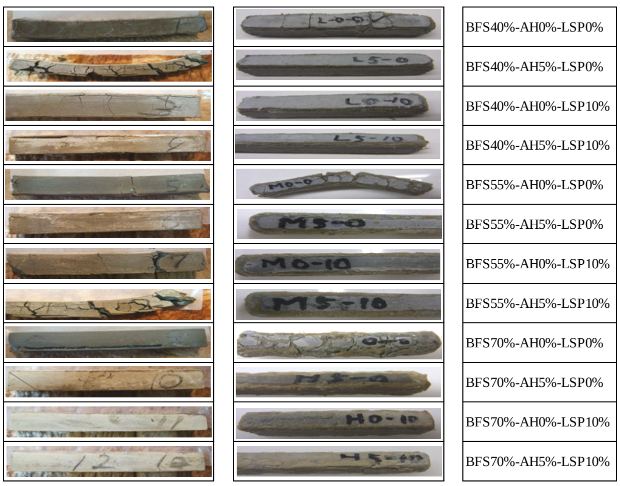


(a) $Na_2SO_4$ solution (b) $MgSO_4$ solution

Fig.2 External appearance of specimens after exposure to 5 mass% $Na_2SO_4$ and $MgSO_4$ solutions

### 3.2 Change of hydration products

Fig.3 shows the change of cement hydration products after exposure to 5 mass% $Na_2SO_4$ solutions. Fig.4 shows the change of cement hydration products after exposure to 5 mass% $MgSO_4$ solutions. The amount of calcium hydroxide decreased at each BFS replacement ratio after exposure to 5 mass% $Na_2SO_4$ and $MgSO_4$ solutions. As for the decrease in amount of calcium hydroxide, the case of $MgSO_4$ solution exposure was larger than in the case of $Na_2SO_4$ solution exposure. In addition, in $MgSO_4$ solution exposure, the amount of calcium hydroxide decreased greatly in early period of exposure, and the generation of the magnesium hydroxide was confirmed.

The amounts of ettringite and gypsum have increased in each BFS replacement ratio after exposure to 5 mass% $Na_2SO_4$ and $MgSO_4$ solutions. And in case of $MgSO_4$ solution exposure, the amount of increase in ettringite and gypsum has grown as time passes. From this result, the mechanism of $MgSO_4$ deterioration could be considered that;

$$Mg^{2+} + Ca(OH)_2 \rightarrow Mg(OH)_2 + Ca^{2+}$$

$$SO_4^{2-} + Ca(OH)_2 + 2H_2O \rightarrow CaSO_4 \cdot 2H_2O + 2(OH)^-$$

$$C_3A \cdot CaSO_4 \cdot 12H_2O_{\text{ monosulfate}} + 2(CaSO_4 \cdot 2H_2O)_{\text{ gypsum}} + 16H_2O \rightarrow C_3A \cdot 3CaSO_4 \cdot 32H_2O_{\text{ ettringite}}$$

In other words, shrinkage occurs due to the reaction that generates magnesium hydroxide as magnesium ion reacts with calcium hydroxide. Expansion occurs due to reaction that generates ettringite as sulfate ion reacts with calcium hydroxide and monosulfate.

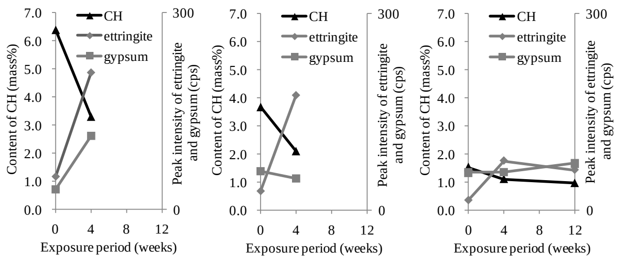


(a) BFS40% (b) BFS55% (c) BFS 70%

Fig.3 Change of cement hydration products after exposure to 5 mass% $Na_2SO_4$ solutions

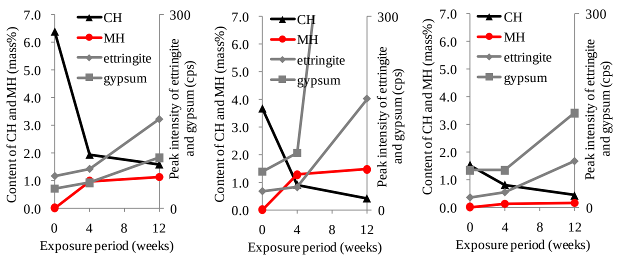


(a) BFS40% (b) BFS55% (c) BFS 70%

Fig.4 Change of cement hydration products after exposure to 5 mass% $MgSO_4$ solutions

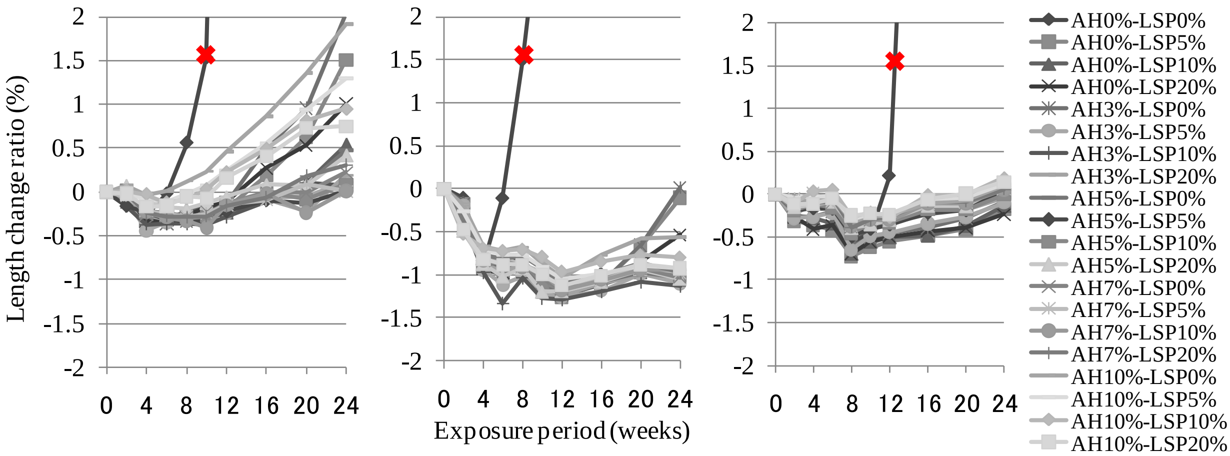


(a) BFS40% (b) BFS55% (b) BFS70%

Fig.5 Length change after exposure to 5 mass% $MgSO_4$ solutions

## 4. Material design to improve $MgSO_4$ resistance

### 4.1 Sulfate resistance evaluated from length change

Fig.5 shows the experiment result of length change test. In the case of AH0%-LSP0%, specimens were deteriorated within 12 weeks regardless of BFS replacement ratio. Except of these, shrinkage and expansion is greatly controlled by BFS replacement ratio. In case of (a) BFS40%, shrinkage ratio was around 0.3% and expansion ratio was 0.5 - 3%. In the case of (b) BFS55%, shrinkage ratio was around 1% and expansion ratio was 0.3 - 1%. In case of (c) BFS70%, shrinkage ratio was around 0.5% and expansion ratio was around 0.5%. Also, the amount of expansion ratio decreased with increasing AH and LSP replacement ratios.

From these results, increasing replacement ratio of BFS, AH and LSP showed increased $MgSO_4$ resistance. In this experiment, BFS40%-AH3~7%-LSP5~10% and BFS70%-AH5~10%-LSP5~20% showed superior $MgSO_4$ resistance. Superior $MgSO_4$ resistance is defined with 0±0.5% of length change ratio.

### 4.2 Relationship between sulfate resistance and calcium hydroxide

Fig.6 shows the relationship between OPC/p and calcium hydroxide (before exposure). OPC/p means mixture ratio of OPC to all powder (OPC+BFS+AH+LSP). The content of calcium hydroxide was significantly controlled by OPC/p. In other words, replacement ratio of BFS increased, the content of calcium hydroxide decreased significantly. As a result, in the case of BFS70%, the content of calcium hydroxide decreased to around 1% regardless of replacement ratio of AH and LSP.

Fig.7 shows the relationship between multiplication length change and calcium hydroxide (before exposure). Multiplication length change means;

Multiplication length change =|maximum amount of shrinkage| + |maximum amount of expansion|

As a result of Fig.7, it could be thought that the relationship between multiplication length change and calcium hydroxide have almost parallel correlation. And, it was thought that multiplication length change has decreased by decreasing the content of calcium hydroxide in case of BFS70%.

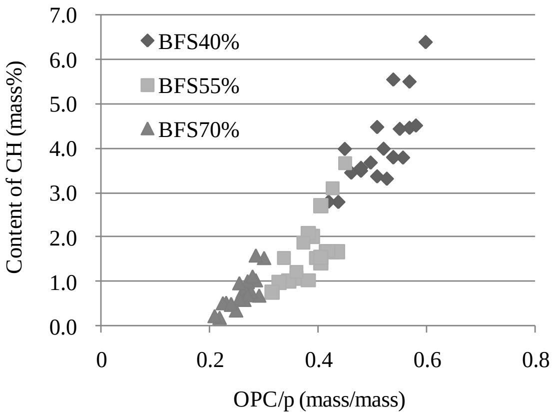


Fig.6 Relationship between OPC/p and calcium hydroxide (before exposure)

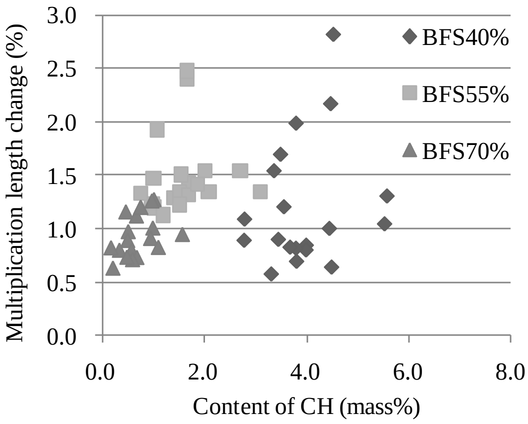


Fig.7 Relationship between multiplication length change and calcium hydroxide (before exposure)

### 4.3 Relationship between sulfate resistance and aluminate hydration products

Fig.8 shows the peak intensity of aluminate hydration products before exposure. In the case of (a) AH0%-LSP0%, the amount of ettringite was few regardless of BFS replacement ratio, and a large amount of monosulfate was confirmed. In case of (b) AH0%-LSP10%, monocarbonate was mainly generated regardless of BFS replacement ratio, and monosulfate was few. In case of (c) AH5%-LSP0%, ettringite was mainly generated regardless of BFS replacement ratio, and monosulfate was confirmed. In case of (d) AH5%-LSP10%, the amount of ettringite and monocarbonate were the largest, monosulfate was few. Therefore it could be considered that $MgSO_4$ resistance improved with increasing the AH replacement ratio because a large amount of ettringite could generate and monosulfate content could decrease in early age. Also, $MgSO_4$ resistance improved with increasing the LSP replacement ratio because monocarbonate content could increase and monosulfate content could decrease in early age.

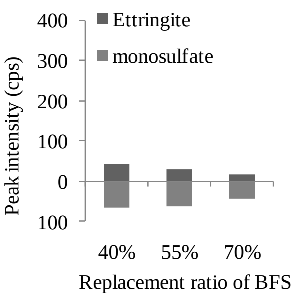

(a) AH0%-LSP0%

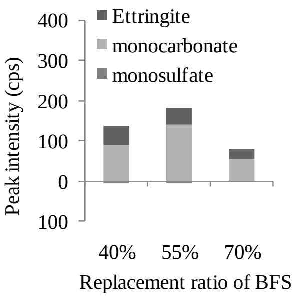

(b) AH0%-LSP10%

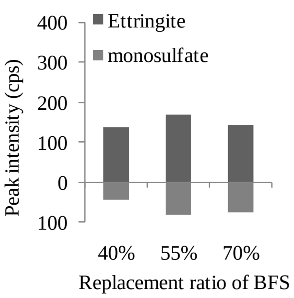

(c) AH5%-LSP0%

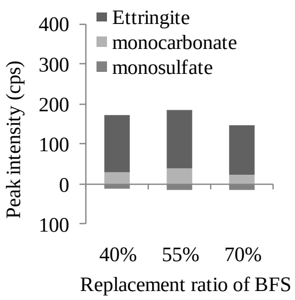

(d) AH5%-LSP10%

Fig.8 Peak intensity of aluminate hydration products before exposure

### 5. Conclusions

The purpose of this research is to clarify $MgSO_4$ deterioration mechanism and to propose material design to improve $MgSO_4$ resistance using BFS-LSP-AH. The experimental results could be concluded as follow.

1) Hydrated cement paste shrank in early ages and then it expanded in case of $MgSO_4$ deterioration while hydrated cement paste only expanded in case of $Na_2SO_4$ deterioration.

2) In case of $MgSO_4$ deterioration, shrinkage occurred due to reaction that generates magnesium hydroxide as magnesium ion reacts with calcium hydroxide. Expansion occurred due to reaction that generates ettringite as sulfate ion reacts with calcium hydroxide and monosulfate. Therefore, it could be considered that control of calcium hydroxide content is most important to improve sulfate resistance, compared with $Na_2SO_4$ deterioration.

3) $MgSO_4$ resistance improved with increasing the BFS replacement ratio because calcium hydroxide content in early age, which causes shrinkage and expansion, could decrease.

4) $MgSO_4$ resistance improved with increasing the AH replacement ratio because a large amount of ettringite could generate and monosulfate content could decrease in early age.

5) $MgSO_4$ resistance improved with increasing the LSP replacement ratio because monocarbonate content could increase and monosulfate content could decrease in early age.

### 【References】

[1] Rasheeduzzafar et al., J.ACI, Proc., Vol.81, No.1, pp.13-20 (1984)
[2] B.P.Bellport, In performance of concrete, ed. EG.Swenson, University of Toronto Press, Toronto, pp.77-92 (1968)
[3] Yun sub Lee et al., Influence on replacement of anhydrite gypsum and lime stone powder at blast furnace slag cement on sulfate attack, Journal of material science, Vol.59, No.10, pp.737-742 (2010)

# Evaluating Infrastructure Funds for Transportation Infrastructure Projects

**Student number: 09M18195 Name: Lei ZHANG Supervisor: Shinya HANAOKA**

交通社会資本整備事業を対象としたインフラファンドの評価

張磊

本研究では、世界各地域における交通社会資本整備事業を対象としたインフラファンドの投資現状について、投資方針と実際の投資状況の両者について分析し、特徴を把握した。また、リターン、リスク、シャープレシオ、ジェンセンアルファなどの評価指標を用いて、インフラファンドのパフォーマンス評価を行った。その結果、インフラファンドが安定した資金ソースになる可能性は今のところ高いとは言えないという結果を得た。

## 1. Introduction

At present, the need for additional transportation infrastructure is increasing, as national economy and social development is developing rapidly in China, India and other developing countries. On the other hand the maintenance of the transportation infrastructure should be done as quickly as possible, since the infrastructure is getting old in the developed countries. The implementation and maintenance of transportation projects requires large initial investment and a long payback period. Therefore, it is almost difficult for the government to afford this construction and operation cost solely due to the limitation of funding. To solve the problem, most of countries in the world have actively introduced private funds through PPP (Public–Private Partnership), in order to implement and maintain the transportation projects.

There is an alternative financing technique that exists in the market known as "infrastructure funds". The institutional investors in Australia and some other developed countries have been actively investing into infrastructure projects in Europe and United States through infrastructure funds. Recently, new funds in India have been set up. The movement to invest into infrastructure projects in Asia has been seen. Therefore infrastructure funds could be expected. (Infrastructure fund is a fund doing investment to the infrastructure projects.

In fact, the infrastructure funds only started recently. So the existing studies about the infrastructure fund for the transportation only contain the basic information of the funds development. There are few researches that focus on the analysis of worldwide infrastructure funds development and the evaluation of the infrastructure funds' performance.

## 2. Research purpose

The evaluation of the possibility of the infrastructure funds for transportation projects as a stable source of funding will be conducted in this thesis. The discussion will follow the two steps, shown as below:

i. Compare and analyze the current statement of investment of the infrastructure funds based on the investment plan, and the ones based on practical investment, by region, investment sectors and phases. Further find out the characteristics of infrastructure funds.

ii. Evaluate the listed infrastructure funds invested in the transportation projects, through return, risk, Sharpe ratio and Jensen's alpha. Further conduct evaluation comparison with infrastructure funds invested in other sectors, transportation-related stocks and REIT. Find out whether the infrastructure funds will become a stable source of funding.

## 3. Analysis of current statement of the investment in infrastructure fund worldwide

### 3.1 Research methodology

#### 1) Research target

i. The analysis of current statement of investment bases on the investment plan of fund manager. This research is aiming to analyze and indentify the characteristics of the infrastructure funds that used in the transportation project, transportation (roads, railways, airport, seaport), energy(energy, renewable energy, natural resources), utilities (utilities, water, water management), as well as telecoms.

ii. While analyzing the current statement of investment based on practical investment, the infrastructure fund in transportation projects is analyzed as research target to understand its characteristics.

#### 2) Data

The data comes from [The 2010 Preqin Infrastructure Review], which was issued by Preqin Ltd. And it represents the most comprehensive edition, with details for over 270infrastructure firms and 450funds.

#### 3) Methodology

i. About analysis based on the investment plan, analysis was conducted in the following four steps:

A) Extract the data from a region-based database.

B) Break down the date that has been extracted in the step A) of [i], by the investment sector and project phase.
C) Organize the data that has been from step A) and B) of [i], by cross table.
D) Analyze and discuss the results.

ii. About analysis based on the practical investment, analysis was conducted in the following steps:
A) From the database of step A) of [i], extract the data of infrastructure funds based on practical investment, through checking fund's homepage and investment business site.
B) Break down the data from database extracted in step A) of [ii], by the investment sector and project phase.
C) Organize the data received from step A) and step B) of [ii], by cross table.
D) Analyze and discuss the results.

## 3.2 Result

Table.1, Table.2 (Europe), Table.4, Table.5 (Asia) are the cross tables of infrastructure funds that based on investment plan and practical investment in Europe and Asia. Table.3, Table.6 shows the current statement of the practical investment in UK and India. Besides, the data in the other region, such as North America, Africa, Latin America, has also been broken down as below.

| Investment sector \ Investment phase | | Greenfield | Brownfield | Greenfield and Brownfield | Total (sector) | Total |
|---|---|---|---|---|---|---|
| Transportation | Transportation | 1 | 19 | 28 | 48 | |
| | Road | 1 | 10 | 19 | 30 | |
| | Railway | 1 | 8 | 16 | 25 | 142 |
| | Seaport | 1 | 9 | 13 | 23 | |
| | Airport | | 6 | 10 | 16 | |
| Energy | Energy | 4 | 12 | 29 | 45 | |
| | Renewable energy | 12 | 8 | 41 | 61 | 113 |
| | Natural energy | | 1 | 6 | 7 | |
| Utilities | Utilities | 1 | 13 | 19 | 33 | |
| | Water | | 11 | 18 | 29 | 86 |
| | Water management | 1 | 7 | 16 | 24 | |
| Telecom | Telecom | 1 | 8 | 7 | 16 | 16 |

**Table.1 Current statement of investment by infrastructure funds based on investment plan of fund manager (Europe)**

| Investment sector \ Investment phase | | Greenfield | Brownfield | Greenfield and Brownfield | Total (sector) | Total |
|---|---|---|---|---|---|---|
| | Road | 1 | 5 | 2 | 8 | |
| | Railway | | 9 | 1 | 10 | 32 |
| | Seaport | | 8 | | 8 | |
| | Airport | | 6 | | 6 | |

**Table.2 Current statement of investment by infrastructure funds based on practical investment (Europe)**

| Investment sector \ Investment phase | | Greenfield | Brownfield | Greenfield and Brownfield | Total (sector) | Total |
|---|---|---|---|---|---|---|
| | Road | | 1 | | 1 | |
| | Railway | | 7 | | 7 | 16 |
| | Seaport | | 2 | | 2 | |
| | Airport | | 6 | | 6 | |

**Table.3 Current statement of investment by infrastructure funds based on practical investment (UK)**

| Investment sector \ Investment phase | | Greenfield | Brownfield | Greenfield and Brownfield | Total (sector) | Total |
|---|---|---|---|---|---|---|
| Transportation | Transportation | 3 | 6 | 18 | 27 | |
| | Road | 3 | 5 | 17 | 25 | |
| | Railway | 1 | 3 | 6 | 10 | 89 |
| | Seaport | 1 | 4 | 10 | 15 | |
| | Airport | 1 | 5 | 6 | 12 | |
| Energy | Energy | 4 | 8 | 21 | 33 | |
| | Renewable energy | 4 | 4 | 13 | 21 | 61 |
| | Natural energy | | 2 | 5 | 7 | |
| Utilities | Utilities | 2 | 5 | 14 | 21 | |
| | Water | | 5 | 18 | 23 | 55 |
| | Water management | | 2 | 9 | 11 | |
| Telecom | Telecom | 1 | 5 | 8 | 14 | 14 |

**Table.4 Current situation of investment by infrastructure funds based on investment plan of fund manager (Asia)**

| Investment sector \ Investment phase | | Greenfield | Brownfield | Greenfield and Brownfield | Total (sector) | Total |
|---|---|---|---|---|---|---|
| | Road | 4 | 3 | 2 | 9 | |
| | Railway | 2 | | | 2 | 18 |
| | Seaport | 1 | 5 | | 6 | |
| | Airport | 1 | | | 1 | |

**Table.5 Current statement of investment by infrastructure funds based on practical investment (Asia)**

| Investment sector \ Investment phase | | Greenfield | Brownfield | Greenfield and Brownfield | Total (sector) | Total |
|---|---|---|---|---|---|---|
| | Road | 3 | | 1 | 4 | |
| | Railway | 2 | | | 2 | 11 |
| | Seaport | 1 | 3 | | 4 | |
| | Airport | 1 | | | 1 | |

**Table.6 Current statement of investment by infrastructure funds based on practical investment (India)**

According to the analysis of the investment plan, and comparison among other sectors, it has been found out that infrastructure funds prefer investing into the transportation projects through the number of infrastructure funds (Table.1, Table.4).From the analysis of practical investment, it shows that the infrastructure funds mainly invested in road and railways, due to increasing needs. Through investigating the data and website, the fact that mix-type infrastructure funds existing in large numbers has been identified. About the investment destination, the infrastructure funds are expanding worldwide, but still, most of them only focused on a few countries like UK and India (from the comparison betweenTable.2 and Table.3, as well as Table.5 and Table.6). About the investment phase, the infrastructure funds are investing into the Greenfield in the developing countries and into the Brownfield in the developed countries. From the comparison investment plan and practical investment, the number of practically invested funds is much smaller than the one based on the investment plan. It has been found out that the infrastructure funds did not carry out as planned.

# 4. Evaluation of the performance of infrastructure funds in transportation projects

## 4.1 Research methodology

### 1) Research target

To evaluate the performance of listed infrastructure funds, the research focused the ones used in transportation projects, that were listed in the stock exchanges (Australia, London, New York, Singapore, South Korea).Then compare with other products such as infrastructure funds used in energy, transportation-related stock and REIT, which are similar with infrastructure funds.

### 2) Data

In Australian stock exchange, 4 infrastructure funds used into transportation projects, 4 funds used into energy projects, 2 transportation-related stocks, 4 REIT (Real Estate Investment Trust) companies, and Australian stock exchange index are abstracted. The monthly price of each target is collected from Yahoo! Finance between Dec. 2005 and 2010, and Australian government bond 10 year yield is used as risk free interest rate here (the theoretical rate of return of an investment with zero risk). Because of the global financial crisis in 2008, the observing period is separated to 2005~2008 and 2008~2010.Furthermore, the similar ways are used to collect the data in the other stock exchange like the one used in the Australian stock exchange.

### 3) Methodology

There are four measurement methods used to evaluate infrastructure funds and other products.

i. Return:

$$R = (P_1 - P_0) / P_0 \qquad (4.1)$$

*Where:* $P_1$ : price in the current month, $P_0$ : price in the last month

If return has positive value, the higher value is better. If it has negative value, it means that it could not generate profit.

ii. Risk:

The risk "$\sigma$" is a standard deviation of the return. Here, the smaller value is better.

iii. Sharp ratio:

The Sharpe ratio is a measurement method of the excess return (or risk premium) per unit of risk in an investment asset or a trading strategy. The Sharpe ratio formula is:

$$S_p = (R_p - R_f) / \sigma \qquad (4.2)$$

*Where:* $R_p$ : return, $R_f$ : risk free interest rate, $\sigma$ : standard deviation of return

The Sharpe ratio is used to characterize how well the return of an asset compensates the investor for the risk taken. The higher the Sharpe ratio number is the better it is. When comparing more than two assets with the return $R_p$ against the same benchmark with return $R_f$, the asset with the higher Sharpe ratio gives more return for the same risk. A negative Sharpe ratio indicates that a risk-free asset would perform better than the financial product being analyzed.

iv. Jensen's alpha:

The Jensen's alpha is used to determine the abnormal return of a security or over the theoretical expected return, which is predicted by a market model. The Jensen's alpha formula is:

$$R_p - R_f = \alpha + \beta (R_m - R_f) + \varepsilon \qquad (4.3)$$

*Where:* $R_p$ : return, $R_f$ : risk free interest rate, $R_m$ : market return, $\varepsilon$: independent normally distributed random variables

This formula is calculated by regression equation. When alpha is significant, if the value is positive, the target product is earning excess returns rather than market. On the other hand, if the value is negative, then the product is earning less return rather than market. When alpha is insignificant, alpha could be considered as 0, which means that the product is earning the proper return regarding for the market.

## 4.2 Result

As the examples, There are results about infrastructure funds in the Australian stock exchange, with observing period 2005~2008 and 2008~2010, shown in Table.7 and Table.8. The infrastructure funds in the other stock exchanges were calculated as below.

| | Return | Risk | Sharpe ratio | Jensen's alpha |
|---|---|---|---|---|
| FT1(Brownfield) | 1.118 | 6.426 | -0.740 | -6.070 |
| FT2(Greenfield) | -1.403 | 7.966 | -0.914 | 0 |
| FT3(Brownfield) | -0.294 | 7.541 | -0.818 | -4.421 |
| FT4(Greenfield) | -0.926 | 8.319 | -0.818 | 0 |
| FE1 | -9.234 | 22.468 | -0.672 | 0 |
| FE2 | -0.997 | 7.731 | -0.889 | 0 |
| FE3 | -1.717 | 8.704 | -0.872 | 0 |
| FE4 | -0.445 | 4.633 | -1.364 | -4.880 |
| **FT-Average** | **-0.376** | **7.563** | **-0.822** | **-2.622** |
| **FE-Average** | **-3.098** | **10.884** | **-0.949** | **-1.220** |
| **Average(total)** | **-1.737** | **9.224** | **-0.886** | **-1.921** |
| ST1 | -0.181 | 7.934 | -0.763 | 0 |
| ST2 | -10.21 | 11.343 | -1.418 | 0 |
| **ST - Average** | **-5.198** | **9.638** | **-1.091** | **0** |
| REIT1 | -4.784 | 12.192 | -0.874 | 0 |
| REIT2 | -7.833 | 23.135 | -0.592 | 0 |
| REIT3 | -1.503 | 6.719 | -1.098 | -3.467 |
| REIT4 | -0.356 | 8.723 | -0.714 | 0 |
| **REIT - Average** | **-3.619** | **12.692** | **-0.820** | **-0.866** |
| ASX | -0.370 | 4.790 | -1.304 | 0 |

**Table.7 Australian stock exchange (2005~2008)**

| | Reture | Risk | Sharpe ratio | Jensen's alpha |
|---|---|---|---|---|
| FT1(Brownfield) | -0.427 | 5.378 | -1.031 | -4.576 |
| FT2(Greenfield) | 0.032 | 14.633 | -0.347 | 0 |
| FT3(Brownfield) | 0.088 | 7.579 | -0.663 | 0 |
| FT4(Greenfield) | -1.491 | 9.994 | -0.661 | 0 |
| FE1 | 3.198 | 31.866 | -0.060 | 0 |
| FE2 | 1.082 | 20.965 | -0.192 | 0 |
| FE3 | -0.991 | 12.176 | -0.501 | -0.576 |
| FE4 | -0.627 | 7.265 | -0.791 | -3.940 |
| **FT-Average** | **-0.449** | **9.396** | **-0.676** | **-1.144** |
| **FE-Average** | **0.665** | **18.068** | **-0.386** | **-1.129** |
| **Average(total)** | **0.107** | **13.732** | **-0.531** | **-1.136** |
| ST1 | 0.367 | 5.397 | -0.880 | 0 |
| ST2 | -5.383 | 28.020 | -0.374 | 0 |
| **ST-Average** | **-2.508** | **16.708** | **-0.627** | **0** |
| REIT1 | 1.685 | 20.117 | -0.170 | 0 |
| REIT2 | 5.640 | 27.440 | 0.018 | 13.128 |
| REIT3 | -1.362 | 16.673 | -0.388 | 0 |
| REIT4 | 1.242 | 9.877 | -0.392 | 0 |
| **REIT-Average** | **1.801** | **18.526** | **-0.233** | **3.282** |
| ASX | 0.860 | 4.512 | -0.943 | 0 |

**Table.8 Australian stock exchange (2008~2010)**

**FT:** Infrastructure Fund (transportation)**, FE:** Infrastructure Fund (energy), **ST:** Transportation-related stock, **REIT:** A-REIT **ASX:** Australian stock exchange

From 2005 to 2008, in the Australian stock exchange, all of the targets have a negative value of return. It means that they could not generate returns. According to the results about risk, it shows that the average of risk value for funds invested in transportation projects is 7.563. It is smaller than the one of other products, which means that the funds invested in the transportation projects, has a lower risk than others. The fund invested in the Greenfield projects has higher risk rather than the one invested in the Brownfield projects, among the funds. On the other hand, according to the results of Sharpe ratio, all of the targets have negative value and the value of the fund invested in the transportation is -0.822. It means that a risk-free asset would perform better than the funds and others. Therefore it couldn't attract the investors. According to the results of the Jensen's alpha, fund invested in transportation is -2.622, transportation-related stock is 0 (when it was considered as insignificant evaluation by t-value), A-REIT is -0.866. It means that all of them are earning the less return regarding for the market risk level. It couldn't attract the investors.

From 2008 to 2010, return of the funds and others are going up, as Australian stock exchange is recovered. But the fund invested in the transportation still had a negative value, -0.449 and it couldn't generate returns during this observing period. From the results of the risk value, it shows that funds are still having lower risk than the others. The fund invested in the Greenfield projects also has higher risk compared with the one invested in the Brownfield projects. On the other hand, all of the targets have a negative value on Sharpe ratio and the value of the fund invested in the transportation is -0.676. It means that a risk-free asset would perform better than the funds and others. But the one of A-REITs called "REIT2" has a positive value on Sharpe ratio. According the results of the Jensen' alpha, fund has a negative value -1.144, but A-REIT has a positive value 3.282. Therefore, the fund is not an attractive asset for the investors. The A-REIT could be considered as a high-risk high-return asset in the Australian stock exchange.

The similar analysis of the other stock exchanges is conducted like the one in the Australian stock exchange, being described above.

In the London stock exchange, return of the funds and others are going up, as London stock market is recovered through the comparison with two observing period. The mix type infrastructure funds (transportation + energy) have high risk. Among the funds, the fund invested in both developed and developing countries has less risk rather than the one, which just invested in the developing countries. According to the results of Sharp ratio, the fund has a negative value, and the Jensen' alpha is 0 or negative value during the observing period. It is not an attractive asset for the investors.

In the New York stock exchange, the mix type infrastructure funds (transportation + energy) have relatively small risk. According to the results of Sharp ratio, the fund has a negative value, and the Jensen's alpha is 0 or during the observing period.

In the Singapore stock exchange, return of the funds and others is going up, as Singapore stock exchange is recovered through the comparison with two observing period. The mix type infrastructure funds (transportation + energy) have high risk, furthermore the value of Sharp ratio is negative, and the Jensen' alpha is 0 or during the observing period.

In the South Korea stock exchange, return of the funds and others is going up, as South Korea stock exchange is recovered through the comparison with two observing period. According to the results of Sharp ratio, the fund has a negative value, and the Jensen's alpha is 0 or negative value during the observing period.

According to the analysis of the performance of infrastructure funds in transportation projects and mix investment sectors in the each stock exchange, the risk of infrastructure funds invested in the transportation projects is almost the smallest among all of the financial products being selected. On the other hand, mix type infrastructure funds for transportation have a high risk. Funds invested in the Greenfield have higher risk rather than the one invested in the Brownfield. And funds invested in the developing countries have higher risk rather than the one invested in the developed and developing countries. According to the result of sharp ratio, value of infrastructure funds is negative in these five stock exchanges. It means that the risk-free asset (government bonds) would perform better than the infrastructure funds. On the other hand, from the result of Jensen's alpha, most of the infrastructure funds' value is negative. It means that the infrastructure funds analyzed in this thesis receive less return than the stock market.

## 5. Conclusion

Since 2004, the infrastructure funds have been developing rapidly. It could become a new source of funding. But in this thesis, according to the analysis of current investment by infrastructure funds, it has been found out that the infrastructure funds did not carry out as planned. In the future, it is hard to tell whether infrastructure funds would keep up their interest in the transportation projects. However, during the observing period, the evaluation of performance of the infrastructure funds tells us that it is not attractive for the investors. Thus, whether the investors would stay with the infrastructure funds is still a question.

## References

[1] Jensen, M. C. [1968], "The Performance of Mutual Funds in the Period 1945-1964," *Journal of Finance*, Vol23, pp.389-416.

[2] Sharpe, W.F.[1964], "Capital Asset Prices: A Theory of Market Equilibrium under Condition of Risk," Journal of Finance, Vol 19(9), pp.425-442.

[3] Preqin Ltd[2010], "The 2010 Preqin Infrastructure Review," Preqin Ltd.

# PREPARATION OF SOLID ACID CATALYSTS FROM BAGASSE FLY ASH

Student Number: 09M18203 Name: Jiaxing BIAN Supervisor: Hirofumi HINODE

# バガスフライアッシュを用いた固体酸触媒の調製

卞佳興

本研究では、砂糖黍工業からの廃棄物であるバガスフライアッシュ(BFA)を原料とした固体酸触媒の開発を行った。調製した固体酸触媒の性能はイソアミルアルコールと酢酸のエステル化反応を用いて評価した。BFAはスルホン化処理によって強い固体酸触媒に変えた。また、キャラクタリゼーション方法として$N_2$吸着による比表面積測定、元素分析、フーリエ変換赤外分光分析(FTIR)および$pH_{zpc}$ 測定を用いた。調製した固体酸触媒はエステル化反応において、2時間、70℃で酢酸イソアミル60%以上の生成率に達して、市販の酸性触媒(Amberlite IR-120 plus)と同等な性能が確認できた。

## 1. Introduction

Sulfuric acid is one of the most popular acid catalysts for practical chemical processes and is widely used in the production of industrially important chemicals. However, the development of environmentally sustainable chemical processes has stimulated the use of solid acid catalysts, because solid acids can be easily separated from the reaction matrix by simple filtration or decantation for repeated use.

Bagasse is the fibrous residue from sugarcane juice extraction, that is valuable as energy resource due to its high calorific value [1]. However, the ash from the combustion process of bagasse in the form of fly ash and bottom ash have not yet been commercially utilized and is causing disposal problems.

The solid acid catalysts available commercially are mainly prepared from expensive precursors such as pure glucose [2], cellulose [3] and so on. Therefore, by using bagasse fly ash (BFA) as low-cost precursor in synthesizing solid acid catalyst, the disposal problem of BFA could be solved and the economic potential of sugarcane industries could also be enhanced. In this study, BFA was used to synthesize acid catalyst through sulfonation method. The performances of synthesized acid catalysts were evaluated using esterification reaction of isoamyl alcohol and acetic acid in a batch reactor. A commercial acidic resin, Amberlite IR-120 plus was also used as catalyst for comparison.

## 2. Experimental

### 2.1 Material

BFA was obtained from PT Madukismo, a sugar company in Indonesia. $H_2SO_4$ (98%), acetic acid (99.9%) and isoamyl alcohol (98%) were purchased from Wako chemical while Amberlite IR-120 plus was from MP Biomedicals.

### 2.2. Preparation of solid acid catalysts

Solid acid catalysts were prepared by sulfonation of BFA using the following procedures. 0.2g of activated carbon or BFA was mixed with 10 ml concentrated $H_2SO_4$ (98%) inside a Teflon-lined stainless steel vessel. The mixture was heated in an oven at 150 ℃ for 24 hours. After treatment, the mixture was cooled to room temperature. The solid product was washed with deionized water until constant pH. The solid product was then dried in an oven at 100 ℃ for 24 hours. The nomenclature of solid acid catalysts samples was showed in Table 1. The sample ID, B-C-S means that BFA was activated by $CO_2$ and then sulfonated. B-S-S means that BFA was activated by steam and then sulfonated. BFA-S means that BFA was directly sulfonated without activation.

Table 1 Nomenclature of solid acid catalysts samples by sulfonation method

| Sample ID | Activated | Activation agent | Sulfonation (S) |
|---|---|---|---|
| B-C-S | yes | $CO_2$ | Yes |
| B-S-S | yes | steam | Yes |
| BFA-S | no | - | Yes |

### 2.3. Solid acid catalysts characterization

The samples textural properties were characterized using nitrogen adsorption at 77 K by Autosorb 1 from Quantachrome. The chemical property analyses were done by measuring zero point charge $pH_{ZPC}$ and also by analyzing the surface functional groups using FTIR spectra analysis.

The ash content of sample was determined by thermogravimetry (Thermo Plus TG8120, Rigaku). Elemental analyses of C, H, N and S were performed on a LECO CHNS932 elemental analysis instrument.

### 2.4.Esterification method

Batch esterification reactions were carried out in a simple batch system at 70℃ for 2 hours. There was no attempt of eliminating water or shifting the equilibrium to enhance the reaction conversion. Each run used a mixture of 0.3 mol acetic acid (99.9%, Wako) and 0.3 mol isoamyl alcohol (98%, Wako) with 1.0, 1.5, 2.0 or 2.5wt % of solid catalyst. After reaction, the conversion of the ester was analyzed by gas chromatography-mass spectrometry (GC-MS). The esterificaton reaction equation for synthesizing isoamyl acetate from isoamyl alcohol and acetic acid was shown as (2.4.1).

$$CH_3COOH + C_5H_{12}O \rightleftharpoons C_7H_{14}O_2 + H_2O \quad (2.4.1)$$

## 3. Results and discussion

### 3.1. Solid acid catalysts characterization

The porosity of specific surface area of BFA and solid acid catalysts was showed in Table 2. After sulfonation, the porosity and specific surface area of all the samples increased.

Table 2 Porosity and specific surface area of BFA and solid acid catalysts

| Sample ID | Porosity | | |
|---|---|---|---|
| | $V_{mic}$ (cc/g) | $V_{mes}$ (cc/g) | $S_{BET}$ ($m^2/g$) |
| B-C-S | 0.407 | 0.102 | 785 |
| B-S-S | 0.642 | 0.114 | 1,231 |
| BFA-S | 0.358 | 0.084 | 824 |
| BFA | 0.207 | 0.018 | 475 |

The compositions of C, H, N and S in samples were analyzed. The results of ultimate analysis were showed in Table 3. BFA-S sample had the highest S content.

Table 3 Ultimate analysis (C, H, N, S) of solid acid catalysts

| Sample ID | Ultimate analysis (wt %) | | | | |
|---|---|---|---|---|---|
| | C | H | N | S | O* |
| B-S-S | 65.00 | 2.15 | 0.27 | 0.60 | 22.28 |
| B-C-S | 73.38 | 0.21 | 0.50 | 0.73 | 11.00 |
| BFA-S | 68.07 | 0.78 | 0.30 | **3.98** | 26.81 |

O* content was calculate by difference

The functional groups on solid acid catalysts were analyzed by FTIR. The result of synthesized solid acid catalysts B-C-S was showed in Figure 1. After sulfonaton, the function group as indicated by peak intensity at 1600 $cm^{-1}$ is carboxylic (-COOH), the peaks of phenolic group (-OH) is from 900 to 1200 $cm^{-1}$. Meanwhile, for sulfonate group ($-SO_3H$) the peaks are at 1,040 and 1,195 $cm^{-1}$.

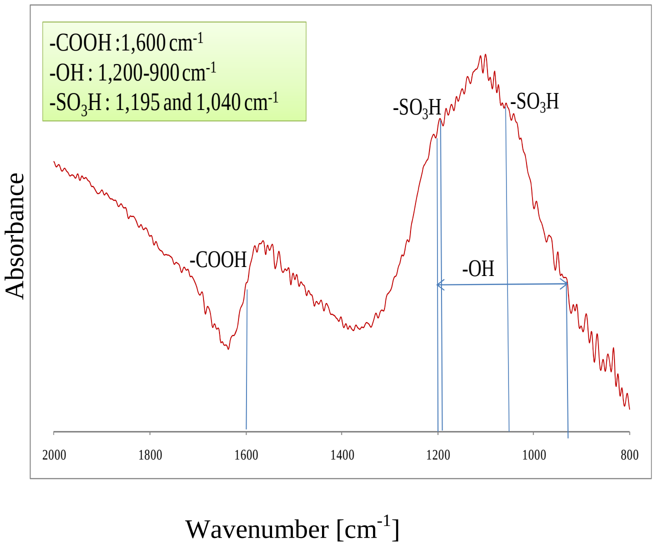


Fig. 1 FTIR spectra of B-C-S

## 3.2. Solid acid catalysts activity

The acid catalytic performance of BFA-S, B-C-S and B-S-S samples was evaluated through the esterification reaction of isoamyl alcohol with acetic acid. The commercial material (Amberlite) was used for a comparison. Figure 2 showed conversion of esterification reaction by several catalysts. The performance of BFA-S sample was higher than that of Amberlite. This result showed that the catalytic activity was affected by the $pH_{zpc}$.value. The esterification reaction mechanism was showed in Figure 3 [4]. The -$SO_3H$ released $H^+$ in the esterification reaction. Therefore, the -$SO_3H$ group had sufficient acidity to contribute significantly to reaction. Catalyst with higher performance in esterification with higher -$SO_3H$ group had the lower $pH_{zpc}$ (stronger acid characteristic).

From the result, it can be suggested that the catalytic activity was independent of specific surface area.

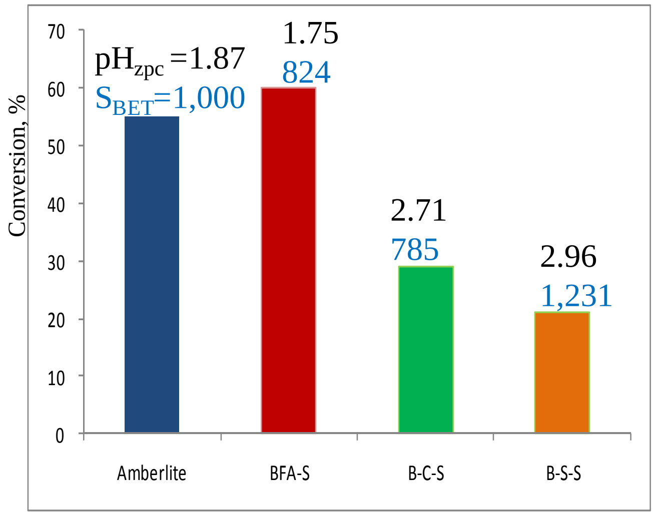


Fig.2 Conversion of isoamyl alcohol by several catalysts

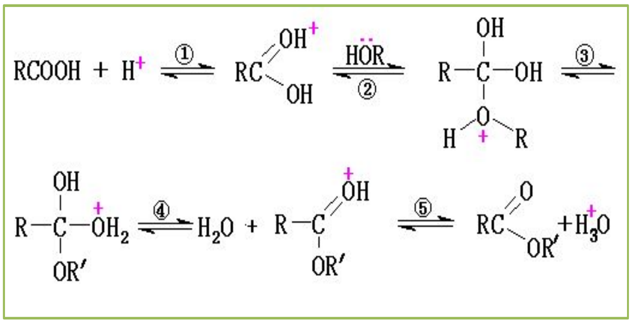

Fig.3 The esterification reaction mechanism

Multiple esterification reaction cycles were carried out to examine the deactivation of BFA-S catalyst. The result of catalystic activity during five reaction cycles of the esterification was showed in Figure 4. The result showed that no significant deactivation was observed for BFA-S during five consecutive esterificaton cycles of acetic acid with isoamyl alcohol at 70℃ for 2 h. The result of $pH_{zpc}$ measurement also showed negligible change in the $pH_{zpc}$ value of BFA-S after five cycles.

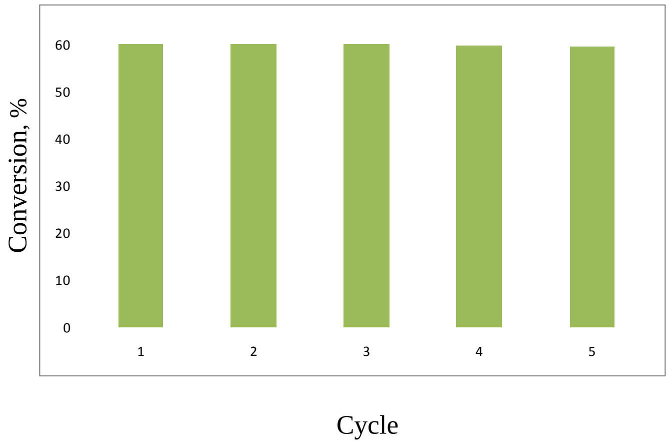


Fig.4 BFA-S activity during five reaction cycles of the esterification

Effect of catalyst to BFA-150 mass ratio on conversion of esterification was showed in Figure 5. From the results, The BFA-S mass ration increased from 1.0 wt % to 2.5 wt %, however, the conversion was not significantly changed. The conversion reached 63.5% with $H_2SO_4$ catalyst. It could be possible that the reaction reached the equilibrium.

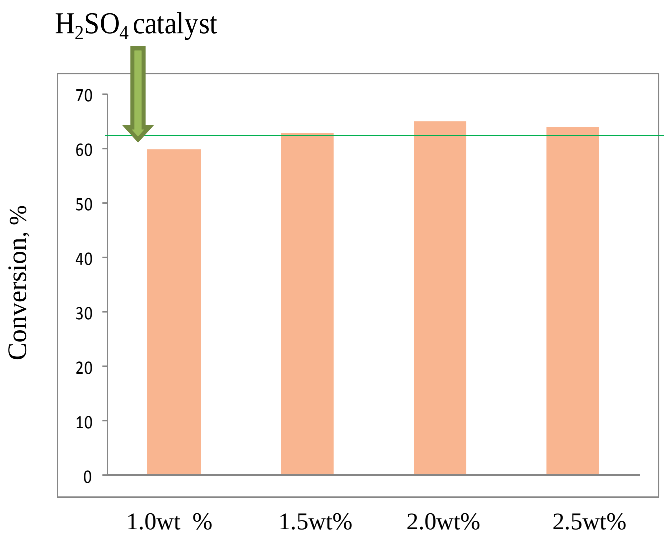


Fig.5 Effect of catalyst to BFA-S mass ratio on conversion of isoamyl alcohol

## Conclusion

Solid acid catalysts have been successfully prepared from BFA by simple sulfonation method. The high performance of synthesized catalyst was evaluated using esterification reaction of isoamyl alcohol and acetic acid at 70℃ for 2 hours in a batch system with conversion of isoamyl alcohol into isoamyl acetate reaching above 60% for catalyst prepared from BFA. The performance of synthesized catalysts was comparable to the commercial acid catalyst (Amberlite IR-120 plus).

## References

[1]V.S. Batra, S. Urbonaite and G. Svensson, ‘Characterization of unburned carbon in bagasse fly ash’, Fuel, vol. 87, (2008) 2972.

[2]A. Takagaki, M. Toda, M. Okamura, J.N. Kondo, S. Hayashi, K. Domen and M. Hara, ‘Esterification of higher faty acids by a novel strong solid acid’, Catalysis Today, vol. 116, (2006) 157-161.

[3]S. Suganuma, K. Nakajima, M. Kitano, D. Yamaguchi, H, Kato, S. Hayashi and M. Hara, ‘Synthesis and acid catalysis of cellulose-derived carbon-based solid acid’, Solid State Sciences, vol. 12, (2010) 1029-1034.

[4]M. Kitano, K. Arai, A. Kodama, T. Kousaka,K. Nakajima, S. Hayashi, M. Hara, ‘Preparation of a sulfonated porous carbon catalyst with high specific surface area’, Catal. Lette. , vol. 131, (2009) 242-249.

# Estimation of CO2 Emission with Development of Rail-based Intermodal Freight Transportation in Inland China

Student Number: 09M18210 Name: Xiaolin FANG Supervisor: Shinya HANAOKA

# 中国内陸部におけるインターモーダル貨物輸送による CO2 排出量の推定

房　小琳

本研究では、中国鉄道コンテナ輸送の現状、課題および方向性を明らかにした上で、今後の中国の経済発展と産業構造の変化に基づき、2020 年から 2050 年までの中国内陸部のコンテナ貨物輸送における鉄道インターモーダル輸送による CO2 排出量を推定した。

**1. Introduction:**

With the development of China economy, $CO_2$ emission volume is getting bigger. Now the $CO_2$ emission by China is 20.2% of that by whole world, as No. 2 following the US. The $CO_2$ emission by China transportation sector is about 20% of that by all sectors in China. In recent years, in China, the share of road transportation was getting higher; however the share of rail transportation was getting lower. From environment view, for per ton-km freight, the $CO_2$ emission by road is about 10 times of that by rail. $CO_2$ emission for per ton-km freight can be reduced by shifting from road based transportation to rail-based intermodal transport system.

The research focuses on the rail container freight transportation of the inland China. There are 2 research purposes. Firstly, clarify the current status, the current issues and the future developing direction of the rail container freight transportation in China. Secondly, each 10 year from 2020 to 2050, estimation of the container transportation volume in China inland, then estimation of $CO_2$ emission volume, based on the modal shift from road transportation to rail transportation.

**2. The current status and issues of Chinese rail freight**

The share of rail freight, measured by ton freight volume and ton-km freight, decreases as compared to road freight in recent years, although rail freight is more suitable to Chinese large land. The growth rate of the Chinese rail freight is slightly slower than that of the China GDP, while any of China road freight and the total freight increases well proportionally with GDP. The reason is the shortage of rail freight's capacity. With the GDP rapid increase after China joined in WTO in 2002, the shortage of rail freight's capacity is getting worse. In 2008 the rail freight's capacity can only meet 40% of the request received by the China railway companies from the market. So the market demand goes to road freight, although railway freight is cheaper especially in the case of middle or long distance freight. The reason of capacity shortage is the shortage of railway construction. In China, railway construction is mainly by invested by government. In the case that the budget of government for railway construction is not enough, the investment of railway construction is not enough. During 2000~2008, the growth rate of operating-km of railway is only 2% each year, while the increase of highway is about 10%~30%. Thus, the freight share of railway decreases in recent years.

**3. The current status and issues of China railway container freight**

**3.1 The current status**

From 1999 to 2007, both the share of road container freight and the share of water-container-freight increase apparently, however the share of railway container freight decreases year by year, from 26% in 1999 to 10% in 2007.Any of China road-container-freight, and the total container freight increases well proportionally with GDP, however the growth rate of the rail container freight is much slower than that of the China GDP especially since 2003.

**3.2 The issues of China railway container freight**

The issues of China railway container freight are due to the following 4 reasons:

a.The shortage of capacity of railway-container

The transportation capability of railway is not enough due to the not-enough investment in the past years. Secondly, government orders that the railway should transport the natural resources such as charcoal, steel, grain and so on with highest priority, which is already above 65% of the total rail capability.

Furthermore, the busy container lines, through which more than 35% container freight are transported, also work as passenger transportation. These lines connect Chinese biggest cities such as Beijing, Shanghai, Guangzhou and so on, between which the passenger transport are becoming heavier and heavier in recent years. Especially during Chinese New Year, in order to make sure that the passengers can go home on time, the freight has to be stopped or reduced frequency of transport.

b. The shortage of facilities related to railway-container transportation

Firstly, the facilities in stations, which can receive/send container freight, are out-dated. The following example is about the status of all stations (609) in 2005: Most of them have no specific workspace for container freight, just sharing workspace with common freight; some of them have no specialized machines to load or unload the container. Most of them have no advanced IT system to manage the freight or the inter-station communication.

Secondly, the shortage of containers and the shortage of container carrying trains make containerization lower. Based on Ministry of Railways, the container freight is about 10% of rail freight, however due to the above reason, only 2% of rail freight is transported by container.

c.The shortage of Railway-Sea Intermodal Freight Transport

After China joined in WTO in 2002，with the trade increase，the freight volume of marine container increases apparently. However, Railway-Sea Intermodal Freight Transport is only 2% of all marine containers，and more

than 80% marine containers depends on road transportation. The reason is that most of railway freight stations are far from seaport.
d. The shortage of door to door service
The shipper has to go to the rail freight station by oneself in order to send or take the freight, because the rail transport companies only transport freight between rail freight stations, which increases both the cost and the delivery time.

## 4 The future development of rail container transportation

The 'medium-and-long-term plan for railway network' central government established in 2007, which explicitly draw the target of infrastructure construction until 2020 and supplies 5 trillion budgets.
The large-scale railway construction will affect container transportation in the following points:
1. The freight transportation will be separated from the passenger transportation in busy container line. In recent years, the passenger volume increases heavily. For line transporting both freights and passengers, it is difficult to improve the capacity of freight. With the construction of high speed railway, the current railway will be used mainly for freight, which will improve the capacity of rail transportation.
2. To construct the centre of container logistics. China government plans to, before 2012, complete the construction of 18 the centers of container logistics which can cover the whole national transportation network. The main functionalities of these centers are:
a. Can load/unload one whole train at one time: Each centre has this kind of advanced machines, which can both improve the transportation efficiency and save energy.
b. Can handle the international containers: In the center, there are customs and CIQ (China Entry-Exit Inspection and Quarantine Bureau).
c. Advanced IT management system
3. The enlargement of Railway-Sea Intermodal Freight Transport. In April 2007, Ministry of Railways adjusted the lines of container transportation. After the adjustment, 56 of 90 container lines connect the harbor. 6 of 18 container logistics centre are near the harbor. With the development of railway infrastructure, more and more lines will connect the harbor.
4. Introduce double-stack train: The double-stack train was introduced into the Beijing-Shanghai line. Compared to traditional line, the transportation capacity is enhanced, the energy consumption per unit freight volume is saved 1/3, and the transportation fee also is saved 25%-40%. After Beijing-Shanghai line, China government plans to construct a transportation network with 4 horizontal and 4 vertical lines. When the plan is finished at 2020, the China transportation capacity will be much better than now.

## 5 Estimation of $CO_2$ emission from 2020 to 2050

The following formula 5.1 is used to calculate the $CO_2$ emission volume for intermodal container freight in China Inland, from 2020 to 2050, for each decade.
$E = \sum M_R * L_R * EF_R$ (5.1)
E: CO2 emission volume (ton)
$M_R$: container freight volume of freight method R (ton)
$L_R$: average container freight distance of freight method R (km)
$EF_R$: $CO_2$ emission volume per ton-km freight for freight method R (ton-$CO_2$/ton-km-freight)
R: freight method, i.e. railway freight and road freight

The dependence of freight volume increment in the factors such as GDP growth, change in production structure, and change in demand is taken into consideration. By considering the above factors, different approaches are used to predict the container freight volume for 2020 and for years beyond 2030, with 2030 inclusively. Besides that, the container freight volume is emphasized in the calculation as it is the main factor that decides the estimation of the $CO_2$ emission.

### 5.1 Estimation of CO2 emission in 2020

#### 5.1.1 Estimation of the container freight volume in 2020

The estimation of railway container freight volume for 2020 is based on the current growth stage of China freight industry. In this current stage, the increment in the freight demand is largely contributed by the growth in economy. Among all, the increment rate in GDP is the most remarkable factor. The GDP growth rate in China towards 2020 is expected to continue the fast growing pace with the similar growth rate as in year 1999 to year 2008. Hence, by referring to the relation between GDP and container freight volume in the past decade, the railway container freight volume and road container freight volume for 2020 can be estimated.

**(1) Estimation of the railway container freight volume**
From year 2003 onward, the increment rate in the railway container freight has been slowed down to a nearly flat trend. Therefore, the railway container freight volume for 2020 is calculated based on the estimated railway freight volume instead of railway container freight volume. The railway container freight volume is therefore can be obtained by replacing the percentage of container freight volume over railway freight volume.
The linear relationship between railway freight volume and GDP from year 1999 to year 2008
Y=136711.5+0.0487 X (5.1.1)
Y: railway freight volume (ten thousands ton)
X: GDP (million dollars)
Estimated GDP value: 8000000 million dollar (National Bureau of Statistics of China, 2005)
Percentage of container freight volume over railway freight volume: 9.7％ (Shenwan Research Institute，2009)
Hence, the railway freight volume for 2020 is 526204 ten thousands ton.
the railway container freight volume for 2020 is **51042 ten thousands ton** (＝526204＊9.7％).

**(2) Estimation of the road container freight volume**
As for the estimation of road container freight volume for 2020, it is known that the increment of road container freight volume is linear proportional to the increment of the GDP from year 1999 to year 2008.
Y=0.0185X-12606.6 (5.1.2)
Y: road container freight volume (ten thousands ton)
X: GDP (million dollars)
The estimated result of road container freight volume for 2020 is **135563 ten thousands ton.**

#### 5.1.2 Estimation of the average container freight distance

**(1) Estimation of the average railway container freight distance**

The OD (origin- destination) of railway container volume for 2020 is estimated based on the OD data of railway container freight for year 2005. The following formula 5.2.1 is used to calculate the average railway container freight distance.

$$\text{Average railway freight distance} = \frac{\sum_{i,j}(\text{container freight between } O_iD_j \times \text{distance between } O_iD_j)}{\sum_{i,j}\text{container freight between } O_iD_j}$$

i, j: 29 province of China

1. Estimation of railway container freight between OD

**Setp1**: By using the average increment rate of GRP in each region for 4 years, which is from year 2005 to year 2008, the GRP increment rate of each region for 2020 is estimated.

**Step2**: By assuming the increment rate of container freight between OD is the same as the average GRP increment rate of O and D, the railway container freight volume between OD for 2020 is estimated.

**Step3**: The calculation result is corrected by using the estimated railway container volume for 2020.

2. Estimation of railway container freight distance between OD. If there exists a plan for a certain route, the distance is calculated using GPS while the other routes are calculated based on the actual distance of the existing railways. Hence, the average railway container freight distance: **1555.6 km**

**(2) Estimation of the average road container freight distance**. Without the OD data of road container freight, the road freight distance for 2020 is estimated using the average freight distance from 1995 to 2007. Through analysis of the average freight distance of road freight from year 1995 to year 2007, the increment of average road freight distance is slow with 16 km in 13 years. Based on this increment pace, the average freight distance for 2020 is estimated as **85km**.

### 5.1.3 Emission of $CO_2$ emission per ton-km freight

**(1)$CO_2$ emission per ton-km freight of railway freight**

The $CO_2$ emission is declined with the revolution of engine and the increment of average load per railway carriage. However, as there is no sufficient evidence to support these factors in 2020, it is hard to predict the related situation in 2020. As for this, the $CO_2$ emission per ton-km freight is estimated according to the China government's target in $CO_2$ emission reduction. Its target in $CO_2$ emission reduction in 2020, it is estimated that the $CO_2$ emission is to be reduced by 35% as compared to $CO_2$ emission in year 2005. Hence, the estimated result of the $CO_2$ emission per ton-km freight of railway freight for 2020 is **174.65 kg/10^4tn-km.**

**(2) $CO_2$ emission per ton-km freight of road freight**

Same as the railway, the $CO_2$ emission of road freight is calculated according to the $CO_2$ reduction target of Chinese government. China have a target in $CO_2$ emission reduction in 2020, it is estimated that the $CO_2$ emission is to be reduced by 10% as compared to $CO_2$ emission in year 2005(2156.17 kg/10^4tn-km).This result is **1940.55 kg/10^4tn-km** in 2020

By composing the above calculated results, the $CO_2$ emission of container freight of China Inland for 2020 is estimated.

Table 5.1 $CO_2$ emission of container freight of Inland China

| | Railway | Road |
|---|---|---|
| ton-km freight (a hundred million ton-km) | 7939.94 | 1152.29 |
| $CO_2$ emission per ton-km freight (kg/10^4tn-km) | 174.65 | 1940.55 |
| $CO_2$ emission (ten thousands ton) | 1386.71 | 2236.07 |
| | **3622.78** | |

### 5.2 Estimation of $CO_2$ emission from 2030 to 2050

#### 5.2.1 Estimation of railway container freight volumes

The railway container freight volumes of 2030 to 2050 are estimated using the estimated data of domestic goods categories of volume of trade in China from 2005 to 2050, and the actual data of applicable freight volume for railway container freight by items in year 2005.

**Step1**: from the estimated data of domestic volume of trade up to 2050, to select 5 goods categories, which can be applied to container transportation are as followed: Metal and machinery; Fishing; Foods; Other manufactures; Agriculture.

**Step2:** the actual data of applicable container freight by items for 2005 is categorized into the matching selected goods categories.

**Step3**: assuming the increment rate of freight volume is equal to the increment rate of volume of trade, the increment rate of the freight volume for 2020 to 2050 is hence calculated.

**Step4**: the freight volume for 2020 to 2050 is obtained by referring the actual data of applicable container freight by categories for 2005.

The reasons for the recalculation of the applicable container freight volume for 2020 are to confirm the reliability of the estimated result in part 5.1.1, and to make assumption for the containerization ratio for 2030 and beyond.

The comparison of the estimated result of railway container freight volume for 2020

Estimated container freight volume from 5.1.1: 51042 (ten thousands ton)

Estimated result of applicable container freight volume in this part: 59155 (ten thousands ton)

Assuming both estimated applicable container freight volumes have to be in same value, the following containerization ratio for 2020 is obtained.

Containerization ratio for 2020: 86.2% (=51042/59155)

The Ministry of Railway of China has aimed to increase the containerization ratio to 50% in 2010 and targeting full capacity coverage of transportation for applicable container freight in 2020. This result is hence consistent with the target set by the Ministry of Railway of China. Therefore, the estimated result of railway container freight volume above is considered reliable.

Finally the containerization ratio for 2030 and beyond is assumed.

As the containerization ratio for 2020 is 86.2%, the containerization ratio for 2030 and beyond are expected to be more than 86.2%. Currently the containerization ratio of Japan is nearly 100% while other developed countries are also having containerization ratio of more than 90%. By referring to this numerical value, the containerization ratio of China for 2050 is estimated to approach 100%. It is assumed that there will be an increment of 4% for each decade for 2030 and beyond. Therefore, the following containerization ratio is assumed: 2030: 90.2%; 2040: 94.2%; 2050: 98.2%

The estimated result of railway container freight volume is **98489 for 2030, 177792 for 2040, and 274322 for 2050 (Unit: ten thousands ton)**.

### 5.2.2 Estimation of road container freight volumes

Road container freight volume = domestic container freight volume + marine container freight volume

Domestic container freight volume refers to the container freight volume with both origin and destination located within the country while marine container freight volume refers to the container freight volume covering import and export.

**(1) Estimation of domestic container freight volume**

According to the statistic of the Ministry of Railway of China, about 80% of domestic container freight volume is handled by railway in recent years. By assuming the same trend in the future, the domestic container freight volume: **2030: 123111; 2040: 222240; 2050: 342903 (Unit: ten thousands ton)**.

**(2) Estimation of marine container freight volume**

The marine container freight volume and the volume of trade data of product import and export for 1999 to 2007

$$Y=4623.36+0.00585X \qquad (5.2.1)$$

X: volume of trade for product import and export (million dollars)

Y: marine container freight volume (ten thousands ton)

By using the volume of trade data for product import and export of China that is extracted from the estimated data of worldwide trade matrix up to 2050, the marine container freight volume for 2030 and beyond is estimated: **2030: 33,867; 2040: 49,703; 2050 64,705 (Unit: ten thousands ton).** Hence, the road container freight volume is as below:

Table 5.2.1: Estimated results of road/railway container freight volume (Unit: ten thousands ton)

| | 2030 | 2040 | 2050 |
|---|---|---|---|
| Road | 156978 | 271943 | 407608 |
| Railway | 105262 | 187733 | 287263 |

### 5.2.3 Correction of railway container freight volume for 2030 to 2050

The estimation of railway container freight volume in part5.2.1, has not considered about the increment of railway-sea intermodal freight volume. It is assumed that the railway-sea intermodal freight volume could reach 20% of marine container freight volume following the future railway infrastructure development and also by referring to the current condition of the developed countries. The estimated result of railway container freight is showed in table5.2.1.

### 5.2.4 Estimation of average transport distance of railway and road container freight for 2030 to 2050

The average transport distance of railway and road container freight for 2030 to 2050 is obtained from the average transport distance of 2020. After 2020, the speed of economy growth of China will be slowed down, and basically complete its major traffic infrastructure building by 2020, so it is estimated that there would not have major change in the transportation distance between OD for 2030 and beyond.

### 5.2.5 Estimation of $CO_2$ emission per ton-km freight

**(1) $CO_2$ emission per ton-km freight of railway freight**

The calculation is based on the double stack train instead of the common container transportation method. The double stack container transportation method is only suitable for the countries with wide area. Currently, the transportation volume of double stack train is about 50% of the total container freight volume in Australia, while there is 60% to 70% for North America. As the double stack container transportation line has not been developed in China now. Therefore, by referring to the current condition of the developed countries and future development of rail-container transportation (part 4), it is assumed that China could have 50% container freight volume as double stack train, and double stack train could reduces 1/3 of its current $CO_2$ emission per ton-km freight.

The $CO_2$ emission per ton-km freight of the rail freight transportation: **145.54 (kg-$CO_2$/10^4tn-km).**

**(2)$CO_2$ emission per ton-km freight of road freight**

The future related information of $CO_2$ emission per ton-km freight cannot be obtained. From 2030 onwards, as China is expected to have economy status approaching developed countries, the $CO_2$ emission per ton-km freight is hence assumed to be similar to the developed countries.

By referring to the $CO_2$ emission per unit freight volume (1350kg-CO2/10^4tn-km) of business-used truck in Japan in 2008, the $CO_2$ emission per ton-km freight in China up to 2050 is estimated to approach 1350kg-$CO_2$/10^4tn-km. It is assumed that there will be a decline of 10% for each decade from 2020 onwards. The result is as below: **2030: 1746; 2040: 1571; 2050: 1414(Unit: kg-$CO_2$/10^4tn-km).**

The $CO_2$ emission of container freight of China Inland for 2030 to 2050 is estimated: **2030: 4713; 2040: 7882; 2050: 11403 (Unit: ten thousands ton)**

## 6. Conclusion

As the wide area of China land is beneficial to the development of rail container freight, the share of rail freight is expected to be increased dramatically following the construction of railway infrastructure and other promoting polities. Therefore, by implementing the rail-based intermodal, the average $CO_2$ emission per ton-km freight in total will be reduced.

**Reference:**

Regmi, M. B. and Hanaoka, S. (2010). A framework to evaluate carbon emissions from freight transport and policies to reduce CO2 emissions through mode shift in Asia, The 3rd International Conference on Transportation and Logistics (T-LOG 2010), Fukuoka.

2005, 2006, 2009 Year Book Of China Transportation And Communications, Year Book House Of China Transportation And Communications.

The Ministry of Railway of China, 2000-2008 Statistics Bulletin Of China Railway.

The Ministry of Transport of China, 2000-2008 Statistics Bulletin Of Road Transportation And Water Transportation.

National Bureau of Statistics Of China, 2006-2009 China Statistical Yearbook.

National Bureau of Statistics Of China, 2008 China Energy Statistical Yearbook.

Shenwan Research Institute, (2009). Investment strategy of railway container transportation

Technical Report of International Development Engineering TRIDE-2011-01, February 15, 2011 (ISSN 1880-8468)

# Pattern Recognition by Kernel Wiener Filter

Student Number: 09M18226 Name: Rui LI Supervisor: Yukihiko YAMASHITA

# ウィナーフィルタを用いたパターン認識

李睿

逆問題のための代表的な手法であるウィナーフィルタ (WF) は，その評価基準が原信号と復元信号の差を原信号空間で直接比較するものであり，構成も容易であるという利点から，極めて広い範囲で応用されている。カーネルウィーナフィルタ (KWF) は，WF にカーネル法を適用したものであり，非線形処理が可能になる。本論文では，KWF を用いたパターン認識に着目する。まず，2 クラス認識における，原信号特徴空間のカーネル関数値と認識率との関係を調べる。そして，交差検定 (CV) の考え方を適用し，復元作用の素ための標本点と評価のための標本点を分ける，交差検定 KWF(CVKWF) を提案する。さらに，計算機実験によって，CVKWF の評価を行う。

## 1 Introduction

An inverse problem is a task to estimate an original signal from its observed data. The inverse problem often occurs in many fields of science and engineering. The restoration of deteriorated images is an application example of the inverse problem.

Let $\mathcal{H}_s$ be an original signal space and $\mathcal{H}_o$ be an observed signal space. An original signal and its observed signal are denoted by $\boldsymbol{f}$ and $\boldsymbol{g}$, respectively. The linear estimation model is given as the following equation:

$$\hat{\boldsymbol{f}} = B\boldsymbol{g}, \tag{1}$$

where $B$ is a bounded linear operator from $\mathcal{H}_o$ to $\mathcal{H}_s$, and $\hat{\boldsymbol{f}}$ is the estimated siganl. This model is illustrated in Fig.1. The linear inverse problem is to find the best estimated signal $\hat{\boldsymbol{f}}$ from the observed signal g.

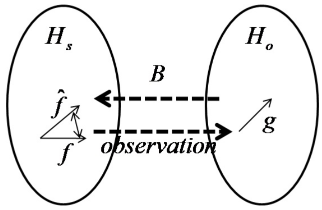


Fig. 1: Inverse problem

The Wiene filter (WF) is an representive solution for the inverse problem. It providers the best estimated signal with respect to the squared error averaged over the original and the observed signals among linear operators. WF directly compares $\boldsymbol{f}$ and $\hat{\boldsymbol{f}}$ in $\mathcal{H}_s$. Moreover, the criterion and realization of WF are so simple that it can be widely applied to many fileds.

According to the Mercer kernel theory, I can obtain an mapping operator by which low dimensional input siganals can mapped into a high diemnsional space (feature space). Nonlinear processing in the original space is realized by linear processing in the feature space. And the Mercer kernel theory provides us a way to calculate the value of inner product in feature space just by their low dimensional original signals. It is called kernel trick.

In this paper, I explain KWF and its application to pattern recognition. To acquire higher recognition results, I analysis the effect on recognition result brought from modfying original category vectors. I propose an effective way to modify the original category vectors and conducted experiments to prove it.

I propose subspace KWF (SKWF) of which filter model is constructed by a different set of samples from that for validation. By applying the cross validation method to SKWF, I propose the cross validated KWF (CVKWF). I show its advatage by experimental results.

## 2 Kernel Wiener Filter

The signals in a space are mapped by a nonlinear function $\boldsymbol{\Phi}$, which is derived from a Mercer kernel, into a reproducing kernel Hilbert Space (RKHS). This space is called the feature space. Generally speaking the feature space has a higher dimension than the original space. In this paper I use the following two kernel functions .

$$k_s(\boldsymbol{f}_x, \boldsymbol{f}_y) =< \boldsymbol{\Phi}_s(\boldsymbol{f}_x), \boldsymbol{\Phi}_s(\boldsymbol{f}_y) >, \tag{2}$$

$$k_o(\boldsymbol{g}_x, \boldsymbol{g}_y) =< \boldsymbol{\Phi}_o(\boldsymbol{g}_x), \boldsymbol{\Phi}_o(\boldsymbol{g}_y) > . \tag{3}$$

The model of KWF is shown in Fig2. $X$ is a restoration operator between $\mathcal{F}_s$ and $\mathcal{F}_o$. Its estimated signal is given by $X\boldsymbol{\Phi}_o(\boldsymbol{g})$. $\hat{\boldsymbol{f}}$ is provided by using $X\boldsymbol{\Phi}_o(\boldsymbol{g})$.

KWF$X$ minimizes the sum of squared errors between $\boldsymbol{\Phi}_o(\boldsymbol{f}_i)$ and its restored signal $X\boldsymbol{\Phi}_o(\boldsymbol{g}_i)$. Then $X$ minimizes the following criterion $J_{KWF}$.

$$J_{KWF} = \frac{1}{L}\sum_{i=1}^{L} \|\boldsymbol{\Phi_s}(\boldsymbol{f}_i) - X\boldsymbol{\Phi_o}(\boldsymbol{g}_i)\|^2. \tag{4}$$

I assume $X$ is given by

$$X = \sum_{i=1}^{L}\sum_{j=1}^{L} h_{ij}\boldsymbol{\Phi}_s(\boldsymbol{f}_i)\boldsymbol{\Phi}_o(\boldsymbol{g}_j)^T. \tag{5}$$

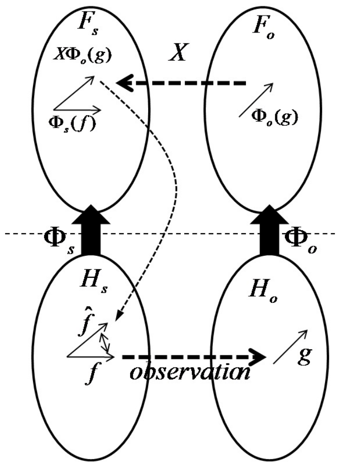


Fig. 2: Inverse problem between $\mathcal{F}_s$ and $\mathcal{F}_o$

For calculation, I define the following $(L \times L)$ matrixes, $H$,$K_g$,$K_s$.

$$H = \begin{bmatrix} h_{11} & h_{12} & \dots & h_{1L} \\ h_{21} & h_{22} & \dots & h_{2L} \\ \vdots & \vdots & \ddots & \vdots \\ h_{L1} & \dots & \dots & h_{LL} \end{bmatrix}, \tag{6}$$

$$K_g = \begin{bmatrix} k_o(\boldsymbol{g}_1, \boldsymbol{g}_1) & k_o(\boldsymbol{g}_1, \boldsymbol{g}_2) & \dots & k_o(\boldsymbol{g}_1, \boldsymbol{g}_L) \\ k_o(\boldsymbol{g}_2, \boldsymbol{g}_1) & k_o(\boldsymbol{g}_2, \boldsymbol{g}_2) & \dots & k_o(\boldsymbol{g}_2, \boldsymbol{g}_L) \\ \vdots & \vdots & \ddots & \vdots \\ k_o(\boldsymbol{g}_L, \boldsymbol{g}_1) & \dots & \dots & k_o(\boldsymbol{g}_L, \boldsymbol{g}_L) \end{bmatrix}, \tag{7}$$

$$K_s = \begin{bmatrix} k_s(\boldsymbol{f}_1, \boldsymbol{f}_1) & k_s(\boldsymbol{f}_1, \boldsymbol{f}_2) & \dots & k_s(\boldsymbol{f}_1, \boldsymbol{f}_L) \\ k_s(\boldsymbol{f}_2, \boldsymbol{f}_1) & k_s(\boldsymbol{f}_2, \boldsymbol{f}_2) & \dots & k_s(\boldsymbol{f}_2, \boldsymbol{f}_L) \\ \vdots & \vdots & \ddots & \vdots \\ k_s(\boldsymbol{f}_L, \boldsymbol{f}_1) & \dots & \dots & k_s(\boldsymbol{f}_L, \boldsymbol{f}_L) \end{bmatrix}. \tag{8}$$

and the following solution.

$$H^T = K_o(K_o K_o)^{\dagger}. \tag{9}$$

Training data are given as pairs $(\boldsymbol{f}_i, \boldsymbol{g}_i) \quad (i = 1, \dots, L)$, where $\boldsymbol{f}_i$ represents the category of $\boldsymbol{g}_i$. Let $\boldsymbol{f}_t^{\dagger}$ indicate the category $t$, $\boldsymbol{g}$ be the unkonwn pattern. To simply the calculation, I substract $\|X\boldsymbol{\Phi}_o(\boldsymbol{g})\|$ which does not depend on the category from the squared error, then, the discriminant function $d_t(\boldsymbol{g})$ is given by

$$\begin{aligned} d_t(\boldsymbol{g}) &\equiv \|\boldsymbol{\Phi}_s(\boldsymbol{f}_t^{\dagger}) - X\boldsymbol{\Phi}_o(\boldsymbol{g})\|^2 - \|X\boldsymbol{\Phi}_o(\boldsymbol{g})\| \\ &= K_s(\boldsymbol{f}_t^{\dagger}, \boldsymbol{f}_t^{\dagger}) \\ &- 2[k_o(\boldsymbol{g}_1, \boldsymbol{g}), \dots, k_o(\boldsymbol{g}_L, \boldsymbol{g})]H^T \begin{bmatrix} K_s(\boldsymbol{f}_t^{\dagger}, \boldsymbol{f}_1) \\ \vdots \\ K_s(\boldsymbol{f}_t^{\dagger}, \boldsymbol{f}_L) \end{bmatrix}. \end{aligned} \tag{10}$$

# 3 Modifying Kernel Function Value

To explain briefly,I assume that $\boldsymbol{\Phi}_o(\boldsymbol{g})$ is a linear combination of $\boldsymbol{\Phi}_o(\boldsymbol{g}_i)$ $(i = 1, \dots, L)$ :

$$\boldsymbol{\Phi}_o(\boldsymbol{g}) = \sum_{i=1}^{L} \alpha_i \boldsymbol{\Phi}_o(\boldsymbol{g}_i). \tag{11}$$

I define vector $\hat{\boldsymbol{h}}$

$$\hat{\boldsymbol{h}} = 2[\alpha_1, \dots, \alpha_L]. \tag{12}$$

and assume that $K$ is regular. Then the discriminant function $d_t(\boldsymbol{g})$ can be described as

$$d_t(\boldsymbol{g}) = K_s(\boldsymbol{f}_t^{\dagger}, \boldsymbol{f}_t^{\dagger}) - \hat{\boldsymbol{h}} \begin{bmatrix} K_s(\boldsymbol{f}_t^{\dagger}, \boldsymbol{f}_1) \\ \vdots \\ K_s(\boldsymbol{f}_t^{\dagger}, \boldsymbol{f}_L) \end{bmatrix}. \tag{13}$$

It's clear I don't have to calculate the kernel function in $\mathcal{H}_s$ but just need its value. Let an angle between $\boldsymbol{\Phi}_s(\boldsymbol{f}_i^{\dagger})$ and $\boldsymbol{\Phi}_s(\boldsymbol{f}_j^{\dagger})$ in $\mathcal{F}_s$ be $\theta_{ij}$, the inner product is obtained as the following eq.(14) by deciding on the value of $\|\boldsymbol{\Phi}_s(\boldsymbol{f}_t^{\dagger})\|$ and $\theta_{ij}$.

$$\begin{aligned} k_s(\boldsymbol{f}_i^{\dagger}, \boldsymbol{f}_j^{\dagger}) &= \boldsymbol{\Phi}_s(\boldsymbol{f}_i^{\dagger})^T \boldsymbol{\Phi}_s(\boldsymbol{f}_j^{\dagger}) \\ &= \|\boldsymbol{\Phi}_s(\boldsymbol{f}_i^{\dagger})\| \cdot \|\boldsymbol{\Phi}_s(\boldsymbol{f}_j^{\dagger})\| \cos\theta_{ij}. \end{aligned} \tag{14}$$

To simply the problem, I just analysis 2-class recognition. $+1$ and $-1$ represent categories. And I suppose the fisrt $L_1$ training data are included in category $+1$, the others are included in category $-1$. Since $K_o$ is fixed, the discriminant function is described by

$$d_t(\boldsymbol{g}) = \|\boldsymbol{f}_t^{\dagger}\|^2 - \hat{\boldsymbol{h}} \begin{bmatrix} K_s(\boldsymbol{f}_{+1}^{\dagger}, \boldsymbol{f}_t^{\dagger}) \\ \vdots \\ K_s(\boldsymbol{f}_{+1}^{\dagger}, \boldsymbol{f}_t^{\dagger}) \\ K_s(\boldsymbol{f}_{-1}^{\dagger}, \boldsymbol{f}_t^{\dagger}) \\ \vdots \\ K_s(\boldsymbol{f}_{-1}^{\dagger}, \boldsymbol{f}_t^{\dagger}) \end{bmatrix} \tag{15}$$

## 3.1 Modifying angles with the same norms

Suppose $\|\boldsymbol{f}_{+1}^{\dagger}\| = \|\boldsymbol{f}_{-1}^{\dagger}\|$, then the differece between 2 discriminant values can be represented as following.

$$d_{+1}(\boldsymbol{g}) - d_{-1}(\boldsymbol{g}) = -\hat{\boldsymbol{h}}\|\boldsymbol{f}_{+1}^{\dagger}\|^2(1 - \cos\theta)\boldsymbol{\mu}, \tag{16}$$

where

$$\boldsymbol{\mu} = [1, \dots, 1, -1, \dots, -1]^T \tag{17}$$

When $\theta$ doesn't equal to 0, the value of $(1 - \cos\theta)$ is always positive. In such case, modifying $\theta$ can't change the recogniton result. Only when $\theta$ the sign of the differece value chages, the recogniton result will change.

### 3.2 Modifying norms with $\cos\theta = 0$

When $\cos\theta = 0$, the difference between 2 discriminant values can be discribed as following.

$$\begin{aligned} d(\boldsymbol{g}) &= d_{+1}(\boldsymbol{g}) - d_{-1}(\boldsymbol{g}) \\ &= \|\boldsymbol{f}^{\dagger}_{+1}\|^2 - \|\boldsymbol{f}^{\dagger}_{-1}\|^2 - \|\boldsymbol{f}^{\dagger}_{+1}\|^2 \sum_{i=1}^{L_1} \alpha_i \\ &+ \|\boldsymbol{f}^{\dagger}_{-1}\|^2 \sum_{j=L_1+1}^{L} \alpha_j. \end{aligned} \tag{18}$$

(19)

I denote the value of $d(\boldsymbol{g})$ by $d_o(\boldsymbol{g})$ when $\|\boldsymbol{f}^{\dagger}_{+1}\| = \|\boldsymbol{f}^{\dagger}_{-1}\| = 1$. I can have

$$d_0(\boldsymbol{g}) = d_{+1}(\boldsymbol{g}) - d_{-1}(\boldsymbol{g}) = \sum_{j=L_1+1}^{L} \alpha_j - \sum_{i=1}^{L_1} \alpha_i, \tag{20}$$

When $\|\boldsymbol{f}^{\dagger}_{+1}\|$ is changed, I have,

$$d(\boldsymbol{g}) = d_0(\boldsymbol{g}) + (\|\boldsymbol{f}^{\dagger}_{+1}\|^2 - 1)\Big(1 - \sum_{i=1}^{L_1} \alpha_i\Big). \tag{21}$$

If $\sum_{i=1}^{L_1} \alpha_i < 1$ and $d_0(\boldsymbol{g}) < 0$, the sign of $d(\boldsymbol{g})$ can chage from minus to plus by increasing $\|\boldsymbol{f}^{\dagger}_{+1}\|$. In this case, modifying norm is an effective way for increasing recognition rate of the $-1$ category. If $\sum_{i=1}^{L_1} \alpha_i > 1$ and $d_0(\boldsymbol{g}) < 0$, increasing $\|\boldsymbol{f}^{\dagger}_{+1}\|$ will not chage the sign of $d(\boldsymbol{g})$.

### 3.3 Modifying $\cos\theta$ with fixed norms

When $\|\boldsymbol{f}^{+}_{+1}\|$ and $\|\boldsymbol{f}^{+}_{-1}\|$ are fixed, I have

$$\begin{aligned} d(\boldsymbol{g}) &= d_{+1}(\boldsymbol{g}) - d_{-1}(\boldsymbol{g}) \\ &= \|\boldsymbol{f}^{\dagger}_{+1}\|^2 - \|\boldsymbol{f}^{\dagger}_{-1}\|^2 \\ &+ (\|\boldsymbol{f}^{\dagger}_{+1}\|\|\boldsymbol{f}^{\dagger}_{-1}\|\cos\theta - \|\boldsymbol{f}^{\dagger}_{+1}\|^2) \sum_{i=1}^{L_1} \alpha_i \\ &+ (\|\boldsymbol{f}^{\dagger}_{-1}\|^2 - \|\boldsymbol{f}^{\dagger}_{+1}\|\|\boldsymbol{f}^{\dagger}_{-1}\|\cos\theta) \sum_{j=L_1+1}^{L} \alpha_j. \end{aligned} \tag{22}$$

When modifying $\cos\theta$, the differece of $\|\boldsymbol{f}^{+}_{+1}\|$ and $\|\boldsymbol{f}^{+}_{-1}\|$ can be control $d(\boldsymbol{g})$.

# 4 Cross-validation KWF(CVKWF)

### 4.1 Subspace KWF(SKWF)

I propose the subspace KWF (SKWF) where data to construct the filter model are different from data for validation. I denote the former data as $(\boldsymbol{f}^1_n, \boldsymbol{g}^1_n)$ $n = 1, \ldots, M$, and denote the later data as $(\boldsymbol{f}^2_n, \boldsymbol{g}^2_n)$ $n = 1, \ldots, L$. Then, the criterion of SKWF $X_S$ is given as

$$J_{SKWF} = \frac{1}{M} \sum_{m=1}^{M} \|\boldsymbol{\Phi}_s(\boldsymbol{f}^1_m) - X_S \boldsymbol{\Phi}_o(\boldsymbol{g}^1_m)\|^2, \tag{23}$$

where

$$X_S = \sum_{i=1}^{c} \sum_{j=1}^{L_2} h_{ij} \boldsymbol{\Phi}_s(\boldsymbol{f}^{\dagger}_i) \boldsymbol{\Phi}_o(\boldsymbol{g}^2_j)^T. \tag{24}$$

### 4.2 CVKWF

I propose to design SKWF by applying the cross validation method. I call the filter the cross validated KWF (CVKWF). Learning data is divided into $A$ folds. Of the $A$ folds, $B$ fold is used for the filter model, and the remaining $A - B$ folds are used for the validation of the filter model. The cross-validation process is then repeated $A$ times. The $A$ results for the filter model are averaged (or otherwise combined) to produce a single estimation. The usage of data for CVKWF($A = N, B = 1$) is shown as Fig.3.

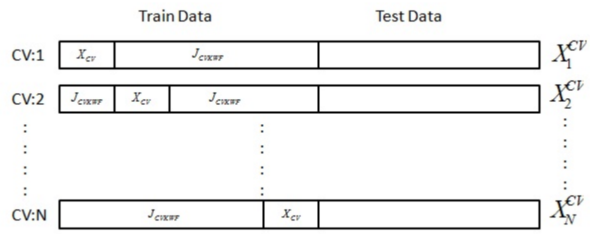


Fig. 3: Usage of data for CVKWF

# 5 Experiment result

In the experiment, I used the CTG data set and Image Segementation data set from UCI Machine Learning Repository. CTG and Image Segementation are both multiclass recogniton data. And I extract class1 and class2 data from CTG and Foliage and Window data from Image Segmentation to conduct 2-class recognition experiment.

### 5.1 Modifying the original signal

Table 1. shows the experiment results of modifying norms with $\cos\theta = 0$. From the result, with increasing the norm of one category, the miss-recognition from the other category to the category becomes larger, and the miss-recognition from the category to the other category becomes fewer.

Table 2. shows the experiment result of modifying $\cos\theta$ with $\|\boldsymbol{f}^{\dagger}_{-1}\| = 1, \|\boldsymbol{f}^{\dagger}_{+1}\| = 1.1$. From the result, modifying

Table 1: KWF FOLIAGE(class +1) WINDOW(class -1) $\cos\theta_{+1-1}$=0 modifing norms

| Norm $\|f^{\dagger}_{+1}\|$ | Norm $\|f^{\dagger}_{-1}\|$ | misrecog-size $+1 \overset{miss}{\to} -1$ | misrecog-size $-1 \overset{miss}{\to} +1$ | mis rate |
|---|---|---|---|---|
| 1 | 1 | 48 | 35 | 13.83 |
| 1 | 1.1 | 41 | 40 | **13.50** |
| 1 | 1.5 | 36 | 49 | 14.17 |
| 1 | 100 | 33 | 59 | 15.33 |
| 1.1 | 1 | 72 | 32 | 17.33 |
| 1.5 | 1 | 77 | 30 | 17.83 |
| 100 | 1 | 93 | 26 | 19.83 |

Table 2: KWF FOLIAGE(class +1) WINDOW(class -1)modifing $\theta$

| | $\|f^{\dagger}_{-1}\| = 1, \|f^{\dagger}_{+1}\| = 1.1$ | | |
|---|---|---|---|
| $\cos\theta_{+1-1}$ | $+1 \overset{miss}{\to} -1$ | $-1 \overset{miss}{\to} +1$ | mis rate |
| 0.9 | 33 | 56 | 14.83 |
| 0.7 | 38 | 48 | 14.33 |
| 0.4 | 41 | 41 | 13.67 |
| 0 | 41 | 40 | 13.50 |
| -0.1 | 41 | 36 | **13.17** |
| -0.5 | 42 | 38 | 13.33 |

the value of $\cos\theta$ can control the difference between the miss-recognitions of two categories.

Table 3. shows experiment results of modifying both norms and $\cos\theta$. From the experiment result, after modifying $\|\boldsymbol{f}^{\dagger}_{+1}\|$ and $\|\boldsymbol{f}^{\dagger}_{-1}\|$, modifying $\theta_{+1-1}$ is an effective way to improve the recognition rate.

### 5.2 CVKWF

In the Table 4. and Table 5., **CVKWF (A-B)** represents that I divide training data into **A** folds and use **B** folds to construct the filter model. Table 4. shows the least mis recogniton rate of KWF, CVKWF, and SVM. **CVKWF(4-3)** is the best recognition rate. Table 5. shows the detail of every CVKWF experiment. I found that I can get better recongnition rate by using **A-1** folds to construct the filter model than by using only **1** fold to construct the filter model.

## 6 Conclusion

In this paper, I investigated the pattern recognition by KWF. I clarified the effect of changing values of a kernel function in the original vectors on recognition. I proposed

Table 3: KWF FOLIAGE(class +1) WINDOW(class -1) modifing cross result

| $\cos\theta_{+1-1}$ | $\|f^{\dagger}_{-1}\|(\|f^{\dagger}_{+1}\| = 1)$ | | | |
|---|---|---|---|---|
| | 1 | 1.1 | 1.5 | 2 |
| 0.4 | 13.83 | 13.67 | 14.33 | 14.67 |
| 0 | 13.83 | 13.50 | 14.17 | 14.50 |
| -0.1 | 13.83 | **13.17** | 14.33 | 14.67 |
| -0.5 | 13.83 | 13.33 | 14.67 | 14.33 |

Table 4: CVKWF,CTG(c1,c2),best result

| | **KWF** | **CVKWF(4-3)** | SVM |
|---|---|---|---|
| **mis rate** | 17.56 | **16.83** | 18.78 |

Table 5: CVKWF,CTG(c1,c2),experiment result detail

| | **miss rate** |
|---|---|
| **CVKWF(2-1)** | 17.80 |
| **CVKWF(3-1)** | 17.32 |
| **CVKWF(3-2)** | 17.07 |
| **CVKWF(4-1)** | 18.29 |
| **CVKWF(4-3)** | **16.83** |
| **CVKWF(5-1)** | 18.05 |
| **CVKWF(5-4)** | 18.05 |

KWF with subspace constraint SKWF. By combining cross validation method to SKWF, I proposed CVKWF. I showed the advantages of proposed methods by experiments of pattern recognition.

## References

[1] Y. Washizawa and Y. Yamashita, Kernel Wiener filter, *JIEICE 6 workshop in computer information-theoretic learning theory*, Nov. 2003, pp.143-148.

[2] Y. Washizawa and Y. Yamashita, Kernel Wiener filter, *JIEICE magazine*, vol.103, no.733, 2003, pp.73-78.

[3] Y. Washizawa and Y. Yamashita, Non-linear Wiener filter in reproducing kernel Hilbert space, *18th International Conference on Pattern Recognition(ICPR'06)*, 2006, pp.967-970.

[4] Young-Chul SONG and Doo-Hyun CHOI, Kernel Adjusted Wiener Filter for Image Enhancement, *Japanese Journal of Applied Physics.*, Part 2 Letters, vol.44, issue.6A, 2005, pp3996-3999.

[5] Hirokazu Yoshino, Chen Dong, Yoshikazu Washizawa, and Yukihiko Yamashita Kernel Wiener Filter and its Application to Pattern Recognition, *IEEE Trans. on Neural Networks*, vol. 21, no. 11, pp.1719–1730, Nov., 2010.

# ASSESSMENT OF OPERATIONAL EFFICIENCY AND SPACE ALLOCATION OF LOW-COST TERMINAL IN AIRPORTS

Student Number: 09M51608 Name: Batari SARASWATI Supervisor: Shinya HANAOKA

This thesis aims to propose models and solutions toward LCT's operational efficiency and space allocation issues so that LCT could become a sustainable concept that can be adopted by many airports. An optimization model is conducted to find the best terminal site and configuration for LCT that minimize the distance travelled by passengers and aircrafts according to the number of aircraft gates desired. Furthermore, an optimization model is also developed to calculate concession space in departure airside and landside in order to maximize potential non-aeronautical revenue.

# 1. Introduction

The low-cost carrier (LCC) industry is growing rapidly for the past decade resulting in a new trend in aviation industry. Airport is one of the elements that influenced heavily by the growth of LCCs [1]. Some have developed the concept of dedicated LCT to accommodate the requirements of LCCs, the concept of which emphasizes on cost and time reduction.

LCT has its own capability to process flights and passengers using a simplified terminal building design. It uses straightforward design without any aesthetic or prestigious value, for instance, LCT do not provide air-bridges and eliminates luxury lounges.

LCT could be redeveloped from existing facilities (old passenger terminal or old cargo terminal) or could be built as a brand- new dedicated terminal. Airports with LCT may benefit from additional traffic from LCC services. Since airport faces large fixed infrastructure costs, each airport with excess capacity can benefit from LCCs services following the fact that airports can do so at low marginal cost per passenger [2].

Despite all the advantages that can be offered by LCT development in airport, the sustainability of this concept is still in question [3]. The fundamental question that the author intended to address is how to ensure the sustainability of LCT despite all the difficulties that it potentially face. There are two potential issues that have been identified: *operational efficiency* and *profitability*.

Operational efficiency discussed in this thesis is a response to LCT characteristic as an additional terminal in airport that subject to space limitation problem. It raises a necessity to effectively determine LCT location and configuration. Profitability issue discussed in this thesis is a response to an increasing pressure from LCCs to lower the level of aeronautical fees. Airport authority has to seek new ways of generating revenues mostly by giving greater attention to commercial (non-aeronautical) revenue.

There are two main objectives of this thesis. The first objective is to determine the effective location and configuration of LCT inside an airport by taking into account passenger walking distance and aircraft taxiing distance. The second objective is to determine space allocation of commercial area inside the LCT building to ensure non-aeronautical revenue maximization. Further elaboration about each objective and its optimization model are provided accordingly.

# 2. Operational Efficiency of LCT

## 2.1 Model Formulation

To determine the location of configuration of LCT inside an airport, there are parameters that need to be considered. The configuration of LCT is determined by passenger walking distance parameter. Meanwhile, the location of LCT toward other facilities inside an airport is very much determined by aircraft taxiing distance parameter. Each of this parameter has its own importance to affect aircraft's turnaround time thus influence operational efficiency at the terminal.

There are 4 terminal configurations discussed: (1) linear, (2) single pier, (3) T-shaped pier, and (4) Y-shaped pier. The average walking distance is calculated as total walking distance required to travel from end point of waiting area to each gates (from the most distant and the closest gate) divided by the number of gates. Notify that in LCC business process, transfer passengers cannot directly travel from one gate to another since most LCCs serve point-to-point flights.

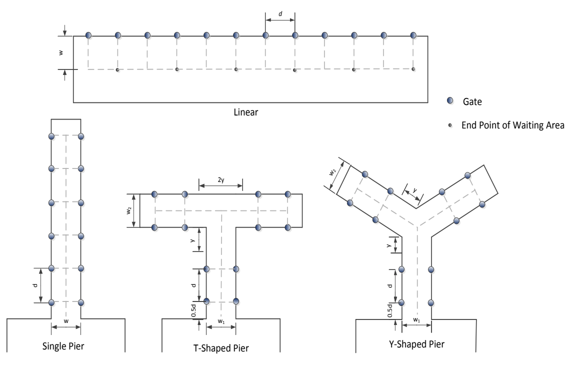


Figure 2-1. LCT configuration

Mathematical model is developed to solve the problem of terminal site and terminal configuration for LCT more systematically. The mathematical model has two objectives. Objective (2.1) minimizes average passenger walking distance (*DW*) from waiting point to aircraft gates. Objective (2.2) minimizes average aircraft taxiing distance (*DT*) required from runways to apron area. The role of $z_{ij}$ is to assure the choice of one site and one configuration for the new terminal. The constraints (2.3) and (2.4) guarantee that the longest length $g(x_{ij})$ and width $h(x_{ij})$ of the gross area needed to build terminal based on the number of aircraft gates desired in new terminal site $i$ with configuration $j$ do not exceed the length and width of the new terminal site, $L_i$ and $W_i$.

$$\text{Min } DW = \sum_i \sum_j z_{ij} f(x_{ij}) \quad (2.1)$$

$$\text{Min } DT = \frac{1}{p} \sum_i z_{ij} \sum_k (d_{ik} + d_{ki}) \quad (2.2)$$

Subject to:

$$g(x_{ij}) \leq L_i \quad \forall\, i,j \quad (2.3)$$

$$h(x_{ij}) \leq W_i \quad \forall\, i,j \quad (2.4)$$

$$\sum_i \sum_j z_{ij} = 1 \quad (2.5)$$

$$z_i, z_j \; \epsilon \; (0,1) \quad \forall\, i,j$$

The weighted sum of the objective method can be applied to solve bi-objective optimization of terminal location and configuration problem. It entails selecting scalar weights ($w_i$) and minimizing the composite objective function. The weight is determined by paired comparison method. In order to obtain the weights ($w_1$ and $w_2$), passenger value of time per unit distance will be compared to aircraft value of time per unit distance. Passenger time value is \$0.00539/m, while the aircraft time value is \$0.01207/m [4], thus $w_1 = 1$ and $w_2 = 2.24$.

## 2.2 Hypothetical Example

To demonstrate how the model works and to verify its usefulness, the hypothetical problem regarding location and configuration of LCT in airport is presented.

Table 2-1. Input data for hypothetical example

| Site ($i$) | | Site 1 | Site 2 | Site 3 | Site 4 |
|---|---|---|---|---|---|
| Area[a] ($m^2$) | | 17,500 | 24,000 | 23,000 | 25,000 |
| | | 155 x 112 | 210 x 114 | 200 x 115 | 200 x 125 |
| Taxiing distance (m) ($d_{ik}$, $d_{ki}$) | Runway 1 | (3000, 4050) | (4000, 3700) | (4500, 4500) | (3000, 4300) |
| | Runway 2 | (2400, 3600) | (2000, 3400) | (3500, 4500) | (3800, 2700) |

There are 4 alternative sites that are suitable for LCT construction in an airport. There are 4 choices of terminal configurations: linear ($j$ = 1), single pier ($j$ = 2), T-shaped pier ($j$ = 3) and Y-shaped pier ($j$ = 4).

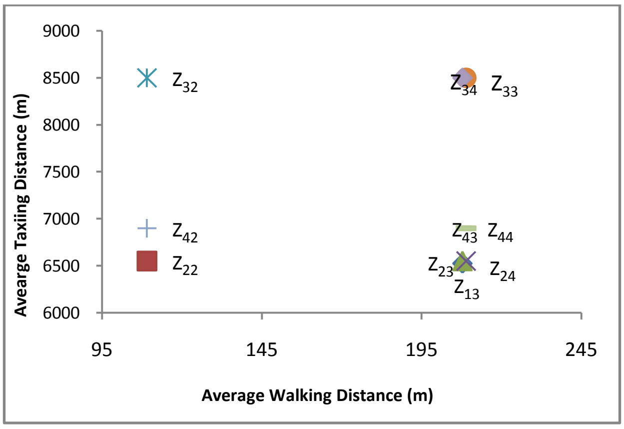


Figure 2-2. Solution graph ($z_{ij}$ = new terminal site $i$ with configuration $j$)

Six $z_{ij}$ excluded from the solution set ($z_{11}$, $z_{12}$, $z_{14}$, $z_{21}$, $z_{31}$, and $z_{41}$) because they do not satisfy constraint (2.3) and (2.4) in the model formulation. As a result, we have ten possible solutions where two of them are non-inferior solutions and achieve Pareto optimality ($z_{13}$ and $z_{22}$). After applying the single objective function with the determined weights, the optimal solution is obtained. A new terminal should be located in site 2 with a single pier configuration ($z_{22}$), with objective function equal with 14,763.01.

Sensitivity analysis is performed to see the effect of different passenger and aircraft value of time to the model result. We change the value of $w_2$ which represents the ratio of aircraft to passenger time value per unit distance (\$/meter). When ratio of aircraft to passenger time value per unit distance achieves 3.974, the solution will shift from $z_{22}$ to $z_{13}$. In addition to that, the solution will shift from $z_{22}$ to $z_{13}$ if the walking distance in $z_{13}$ is reduced 20.6% into 165 meter.

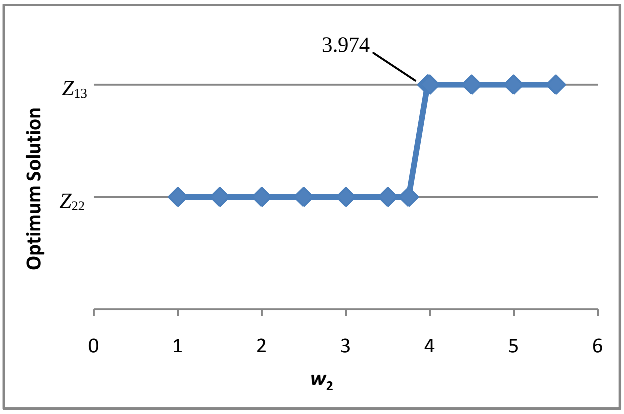


Figure 2-3. Sensitivity analysis for terminal location and configuration

# 3. Space Allocation of LCT

## 3.1 Model Formulation

Non-aeronautical (commercial) revenue is very important for LCT [5]. Airport authorities need to seize the business opportunity from LCC passengers so that they can compensate the lost in aeronautical revenue. This issue is accommodated in this thesis through further discussion in optimizing the allocation of commercial space inside LCT building to ensure revenue maximization. The basic concept of the optimization model was adapted from Hsu and Chao (2005) [6] with several customizations to suit LCT characteristics.

The very nature of simple design of LCTs might results in less extensive range of facilities compared with ordinary terminal. This study categorizes the store variety in LCT into four main types: (1) Food and beverage store, (2) Travel convenience store, (3) Specialized store, (4) Duty-free Store.

The idea of the optimization model is to allocate space for commercial activity in LCT that ensures revenue maximization. This study focus on departure area since departure area is counted as more reliable source of commercial revenue compared to arrival area.

$$Max\ TR = \sum_{k=1}^{l}\sum_{j=1}^{m}\sum_{i=1}^{n} R_{ijk}\, X_{ijk} \quad (3.1)$$

Subject to:

$$\sum_{i=1}^{n} X_{ijk} \le A_{jk} \quad \forall k = 1,\dots,l;\ j = 1,\dots,m \quad (3.2)$$

$$\sum_{k=1}^{l} X_{ijk} \le S_{ij} \quad \forall i = 1,\dots,n;\ j = 1,\dots,m \quad (3.3)$$

*TR* represents the total concession revenue in the LCT. $X_{ijk}$ acts as the variable decision, represents square meter area for concession type *i* in location *j* (departure airside/landside) and location *k* (<10 m, 10-50 m, >50 m from entrance point). $X_{ijk}$ has to be in the range between $S_{ij}$ (minimum area required to meet terminal design standard) and $A_{jk}$ (commercial space available).

$$R_{ijk} = \left(C_{ijk}\, AS_i + AC_{ijk}\, F_i\right) PB_{ijk} \quad (3.4)$$

Concession revenue is calculated based on charge per square meter area ($C_{ijk}$), in addition to certain percentage of sales ($F_i$), where $PB_{ijk}$ denotes number of potential buyers for each concession type *i* in location (*j*,*k*).

To define number of potential buyers, LCC passenger dwelling time and LCC passenger preferences toward concessions are incorporated into the model. Potential buyer means individual that can reach certain concession $X_{ijk}$ and remain there longer than the shortest duration required for consumption activities ($TO_i$), defined as follows:

(1) Number of potential buyers in airside. Departure airside is defined as the secured area beyond passport control that can only be accessed by departure passengers who have valid ticket and have completed check-in, security and immigration processes. Let $\theta_{pf}$ denotes the airside dwelling time of departure passenger *p* who take flight *f*, where shortly $\theta_{pf}$ is expressed as probability distribution function $F(\theta)d\theta$.

$$\theta_{pf} = tb_f - th_{pf} - \left(tc + ti + ts + \frac{D_f}{v}\right) \quad (3.5)$$

$$PB_{i1k} = \sum_f \sum_g \sum_v PB_{ivgk}\, P_f\, e_v \quad (3.6)$$

$$PB_{ivgk} = \begin{cases} \int_{a_g}^{b_g} F(\theta)d\theta\,;\ \text{if } b_g - T \ge TO_{ivg} \text{ where } T = T + TO_{ivg} + \frac{D_k}{V} \\ 0;\ \text{otherwise} \end{cases} \quad (3.7)$$

Equation 3.7 calculates number of potential buyers in every concession as the sum of those who have dwell time range more than minimum time required to undertake consumption activity ($b_g - T \ge TO_{ivg}$). Index *v* denotes index for number of passenger preference types toward concessions (*n* type of concessions in LCT results in *n!* passenger preferences). Boarding time of flight *f* is denoted by $t_{bf}$, while $th_{pf}$ denotes check-in time of departure passenger *p* who takes flight *f*. Time required for passenger to complete check-in, security, immigration processes are denoted by $t_c$, $t_s$, $t_i$ respectively. $D_f$ indicates the total walking distance of passenger flight *f* to complete all compulsory processes. $P_f$ denotes number of passengers in flight *f*. Variable *T* acts as temporary variable that denotes the accumulation of passenger shopping time, initial value of *T* = 0.

(2) Number of potential buyers in landside. Departure landside is defined as the area before the passport control which can be accessed by anyone (passengers and well-wishers/visitors) since it has no entry barriers. Let $t_{pf}$ denotes the landside dwelling time of departure passenger *p* who take flight *f*, where shortly $t_{pf}$ is expressed as probability distribution function $F(t)dt$. Variable $ta_{pf}$ indicates arrival time in terminal, *r* denotes ratio of well-wishers to departure passengers, $w_{ik}$ denotes probability of well-wishers to choose concessions.

$$t_{pf} = th_f - ta_{pf} \quad (3.8)$$

$$PB_{i1k} = \sum_f \sum_g \sum_v PB_{ivgk}\, P_f\, e_v + \sum_f P_f\, r\, w_{ik} \quad (3.9)$$

$$PB_{ivgk} = \begin{cases} \int_{a_g}^{b_g} F(t)dt\,;\ \text{if } b_g - T \ge TO_{ivg} \text{ where } T = T + TO_{ivg} + \frac{D_k}{V} \\ 0;\ \text{otherwise} \end{cases} \quad (3.10)$$

## 3.2 Case Study

This study chooses Terminal 3 Soekarno-Hatta International Airport as an example to demonstrate the feasibility and usefulness of the constructed models for terminal commercial space allocation. Soekarno-Hatta International Airport is located in Jakarta, Indonesia. There are 2 LCCs operate in Terminal 3, AirAsia and Mandala Air.

An online survey was conducted on December 23rd 2010 – January 24th 2011 to reveal passenger stated preference toward concessions. The total number of collected data is 296, with 222 of them are passengers and 74 of them are well-wishers.

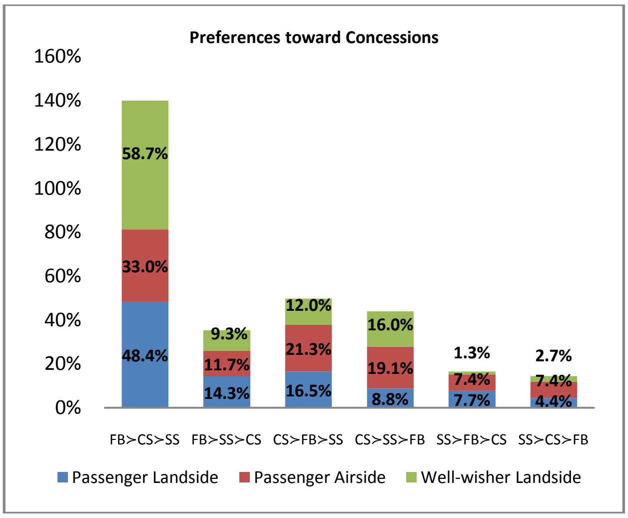


Figure 3-1. Terminal user preferences toward concessions

Passenger dwelling time distribution is also observed. The dwelling time observed in this study is a result of observation towards passenger arrival time, check-in time and flight boarding time. Beta distribution is found as the most fitted probability density function for passenger dwelling times in Terminal 3. At average, AirAsia and Mandala Airlines passengers comes 1.5 - 2 minutes after the check-in counter open. The mean of dwelling time in airside is 66 minutes for AirAsia and 63 minutes for Mandala Air passengers.

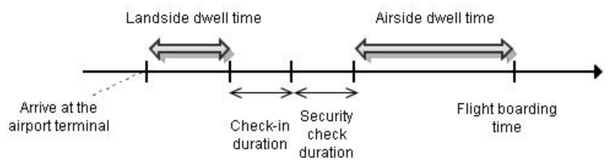


Figure 3-2. Landside and airside dwell time

This study applies the models formulated in previous section to allocate spaces and positions for concessions in Terminal 3. Under current commercial strategy of airside and landside split, the terminal has relatively unbalanced arrangement. There are 136 $m^2$ (8.09%) differences between the space demand and the capacity in airside, while there are 946 $m^2$ (62.2%) differences between space demand and the capacity in landside.

Table 3-1. Optimal square meters and position for concessions

| Concessions (i) | Space demand ($m^2$) | Allocated space ($m^2$) at departure airside | | | Space demand ($m^2$) | Allocated space ($m^2$) at departure landside | | |
|---|---|---|---|---|---|---|---|---|
| | | < 10 m | 10 - 50 m | > 50 m | | < 10 m | 10 - 50 m | > 50 m |
| Food and Beverage | 690 | 220 | 470 | 0 | 360 | 360 | 0 | 0 |
| Travel Convenience | 624 | 0 | 0 | 624 | 145 | 20 | 125 | 0 |
| Specialized Store | 230 | 0 | 170 | 60 | 69 | 0 | 69 | 0 |
| Total space demand | 1544 | 220 | 640 | 684 | 574 | 380 | 194 | 0 |
| Capacity | 1680 | 220 | 640 | 820 | 1520 | 380 | 560 | 580 |
| Area occupied | 878 | 220 | 640 | 18 | 659 | 380 | 279 | 0 |

Terminal 3 authority intends to attract other terminal users beside passengers (visitors, well-wishers and greeters) to visit and consume in concessions; they put quite large area in departure landside. However, in Terminal 3, the ratio of well-wishers to passengers is quite low ($r$ = 0.2) since it only serves domestic short-haul flights.

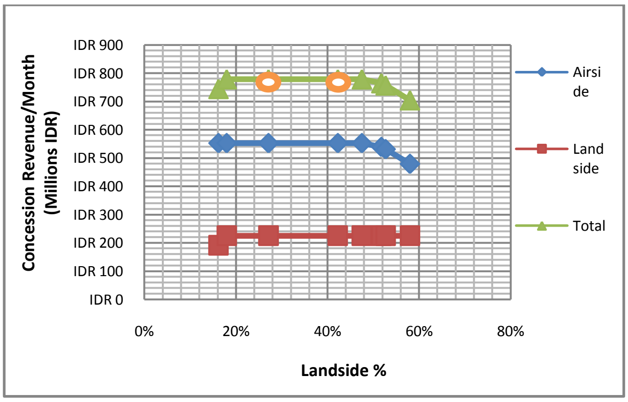


Figure 3-3. Optimal landside – airside split

1 USD ≅ 9,009 IDR

Sensitivity analysis is conducted to see how the revenue is influenced by the changes in commercial space available in departure area. When the available space in landside area is reduced 9.8% from the demand (518 $m^2$), the revenue is potentially decreased around 15.04%. When the available space in airside area is reduced 10.5% from the demand, the revenue is potentially decreased around 13.3%. Moreover, 5% increase in well-wishers ratio results in 4.2% increase in revenue; and 10% increase in number of passengers who arrive 30 minutes before check-in time, results in 8% increase in revenue.

For Terminal 3 which serves domestic flights, the ideal airside – landside split in departure area is 72.9% – 27.1% (where the actual space available split is 52.5% – 47.5%). From the available space, only 47.7% (878 $m^2$) and 43.4% (659 $m^2$) are currently utilized for concessions in airside and landside, respectively.

# 4. Conclusions

The issue of whether "LCTs are good for airports" is certainly controversial in the air transport industry. From an organizational standpoint, the airports and airlines have diametrically opposite views on the matter. This thesis has tackled two problems that potentially arose in LCT development: operational efficiency and profitability.

- Single pier is the most suitable configuration for LCT since it gives shortest walking distance and also requires smallest construction area.
- Solution with shorter aircraft taxiing distance is more preferable than shorter passenger walking distance.
- The demography of LCC passengers is dominated by young people with relatively low income level who travel for leisure purposes. This characteristic becomes one of the factors that influence passenger behavior toward concessions in LCT.
- The stores with highest potential revenue should be allocated in the more accessible positions with higher passenger flow.
- Sales from the airside still accounts for greater amount of retail revenue. For terminal with low number of non-travelling customers (visitors, well-wishers), more commercial space should be allocated in airside.

With better understanding of the nature of the LCT, including its shortages and opportunities, LCT could become a sustainable concept that can be adopted by many airports all over the world.

# References

[1] Centre of Asia Pacific Aviation, "Low-Cost Airport Terminals Report," CAPA, Sydney, 2009.

[2] Barret, S.D., "How do the demands for airport services differ between full-service carriers and low-cost carriers," Air Transport Management Vol 10, pp. 33-39, 2004.

[3] De Neufville, R., "Accommodating low-cost airlines at main airports," Transportation Research Board (TRB), 2006.

[4] US Federal Aviation Administration. "Economic Values for Evaluation of FAA Investment and Regulatory Program," Office of Aviation Policy, US Department of Transportation, 2007.

[5] Graham, A., "How important are commercial revenues to today's airports," Air Transport Management Vol 15, 106 – 111, 2009.

[6] Hsu, C., Chao, C., "Space allocation for commercial activities at international passenger terminals," Transportation Research E Vol 41, 29 – 51, 2005.